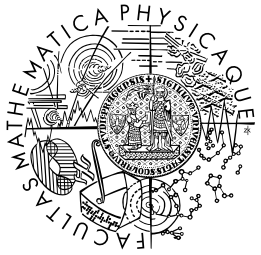

FACULTY
OF MATHEMATICS
AND PHYSICS
Charles University

DOCTORAL THESIS

Viktor Skoupý

Gravitational wave templates from Extreme Mass Ratio Inspirals

Institute of Theoretical Physics

Supervisor of the doctoral thesis:	Georgios Loukes Gerakopoulos, Ph.D.
Study programme:	Theoretical Physics, Astronomy and Astrophysics
Study branch:	P4F1

Prague 2023

I declare that I carried out this doctoral thesis independently, and only with the cited sources, literature and other professional sources. It has not been used to obtain another or the same degree.

I understand that my work relates to the rights and obligations under the Act No. 121/2000 Sb., the Copyright Act, as amended, in particular the fact that the Charles University has the right to conclude a license agreement on the use of this work as a school work pursuant to Section 60 subsection 1 of the Copyright Act.

In ..... date ....

Author's signature

I would like to express my heartfelt gratitude to my supervisor, Georgios Lukes-Gerakopoulos, for his unwavering guidance, invaluable insights, and continuous support throughout the journey of this thesis. I am truly grateful for the enriching discussions and feedback from my formal consultant Tomáš Ledvinka, informal consultant Vojtěch Witzany and other colleagues and collaborators. While there are too many collaborators to name individually, your contributions are deeply acknowledged and greatly appreciated. I extend my deepest appreciation to my family and partner for their unwavering love, encouragement, and constant belief in my abilities. Lastly, I am indebted to all those who contributed to this endeavor, directly or indirectly.

Work on this thesis was supported by the fellowship Lumina Quaeruntur No. LQ100032102 of the Czech Academy of Sciences. Computational resources were provided by the e-INFRA CZ project (ID:90140), supported by the Ministry of Education, Youth and Sports of the Czech Republic.

Title: Gravitational wave templates from Extreme Mass Ratio Inspirals

Author: Viktor Skoupý

Institute: Institute of Theoretical Physics

Supervisor: Georgios Loukes Gerakopoulos, Ph.D., Astronomical Institute of the Czech Academy of Sciences

Abstract: Future space-based gravitational-wave detectors will require highly accurate gravitational wave templates for detecting extreme mass ratio inspirals and estimating their parameters. These templates must include the postadiabatic effects like the spin of the secondary body. Therefore, we investigate the influence of the secondary spin on the motion around a Kerr black hole, calculate the corresponding gravitational-wave fluxes to produce flux-driven inspirals and reveal the shifts of the gravitational-wave phases induced by the secondary's spin. In particular, this study begins by considering eccentric equatorial orbits, where we obtain the constants of motion and fundamental frequencies using the Mathisson-Papapetrou-Dixon equations. Next, we derive the linear-in-spin parts of these quantities. We introduce a new Teukolsky equation solver in the frequency domain to calculate the energy and angular momentum fluxes from these trajectories. We use the obtained fluxes to adiabatically evolve the orbital parameters and to find the spin-induced phase shifts. For off-equatorial orbits, a frequency-domain approach is employed to determine the trajectories in the linear-in-spin regime and to compute the respective fluxes. The agreement between the frequency-domain fluxes and those acquired using an existing time-domain solver verifies our findings.

Keywords: gravitational waves, black holes, perturbation theory, self-force

Contents

Introduction

Gravitational waves (GWs) generated by an inspiral and a subsequent merge of two black holes (BHs) were first detected in 2015 by the LIGO/Virgo collaboration [1]. Subsequently, LIGO/Virgo, joined by KAGRA in later runs, observed many other compact binary inspirals and coalescences [2, 3, 4] including an inspiral of two neutron stars (NSs) [5, 6], a coalescence of two objects with asymmetric masses [7, 8] and a NS-BH coalescence [9]. These detections provided an opportunity to test general relativity and estimate the parameters of such systems with unprecedented precision. While the detectors mentioned above operate in the kHz regime, GWs with nHz frequencies can be detected with pulsar timing arrays. Recently, several collaborations found an evidence of a stochastic GW background [10, 11, 12, 13]. Although the origin of this background has not been verified, one of the prominent candidates are overlapping signals from supermassive black hole binaries. As a result of these detections, a new era of GW astronomy has begun with more GW detectors projects in preparation.

One particular type of in preparation detectors are the space-based detectors like LISA [14], TianQin [15] and Taiji [16]. These detectors will operate in the mHz regime, which lies between the previously mentioned bands. Among the promising sources for the space-based detectors are the extreme mass ratio inspirals (EMRIs) [17]. These systems consist of a stelar-mass compact object such as a BH or a NS orbiting in a close vicinity of a massive BH. The mass ratio $q = \mu/M$ of such binary system, where M is the mass of the the large (primary) BH and μ is the mass of the smaller (secondary) body, lies between 10^{-7} and 10^{-4}.

In an EMRI, the secondary body is slowly inspiraling towards the primary because of gravitational radiation reaction. Energy and angular momentum are slowly carried away in the form of GWs in the 1 mHz band. Because the secondary body is expected to complete between 10^4 and 10^5 densely nested inspiraling orbits in the strong gravity regime, the detection of such GWs will give us a unique opportunity to map the strong-field spacetime around massive BHs. Furthermore, these detections will have an astrophysical impact by allowing us to study the population of massive BHs and a cosmological one by allowing us to determine the expansion history of the Universe through measuring the Hubble constant [17].

To achieve the aforementioned goals, the parameters of each EMRI system must be estimated with high precision. LISA and other similar GW detectors are expected to simultaneously receive many signals from EMRIs and other sources. Since these signals will overlap, matched filtering will be employed to accurately discern them. This method relies on comparing the combined signal with many waveform templates of the expected sources. Although for the detection of strong EMRI signals it might be possible to use simpler kludge models [18], for the detection of weaker signals and for the parameter estimation the templates must be modeled with high accuracy. Because the GW phase accumulates to $\mathcal{O}(q^{-1})$ during the inspiral, to achieve subradian accuracy, the phase must be modeled to subleading order.

The fact that the mass ratio q of an EMRI is very small allows us to employ

perturbation theory to describe it [19]. In this framework, the spacetime can be expanded around the background spacetime of the primary in powers of the mass ratio. Having this in mind, we can study the motion of the secondary body on the background spacetime. While orbiting around the primary body, the secondary is perturbing the background spacetime. Without this perturbation, the motion would be governed by the geodesic equation for a nonspinning secondary and by the Mathisson-Papapetrou-Dixon (MPD) equations for a spinning secondary. When the perturbation is present, it creates a force called the *self-force* which drives the body away from the zeroth-order nonperturbed trajectory. This force has a dissipative part which causes the decay of the orbit, but also a conservative part; it can be expanded in the mass ratio to first-order and second-order self-force.

Because this self-force is of the order of the mass ratio and, thus, the inspiral is slow, we can describe the system as a body moving on an orbit parametrized by given orbital parameters which are slowly evolving on the inspiral timescale, that is much longer than the orbital timescale. This is known as the *two timescale approximation*. Using this approximation, it was proven in [20] that the leading "adiabatic" term of the GW phase can be calculated from the average of the dissipative part of the first-order self-force, while the subleading "postadiabatic" term is composed of three parts: the oscillating piece of the dissipative part of the first-order self-force, the conservative part of the first-order self-force and the average of the dissipative part of the second-order self-force. To achieve subradian accuracy, the postadiabatic term must be taken into account since the adiabatic and postadiabatic terms are $\mathcal{O}(q^{-1})$ and $\mathcal{O}(q^0)$, respectively.

It was proven for a nonspinning secondary [21] that, due to the *flux-balance laws*, the rate of change of the energy and angular momentum of the system is equal to the energy and angular momentum GW flux. In particular, the rate of change of each of these quantities is equal to minus the sum of their flux to infinity and their flux to the horizon of the central BH. Thus, the adiabatic term can be calculated by adiabatically evolving the obits using the fluxes without the need of the full perturbation and the self-force. This fact was also proven for a spinning secondary [22, 23]. Because the spin of the secondary σ is of the order of the mass ratio, the relative spin correction to the fluxes is of $\mathcal{O}(q)$. During the inspiral, this accumulates to $\mathcal{O}(q^0)$ correction to the phases, because the duration is proportional to $\mathcal{O}(q^{-1})$. Therefore, this phase shift is of the same order as the rest of the postadiabatic terms mentioned above and the spin of the secondary must be taken into account to achieve the subradian accuracy.

The computation of fluxes for EMRIs has been widely studied in different setups since the 1990s. Table 1 summarizes works calculating GW fluxes and flux-driven inspirals of various orbital configurations. For brevity, only fully relativistic fluxes are mentioned, i.e. works calculating the fluxes as a post-Newtonian (PN) expansion are omitted. In this thesis we present the calculation of GW fluxes from eccentric equatorial orbits of spinning particles in the Kerr spacetime with aligned spins as introduced in Ref. [39] that is attached in Appendix A.1, along with their linearization in the secondary spin and calculation of the respective adiabatic inspirals as introduced in Ref. [40] that is attached in Appendix A.2. Furthermore, we present the calculation of GW fluxes from generic orbits of spinning particles in the Kerr spacetime as introduced in Ref. [41] attached in

Authors, Ref.	a	e	I	σ	inspirals
Shibata [24], Hughes [25]	✓		✓		
Cutler et al. [26]		✓	✓		
Shibata [27], Glampedakis and Kennefick [28]	✓	✓			
Finn and Thorne [29]	✓				✓
Hughes [30]	✓		✓		✓
Drasco and Hughes [31]	✓	✓	✓		
Han [32], Harms et al. [33]	✓			✓	
Nagar et al. [34], Akcay et al. [22]				✓	
Piovano et al. [35, 36]	✓			✓	✓
Fujita and Shibata [37]	✓	✓			✓
Hughes et al. [38]	✓	✓	✓		✓
Skoupý and Lukes-Gerakopoulos [39]	✓	✓		✓	
Skoupý and Lukes-Gerakopoulos [40]	✓	✓		✓	✓
Skoupý et al. [41]	✓	✓	✓	✓	

Table 1: A summary of works calculating GW fluxes from an EMRI. The simplest cases of work concern circular orbits around a Schwarzschild BH, i.e., the Kerr parameter a and the eccentricity e are zero. While for a primary Kerr BH, the orbits can span from an equatorial one to an inclined one. In this table the second column indicates whether the central BH is spinning ($a \neq 0$) or not; the third column indicates if the orbits are eccentric ($e \neq 0$); the fourth column indicates if the orbits are inclined with respect to the equatorial plane ($I \neq 0$); the fifth column indicates whether the secondary body is spinning ($\sigma \neq 0$) or not. This table extends Table I of Ref. [31] by including later works.

Appendix A.3.

The rest of the thesis is organized as follows. In Chapter 1 the motion of spinning bodies is described with focus given on equatorial and generic orbits in the Kerr spacetime. Chapter 2 deals with the black hole perturbation theory and self-force. In particular, it describes the calculation of the GW fluxes from orbits calculated in the previous chapter. Chapter 3 presents the equations for the adiabatic evolution using these fluxes and the phase shifts due to the secondary spin. Finally, Chapter 4 discusses the numerical methods for the calculation of: equatorial and generic trajectories of spinning particles, the GW fluxes generated by these trajectories and the adiabatic inspirals in the equatorial plane while presenting the respective results.

Notation

Throughout this work, geometric units are used, where the speed of light and the gravitational constant are set to unity as $c = G = 1$. Spacetime indices are denoted by greek letters and run from 0 to 4, whereas tetrad indices are denoted with latin letters from the beginning of the alphabet. A partial derivative is denoted by a comma, like $\partial_\mu U_\nu = U_{\nu,\mu}$, while a covariant derivative is denoted by semicolon, like $\nabla_\mu U_\nu = U_{\nu;\mu}$. The Riemann tensor is defined as $R^\mu{}_{\nu\kappa\lambda} = \Gamma^\mu{}_{\nu\lambda,\kappa} - \Gamma^\mu{}_{\nu\kappa\lambda} + \Gamma^\mu{}_{\rho\kappa}\Gamma^\rho{}_{\nu\lambda} - \Gamma^\mu{}_{\rho\lambda}\Gamma^\rho{}_{\nu\kappa}$ and the sign of the Levi-Civita tensor $\epsilon^{\alpha\beta\gamma\delta}$ is defined as $\epsilon^{0123} = 1/\sqrt{-g}$. The signature of the metric is $(-,+,+,+)$.

1. Dynamics of spinning bodies in curved spacetimes

EMRIs can be modeled as compact spinning bodies moving on a BH background spacetime. For such modeling, we take into account that an isolated extended body can be described by its multipolar expansion given by the Mathisson's gravitational skeleton approach [42, 43]. If the body is compact, i.e., its stress-energy tensor $T^{\mu\nu}$ has a small support in comparison with the characteristic length of the background spacetime, the multipole moments can be defined as [44]

$$\int_{x^0=\text{const}} T^{\mu\nu}\delta x^{\alpha_1}\dots\delta x^{\alpha_n}\sqrt{-g}\,\mathrm{d}^3x\ , \tag{1.1}$$

where $\delta x^\alpha = x^\alpha - z^\alpha$ is a deviation from some representative worldline $z^\alpha(\tau)$ and g is the determinant of the background metric.

For compact bodies like BHs and NSs, the expansion can be truncated at the dipole level leaving only for the approximation the monopole and dipole terms. These multipoles are represented by the linear momentum P^μ and the spin tensor $S^{\mu\nu}$ which are defined as [44]

$$S^{\mu\nu} = \int_{x^0=\text{const}} \left(T^{\nu 0}\delta x^\mu - T^{\mu 0}\delta x^\nu\right)\sqrt{-g}\mathrm{d}^3x\ , \tag{1.2a}$$

$$P^\mu = \int_{x^0=\text{const}} T^{\mu 0}\sqrt{-g}\mathrm{d}^3x + \Gamma^\mu{}_{\rho\sigma}\frac{v^\rho}{v^0}S^{\sigma 0}\ , \tag{1.2b}$$

where $\Gamma^\mu{}_{\rho\sigma}$ is the Christoffel symbol, $v^\mu = \mathrm{d}z^\mu/\mathrm{d}\tau$ is the four-velocity of the representative worldline, and τ is the proper time. We use the adapted coordinates of Kyrian and Semerák [44] where $\delta x^0 = 0$. For covariant derivation see [45].

The stress-energy tensor in this *pole-dipole approximation* can be written as [46, 47]

$$T^{\mu\nu} = \int \mathrm{d}\tau\left(P^{(\mu}v^{\nu)}\frac{\delta^4(x^\sigma - z^\sigma(\tau))}{\sqrt{-g}} - \nabla_\rho\left(S^{\rho(\mu}v^{\nu)}\frac{\delta^4(x^\sigma - z^\sigma(\tau))}{\sqrt{-g}}\right)\right)\ . \tag{1.3}$$

The linear momentum P^μ and the spin tensor $S^{\mu\nu}$ can be reconstructed from the covariant form of the surface integrals (1.2) and the stress-energy tensor (1.3) [48]. This form of the stress energy tensor has been derived from the field outside the body using matched asymptotics [49] and, apart from material bodies, holds for BHs and exotic bodies.

1.1 Mathisson-Papapetrou-Dixon equations

From the conservation law of the stress-energy tensor (1.3) $T^{\mu\nu}{}_{;\nu} = 0$ the MPD equations can be derived in the form

$$\frac{\mathrm{D}P^\mu}{\mathrm{d}\tau} = -\frac{1}{2}R^\mu{}_{\nu\alpha\beta}v^\nu S^{\alpha\beta}\ , \tag{1.4a}$$

$$\frac{\mathrm{D}S^{\mu\nu}}{\mathrm{d}\tau} = P^\mu v^\nu - v^\mu P^\nu\ , \tag{1.4b}$$

where $R^{\mu}{}_{\nu\alpha\beta}$ is the Riemann tensor. These are the evolution equations for the four-momentum P^{μ} and the spin tensor $S^{\mu\nu}$.

However, this system of equations is insufficient to fully describe the evolution since only 10 equations are available for 14 variables $(z^{\mu}, P^{\mu}, S^{\mu\nu})$[1]. This issue is related to the observer-dependence of the center of mass in general relativity. To close the system, a so called spin supplementary condition (SSC)

$$S^{\mu\nu}V_{\nu} = 0 \tag{1.5}$$

must be imposed, where V^{μ} is a timelike vector. For the reference vector V^{μ} the center of mass coincides with the representative worldline. Eq. (1.5) consists of three linearly independent equations. The fourth constraint in our work comes from imposing the normalization of the four-velocity

$$v^{\mu}v_{\mu} = -1 \ . \tag{1.6}$$

Several SSCs have been suggested [50, 51, 52, 44]. In this work we use the Tulczyjew-Dixon SSC [52, 53]

$$S^{\mu\nu}P_{\nu} = 0 \ . \tag{1.7}$$

Under this SSC the mass of the spinning body μ and the magnitude of its spin S defined as

$$\mu = \sqrt{-P^{\mu}P_{\mu}} \ , \qquad S = \sqrt{\frac{S^{\mu\nu}S_{\mu\nu}}{2}} \tag{1.8}$$

are conserved along the evolution.

Once we set the SSC using Eq. (1.7), the four-velocity can be expressed using the four-momentum and spin tensor as [54, 55]

$$v^{\mu} = \frac{\mathsf{m}}{\mu}\left(u^{\mu} + \frac{\frac{1}{2\mu^2}S^{\mu\nu}R_{\nu\rho\kappa\lambda}u^{\rho}S^{\kappa\lambda}}{1+\frac{1}{4\mu^2}R_{\alpha\beta\gamma\delta}S^{\alpha\beta}S^{\gamma\delta}}\right) \ , \tag{1.9}$$

where $\mathsf{m} \equiv -P^{\mu}v_{\mu}$ is the mass of the particle with respect to the four-velocity which can be determined from the four-velocity normalization (1.6) and u^{μ} is specific four-momentum defined as

$$u^{\mu} = \frac{P^{\mu}}{\mu} \ . \tag{1.10}$$

It is convenient to define the spin four-vector S^{μ} as

$$S_{\mu} = -\frac{1}{2}\epsilon_{\mu\nu\rho\sigma}u^{\nu}S^{\rho\sigma} \ , \qquad S^{\mu\nu} = \epsilon^{\mu\nu\rho\sigma}u_{\rho}S_{\sigma} \ . \tag{1.11}$$

It can be proven that $S = \sqrt{S^{\mu}S_{\mu}}$. From the antisymmetry of $\epsilon_{\mu\nu\rho\sigma}$ and Eq. (1.11) it holds that $S^{\mu}u_{\mu} = 0$, while contracting Eq. (1.9) with S^{μ} leads to $S^{\mu}v_{\mu} = 0$. From Eqs. (1.4) and (1.11) the spin vector follows the evolution equation

$$\frac{\mathrm{D}S^{\mu}}{\mathrm{d}\tau} = -\frac{1}{\mu}u^{\mu}R^{*}_{\alpha\beta\gamma\delta}S^{\alpha}v^{\beta}u^{\gamma}S^{\delta} \ , \tag{1.12}$$

[1]Note that the tensor $S^{\mu\nu}$ is skew-symmetric and, thus, has 6 independent components.

where

$$R^*_{\alpha\beta\gamma\delta} = \frac{1}{2} R_{\alpha\beta}{}^{\mu\nu} \epsilon_{\mu\nu\gamma\delta} \tag{1.13}$$

is the right dual of the Riemann tensor.

For the spin magnitude it is convenient to define a dimensionless spin parameter

$$\sigma = \frac{S}{\mu M} \ . \tag{1.14}$$

When the small body is an extremal Kerr BH, the spin magnitude is $S = \mu^2$ and, therefore, $\sigma = q$. Because of this, for an EMRI it holds $\sigma = \mathcal{O}(q)$ and any spin effects of the secondary are suppressed by the first power of the mass ratio. Hence, the motion is often linearized in σ and all the contributions $\mathcal{O}(\sigma^2)$ can be discarded. This justifies why in our calculations for spinning bodies the spin-induced quadrupole moment is neglected.

After linearizing in σ, the four-momentum and four-velocity are parallel, i.e., $P^\mu = \mu v^\mu$, and the MPD equations take the form

$$\frac{\mathrm{D}P^\mu}{\mathrm{d}\tau} = -\frac{1}{2} R^\mu{}_{\nu\alpha\beta} u^\nu S^{\alpha\beta} \ , \tag{1.15a}$$

$$\frac{\mathrm{D}S^{\mu\nu}}{\mathrm{d}\tau} = 0 \tag{1.15b}$$

with the equation for the spin four-vector

$$\frac{\mathrm{D}S^\mu}{\mathrm{d}\tau} = 0 \ . \tag{1.16}$$

1.2 Constants of motion

When the background spacetime is equipped with a Killing vector field ξ^μ satisfying $\xi_{(\mu;\nu)} = 0$, for every such Killing vector there exist a constant of motion in the form [53]

$$\mathcal{C} = \xi^\mu P_\mu - \frac{1}{2} \xi_{\mu;\nu} S^{\mu\nu} \ . \tag{1.17}$$

This constant of motion is conserved even in the nonlinear case. To prove the conservation of $\mathcal{C}$, one can use the identity $\nabla_\alpha \nabla_\gamma \xi_\beta = \xi^\delta R_{\delta\alpha\gamma\beta}$.

In axisymmetric and stationary spacetimes such as the Kerr spacetime there exist two Killing vectors, a timelike one[2] and a spacelike one. The constants of motion that arise from these symmetries are the energy and the component of the total angular momentum parallel to the symmetry axis. However, it was proven that under Tulczyjew-Dixon SSC this system has five degrees of freedom [56] and, thus, two more constants of motion are needed on top of the energy, angular momentum and mass of the body to make the system integrable. No such constants of motion exist in the fully nonlinear case and, therefore, the system is non-integrable. It has been shown numerically that the effect of the non-integrability is driven by quadratic-in-spin terms in the Schwarzschild spacetime [57], which is the nonrotating spherically symmetric limit of the Kerr spacetime.

[2]With the exception of a region called ergoregion near the horizon where both vectors are spacelike.

Rüdiger [58, 59] found two additional quantities which are conserved up to linear order in spin when the spacetime admits a Killing-Yano tensor which satisfies $Y_{(\mu\nu)} = 0$ and $Y_{\mu(\nu;\rho)} = 0$. These quantities can be written as

$$C_Y = Y_{\mu\nu} P^\mu S^\nu \,, \tag{1.18}$$

$$K_R = Y_{\mu\kappa} Y_\nu{}^\kappa P^\mu P^\nu + 2\mu Z_{;\mu} S^\mu + 2\mu^{-1} Y_{\mu\kappa} P^\mu S^\kappa \xi_\nu P^\nu \,, \tag{1.19}$$

where $Z = Y_{\kappa\lambda} Y_{\mu\nu} \epsilon^{\kappa\lambda\mu\nu}/8$ and ξ_ν is the timelike Killing vector. For these quasi-conserved quantities it holds

$$\frac{\mathrm{d}C_Y}{\mathrm{d}\tau} = \mathcal{O}\big(\sigma^2\big) \,, \qquad \frac{\mathrm{d}K_R}{\mathrm{d}\tau} = \mathcal{O}\big(\sigma^2\big). \tag{1.20}$$

Therefore, the system is nearly integrable when linearized in σ.

1.3 Motion in the Kerr spacetime

An EMRI can be described as a small body moving in a Kerr BH spacetime background, which is described by the following metric tensor written in rational polynomial coordinates

$$\begin{aligned} \mathrm{d}s^2 = &-\Big(1 - \frac{2Mr}{\Sigma}\Big)\mathrm{d}t^2 - \frac{4aMr(1-z^2)}{\Sigma}\mathrm{d}t\mathrm{d}\phi \\ &+ \frac{\Sigma}{\Delta}\mathrm{d}r^2 + \frac{\Sigma}{1-z^2}\mathrm{d}z^2 + \frac{(\varpi^4 - a^2\Delta(1-z^2))(1-z^2)}{\Sigma}\mathrm{d}\phi^2 \,, \end{aligned} \tag{1.21}$$

where

$$\begin{aligned} \Sigma &= r^2 + a^2 z^2 \,, \\ \Delta &= r^2 - 2Mr + a^2 \,, \\ \varpi^2 &= r^2 + a^2 \,. \end{aligned}$$

These coordinates are related to the standard Boyer-Lindquist coordinates with $z = \cos\theta$.

This metric tensor has two parameters, namely the mass M and the specific angular momentum a, also known as the Kerr parameter. It describes a rotating BH in vacuum with an outer and an inner horizon located at

$$r_\pm = M \pm \sqrt{M^2 - a^2} \,. \tag{1.22}$$

It is equipped with two Killing vectors, one timelike

$$\xi^\mu_{(t)} \partial_\mu = \partial_t \tag{1.23}$$

related to the stationarirty and one spacelike

$$\xi^\mu_{(\phi)} \partial_\mu = \partial_\phi \tag{1.24}$$

related to the axisymmetry. These vectors satisfy the Killing equation $\xi_{(\mu;\nu)} = 0$. On top of that, there exist a Killing-Yano tensor

$$Y_{\mu\nu}\, \mathrm{d}x^\mu \wedge \mathrm{d}x^\nu = az\, \mathrm{d}r \wedge \Big(\mathrm{d}t - a(1-z^2)\mathrm{d}\phi\Big) + r\, \mathrm{d}z \wedge \Big(a\mathrm{d}t - \varpi^2 \mathrm{d}\phi\Big) \,. \tag{1.25}$$

From this tensor, a Killing tensor $K_{\mu\nu} = Y_{\mu\rho}Y_{\nu}{}^{\rho}$ can be defined, which satisfies $K_{(\mu\nu)} = 0$ and $K_{(\mu\nu;\rho)} = 0$.

Thanks to these symmetries, the following quantities are conserved:

$$E = -\xi^{\mu}_{(t)}u_{\mu} + \frac{1}{2\mu}\xi^{(t)}_{\mu;\nu}S^{\mu\nu} = -u_t + \frac{1}{2\mu}g_{t\mu,\nu}S^{\mu\nu} \,, \tag{1.26}$$

$$J_z = \xi^{\mu}_{(\phi)}u_{\mu} - \frac{1}{2\mu}\xi^{(\phi)}_{\mu;\nu}S^{\mu\nu} = u_{\phi} - \frac{1}{2\mu}g_{\phi\mu,\nu}S^{\mu\nu} \,, \tag{1.27}$$

$$C_Y = \mu^{-1}Y_{\mu\nu}u^{\mu}S^{\nu} \,, \tag{1.28}$$

$$K_R = K_{\mu\nu}u^{\mu}u^{\nu} + 2\mu^{-1}Z_{,\mu}S^{\mu} + 2\mu^{-1}Y_{\mu\kappa}u^{\mu}S^{\kappa}\xi^{(t)}_{\nu}u^{\nu} \,, \tag{1.29}$$

where $Z = arz$. They can be respectively interpreted as the total specific energy measured at infinity, component of the total specific angular momentum parallel to the symmetry axis measured at infinity, projection of the specific spin vector to the total orbital angular momentum and Carter-like constant. Note that the last two quantities are conserved up to linear order in σ.

1.3.1 Motion in the equatorial plane

Because of the reflection symmetry around the equatorial plane in the Kerr spacetime, equatorial orbits can be found much more easily than the generic ones as is shown in this Section. If the particle is confined to the equatorial plane, it must hold $z = 0$ and $v^z = 0$. From the ortoghonality $S^{\mu}v_{\mu} = 0$, all components of the spin vector except the z component must be zero, i.e.,

$$S_{\mu} = S_z\delta^z_{\mu} \,. \tag{1.30}$$

From the normalization of the spin vector, it holds $S_z = rS$, where the sign is chosen such that for the spin aligned with the symmetry axis $S > 0$ and for antialigned spin $S < 0$[3].

Using Eq. (1.11) the nonzero components of the spin tensor can be found as [60]

$$S^{tr} = -S^{rt} = -S\frac{u_{\phi}}{r} \,, \tag{1.31a}$$

$$S^{t\phi} = -S^{\phi t} = S\frac{u_r}{r} \,, \tag{1.31b}$$

$$S^{r\phi} = -S^{\phi r} = -S\frac{u_t}{r} \,. \tag{1.31c}$$

From Eqs. (1.26), (1.27) and (1.31), we can express u_t and u_{ϕ} in terms of E, J_z and σ in the form [60]

$$u_t = \frac{-E + \frac{\sigma M^2}{r^3}(J_z - aE)}{1 - \frac{\sigma^2 M^3}{r^3}} \,, \tag{1.32}$$

$$u_{\phi} = \frac{J_z - \sigma ME - a\frac{\sigma M^2}{r^3}(J_z - aE)}{1 - \frac{\sigma^2 M^3}{r^3}} \,. \tag{1.33}$$

[3]The sign of S_{θ} is opposite if we use Boyer-Lindquist coordinates since $\mathrm{d}\theta/\mathrm{d}z\,\big|_{z=0} = -1$.

Finally, using the four-velocity relation (1.9) and the normalization of the four-momentum, the equations of motion can be reformulated as [61, 39]

$$\Sigma_\sigma \Lambda_\sigma \frac{\mathrm{d}t}{\mathrm{d}\tau} = \frac{\mathsf{m}}{\mu} V^t \,, \tag{1.34a}$$

$$\Sigma_\sigma \Lambda_\sigma \frac{\mathrm{d}r}{\mathrm{d}\tau} = \pm \frac{\mathsf{m}}{\mu} \sqrt{R_\sigma(r)} \,, \tag{1.34b}$$

$$\Sigma_\sigma \Lambda_\sigma \frac{\mathrm{d}\phi}{\mathrm{d}\tau} = \frac{\mathsf{m}}{\mu} V^\phi \,, \tag{1.34c}$$

where

$$\begin{aligned}
\Sigma_\sigma &= r^2 \left(1 - \frac{\sigma^2 M^3}{r^3}\right) , \\
\Lambda_\sigma &= \left(1 + \frac{1}{4\mu^2} R_{\alpha\beta\gamma\delta} S^{\alpha\beta} S^{\gamma\delta}\right) \left(1 - \frac{\sigma^2 M^3}{r^3}\right)^{-1} = 1 - \frac{3\sigma^2 M^3 r x^2}{\Sigma_\sigma^3} \,, \\
\frac{\mathsf{m}}{\mu} &= \Lambda_\sigma \sqrt{\frac{1 - \frac{\sigma^2 M^3}{r^3}}{-1 + 2\Lambda_\sigma - (2 - \Lambda_\sigma)\frac{\sigma^2 M^3}{r^3}}} \,, \\
V^t &= a\left(1 + \frac{3\sigma^2}{r\Sigma_\sigma}\right) x + \frac{\varpi^2}{\Delta} P_\sigma \,, \\
R_\sigma &= P_\sigma^2 - \Delta\left(\frac{\Sigma_\sigma^2}{r^2} + x^2\right) , \\
V^\phi &= \left(1 + \frac{3\sigma^2}{r\Sigma_\sigma}\right) x + \frac{a}{\Delta} P_\sigma \,, \\
P_\sigma &= \Sigma_\sigma E - \left(a + \frac{\sigma}{r}\right) x \,, \\
x &= J_z - (a + \sigma M) E \,.
\end{aligned}$$

It is convenient to switch the parametrization of the equations from proper time τ to a parameter λ similar to the Carter-Mino time defined as

$$\frac{\mathrm{d}\tau}{\mathrm{d}\lambda} = \frac{\mu \Sigma_\sigma \Lambda_\sigma}{\mathsf{m}} = r^2 \sqrt{\left(1 - \frac{\sigma^2 M^3}{r^3}\right)\left(-1 + 2\Lambda_\sigma - (2 - \Lambda_\sigma)\frac{\sigma^2 M^3}{r^3}\right)} \,. \tag{1.35}$$

In this work we are interested in bound orbits which are confined to a region between their turning points $r_2 \leq r \leq r_1$. It is convenient to parametrize the orbit with semi-latus rectum p and eccentricity e, which are defined using the aforementioned turning points as

$$r_1 = \frac{pM}{1 - e} \,, \qquad r_2 = \frac{pM}{1 + e} \tag{1.36}$$

with the inverse relation reading

$$p = \frac{2 r_1 r_2}{M(r_1 + r_2)} \,, \qquad e = \frac{r_1 - r_2}{r_1 + r_2} \,. \tag{1.37}$$

Then it is possible to find the constants of motion E and J_z as functions of these orbital parameters. To do this, in [39] we used a similar approach to the one used

for geodesic motion in Ref. [62]. At the turning points the radial velocity from Eq. (1.34b) must vanish, i.e.

$$R_\sigma(r_1) = 0 \,, \qquad R_\sigma(r_2) = 0 \,. \tag{1.38}$$

This is a set of quadratic equations for E and J_z which can be solved as

$$E = \frac{\kappa\rho + 2\tilde{\sigma}\Big(\epsilon - \operatorname{sgn} J_z\sqrt{\epsilon^2 + \kappa\zeta}\Big)}{\rho^2 + 4\eta\tilde{\sigma}} \,, \tag{1.39a}$$

$$J_z = \frac{-2\kappa\eta + \rho\Big(\epsilon - \operatorname{sgn} J_z\sqrt{\epsilon^2 + \kappa\zeta}\Big)}{(\rho^2 + 4\eta\tilde{\sigma})E} \,, \tag{1.39b}$$

where the coefficients κ, ρ, $\tilde{\sigma}$, ϵ, ζ, and η are functions of a, p, e, and σ as defined in Eqs. (33), (36), and (37) in [39]. The sign of J_z is positive for prograde orbits and negative for retrograde orbits.

Using Eqs. (1.34) it is possible to find the orbital frequencies. To achieve this, we reparametrize the orbits using the relativistic anomaly χ_r defined as

$$r = \frac{pM}{1 + e\cos\chi_r} \,. \tag{1.40}$$

Then, the equations of motion for t and ϕ in the *Darwin parametrization* read, respectively,

$$\frac{\mathrm{d}t}{\mathrm{d}\chi_r} = V^t(r(\chi_r))\sqrt{\frac{1-e^2}{p^2 J(\chi_r)}} \,, \tag{1.41a}$$

$$\frac{\mathrm{d}\phi}{\mathrm{d}\chi_r} = V^\phi(r(\chi_r))\sqrt{\frac{1-e^2}{p^2 J(\chi_r)}} \,, \tag{1.41b}$$

where $J(\chi_r)$ is defined in Eq. (B8) in Ref. [40].

The motion from the pericenter to the apocenter and back to the pericenter corresponds to χ_r going from 0 to 2π. Therefore, the time and the azimuthal phase accumulated between two successive passages through the pericenter reads, respectively,

$$T_r = 2\frac{\sqrt{1-e^2}}{p}\int_0^\pi \frac{V^t(r(\chi_r))}{\sqrt{J(\chi_r)}}\mathrm{d}\chi_r \,, \tag{1.42a}$$

$$\Delta\phi = 2\frac{\sqrt{1-e^2}}{p}\int_0^\pi \frac{V^\phi(r(\chi_r))}{\sqrt{J(\chi_r)}}\mathrm{d}\chi_r \,, \tag{1.42b}$$

where we used the fact that the integrand is even around $\chi_r = \pi$. Then, the coordinate-time frequencies can be expressed as

$$\Omega_r = \frac{2\pi}{T_r} \,, \qquad\qquad \Omega_\phi = \frac{\Delta\phi}{T_r} \,. \tag{1.43a}$$

The evolution of the coordinate time and the azimuthal coordinate can be expressed as a linearly growing part plus an oscillating part as

$$t(\chi_r) = \frac{T_r}{2\pi}\chi_r + \sum_{n=1}^{\infty} t_n \sin(n\chi_r) \,, \tag{1.44a}$$

$$\phi(\chi_r) = \frac{\Delta\phi}{2\pi}\chi_r + \sum_{n=1}^{\infty} \phi_n \sin(n\chi_r) \,, \tag{1.44b}$$

where the Fourier coefficients can be found using the cosine transform as

$$t_n = 2\frac{\sqrt{1-e^2}}{\pi np}\int_0^\pi \frac{V^t(r(\chi_r))}{\sqrt{J(\chi_r)}}\cos(n\chi_r)\mathrm{d}\chi_r \ , \tag{1.45a}$$

$$\phi_n = 2\frac{\sqrt{1-e^2}}{\pi np}\int_0^\pi \frac{V^\phi(r(\chi_r))}{\sqrt{J(\chi_r)}}\cos(n\chi_r)\mathrm{d}\chi_r \ . \tag{1.45b}$$

Here we assume that the particle starts at the pericenter. For generic initial phases χ_{r0} and ϕ_0 the relations read

$$t(\chi_r) = \check{t}(\chi_r + \chi_{r0}) - \check{t}(\chi_{r0}) \ , \tag{1.46a}$$

$$r(\chi_r) = \check{r}(\chi_r + \chi_{r0}) \ , \tag{1.46b}$$

$$\phi(\chi_r) = \phi_0 + \check{\phi}(\chi_r + \chi_{r0}) - \check{\phi}(\chi_{r0}) \ . \tag{1.46c}$$

The check mark denotes the fiducial trajectory with zero initial phases.

Linearization in the secondary spin

As was stated earlier, it is reasonable to linearize the system in σ. There are several options how to do this linearization which depend on the reference geodesic. Any geodesics can be used as a reference, however, there are few choices that are more convenient for our calculations.

The first method, on which we focus, relies on fixing the orbital parameters p and e and expanding various quantities as

$$f(p,e,\sigma) = p^{(\mathrm{g})}(p,e) + \sigma\ \delta f\Big|_{p,e}(p,e) + \mathcal{O}\big(\sigma^2\big) \ , \tag{1.47}$$

where

$$f^{(\mathrm{g})}(p,e) = f(p,e,0) \ , \qquad \delta f\Big|_{p,e}(p,e) = \frac{\partial f}{\partial\sigma}\bigg|_{\sigma=0} \ . \tag{1.48}$$

The orbital frequencies are then linearized as

$$\Omega_i(p,e,\sigma) = \Omega_i^{(\mathrm{g})}(p,e) + \sigma\delta\Omega_i(p,e) + \mathcal{O}\big(\sigma^2\big) \ . \tag{1.49}$$

The advantage of this method is that the quantities such as the frequencies or constants of motion are often formulated as functions of p, e, and σ.

However, for other quantities such a energy and angular momentum fluxes, it is convenient to linearize them with respect to a geodesic with the same frequencies. Formally, we can write

$$f(\Omega_i,\sigma) = f^{(\mathrm{g})}(\Omega_i) + \sigma\ \delta f\Big|_{\Omega_i}(\Omega_i) + \mathcal{O}\big(\sigma^2\big) \ , \tag{1.50}$$

where

$$f^{(\mathrm{g})}(\Omega_i) = f(\Omega_i,0) \ , \qquad \delta f\Big|_{\Omega_i}(\Omega_i) = \frac{\partial f}{\partial\sigma}\bigg|_{\sigma=0} \ . \tag{1.51}$$

The linear parts $\delta f|_{p,e}$ and $\delta f|_{\Omega_i}$ are in general different and it is possible to calculate one from the other. To find the relation between them, we linearize the orbital parameters as

$$p(\Omega_i, \sigma) = p^{(\mathrm{g})}(\Omega_i) + \sigma \delta p(\Omega_i) + \mathcal{O}\left(\sigma^2\right) , \tag{1.52a}$$

$$e(\Omega_i, \sigma) = e^{(\mathrm{g})}(\Omega_i) + \sigma \delta e(\Omega_i) + \mathcal{O}\left(\sigma^2\right) . \tag{1.52b}$$

However, the dependence of p and e on Ω_i is not known in general. To find the linear parts, one can use the relations [40]

$$\delta p = \frac{\frac{\partial \Omega_\phi^{(\mathrm{g})}}{\partial e}\delta\Omega_r - \frac{\partial \Omega_r^{(\mathrm{g})}}{\partial e}\delta\Omega_\phi}{\left|J_{(\Omega_i)}\right|} , \tag{1.53a}$$

$$\delta e = \frac{-\frac{\partial \Omega_\phi^{(\mathrm{g})}}{\partial p}\delta\Omega_r + \frac{\partial \Omega_r^{(\mathrm{g})}}{\partial p}\delta\Omega_\phi}{\left|J_{(\Omega_i)}\right|} , \tag{1.53b}$$

where the Jacobian determinant is

$$\left|J_{(\Omega_i)}\right| = \frac{\partial \Omega_r^{(\mathrm{g})}}{\partial p}\frac{\partial \Omega_\phi^{(\mathrm{g})}}{\partial r} - \frac{\partial \Omega_r^{(\mathrm{g})}}{\partial r}\frac{\partial \Omega_\phi^{(\mathrm{g})}}{\partial p} \tag{1.54}$$

and $\delta\Omega_i$ are from Eq. (1.49). δp and δe calculated from Eq. (1.53) are functions of p and e and they can be interpreted as shift in p and e when a geodesic with orbital parameters p and e is perturbed by the spin, while keeping the frequencies fixed.

Linear parts of other quantities such as energy or angular momentum with fixed frequencies can be calculated as

$$\delta f\Big|_{\Omega_i}(p,e) = \delta f\Big|_{p,e} + \frac{\partial f^{(\mathrm{g})}}{\partial p}\delta p + \frac{\partial f^{(\mathrm{g})}}{\partial e}\delta e . \tag{1.55}$$

This is again a function of p and e which can be understood as the orbital parameters of the reference geodesics.

To calculate the linear part of the coordinate time and the azimuthal coordinate as functions of χ_r, the formulas (1.45) can be linearized. The linear part of the radial coordinate with fixed frequencies reads

$$\delta r(\chi_r) = \frac{\delta p M}{1 + e\cos\chi_r} - \frac{pM\delta e\cos\chi_r}{(1+e\cos\chi_r)^2} . \tag{1.56}$$

1.3.2 Offequatorial motion

The off-equatorial motion is much more involved and, so far, in the linear-in-spin regime it has been solved only by Witzany using Hamilton-Jacobi equation [63] and by Drummond and Hughes in the frequency domain [64, 65]. Here we describe the latter approach.

When the system is linearized in the secondary spin, Eq. (1.16) can be written as

$$\frac{\mathrm{d}S^\mu}{\mathrm{d}\tau} + \Gamma^\mu{}_{\alpha\beta}u^\alpha S^\beta = 0 . \tag{1.57}$$

Since the vector S^μ is proportional to σ, we can neglect the linear-in-spin contribution to $\Gamma^\mu{}_{\alpha\beta}$ and u^β and take their geodesic values. Then, Eq. (1.57) describes a vector S^μ parallely transported on a geodesic. This topic was studied by Marck in Ref. [66]. It is convenient to describe the parallel transport in tetrad formalism, where some of the tetrad legs are parallel transported. The zeroth leg can be constructed from the geodesic velocity $\hat{u}^\mu$

$$e_{0\mu}\mathrm{d}x^\mu = -\hat{E}\,\mathrm{d}t + \frac{\frac{\mathrm{d}\hat{r}}{\mathrm{d}\lambda}}{\Delta}\,\mathrm{d}r + \frac{\frac{\mathrm{d}\hat{z}}{\mathrm{d}\lambda}}{1-z^2}\,\mathrm{d}z + \hat{L}_z\,\mathrm{d}\phi \tag{1.58a}$$

which is parallel transported from the definition. The hat denotes quantities related to the reference geodesics[4]. Another leg can be defined as the normalized total orbital angular momentum $l^\mu = Y_\nu{}^\mu \hat{u}^\nu$ which is parallel transported because of the properties of the Killing-Yano tensor. The components of this tetrad leg read

$$\begin{aligned} e_{3\mu}\mathrm{d}x^\mu = \frac{1}{\sqrt{\hat{K}}}\Bigg(& a\frac{r\frac{\mathrm{d}\hat{z}}{\mathrm{d}\lambda} + z\frac{\mathrm{d}\hat{r}}{\mathrm{d}\lambda}}{\Sigma}\mathrm{d}t - az\frac{\varpi^2\hat{E} - a\hat{L}_z}{\Delta}\mathrm{d}r \\ & - r\frac{(1-z^2)a\hat{E} - \hat{L}_z}{1-z^2}\mathrm{d}z - \frac{a^2 z(1-z^2)\frac{\mathrm{d}\hat{r}}{\mathrm{d}\lambda} + r\varpi^2\frac{\mathrm{d}\hat{z}}{\mathrm{d}\lambda}}{\Sigma}\mathrm{d}\phi\Bigg)\,. \end{aligned} \tag{1.58b}$$

The remaining legs e_1^μ and e_2^μ are chosen such that they are orthogonal to e_0^μ and e_3^μ. Their components are

$$\begin{aligned} e_{1\mu}\mathrm{d}x^\mu = \frac{1}{\sqrt{\hat{K}}}\Bigg(& \frac{-\Xi r\frac{\mathrm{d}\hat{r}}{\mathrm{d}\lambda} + \frac{a^2 z}{\Xi}\frac{\mathrm{d}\hat{z}}{\mathrm{d}\lambda}}{\Sigma}\mathrm{d}t + \Xi r\frac{\varpi^2\hat{E} - a\hat{L}_z}{\Delta}\mathrm{d}r \\ & - \frac{az}{\Xi}\frac{(1-z^2)a\hat{E} - \hat{L}_z}{1-z^2}\mathrm{d}z + a\frac{\Xi r(1-z^2)\frac{\mathrm{d}\hat{r}}{\mathrm{d}\lambda} - \frac{z}{\Xi}\varpi^2\frac{\mathrm{d}\hat{z}}{\mathrm{d}\lambda}}{\Sigma}\mathrm{d}\phi\Bigg)\,, \end{aligned} \tag{1.58c}$$

$$\begin{aligned} e_{2\mu}\mathrm{d}x^\mu = & \left(-\frac{\hat{E}}{\Xi} + \frac{(1-\Xi^2)(\varpi^2\hat{E} - a\hat{L}_z)}{\Xi\Sigma}\right)\mathrm{d}t + \frac{\Xi}{\Delta}\frac{\mathrm{d}\hat{r}}{\mathrm{d}\lambda}\mathrm{d}r \\ & + \frac{1}{\Xi(1-z^2)}\frac{\mathrm{d}\hat{z}}{\mathrm{d}\lambda}\mathrm{d}z + \left(\Xi\hat{L}_z - \frac{(1-\Xi^2)\varpi^2((1-z^2)a\hat{E} - \hat{L}_z)}{\Xi\Sigma}\right)\mathrm{d}\phi\,, \end{aligned} \tag{1.58d}$$

where

$$\Xi = \sqrt{\frac{\hat{K} - a^2 z^2}{\hat{K} + r^2}}\,, \tag{1.59}$$

and they are not parallel transported.

In this tetrad the solution takes a simple form

$$S^\mu = S_\perp(\cos\psi_p e_1^\mu + \sin\psi_p e_2^\mu) + S_\parallel e_3^\mu \tag{1.60}$$

[4]Note that, to keep the notation similar with the original papers, we denote the geodesic part of equatorial quantities with superscript (g) and of offequatorial quantities with a hat. Linear-in-spin parts are denoted with δ for equatorial quantities and with subscript or superscript S for offequatorial quantities.

where ψ_p is a function of time and $S_\perp$ and $S_\parallel$ are constants which satisfy $S_\parallel^2 + S_\perp^2 = S^2$. The spin vector can be interpreted as a vector precessing around the total orbital angular momentum with precession phase ψ_p satisfying the evolution equation

$$\frac{\mathrm{d}\psi_p}{\mathrm{d}\lambda} = -\sqrt{\hat{K}}\left(\frac{(r^2+a^2)\hat{E} - a\hat{L}_z}{\hat{K}+r^2} + a\frac{\hat{L}_z - a(1-z^2)\hat{E}}{\hat{K}-a^2z^2}\right) , \tag{1.61}$$

where λ is the Carter-Mino time satisfying $\mathrm{d}\tau/\mathrm{d}\lambda = \Sigma$. The average rate of change of ψ_p can be interpreted as the (Carter-Mino time) frequency Υ_s. Analytic solution for Υ_s and $\psi_p(\lambda)$ was found by van de Meent in [67].

The constant $S_\parallel$ represents the projection of the spin vector to the orbital angular momentum and is related to the Rüdiger's constant as $C_Y = \sqrt{\hat{K}}S_\parallel$.

Description in the frequency domain

Drummond and Hughes [64, 65] found a procedure to numerically calculate the linear correction to the trajectory in frequency domain with respect to a reference geodesic with the same orbital parameters p, e and I, where p and e are defined in Eqs. (1.37) and I is defined from the polar turning point z_1 as $\sin I = z_1$. Because in the generic case the radial turning point depends on z and the polar turning point depends on r, the orbit is parametrized as follows

$$r = \frac{pM}{1 + e\cos(\Upsilon_r\lambda + \delta\hat{\chi}_r(\lambda) + \delta\chi_r^S(\lambda))} + \mathfrak{r}^S(\lambda) , \tag{1.62a}$$

$$z = \sin I \cos\Big(\Upsilon_z\lambda + \delta\hat{\chi}_z(\lambda) + \delta\chi_z^S(\lambda)\Big) + \mathfrak{z}^S(\lambda) , \tag{1.62b}$$

where $\mathfrak{r}^S(\lambda)$ and $\mathfrak{z}^S(\lambda)$ represent the corrections to the turning points and they average to zero.

The radial and polar frequencies with respect to the Carter-Mino time are

$$\Upsilon_r = \hat{\Upsilon}_r + \Upsilon_r^S , \tag{1.62c}$$

$$\Upsilon_z = \hat{\Upsilon}_z + \Upsilon_z^S . \tag{1.62d}$$

Corrections to the four-velocity are parametrized as

$$u_t = -\hat{E} + u_t^S(\lambda) , \tag{1.62e}$$

$$u_\phi = \hat{L}_z + u_\phi^S(\lambda) . \tag{1.62f}$$

In these equations the hat denotes geodesic quantities and the superscript S denotes the linear-in-spin parts.

Quantities in Eqs. (1.62) can be decomposed into Fourier modes as

$$u_{t,\phi}^S = \sum_{n,k,j} u_{t,\phi,nkj} e^{-in\Upsilon_r\lambda - ik\Upsilon_z\lambda + ij\Upsilon_s\lambda} , \tag{1.63a}$$

$$\delta\chi_r^S = \sum_{n\neq 0} \delta\chi_{r,n}^S e^{-in\Upsilon_r\lambda} , \tag{1.63b}$$

$$\delta\chi_z^S = \sum_{k\neq 0} \delta\chi_{z,k}^S e^{-ik\Upsilon_z\lambda} , \tag{1.63c}$$

$$\mathfrak{r}^S = \sum_{n,k,j} \mathfrak{r}_{nkj} e^{-in\Upsilon_r\lambda - ik\Upsilon_z\lambda + ij\Upsilon_s\lambda} \,, \tag{1.63d}$$

$$\mathfrak{z}^S = \sum_{n,k,j} \mathfrak{z}_{nkj} e^{-in\Upsilon_r\lambda - ik\Upsilon_z\lambda + ij\Upsilon_s\lambda} \,, \tag{1.63e}$$

where n and k are summed from $-\infty$ to $+\infty$ and j from -1 to 1. In Eq. (1.63d) k and j cannot be simultaneously zero and in Eq. (1.63e) n and j cannot be simultaneously zero. After expanding Eqs. (1.15a) and (1.6) to linear order in σ, the Fourier coefficients in Eqs. (1.63) with the corrections to the frequencies can be found as a solution to a system of linear equations.

Because the frequencies of a trajectory of a spinning particle are different from the geodetic frequencies, when the deviation of the coordinates is calculated, it contains a secularly growing part [64, 65]. Therefore, it is convenient to parametrize the orbit with phases defined as

$$w_r = \Upsilon_r \lambda \,, \tag{1.64a}$$

$$w_z = \Upsilon_z \lambda \,, \tag{1.64b}$$

$$w_s = \Upsilon_s \lambda \,. \tag{1.64c}$$

Then we can find the corrections to the coordinates as $r = \hat{r}(w_r) + r^S(w_r, w_z, w_s)$ and $z = \hat{z}(w_z) + z^S(w_r, w_z, w_s)$, where

$$r^S = \frac{peM\delta\chi_r^S(w_r)\sin(w_r + \delta\hat{\chi}_r(w_r))}{(1 + e\cos(w_r + \delta\hat{\chi}_r(w_r)))^2} + \mathfrak{r}^S(w_r, w_z, w_s) \,, \tag{1.65a}$$

$$z^S = -\sin I \delta\chi_z^S(w_z)\sin(w_z + \delta\hat{\chi}_z(w_z)) + \mathfrak{z}^S(w_r, w_z, w_s) \,. \tag{1.65b}$$

To find the corrections to the frequencies Γ and Υ_ϕ, one has to calculate the linear part of the four-velocity with respect to Carter-Mino time

$$U^\mu = \Sigma u^\mu = \hat{U}^\mu + U_S^\mu \tag{1.66}$$

and calculate the average of $U_S^{t,\phi}$, i.e., the Fourier component $U_{S,000}^{t,\phi}$. Then, the coordinate frequencies can be found as

$$\Omega_r = \frac{\hat{\Upsilon}_r + \Upsilon_r^S}{\hat{\Gamma} + \Gamma^S} \,, \tag{1.67a}$$

$$\Omega_z = \frac{\hat{\Upsilon}_z + \Upsilon_z^S}{\hat{\Gamma} + \Gamma^S} \,, \tag{1.67b}$$

$$\Omega_s = \frac{\hat{\Upsilon}_s + \Upsilon_s^S}{\hat{\Gamma} + \Gamma^S} \,. \tag{1.67c}$$

Similarly, from the four-velocity U^μ, the coordinate time $t(\lambda)$ and the azimuthal coordinate $\phi(\lambda)$ can be calculated. As in the geodesic case, they can be written as a secularly growing part and an oscillating part as

$$t(\lambda) = \Gamma\lambda + \Delta t(\Upsilon_r\lambda, \Upsilon_z\lambda, \Upsilon_s\lambda) \,, \tag{1.68}$$

$$\phi(\lambda) = \Upsilon_\phi\lambda + \Delta t(\Upsilon_r\lambda, \Upsilon_z\lambda, \Upsilon_s\lambda) \,, \tag{1.69}$$

where the linear corrections to the oscillating parts can be found using Eq. (35) in Ref. [41].

2. Perturbation theory and the self-force

Because it is not possible to calculate the dynamical spacetime describing an EMRI analytically or by numerically evolving the Einstein equations, perturbation theory is often used instead [68, 19]. In the perturbation framework the exact spacetime $g_{\mu\nu}^{\text{exact}}$ which captures both the fields of the primary and the secondary along with the gravitational radiation, can be expanded in the mass ratio as

$$g_{\mu\nu}^{\text{exact}} = g_{\mu\nu} + \epsilon h_{\mu\nu}^{(1)} + \epsilon^2 h_{\mu\nu}^{(2)} + \mathcal{O}\left(\epsilon^3\right) = g_{\mu\nu} + h_{\mu\nu} \ , \tag{2.1}$$

where $g_{\mu\nu}$ is the unperturbed background spacetime of the primary BH, $h_{\mu\nu}^{(n)}$ is the n-th order perturbation and ϵ is a bookkeeping parameter counting the powers of the mass ratio and it can be later set to 1. The series is often truncated at second order in ϵ since such approximation is sufficient for EMRI modelling [20]. The stress-energy tensor of the secondary body is expanded in the mass ratio as well as $T^{\mu\nu} = \epsilon T_{(1)}^{\mu\nu} + \epsilon^2 T_{(2)}^{\mu\nu}$. Terms proportional to the secondary spin are present in $T_{(2)}^{\mu\nu}$ since $S = \mathcal{O}(\epsilon^2)$. After expanding the Einstein's field equations, the zeroth order corresponds to vacuum Einstein's equations whose solution is the Kerr spacetime. The next two orders read

$$\delta G_{\mu\nu}[h^{(1)}] = T_{\mu\nu}^{(1)} \ , \tag{2.2a}$$

$$\delta G_{\mu\nu}[h^{(2)}] = T_{\mu\nu}^{(2)} - \delta^2 G_{\mu\nu}[h^{(1)}, h^{(1)}] \ , \tag{2.2b}$$

where $\delta G_{\mu\nu}$ and $\delta^2 G_{\mu\nu}$ are the first and second order terms in the expansion of the Einstein tensor and their form can be found in Eqs. (3)-(6) in [19]. In this work we discard the second term on the right hand side of Eq. (2.2b) and solve the equations as[1]

$$\delta G_{\mu\nu}[h^{(1)} + h^{(2)S}] = T_{\mu\nu} \tag{2.3}$$

with the unexpanded skeleton source from Eq. (1.3) and $h^{(2)S}$ denoting the term linear in S. This approach is justified because we take into account only the terms linear in the mass of the particle μ and in the secondary spin S, i.e., we neglect the quadratic term which can be treated separately [23].

The perturbation $h_{\mu\nu}$ can be split into a singular field $h_{\mu\nu}^{\mathcal{S}}$ and a regular field $h_{\mu\nu}^{\mathcal{R}}$, i.e. $h_{\mu\nu} = h_{\mu\nu}^{\mathcal{R}} + h_{\mu\nu}^{\mathcal{S}}$. The regular field satisfies the homogeneous Einstein's equations and the singular field, which is derived using matched asymptotics method [69, 70], captures the local behavior of the spacetime around the secondary body. It has been proven that according to the *generalized equivalence principle* the motion of the secondary body with any multipole structure can be described as a motion of a particle in an effective metric given by $\tilde{g}_{\mu\nu} = g_{\mu\nu} + h_{\mu\nu}^{\mathcal{R}}$ [71]. In order to find the equations of motion for a spinning secondary in the background spacetime $g_{\mu\nu}$, the MPD equations (1.15) are expanded in the mass ratio. After the expansion of the covariant derivative and the Riemann tensor to first order in σ and ϵ and correcting the proper time using Eq. (36) that can be

[1] Instead of these equation, we use Teukolsky formalism described in Section 2.1

found in Ref. [72], we obtain

$$\frac{\mathrm{D}^2 z^\mu}{\mathrm{d}\tau^2} = -\frac{1}{2} R^\mu{}_{\nu\alpha\beta} u^\nu s^{\alpha\beta} \Big(1 - \frac{1}{2} h^{\mathcal{R}}_{\rho\sigma} u^\rho u^\sigma\Big) - \frac{1}{2} P^{\mu\nu} \Big(\Big(2h^{\mathcal{R}}_{\nu\rho;\sigma} - h^{\mathcal{R}}_{\rho\sigma;\nu}\Big) u^\rho u^\sigma - \Big(2h^{\mathcal{R}}_{\nu(\sigma;\alpha)\beta} - h^{\mathcal{R}}_{\sigma\alpha;\nu\beta}\Big) u^\sigma s^{\alpha\beta}\Big) \,, \tag{2.4a}$$

$$\frac{\mathrm{D}s^{\mu\nu}}{\mathrm{d}\tau} = u^\rho s^{\sigma[\mu} g^{\nu]\lambda} \Big(h^{\mathcal{R}}_{\lambda\rho;\sigma} + h^{\mathcal{R}}_{\lambda\sigma;\rho} - h^{\mathcal{R}}_{\rho\sigma;\nu}\Big) \,, \tag{2.4b}$$

where z^μ is the position of the particle, $s^{\mu\nu} = S^{\mu\nu}/\mu$ is the specific spin tensor, and $P^{\mu\nu} = g^{\mu\nu} + u^\mu u^\nu$ is orthogonal projector to the four-velocity. The first term in Eq. (2.4a) can be interpreted as the spin-curvature force with a correction to the proper time. The first term in the parentheses on the second line reduces to the MiSaTaQuWa force [73, 74] for zero spin and the second term in the parentheses represents correction to the spin-curvature force induced by the metric perturbation. Eqs. (2.4) can be interpreted as the MPD equations in the background spacetime with additional terms which we call the self-force and self-torque. In general, the force terms can be split into terms proportional to ϵ which are called first-order self-force and terms proportional to ϵ^2 called second-order self-force. Eqs. (2.4) are identical to Eqs. (6) in [23] with some second-order terms neglected.

To solve the whole inspiral directly from the field equations (2.2) and the equations of motion (2.4) is a difficult task since they are coupled and both systems of equations must be solved simultaneously. Therefore, several approximations must be used. One of these, the *two timescale approximation* [20], relies on the separation of the orbital and radiation-reaction timescales. Since the loss of energy and angular momentum is of the order of the mass ratio, these parameters evolve on much slower timescale than is the orbital timescale. The governing equations can be separated into equations for variables evolving in the fast (orbital) timescale and for those evolving in the slow (radiation-reaction) timescale. Therefore, the evolution can be interpreted as an orbit with slowly evolving parameters, which would be constant without the presence of the self-force. When the system is described with action-angle variables, the evolution of the angles ψ^μ can be expressed as

$$\psi^\mu = \frac{1}{q}\Big(\psi^\mu_0(qt) + q\psi^\mu_1(qt) + \mathcal{O}\Big(q^2\Big)\Big) \,, \tag{2.5}$$

where the terms in the parentheses are respectively called the *adiabatic* and *postadiabatic* term. To find the adiabatic term, only the time average of the dissipative (time-antisymmetric) part of the first-order self-force is needed, as was first proven by Mino [21]. For the postadiabatic term, the rest of the first order self-force, i.e. the oscillating dissipative part and the conservative (time-symmetric) part, is needed along with the time average of the dissipative part of the second order self-force.

The angle variables (2.5) are directly related to the GW phases. Thus, Eq. (2.5) shows that during the inspiral, $\mathcal{O}(q^{-1})$ radians are accumulated in the leading term before the plunge. In order to accurately model the waveform with subradian precision, the postadiabatic term must be taken into account as well.

Thanks to the flux-balance laws [21, 75], the adiabatic term can be found using asymptotic fluxes to infinity and through the horizon of the central BH.

Thus, one can avoid the local calculation of the self-force and its regularization. For an EMRI with spinning secondary it was proven [22, 23] from Eqs. (2.4) that the asymptotic fluxes of energy and angular momentum are equal to the rate of change of energy and angular momentum of the system defined in Eqs. (1.26) and (1.27). Since the spin contribution to the fluxes is $\mathcal{O}(\sigma) = \mathcal{O}(q)$, it influences the phase at the postadiabatic order. This suggest that only the spin contribution to the fluxes is needed without the calculation of the spin-dependence of the local self-force, at least in the equatorial plane, where only energy and angular momentum are needed to parametrize the orbits. Thus, the rest of this Chapter describes the calculation of the asymptotic GW fluxes from orbits of spinning particles in the Kerr spacetime.

2.1 Gravitational-wave fluxes

To calculate the GW fluxes in a Kerr background, we employ the Newmann-Penrose formalism in which all tensorial quantities are projected into a null tetrad l^μ, n^μ, m^μ, and $\bar{m}^\mu$, where the bar denotes a complex conjugate. We use the Kinnersley tetrad [76]

$$l^\mu \partial_\mu = \frac{\varpi^2}{\Delta}\partial_t + \partial_r + \frac{a}{\Delta}\partial_\phi \,, \tag{2.6a}$$

$$n^\mu \partial_\mu = \frac{\varpi^2}{2\Sigma}\partial_t - \frac{\Delta}{2\Sigma}\partial_r + \frac{a}{2\sigma}\partial_\phi \,, \tag{2.6b}$$

$$m^\mu \partial_\mu = \frac{\sqrt{1-z^2}}{\bar{\zeta}\sqrt{2}}\left(ia\partial_t - \partial_z + \frac{i}{1-z^2}\partial_\phi\right) , \tag{2.6c}$$

where $\bar{\zeta} = r + iaz$. The GW fluxes to infinity and through the horizon of the BH are encoded in the perturbation of the Weyl scalars

$$\Psi_0 = -C_{\alpha\beta\gamma\delta} l^\alpha m^\beta l^\gamma m^\delta \,, \tag{2.7a}$$

$$\Psi_4 = -C_{\alpha\beta\gamma\delta} n^\alpha \bar{m}^\beta n^\gamma \bar{m}^\delta \,, \tag{2.7b}$$

where $C_{\alpha\beta\gamma\delta}$ is the Weyl tensor. At large radius the dominant components of the metric perturbation in the radiation gauge are h_{mm} and $h_{\bar{m}\bar{m}} \equiv h = h_+ - ih_\times$, where h is the strain and $h_{+,\times}$ are the polarizations. From Eq. (2.7b) the strain at infinity is related to Ψ_4 as

$$\Psi_4(r \to \infty) = -\frac{1}{2}\frac{\mathrm{d}^2 h}{\mathrm{d}t^2} \,. \tag{2.8}$$

2.1.1 Teukolsky equation

Teukolsky found a decoupled master equation [77]

$$\begin{aligned}\left(\frac{(r^2+a^2)^2}{\Delta} - a^2(1-z^2)\right)\frac{\partial^2 {}_s\psi}{\partial t^2} + \frac{4Mar}{\Delta}\frac{\partial^2 {}_s\psi}{\partial t \partial \phi} + \left(\frac{a^2}{\Delta} - \frac{1}{1-z^2}\right)\frac{\partial^2 {}_s\psi}{\partial \phi^2} \\ - \Delta^{-s}\frac{\partial}{\partial r}\left(\Delta^{s+1}\frac{\partial_s \psi}{\partial r}\right) - \frac{\partial}{\partial z}\left((1-z^2)\frac{\partial_s \psi}{\partial z}\right) - 2s\left(\frac{a(r-M)}{\Delta} + \frac{iz}{1-z^2}\right)\frac{\partial_s \psi}{\partial \phi} \\ - 2s\left(\frac{M(r^2-a^2)}{\Delta} - r - iaz\right)\frac{\partial_s \psi}{\partial t} + \left(\frac{s^2 z^2}{1-z^2} - s\right){}_s\psi = 4\pi\Sigma T\end{aligned} \tag{2.9}$$

for a linear perturbation of the Kerr metric expressed by the spin-weighted variable ${}_s\psi$ describing different field perturbations. In particular, for $s = 0$ we have a scalar field, for $s = \pm 1$ an electromagnetic field, and for $s = \pm 2$ a gravitational one. In the latter case, the field variables are

$$ {}_2\psi = \Psi_0 \ , \tag{2.10a} $$

$$ {}_{-2}\psi = \zeta^4 \Psi_4 \ . \tag{2.10b} $$

The source term T is defined in Table I and Eq. (2.15) in [77] and it is constructed from the stress-energy tensor.

Solutions in the frequency domain

The main advantage of the Teukolsky equation (TE) (2.9) is the separability in the frequency domain. The field variable ${}_s\psi$ can be decomposed into Fourier and multipolar modes as

$$ {}_s\psi = \sum_{l,m} \frac{1}{2\pi} \int_{-\infty}^{\infty} \mathrm{d}\omega \, {}_s\psi_{lm\omega}(r) \, {}_sS_{lm}^{a\omega}(z) e^{-i\omega t + im\phi} \ , \tag{2.11} $$

where ω is the frequency and m and l multipolar indices. With this decomposition it is possible to find separate ordinary differential equations for the radial part ${}_s\psi_{lm\omega}(r)$ and the angular part ${}_sS_{lm}^{a\omega}(z)$ in the form

$$ \Delta^{-s} \frac{\mathrm{d}}{\mathrm{d}r} \left(\Delta^{s+1} \frac{\mathrm{d}_s\psi_{lm\omega}}{\mathrm{d}r} \right) + \left(\frac{K^2 - 2is(r-M)K}{\Delta} + 4is\omega r - {}_s\lambda_{lm\omega} \right) {}_s\psi_{lm\omega} = {}_s\mathcal{T}_{lm\omega} \ , \tag{2.12} $$

$$ \frac{\mathrm{d}}{\mathrm{d}z} \left((1-z^2) \frac{\mathrm{d}_sS_{lm}^{a\omega}}{\mathrm{d}z} \right) + \left(-\frac{(m+sz)^2}{1-z^2} + (a\omega z - s)^2 - s(s-1) + {}_sA_{lm}^{a\omega} \right) {}_sS_{lm}^{a\omega} = 0 \ , \tag{2.13} $$

where $K = \varpi^2\omega - am$ and ${}_s\lambda_{lm\omega}$ with ${}_sA_{lm}^{a\omega}$ are the separation constants related as ${}_s\lambda_{lm\omega} = {}_sA_{lm}^{a\omega} + a^2\omega^2 - 2ma\omega$. Although there are no closed-form solutions to these equations, it is much more computationally expensive to find the solution for the partial differential equation (2.9).

The solutions to the angular equation (2.13) ${}_sS_{lm}^{a\omega}(z)$ are called the spin-weighted spheroidal harmonics and are normalized as

$$ \int_{-1}^{1} \mathrm{d}z \int_0^{2\pi} \mathrm{d}\phi \, {}_sS_{lm}^{a\omega}(z,\phi) \overline{{}_sS_{l'm'}^{a\omega}(z,\phi)} = \delta_{ll'}\delta_{mm'} \ , \tag{2.14} $$

where ${}_sS_{lm}^{a\omega}(z,\phi) \equiv {}_sS_{lm}^{a\omega}(z) e^{im\phi}$. They reduce to spin-weighted spherical harmonics $Y_{lm}(z,\phi)$ as $a\omega \to 0$ with the eigenvalue behaving as ${}_sA_{lm}^{a\omega} \to (l-s)(l+s+1)$.

Because the $s = \pm 2$ cases are related through the Teukolsky-Starobinsky identities [78, 79], one can be calculated from the other and, thus, we focus on the $s = -2$ case, i.e. the Ψ_4 variable, and drop the $s = -2$ subscript.

The asymptotic behavior of the radial solution $\psi_{lm\omega}$ can be written as [38]

$$ \psi_{lm\omega}(r \to \infty) = C_{lm\omega}^{+} r^3 e^{i\omega r^*} \ , \tag{2.15a} $$

$$ \psi_{lm\omega}(r \to r_+) = C_{lm\omega}^{-} \Delta e^{-ik_{\mathcal{H}} r^*} \ , \tag{2.15b} $$

where $C^{\pm}_{lm\omega}$ are the asymptotic amplitudes, $k_{\mathcal{H}} = \omega - am/(2Mr_+)$ is the frequency at the horizon and r^* is the tortoise coordinate defined as $\mathrm{d}r^*/\mathrm{d}r = \varpi^2/\Delta$. The amplitudes can be found using the Green function method as

$$C^{\pm}_{lm\omega} = \frac{1}{W}\int_{r_+}^{\infty} \frac{R^{\mp}_{lm\omega}(r)\mathcal{T}_{lm\omega}}{\Delta^2}\mathrm{d}r \ , \tag{2.16}$$

where $W = \Big((\partial_r R^+_{lm\omega})R^-_{lm\omega} - R^+_{lm\omega}\partial_r R^-_{lm\omega}\Big)/\Delta$ is the invariant Wronskian and $R^{\pm}_{lm\omega}$ are homogeneous solutions of radial TE (2.12) satisfying purely outgoing boundary conditions at infinity and purely ingoing boundary conditions at the horizon.

It was proven [35] that the source term can be expressed in the form

$$\mathcal{T}_{lm\omega} = \int_{-\infty}^{\infty}\mathrm{d}t\int_{-1}^{1}\mathrm{d}z\int_{0}^{2\pi}\mathrm{d}\phi\,\Delta^2\sum_{ab}\mathcal{T}_{ab}e^{i\omega t - im\phi} \ , \tag{2.17}$$

where we sum over the pairs of tetrad legs $ab = nn, n\bar{m}, \bar{m}\bar{m}$ and

$$\mathcal{T}_{ab} = \sum_{i=0}^{I_{ab}}\frac{\partial^i}{\partial r^i}\Big(f^{(i)}_{ab}\sqrt{-g}T_{ab}\Big) \tag{2.18}$$

with $I_{nn} = 0$, $I_{n\bar{m}} = 1$, and $I_{\bar{m}\bar{m}} = 2$. The functions $f^{(i)}_{ab}(r,z)$ can be found in Eqs. (B4) in [41] and T_{ab} are projections of the stress-energy tensor (1.3) which can be expressed as [48]

$$\sqrt{-g}T_{ab} = \int \mathrm{d}\tau\Big((A^{\mathrm{m}}_{ab} + A^{\mathrm{d}}_{ab})\delta^4 - \partial_\rho\Big(B^{\rho}_{ab}\delta^4\Big)\Big) \ , \tag{2.19}$$

where all quantities are defined in Eqs. (49) in [41]. After substituting this form of the stress-energy tensor to Eq. (2.18) and using Eqs. (2.16) and (2.17), the amplitudes can be expressed as

$$C^{\pm}_{lm\omega} = \int_{-\infty}^{\infty}\frac{\mathrm{d}\tau}{\Sigma}e^{i\omega t(\tau) - im\phi(\tau)}I^{\pm}_{lm\omega}(r(\tau), z(\tau), u_a(\tau), S_{ab}(\tau)) \ , \tag{2.20}$$

where we defined the function $I^{\pm}_{lm\omega}(r, z, u_a, S_{ab})$ which can be found in Eq. (52) of [41].

At this point we can use the the discrete Fourier spectrum of the orbits to show that the frequency spectrum of the fluxes is discrete as well. Following the approach used in [31] for geodesic fluxes, we calculate the fluxes from orbits of spinning particles as follows. After changing the parametrization to Carter-Mino time λ, the coordinates r and z, the four-velocities u_a and the spin tensor S_{ab} can be written as functions of time whose spectrum consists of the frequencies Υ_r, Υ_z and Υ_s or their combinations. Furhemore, coordinates t and ϕ can be written as secularly growing part plus an oscillating part (1.68). Thus, the amplitudes take the form

$$C^{\pm}_{lm\omega} = \int_{-\infty}^{\infty}\mathrm{d}\lambda e^{i(\omega\Gamma - m\Upsilon_\phi)\lambda}J^{\pm}_{lm\omega}(r(\lambda), z(\lambda), u_a(\lambda), S_{ab}(\lambda)) \ , \tag{2.21}$$

where

$$J^{\pm}_{lm\omega} = e^{i\omega\Delta t - im\Delta\phi}I^{\pm}_{lm\omega}(r, z, u_a, S_{ab}) \tag{2.22}$$

is a function of Carter-Mino time with the same frequencies, which can be decomposed as

$$J^{\pm}_{lm\omega} = \sum_{nkj} J^{\pm}_{lmnkj} e^{-in\Upsilon_r\lambda - ik\Upsilon_z\lambda - ij\Upsilon_s\lambda} \,. \tag{2.23}$$

After substituting this expansion into (2.21) and using properties of the delta function, the amplitudes can be written as a sum over discrete frequencies

$$C^{\pm}_{lm\omega} = \sum_{nkj} C^{\pm}_{lmnkj} \delta(\omega - \omega_{mnkj}) \,, \tag{2.24}$$

where $\omega_{mnkj} = m\Omega_\phi + n\Omega_r + k\Omega_z + j\Omega_s$ and the partial amplitudes can be expressed as [41]

$$\begin{aligned} C^{\pm}_{lmnkj} = \frac{1}{(2\pi)^2\Gamma} \int \mathrm{d}w_r \int \mathrm{d}w_z \int \mathrm{d}w_s \, e^{-inw_r - ikw_z - ijw_s} I^{\pm}_{lmnkj}(w_r, w_z, w_s) \\ \times \exp(i\omega_{mnkj}\Delta t(w_r, w_z, w_s) - im\Delta\phi(w_r, w_z, w_s)) \,. \end{aligned} \tag{2.25}$$

This is the most general form for off-equatorial orbits with precessing spin. In simpler configurations like equatorial orbits, this expression can be simplified since the integration over w_z and w_s is trivial. After changing the integration variable to χ_r as defined in Eq. (1.40), expression (2.25) reads

$$C^{\pm}_{lmn} = \Omega_r \int \mathrm{d}\chi_r \frac{\mathrm{d}\lambda}{\mathrm{d}\chi_r} I^{\pm}_{lmn}(\chi_r) \exp(i\omega_{mn} t(\chi_r) - im\phi(\chi_r)) \,, \tag{2.26}$$

which is identical to Eq. (49) in [40] up to a normalization factor of $I^{\pm}_{lmn}$ due to different definitions. Here we dropped the k and j indices since the only nonzero modes are $k = j = 0$.

The strain at infinity can be expressed from Eqs. (2.8), (2.10b), (2.11) and (2.15a) as

$$h = -\frac{2}{r} \sum_{lmnkj} \frac{C^{+}_{lmnkj}}{\omega^2_{mnkj}} S^{a\omega_{mnkj}}_{lm}(z) e^{-i\omega u + im\phi} \,, \tag{2.27}$$

where $u = t - r^*$ is the retarded coordinate and (r, z, ϕ) are the coordinates of the observer. Such a waveform coming from a conservative orbit is often called *snapshot waveform* and consists of multiple "voices" with different frequencies characterized by the m, n, k, and j numbers.

The partial amplitudes $C^{\pm}_{lmnkj}$ can be used for the calculation of the averaged energy and angular momentum fluxes to the future null infinity $\mathcal{J}^+$ and through the future horizon $\mathcal{H}^+$. The respective formulas read [79]

$$\left\langle \mathcal{F}^{E\mathcal{J}^+} \right\rangle = \sum_{lmnkj} \frac{\left|C^{+}_{lmnkj}\right|}{4\pi\omega^2_{mnkj}} \,, \qquad \left\langle \mathcal{F}^{E\mathcal{H}^+} \right\rangle = \sum_{lmnkj} \alpha_{lmnkj} \frac{\left|C^{-}_{lmnkj}\right|}{4\pi\omega^2_{mnkj}} \,, \tag{2.28a}$$

$$\left\langle \mathcal{F}^{J_z\mathcal{J}^+} \right\rangle = \sum_{lmnkj} \frac{m\left|C^{+}_{lmnkj}\right|}{4\pi\omega^3_{mnkj}} \,, \qquad \left\langle \mathcal{F}^{J_z\mathcal{H}^+} \right\rangle = \sum_{lmnkj} \alpha_{lmnkj} \frac{m\left|C^{-}_{lmnkj}\right|}{4\pi\omega^3_{mnkj}} \,, \tag{2.28b}$$

where the coefficient for the horizon fluxes is

$$\alpha_{lmnkj} = \frac{256(2Mr_+)^5 k_{\mathcal{H}} (k^2_{\mathcal{H}} + 4\epsilon^2)(k^2_{\mathcal{H}} + 16\epsilon^2)\omega^3_{mnkj}}{\left|C_{lm\omega_{mnkj}}\right|^2} \tag{2.29}$$

with $\epsilon = \sqrt{M^2 - a^2}/(4Mr_+)$ and the Teukolsky-Starobinsky constant is [78]

$$|C_{lm\omega}|^2 = \Big((\lambda_{lm\omega}+2)^2 + 4a\omega(m-a\omega)\Big)\Big(\lambda_{lm\omega}^2 + 36a\omega(m-a\omega)\Big) \\ - 48a\omega(2\lambda_{lm\omega}+3)(m-2a\omega) + 144\omega^2\Big(M^2-a^2\Big)\,. \quad (2.30)$$

The above formulas are summed over all indices l, m, n, k, j. However, since the $j = \pm 1$ amplitudes are proportional to the perpendicular component of the spin $\sigma_\perp = \mathcal{O}(\sigma)$, the fluxes from these modes behave as $\mathcal{O}(\sigma^2)$. Therefore, they can be neglected in the linear-in-spin approximation and only the $j = 0$ modes can be taken into account in the waveform (2.27). Furthermore, since the perpendicular component of the spin is purely oscillating, it does not contribute to the $j = 0$ mode. Thus, when the fluxes are linearized in σ, they depend only on the parallel component of the spin $\sigma_\parallel$.

Solutions in the time domain

In some cases, e.g. when the source cannot be decomposed in the frequency domain, it is convenient to numerically solve the TE (2.9) in the time domain. In this work we use the time-domain TE solver called *Teukode* by E. Harms, S. Bernuzzi et al. described in [80]. The authors transformed the TE into hyperboloidal horizon-penetrating coordinates $(\tau, \rho, \theta, \varphi)$ in which the horizon and future null infinity lie at finite radial coordinates ρ_+ and ρ_S and, therefore, the fluxes at infinity and the horizon can be easily extracted. Furthermore, because of the hyperbolicity, the boundary conditions are trivial since the outgoing (ingoing) radial coordinate velocity vanishes at the horizon (future null infinity).

The field variable is rescaled as $\psi \mapsto \Delta^{-s} r^{-1}{}_s \psi$ and decomposed into azimuthal modes $\psi = \sum_m \psi_m(\tau, \rho, \theta) e^{im\varphi}$. Then, the equation takes the form

$$\Big(C_{\tau\tau}\partial_\tau^2 + C_{\tau\rho}\partial_\tau\partial_\rho + C_{\rho\rho}\partial_\rho^2 + C_{\theta\theta}\partial_\theta^2 + C_\tau\partial_\tau + C_\rho\partial_\rho + C_\theta\partial_\theta + C_0\Big)\psi_m = S_s\,, \quad (2.31)$$

where the coefficients are functions of ρ, θ, m, and s while S_s is the source term. This equation is solved numerically by the method of lines with finite differences in space and a 4th order Runge-Kutta scheme in time.

The source term S_s is constructed from the stress-energy tensor (1.3) and its derivatives. Hence, the source term contains up to third derivative of the delta function. These derivatives must be appropriately represented on the discrete grid in ρ and θ to accurately calculate the GW fluxes. One way is to represent the delta functions as narrow Gaussian peaks. The advantage is the easy implementation and calculation of the derivatives. However, this method is slow since the exponential function must be repeatedly calculated at each grid point.

Another option is to use a discrete representation that satisfies the properties of delta function and its derivatives. Such representation was used in [81] and is implemented in the *Teukode* up to second derivative. However, for the spinning particle third derivative is needed. Thus, we implemented a piecewise-polynomial representation described in [82]. The advantage is the rapid calculation, however, the non-smoothness creates noise in some cases.

The strain at infinity is calculated by numerically integrating Eq. (2.8), while

the energy and angular momentum fluxes to infinity are calculated as [80]

$$\mathcal{F}^{E\mathcal{J}^+} = \frac{1}{16\pi}\sum_m \int_{-1}^{1} \mathrm{d}z \left|r\dot{h}_m\right|^2 , \tag{2.32a}$$

$$\mathcal{F}^{J_z\mathcal{J}^+} = \frac{1}{16\pi}\,\mathrm{Im}\left\{\sum_m m \int_{-1}^{1} \mathrm{d}z \overline{(r\dot{h}_m)}(rh_m)\right\} . \tag{2.32b}$$

2.1.2 Linearization of the fluxes

As was mentioned before, for EMRI modelling, it is sufficient to truncate the fluxes at linear order in the secondary spin, since that order corresponds to the postadiabatic term. Similarly to the linearization of the trajectory described in Section 1.3.1, the linearization of the fluxes can be done with different choices of the reference geodesics.

When linearizing the amplitudes with respect to a geodesic with the same orbital parameters p, e, and I, the dependence on these parameters can be expressed as $C^{\pm}_{lmnk} = C^{\pm}_{lmnk}(p, e, I, \Omega_i(p, e, I, \sigma), \sigma)$, where we explicitly showed the dependence on Ω_i. Then, the linearized expression reads

$$C^{\pm}_{lmnk}(p, e, I, \sigma) = C^{\pm(\mathrm{g})}_{lmnk}(p, e, I) + \mathcal{O}\left(\sigma^2\right) + \sigma\delta C^{\pm}_{lmnk}(p, e, I) \tag{2.33}$$

where

$$\delta C^{\pm}_{lmnk}(p, e, I) = \left(\frac{\partial C^{\pm}_{lmnk}}{\partial\sigma} + \frac{\partial C^{\pm}_{lmnk}}{\partial\Omega_i}\frac{\partial\Omega_i}{\partial\sigma}\right)\bigg|_{\sigma=0} . \tag{2.34}$$

However, to calculate the derivative of $C^{\pm}_{lmnk}$ with respect to Ω_i, one has to find the derivative of the homogeneous solution of the radial TE $R^{\pm}_{lm\omega}$ and the angular TE $S^{a\omega}_{lm}$ along with the eigenvalue $\lambda_{lm\omega}$ with respect to the frequency ω. This was done e.g. in [36] for circular orbits.

To avoid the complicated calculations of the derivatives of the homogeneous solutions with respect to the frequency, we chose a reference geodesics with the same frequencies. The set of frequencies which are kept fixed depends on the configuration of the orbit. For circular orbit, the azimuthal frequency Ω_ϕ can be fixed while keeping the orbit circular [83]. For eccentric equatorial orbits we fix the azimuthal and radial frequencies Ω_r and Ω_ϕ. In this setup the circular orbits become eccentric when perturbed with the secondary's spin. For generic off-equatorial orbits it is convenient to fix all frequencies Ω_r, Ω_z and Ω_ϕ, however, the linear part of the fluxes has not yet been calculated in this case. Therefore, we present the linearization of the equatorial fluxes [40].

For equatorial orbit we can formally write

$$C^{\pm}_{lmn} = C^{\pm}_{lmn}(p(\Omega_{r,\phi}, \sigma), e(\Omega_{r,\phi}, \sigma), \Omega_{r,\phi}, \sigma) , \tag{2.35}$$

The linear part with respect to a geodesic with the same radial and azimuthal frequency then reads

$$\delta C^{\pm}_{lmn}\Big|_{\Omega_{r,\phi}} = \frac{\partial C^{\pm}_{lmn}}{\partial\sigma} + \frac{\partial C^{\pm}_{lmn}}{\partial p}\delta p + \frac{\partial C^{\pm}_{lmn}}{\partial e}\delta e \tag{2.36}$$

where δp and δe are defined in Eqs. (1.53). These linear parts of the amplitudes can be calculated by linearization of the integrand in Eq. (2.26).

From linearizing the energy and the angular momentum fluxes (2.28) we obtain

$$\delta\mathcal{F}^{E\mathcal{J}^+}_{lmn} = \frac{\mathrm{Re}\left\{\delta C^+_{lmn}\right\}\mathrm{Re}\left\{C^{+(\mathrm{g})}_{lmn}\right\} + \mathrm{Im}\left\{\delta C^+_{lmn}\right\}\mathrm{Im}\left\{C^{+(\mathrm{g})}_{lmn}\right\}}{2\pi\omega^2_{mn}} \tag{2.37}$$

$$\delta\mathcal{F}^{E\mathcal{H}^+}_{lmn} = \alpha_{lmn}\frac{\mathrm{Re}\left\{\delta C^-_{lmn}\right\}\mathrm{Re}\left\{C^{-(\mathrm{g})}_{lmn}\right\} + \mathrm{Im}\left\{\delta C^-_{lmn}\right\}\mathrm{Im}\left\{C^{-(\mathrm{g})}_{lmn}\right\}}{2\pi\omega^2_{mn}} \tag{2.38}$$

$$\delta\mathcal{F}^{J_z\mathcal{J}^+}_{lmn} = m\frac{\mathrm{Re}\left\{\delta C^+_{lmn}\right\}\mathrm{Re}\left\{C^{+(\mathrm{g})}_{lmn}\right\} + \mathrm{Im}\left\{\delta C^+_{lmn}\right\}\mathrm{Im}\left\{C^{+(\mathrm{g})}_{lmn}\right\}}{2\pi\omega^3_{mn}} \tag{2.39}$$

$$\delta\mathcal{F}^{J_z\mathcal{H}^+}_{lmn} = \alpha_{lmn}m\frac{\mathrm{Re}\left\{\delta C^-_{lmn}\right\}\mathrm{Re}\left\{C^{-(\mathrm{g})}_{lmn}\right\} + \mathrm{Im}\left\{\delta C^-_{lmn}\right\}\mathrm{Im}\left\{C^{-(\mathrm{g})}_{lmn}\right\}}{2\pi\omega^3_{mn}} \tag{2.40}$$

where δ denotes the linear part with fixed frequencies $\Omega_{r,\phi}$.

Using Eq. (1.55) we can calculate the linear part with fixed p and e from the linear part with fixed $\Omega_{r,\phi}$ as

$$\delta\mathcal{F}\Big|_{p,e} = \delta\mathcal{F}\Big|_{\Omega_{r,\phi}} - \frac{\partial\mathcal{F}^{(\mathrm{g})}}{\partial p}\delta p - \frac{\partial\mathcal{F}^{(\mathrm{g})}}{\partial e}\delta e\,, \tag{2.41}$$

where $\mathcal{F}$ stands for any of the flux 2.28 and the partial derivatives of the geodesic fluxes $\mathcal{F}^{(\mathrm{g})}$ can be found numerically when the fluxes are calculated on a grid and interpolated, as we describe in Section 4.2.5.

3. Flux-driven inspirals

As was described in the previous section, the leading adiabatic order of the GW phase from an EMRI together with the secondary-spin correction can be found from the rate of change of the energy and angular momentum of the system. Due to the flux-balance laws, the average rate of change of these constants can be calculated from the asymptotic fluxes as [22, 23]

$$\left\langle \frac{\mathrm{d}E}{\mathrm{d}t} \right\rangle = -\left\langle \mathcal{F}^{E\mathcal{J}^+} + \mathcal{F}^{E\mathcal{H}^+} \right\rangle \equiv \dot{E} \,, \tag{3.1}$$

$$\left\langle \frac{\mathrm{d}J_z}{\mathrm{d}t} \right\rangle = -\left\langle \mathcal{F}^{J_z\mathcal{J}^+} + \mathcal{F}^{J_z\mathcal{H}^+} \right\rangle \equiv \dot{J}_z \,, \tag{3.2}$$

where the dot denotes an average coordinate-time derivative. These fluxes are sufficient to calculate an adiabatic evolution of equatorial orbits. However, to evolve generic off-equatorial orbits of spinning bodies, the evolution of the parallel component of the spin $\sigma_\parallel$ and of the Carter-like constant K_R is needed as well. The formula for the latter is, so far, only known in the case with nonspinning secondary where it reads [75, 38]

$$\left\langle \frac{\mathrm{d}Q}{\mathrm{d}t} \right\rangle = -\sum_{lmnk} \frac{(\mathcal{L}_{mnk} + k\Upsilon_\theta)\left(\left|C^+_{lmnk}\right|^2 + \alpha_{lmnk}\left|C^-_{lmnk}\right|^2\right)}{2\pi\omega^3_{mnk}} \,, \tag{3.3}$$

where $Q = K - (aE - L_z)^2$,

$$\mathcal{L}_{mnk} = L_z m \left\langle \frac{z^2}{1-z^2} \right\rangle_\lambda - a^2 E \omega_{mnk} \left\langle z^2 \right\rangle_\lambda \tag{3.4}$$

and the angle brackets with subscript λ denote averaging over one period of polar motion in Carter-Mino time.

3.1 Waveform of an adiabatic inspiral

Since many quantities including the asymptotic GW fluxes are functions of the orbital parameters p, e and I, it is more convenient to evolve the orbital parameters instead of the constants of motion. In particular, once we have the evolution of E, J_z and K_R, we can calculate the evolution of the orbital parameters p, e and I from the relation

$$\begin{pmatrix} \dot{p} \\ \dot{e} \\ \dot{I} \end{pmatrix} = \begin{pmatrix} \partial_p E & \partial_e E & \partial_I E \\ \partial_p J_z & \partial_e J_z & \partial_I J_z \\ \partial_p K_R & \partial_e K_R & \partial_I K_R \end{pmatrix}^{-1} \begin{pmatrix} \dot{E} \\ \dot{J}_z \\ \dot{K}_R \end{pmatrix} . \tag{3.5}$$

Using these equations, the orbital parameters can be evolved from a set of initial conditions p_0, e_0 and I_0. From this evolution, the waveform can be expressed as [19]

$$h = \frac{1}{r} \sum_{lmnkj} A_{lmnkj}(t) S^{a\omega_{mnkj}(t)}_{lm}(z) e^{-i\Phi_{mnkj}(t) + im\phi} \,, \tag{3.6}$$

where the amplitudes are calculated from the slowly evolving parameters as

$$A_{lmnkj}(t) = -\frac{2C^{+}_{lmnkj}(p(t), e(t), I(t))}{\omega^{2}_{mnkj}(p(t), e(t), I(t))} \ . \tag{3.7}$$

The amplitudes C^{+}_{lmnkj} are calculated from an orbit with zero initial phases w_{r0}, w_{z0}, ϕ_0, and ψ_{p0}. Note that for nonzero initial phases, an additional phase factor must be included [38]. The phase Φ_{mnkj} is calculated from the slowly evolving frequency as

$$\Phi_{mnkj}(t) = \int_0^t \omega_{mnkj}(p(t'), e(t'), I(t'))\mathrm{d}t' \ . \tag{3.8}$$

This phase can be split into azimuthal, radial, polar and precession phase

$$\Phi_{mnkj} = m\Phi_\phi + n\Phi_r + k\Phi_z + j\Phi_s \tag{3.9}$$

and they can be calculated separately as

$$\Phi_i(t) = \int_0^t \Omega_i(p(t'), e(t'), I(t'))\mathrm{d}t' \ , \tag{3.10}$$

where $i = \phi, r, z, s$.

Since for fully generic inspirals with spinning secondary the evolution of the Carter constant K_R and of the parallel component of the spin $\sigma_\parallel$ are still missing and have to be calculated, in the rest of this section we confine our calculations to the equatorial plane. We assume that the magnitude of the spin $\sigma = \sigma_\parallel$ is conserved. In that case the system can be parametrized by p and e and only the fluxes of E and J_z are needed for their evolution, which can be calculated as

$$\begin{pmatrix} \dot{p} \\ \dot{e} \end{pmatrix} = \begin{pmatrix} \partial_p E & \partial_e E \\ \partial_p J_z & \partial_e J_z \end{pmatrix}^{-1} \begin{pmatrix} \dot{E} \\ \dot{J}_z \end{pmatrix} . \tag{3.11}$$

These formulas can be explicitly written as [40]

$$\frac{\mathrm{d}p}{\mathrm{d}t} = \frac{\frac{\partial J_z}{\partial e}\dot{E} - \frac{\partial E_z}{\partial e}\dot{J}_z}{\left|J_{(E,J_z)}\right|} \equiv \dot{p}(p(t), e(t), \sigma) \ , \tag{3.12a}$$

$$\frac{\mathrm{d}e}{\mathrm{d}t} = \frac{-\frac{\partial J_z}{\partial p}\dot{E} + \frac{\partial E_z}{\partial p}\dot{J}_z}{\left|J_{(E,J_z)}\right|} \equiv \dot{e}(p(t), e(t), \sigma) \ , \tag{3.12b}$$

where the Jacbian between (E, J_z) and (p, e) reads

$$\left|J_{(E,L_z)}\right| = \frac{\partial E}{\partial p}\frac{\partial J_z}{\partial e} - \frac{\partial E}{\partial e}\frac{\partial J_z}{\partial p} \ . \tag{3.13}$$

To separate the spin-independent part and the correction due to the secondary spin, we can linearize the evolving parameters in σ as

$$p(t) = p^{(\mathrm{g})}(t) + \sigma\delta p(t) \ , \tag{3.14}$$

$$e(t) = e^{(\mathrm{g})}(t) + \sigma\delta e(t) \ , \tag{3.15}$$

where δp and δe are functions of time and are not to be confused with the expressions (1.53). The geodesic parts $p^{(\mathrm{g})}$ and $e^{(\mathrm{g})}$ describe the leading adiabatic part

of the inspiral and are evolved through Eqs. (3.14) with geodesic values of the fluxes and the constants of motion. The quantities δp and δe can be calculated using the evolution equations

$$\frac{\mathrm{d}\delta p}{\mathrm{d}t} = \left(\frac{\partial \dot{p}}{\partial \sigma} + \frac{\partial \dot{p}}{\partial p}\delta p(t) + \frac{\partial \dot{p}}{\partial e}\delta e(t)\right)\bigg|_{p^{(\mathrm{g})}(t),e^{(\mathrm{g})}(t),\sigma=0} , \tag{3.16a}$$

$$\frac{\mathrm{d}\delta e}{\mathrm{d}t} = \left(\frac{\partial \dot{e}}{\partial \sigma} + \frac{\partial \dot{e}}{\partial p}\delta p(t) + \frac{\partial \dot{e}}{\partial e}\delta e(t)\right)\bigg|_{p^{(\mathrm{g})}(t),e^{(\mathrm{g})}(t),\sigma=0} , \tag{3.16b}$$

where the derivatives of $\dot{p}$ and $\dot{e}$ defined in Eqs. (3.12) with respect to σ are taken with fixed p and e, i.e., we use the linear parts of the fluxes $\delta\mathcal{F}|_{p,e}$ from Eq. (2.41). Explicit expressions of the derivatives of $\dot{p}$ and $\dot{e}$ can be found in Appendix C of [40].

The phases can be expanded in the secondary spin as well as

$$\Phi_{r,\phi} = \Phi^{(\mathrm{g})}_{r,\phi}(t) + \sigma\delta\Phi_{r,\phi}(t) , \tag{3.17}$$

where the geodesic (adiabatic) part $\Phi^{(\mathrm{g})}_{r,\phi}$ is calculated from Eq. (3.10) with $\sigma = 0$ and the linear part can be found as

$$\delta\Phi_i = \int_0^t \mathrm{d}t' \left(\frac{\partial \Omega_i}{\partial \sigma} + \frac{\partial \Omega_i}{\partial p}\delta p(t') + \frac{\partial \Omega_i}{\partial e}\delta e(t')\right)\bigg|_{p^{(\mathrm{g})}(t'),e^{(\mathrm{g})}(t'),\sigma=0} . \tag{3.18}$$

After multiplying this phase shift by σ, it is $\mathcal{O}(1)$ at the end of the inspiral and, thus, is comparable to the other postadiabatic effects.

3.2 Initial conditions

Different choices of the initial conditions for δp and δe lead to different results in phase shifts, which correspond to distinct pairs of inspirals of a spinning and nonspinning secondary that are being compared.

The easiest choice is

$$\delta p(t_0) = 0 , \qquad \delta e(t_0) = 0 , \tag{3.19}$$

which corresponds to comparing inspirals which start at the same p and e. However, since p and e are not observable from the GW signal unlike the frequencies, it is more convenient to match the initial frequencies instead.

When the initial conditions are set to

$$\delta p(t_0) = \delta p(p^{(\mathrm{g})}_0, e^{(\mathrm{g})}_0) , \qquad \delta e(t_0) = \delta e(p^{(\mathrm{g})}_0, e^{(\mathrm{g})}_0) , \tag{3.20}$$

where we use the formulas (1.53) on the right hand side, the initial shifts of the frequency defined from the integrand in Eq. (3.18) vanish. Therefore, the initial frequencies of the inspiral of a spinning and a nonspinning secondary are the same. Note that only the radial and azimuthal frequencies are matched since the polar frequency is not observable in the equatorial case. Eq. (3.20) can be generalized for generic orbits and initial conditions for p, e and I with matched frequencies Ω_ϕ, Ω_r and Ω_z.

In similar manner for circular orbits, it is convenient to fix only the azimuthal frequency since other frequencies are not observable. Then, the initial conditions can be chosen as

$$\delta p(t_0) = -\frac{\frac{\partial \Omega_\phi}{\partial \sigma}}{\frac{\partial \Omega_\phi}{\partial p}} , \qquad \delta e(t_0) = 0 . \tag{3.21}$$

This formula is valid even in the eccentric case which will be useful for the comparisons of eccentric and quasicircular inspirals.

4. Numerical results

In this section we describe numerical calculations of spinning particle's trajectories and their respective asymptotic GW fluxes as described in previous chapters both for equatorial and generic cases. We also present the calculation of adiabatic inspirals on the equatorial plane.

All these calculations have been done in *Mathematica* or in C using the *Teukode*. This work makes use of the *Black Hole Perturbation Toolkit* (BHPT) [84].

4.1 Calculation of the trajectories

4.1.1 Equatorial orbits

We start with equatorial trajectories being calculated for given orbital parameters p and e and a Kerr parameter a[1]. To achieve this, we calculate the constants of motion from Eqs. (1.39) and the frequencies from Eqs. (1.43), where the latter are evaluated as a numerical integral of the expressions in Eqs. (1.42). Since the integrands are periodic in χ_r, we employ the midpoint rule to achieve exponential convergence [85]. The coordinates $t(\chi_r)$ and $\phi(\chi_r)$ are calculated from Eqs. (1.44) with the coefficients found using discrete cosine transform.

On the other hand, to calculate the linear part of the trajectory with fixed frequencies, we first calculate the geodesic values followed by the linear parts of the constants of motion calculated with fixed p and e, i.e. $\delta E|_{p,e}$ and $\delta J_z|_{p,e}$, from Eq. (1.47). Then we calculate the derivatives of the frequencies with respect to p, e and σ by numerically integrating the derivatives of the integrands in Eqs. (1.42). A *Mathematica* notebook containing the calculation of these derivatives can be found in the supplemental material of Ref. [40]. Using these derivatives of the frequencies we calculate δp and δe from Eqs. (1.53). Then, using Eqs. (1.55) and (1.56) we calculate the linear corrections to the constants of motion and to the coordinates with fixed frequencies.

In Figure 4.1 we show the dependence of t on χ_r for an orbit of spinning and nonspinning particle along with the linear part δt. Because the frequencies are matched, after one radial period the difference vanishes.

4.1.2 Generic orbits

Generic orbits along with the spin corrections are calculated using the approach developed by Drummond and Hughes [64, 65]. The orbits are parametrized by p, e and I using Eqs. (1.62). The geodesic part of the orbit is calculated using the *KerrGeodesic* package [86] from the BHPT.

First, we calculate the functions $\mathcal{R}_t$ and $\mathcal{R}_\phi$ defined in Eqs. (C5a) and (C5b) in Ref. [41] on a grid in w_r and w_z. Then, their Fourier coefficients are calculated

[1] If not mentioned otherwise, we set the mass M to 1 because the resulting quantities can be rescaled accordingly.

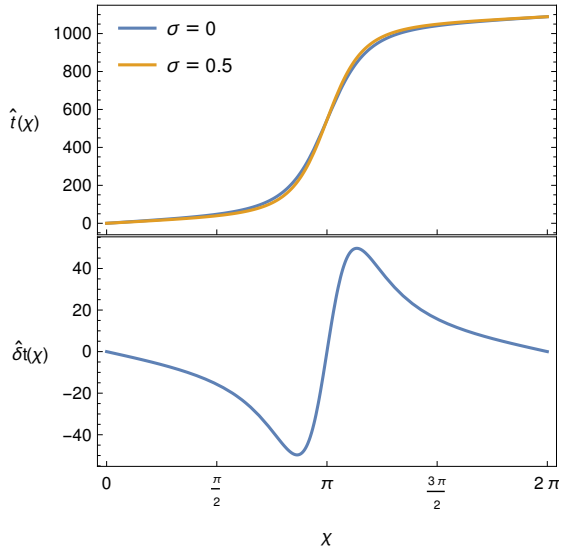

Figure 4.1: Dependence of t on χ_r for orbits with spinning and nonspinning particle. (Note that, following Refs. [39, 40], here the hat denotes dimensionless quantities. This notation is also used in Figs. 4.4, 4.9, 4.13, 4.16, and 4.17.)

as

$$\mathcal{R}_{t,\phi,nk} = \sum_{ab} \mathcal{R}_{t,\phi}(w_r^a, w_z^b) F_n^a G_k^b \,, \tag{4.1}$$

where the matrices of discrete Fourier transform read

$$F_n^a = \exp\left(\frac{\pi i n}{N_r}(1+2a)\right)\frac{1}{N_r} \,, \tag{4.2}$$

$$G_k^b = \exp\left(\frac{\pi i k}{N_z}(1+2b)\right)\frac{1}{N_z} \,, \tag{4.3}$$

with N_r and N_z being the numbers of steps in the w_r and w_z direction. From the Fourier coefficients (4.1) the oscillating parts of $u^S_{t,\phi}$ are calculated by integrating Eq. (3.24) in Ref. [65] as

$$u^S_{t,\phi,nk} = \frac{i\mathcal{R}_{t,\phi,nk}}{n\Upsilon_r + k\Upsilon_z} \tag{4.4}$$

for $n \neq 0$ or $k \neq 0$.

Then, the remaining Fourier coefficients $u^S_{t,00}$, $u^S_{\phi,00}$ along with the Fourier coefficients $\delta\chi^S_{r,n}$, $\delta\chi^S_{z,k}$, $\mathfrak{r}^S_{nk}$, $\mathfrak{z}^S_{nk}$ and the frequency corrections Υ^S_r and Υ^S_z are found by solving a system of linear equations

$$\mathbf{M}\cdot\mathbf{v} + \mathbf{c} = 0 \,. \tag{4.5}$$

The vector $\mathbf{v}$ contains the unknown quantities, while the matrix $\mathbf{M}$ is constructed from the r and z component of the spin-curvature force along with the equation for the normalization of the four-velocity. The component of this matrix contain the Fourier coefficients of the functions $\mathcal{F}_{r,\mathfrak{r}}$, $\mathcal{G}_{r,\mathfrak{r},\theta,\mathfrak{z}}$, $\mathcal{H}_{r,\mathfrak{r},\theta,\mathfrak{z}}$, $\mathcal{I}_{1r,1\theta,2,3}$, $\mathcal{Q}_{\theta,\mathfrak{z}}$, $\mathcal{S}_{r,\mathfrak{r},\theta,\mathfrak{z}}$, $\mathcal{T}_{r,\mathfrak{r},\theta,\mathfrak{z}}$, $\mathcal{U}_{1r,1\theta,2,3}$, $\mathcal{K}_{r,\mathfrak{r},\theta,\mathfrak{z}}$, $\mathcal{M}_{r,\mathfrak{r},\theta,\mathfrak{z}}$, $\mathcal{N}_{1r,1\theta}$, which are defined in the supplemental material of [64] and are calculated analogously to $\mathcal{R}_{t,\phi,nk}$. Finally, the vector $\mathbf{c}$ contains the Fourier coefficients of the functions $\mathcal{J}$, $\mathcal{V}$ and $\mathcal{P}$ defined in Eqs. (C5) of Ref. [41].

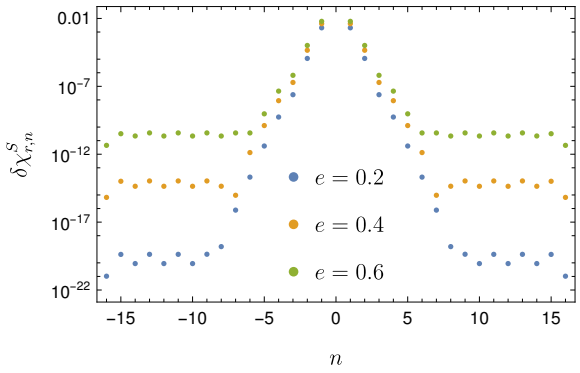

Figure 4.2: Fourier coefficients $\delta\chi^S_{r,n}$ for an orbit with $a = 0.9M$, $p = 15$, $I = 15°$, and different e.

Because of the reflection symmetry around the equatorial plane, the Fourier expansions contain only certain k modes. In particular, $u^S_{t,\phi,nk}$, $\delta\chi^S_{z,k}$ and $\mathfrak{r}^S_{nk}$ consist of even k modes while $\mathfrak{z}^S_{nk}$ consists of odd k modes. Further, the Fourier expansion of the radial component of the spin-curvature force and the equation for the normalization of the four-velocity contain even k modes and the z component of the spin-curvature force contains odd k modes. This allows us to reduce the number of columns and rows of the matrix $\mathbf{M}$, which reduces the error originating from numeric manipulations of large matrices.

With these simplifications, the vector $\mathbf{v}$ contains a total of $4+2n_{\max}+2k_{\max}+4n_{\max}k_{\max}$ unknown coefficients, hence, $\mathbf{M}$ has this number of columns. The total number of equations, thus the number of rows of $\mathbf{M}$, is $2 + 3k_{\max} + 4n_{\max} + 6k_{\max}n_{\max}$. Therefore, the system is overconstrained and $\mathbf{M}$ is a rectangular matrix. Thus, we solve the system using the least squares method.

Because of this approximative solution, not all Fourier coefficients are calculated accurately. In Fig. 4.2 we show a logarithmic plot of the Fourier coefficients $\delta\chi^S_{r,n}$ for $a = 0.9M$, $p = 15$, $I = 15°$ and different eccentricities. We can see that after certain value of $|n|$ the Fourier coefficients stop converging. For higher eccentricities this happens for lower n. The same behavior occurs for $\delta\chi^S_{z,k}$ and other Fourier coefficients. Therefore, not all Fourier coefficients are reliable and we must chose very high $n_{\max}$ or $k_{\max}$ to have accurate results for high eccentricities or inclinations.

4.2 Calculation of the fluxes

From the trajectories of spinning particles we calculate the GW fluxes, i.e. the partial amplitudes $C^{\pm}_{lmnk}$ and the linear-in-spin parts $\delta C^{\pm}_{lmn}$ for equatorial orbits and $C^{\pm}_{S,lmnk}$ for generic orbits.

4.2.1 Equatorial fluxes

In the following paragraphs we first describe the calculation of fluxes from eccentric equatorial orbits [39]. The partial amplitudes $C^{\pm}_{lmn}$ are calculated by numerically integrating Eq. (2.26). We employ the midpoint rule because it is exponentially converging for periodic functions. The integration error de-

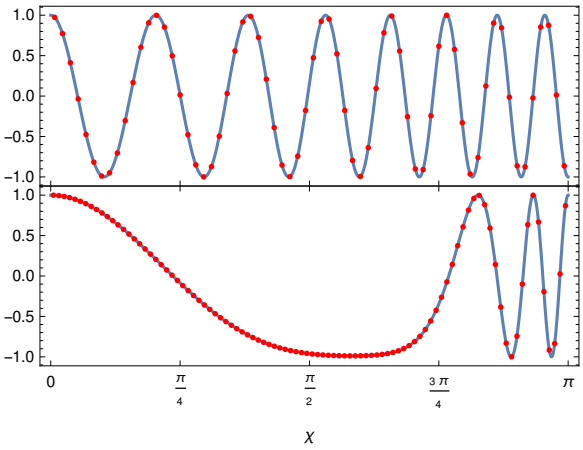

Figure 4.3: Real part of $\exp(i(\omega_{mn}t(\chi_r) - m\phi(\chi_r)))$ for orbits with $a = 0.9M$, $\sigma = -0.5$, $p = 12$, $e = 0.2$, $m = 2$, $n = 15$ (top) and $a = 0.9M$, $\sigma = -0.5$, $p = 12$, $e = 0.8$, $m = 2$, $n = 4$ (bottom). The red dots show points where the function is evaluated for the numerical integration.

pends on the number of steps which is determined as follows. We assume that the main oscillating part of the integrand comes from the exponential term $\exp(i\omega_{mn}t(\chi_r) - im\phi(\chi_r))$. The behavior of this function is depicted in Fig. 4.3 for orbits with different eccentricities and mode numbers. The "frequency" of the oscillations is higher for higher n and higher eccentricity and can be expressed as

$$\omega_{mn}\frac{\mathrm{d}t}{\mathrm{d}\chi_r} - m\frac{\mathrm{d}\phi}{\mathrm{d}\chi_r} = \Big(\omega_{mn}V^t(\chi_r) - mV^\phi(\chi_r)\Big)\sqrt{\frac{1-e^2}{p^2 J(\chi_r)}} \equiv \varphi'_{mn}(\chi) \tag{4.6}$$

Thus we choose the number of steps as

$$\max\{|8\lceil\varphi'_{mn}(0)\rceil|, |8\lceil\varphi'_{mn}(\pi)\rceil|, 32\} \tag{4.7}$$

to guarantee that each oscillation has at least 4 points. This procedure ensures that the integrand is evaluated at low number of points while keeping the relative error below 10^{-6} across the parameter space.

The homogeneous radial solutions $R^{\pm}_{lm\omega}(r)$ are calculated using the *Teukolsky* package [87] of the BHPT, which numerically integrates the TE in hyperboloidal coordinates with initial conditions calculated with the Mano-Suzuki-Takasugi method [88]. The spin weighted spheroidal harmonics are calculated using the *SpinWeightedSpheroidalHarmonics* package [89] of the BHPT as well with the Leaver's method [90].

In Fig. 4.4 we show the absolute value of the amplitudes $\left|C^{+}_{lmn}\right|$ from eccentric equatorial orbit with $a = 0.9M$, $\sigma = -0.5$, $p = 12$, and $e = 0.2$ for the dominant $m = 2$ mode. We can see that the partial amplitudes converge to zero exponentially with increasing $|n|$ and they decrease with l. Note that for astrophysical systems the value of the spin is of the same order as the mass ratio, i.e., $\sigma \leq q \ll 1$. However the fluxes can be calculated with spins much higher and numerically linearized afterwards. Furthermore, high values of spin are chosen to make the spin contribution visible in the plots.

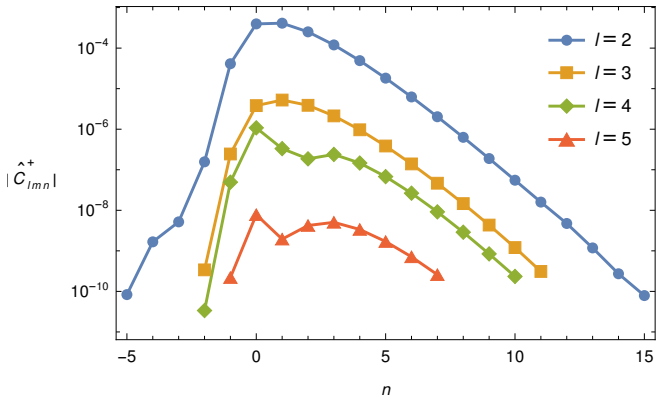

Figure 4.4: Partial amplitudes for eccentric equatorial orbit with $a = 0.9M$, $\sigma = -0.5$, $p = 12$, $e = 0.2$, and $m = 2$.

$f(w_r, w_z)$	r^S	z^S	U_S^r	U_S^z	Δt^S	$\Delta\phi^S$
$f(2\pi - w_r, 2\pi - w_z)$	$+$	$+$	$-$	$-$	$-$	$-$
$f(w_r, w_z + \pi)$	$+$	$-$	$+$	$-$	$+$	$+$

Table 4.1: Symmetries of the linear part of the trajectory

Linearization in the secondary spin

In the previous section we described the calculation of the nonlinearized partial amplitudes $C^{\pm}_{lmn}(p, e, \sigma)$. For the equatorial case we can calculate the linear-in-spin part $\delta C^{\pm}_{lmn}$ separately in the fixed frequency framework using Eq. (2.36). The linear-in-spin parts δC^{+}_{lmn} are calculated similarly to the nonlinearized case by integrating the derivative of the integrand of Eq. (2.26).

To verify the linear-in-spin part of the amplitude, we compare them with numerical derivatives of the nonlinearized amplitudes. The derivative is calculated as

$$\delta C^{\pm\mathrm{num}}_{lmn} = \frac{C^{\pm}_{lmn}(p^+, e^+, \sigma) - C^{\pm}_{lmn}(p^-, e^-, -\sigma)}{2\sigma} + \mathcal{O}\left(\sigma^2\right) . \tag{4.8}$$

To ensue that the frequencies of the trajectories of the spinning and nonspinning particles are the same, for given $p^{(\mathrm{g})}$ and $e^{(\mathrm{g})}$ we numerically solve

$$\Omega_r(p^{\pm}, e^{\pm}, \pm\sigma) = \Omega_r^{(\mathrm{g})}(p^{(\mathrm{g})}, e^{(\mathrm{g})}) , \tag{4.9a}$$

$$\Omega_\phi(p^{\pm}, e^{\pm}, \pm\sigma) = \Omega_\phi^{(\mathrm{g})}(p^{(\mathrm{g})}, e^{(\mathrm{g})}) \tag{4.9b}$$

for $p^{\pm}$ and $e^{\pm}$. In Fig. 4.5 the relative truncation error $\left|1 - \delta C^{\pm\mathrm{num}}_{lmn}/\delta C^{\pm}_{lmn}\right|$ is plotted for different orbital parameters and mode numbers. We can see that the error behaves as $\mathcal{O}(\sigma^2)$. Therefore, the linear part is consistent with the nonlinear result.

4.2.2 Generic fluxes

The generic fluxes with parallel spin are calculated similarly as the equatorial fluxes by integrating Eq. (2.25) over w_r and w_z (integration over w_s is trivial for parallel spin). Analogously to the equatorial case, the number of steps in w_r and

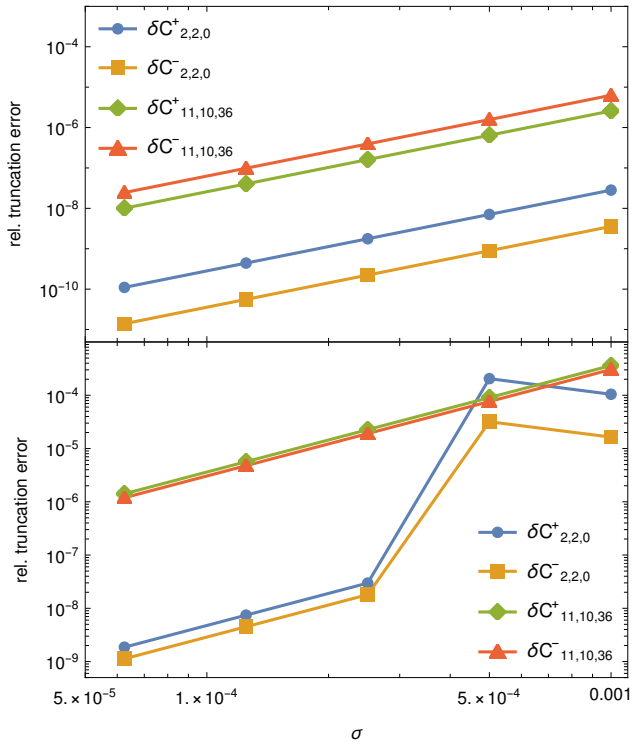

Figure 4.5: Dependence of the relative truncation error calculated from the numerical derivative of the nonlinearized amplitudes and the linear part with fixed frequencies on the value of the spin. The orbital parameters are $a = 0.9M$, $p^{(\mathrm{g})} = 12$, $e^{(\mathrm{g})} = 0.6$ (top) and $a = 0.9M$, $p^{(\mathrm{g})} = 4$, $e^{(\mathrm{g})} = 0.4$ (nottom). The relative truncation error behaves as $\mathcal{O}(\sigma^2)$ which indicates that the linear part is correct.

w_z is chosen as

$$\max\{|16\lceil\varphi_r'(0)+n\rceil|, |16\lceil\varphi_r'(\pi)+n\rceil|, 32\}\,, \tag{4.10a}$$
$$\max\{|8\lceil\varphi_z'(0)+k\rceil|, |8\lceil\varphi_z'(\pi/2)+k\rceil|, 32\}\,, \tag{4.10b}$$

respectively, where $\varphi_y(w_y) = \omega_{mnk}\Delta\hat{t}_y(w_y) - m\Delta\hat{\phi}_y(w_y)$ for $y = r, z$. Similarly to [31], we exploit the symmetries of the trajectory to write the integral (2.25) as a sum of four integrals over $0 < w_r < \pi$ and $0 < w_z < \pi$. For the geodesic quantities, these symmetries read $f(2\pi - w_y) = f(w_y)$ for $\hat{r}(w_r)$ and $\hat{z}(w_z)$ and $f(2\pi - w_y) = -f(w_y)$ for $\Delta\hat{t}_{r,z}(w_{r,z})$, $\Delta\hat{\phi}_{r,z}(w_{r,z})$, $\hat{U}^r(w_r)$ and $\hat{U}^z(w_z)$. Similar symmetries hold for the linear part of the trajectory, namely $f(w_r, w_z) = \pm f(2\pi - w_r, 2\pi - w_z)$ and $f(w_r, w_z) = \pm f(w_r, w_z + \pi)$, where the functions and respective signs are listed in Table 4.1. The latter symmetry holds thanks to the reflection symmetry around the equatorial plane.

Because each offequatorial trajectory is calculated up to linear order in σ, the fluxes are accurate up to this order as well. Therefore, if we want to compare the generic fluxes with non-linearized equatorial or time-domain fluxes, we have to compare the linear-in-spin parts. These linear parts are extracted using fourth-order finite difference formula which reads

$$f^S = \frac{\frac{1}{12}f(-2\sigma) - \frac{2}{3}f(-\sigma) + \frac{2}{3}f(\sigma) - \frac{1}{12}f(2\sigma)}{\sigma}\,. \tag{4.11}$$

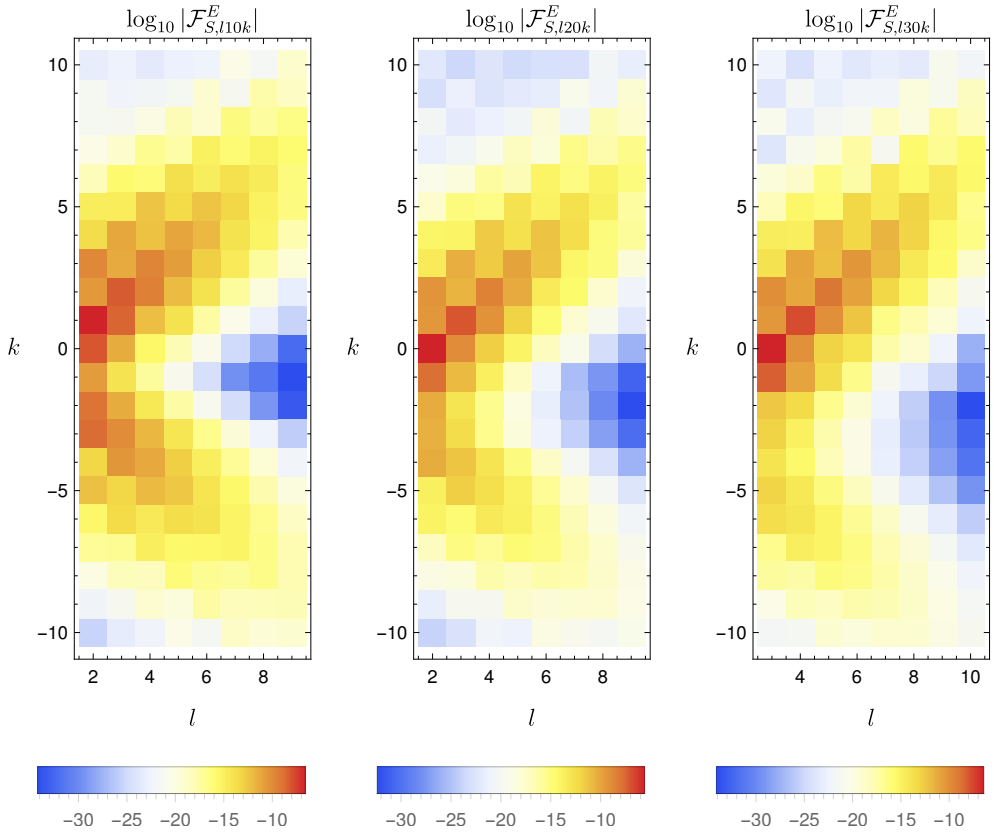

Figure 4.6: Linear-in-spin parts of the energy fluxes from a nearly spherical orbit with $a = 0.9M$, $p = 10$, and $I = 30°$ for $m = 1$ (left), $m = 2$ (middle), and $m = 3$ (right) and for different l and k.

In this way we calculate the linear-in-spin parts of the amplitudes $C^{\pm}_{S,lmnk}$ and of the fluxes $\mathcal{F}^{E,J_z}_S$. From the order of the method and the step size, which we set to $\sigma = 0.05$, we estimate the error to be of the order 10^{-5}.

We plot the linear parts of the energy fluxes from nearly spherical orbits with $e = 0$ in Fig. 4.6 for different m, l and k. We can see that for given l the maximum lies at $k = l - m$. In Fig. 4.7 we plot the sum over l of the energy flux from generic off-equatorial orbit for different m, n and k.

Not all the linear parts of the partial amplitudes can be calculated accurately. Because the Fourier coefficients of the linear part of the trajectory $\delta\chi^S_{r,n}$, $\delta\chi^S_{z,k}$, etc. stop converging after certain $|n|$ and $|k|$, the linear parts of the partial amplitudes stop converging as well, this can be seen in Fig. 4.8.

To check our calculations, we have verified that the generic fluxes converge to the equatorial value for decreasing I. Details can be found in Ref. [41] in Figs. 4 and 5.

4.2.3 Comparisons of time-domain and frequency-domain results

To further verify our frequency-domain results, we compare the m-modes of the strain rh_m and the energy flux to infinity $\mathcal{F}^{E\mathcal{J}^+}_m$ with time-domain results obtained with the *Teukode*.

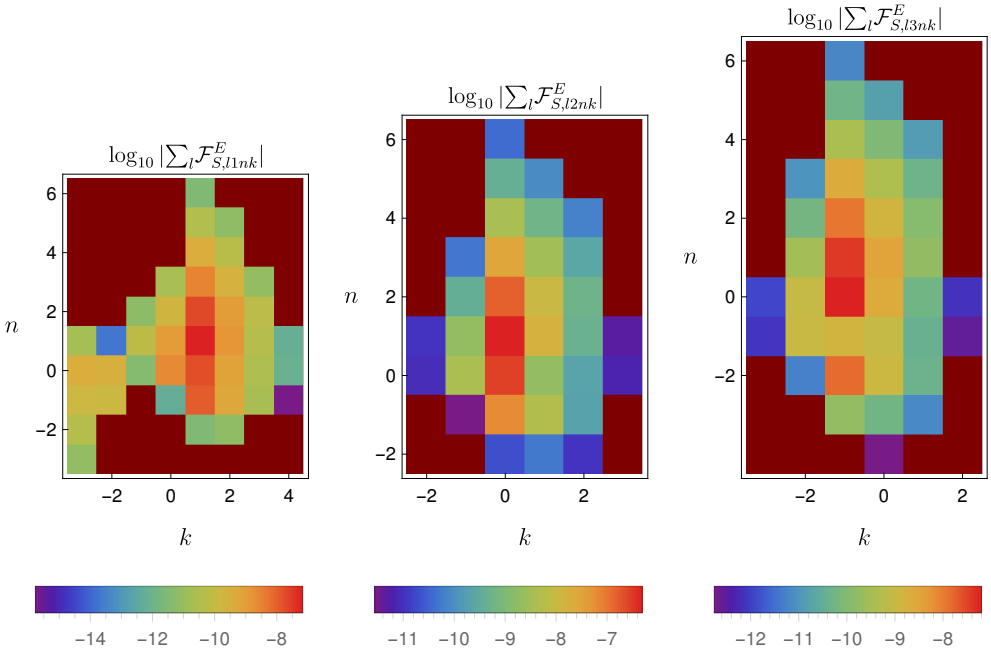

Figure 4.7: Linear-in-spin parts of the energy flux from a generic orbit summed over l for $a = 0.9M$, $p = 12$, $e = 0.2$, $I = 30°$, and $m = 1$ (left), $m = 2$ (middle), and $m = 3$ (right) for different n and k.

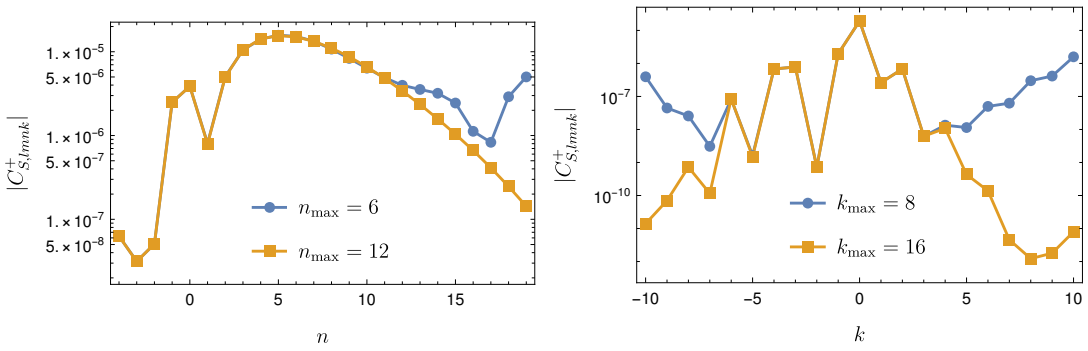

Figure 4.8: Dependence of the linear-in-spin parts of the partial amplitudes $C^+_{S,lmnk}$ on n for different $n_{\max}$ and $a = 0.9M$, $p = 15$, $e = 0.5$, and $I = 15°$ (left) and on k for different $k_{\max}$ and $a = 0.9M$, $p = 15$, $e = 0.2$, and $I = 60°$ (right). The linear parts of the partial amplitudes stop converging because of the finite number of the Fourier coefficients of the linear part of the trajectory as can be seen in Fig. 4.2.

To calculate the time-domain fluxes, the trajectory is needed as a time series. In the equatorial case we first calculate the initial conditions for given a, σ, p, and e from Eqs. (1.34). Then, we use them in an implicit Gauss-Runge-Kutta integrator of MPD equations (1.4) to find the trajectory. This trajectory is subsequently used as an input to the *Teukode*. Because of the discretization error, we run the *Teukode* for several resolutions in ρ and θ direction, namely, $N_\rho \times N_\theta = 1200 \times 100$, 1704×142, 2400×200, 3384×282, and 4800×400, to verify that the error decreases with increasing resolution.

The delta function and its derivatives in the source term is approximated with

12th order piecewise polynomial or Gaussian function. Even if in most cases we have used the piecewise polynomial, since it is faster and more accurate, however, in some extreme cases this approximation causes a noise and the Gaussian approximation must be used instead.

To find the error we calculate the relative difference of the strain calculated in time domain and frequency domain

$$\delta h_m = \left| 1 - \frac{h_m^{\mathrm{td}}}{h_m^{\mathrm{fd}}} \right| . \tag{4.12}$$

The strain is extracted at $r = \infty$ and $\theta = \pi/2$ as a function of the retarded time u. The frequency-domain strain is calculated using Eq. (2.27) as a sum over l and n. We assume that the error of the frequency domain solution is much lower than the error of the time domain solution. In Fig. 4.9 we show such relative differences for different m-modes and resolutions. From this plot we can see that with decreasing step length $\Delta\rho = (\rho_S - \rho_+)/N_\rho$ the relative error decreases, but the noise increases. This noise is caused by the non-smoothness of the piecewise polynomials. When the delta function is approximated with the Gaussian function, the amplitude of the noise is lower, however, the accuracy is lower because the Gaussian approximation is wider and poorly represents a point particle.

To investigate the convergence of the time-domain solution to the frequency-domain solution, we calculate the relative difference of the energy flux to infinity for given m as

$$\delta \mathcal{F}_m^{E\mathcal{J}^+} = \left| 1 - \frac{\mathcal{F}_{m,\mathrm{td}}^{E\mathcal{J}^+}}{\mathcal{F}_{m,\mathrm{fd}}^{E\mathcal{J}^+}} \right| . \tag{4.13}$$

The time-domain energy flux is calculated as an average over two radial periods from 350 to $350 + 2T_r$ of the formula (2.32a). We plot the result with respect to the step length in the ρ direction in Fig. 4.10 for different values of the secondary spin. The relative differences decrease with decreasing step length except the $m = 1$ case for $N_\rho = 4800$ where the noise becomes significant. This is caused by the fact that the value of the flux for $m = 1$ is small and the noise becomes significant at this resolution.

In Fig. 4.11 we again plot the convergence of the relative difference for different eccentricities. Similarly to the previous plot, in some cases such as high eccentricities the noise becomes visible and the relative difference does not converge. This is caused by the fast motion of the particle and the subsequent change of the shape of the delta function approximated with the piecewise polynomial, which depends on the position between the grid points. Therefore, we repeat the calculation in some cases with a Gaussian function in the ρ direction and a piecewise polynomial in the θ direction or with Gaussian function in both directions. Then, the relative difference converges.

We also compare nearly spherical and generic fluxes calculated in time domain and frequency domain. Because, unlike the equatorial fluxes, the generic fluxes in frequency domain are calculated up to linear order in spin, whereas the time domain fluxes are nonlinearized, we compare the time domain and frequency domain linear parts in spin of the energy fluxes at infinity $\mathcal{F}_{S,m}^{E\mathcal{J}^+}$ for given m.

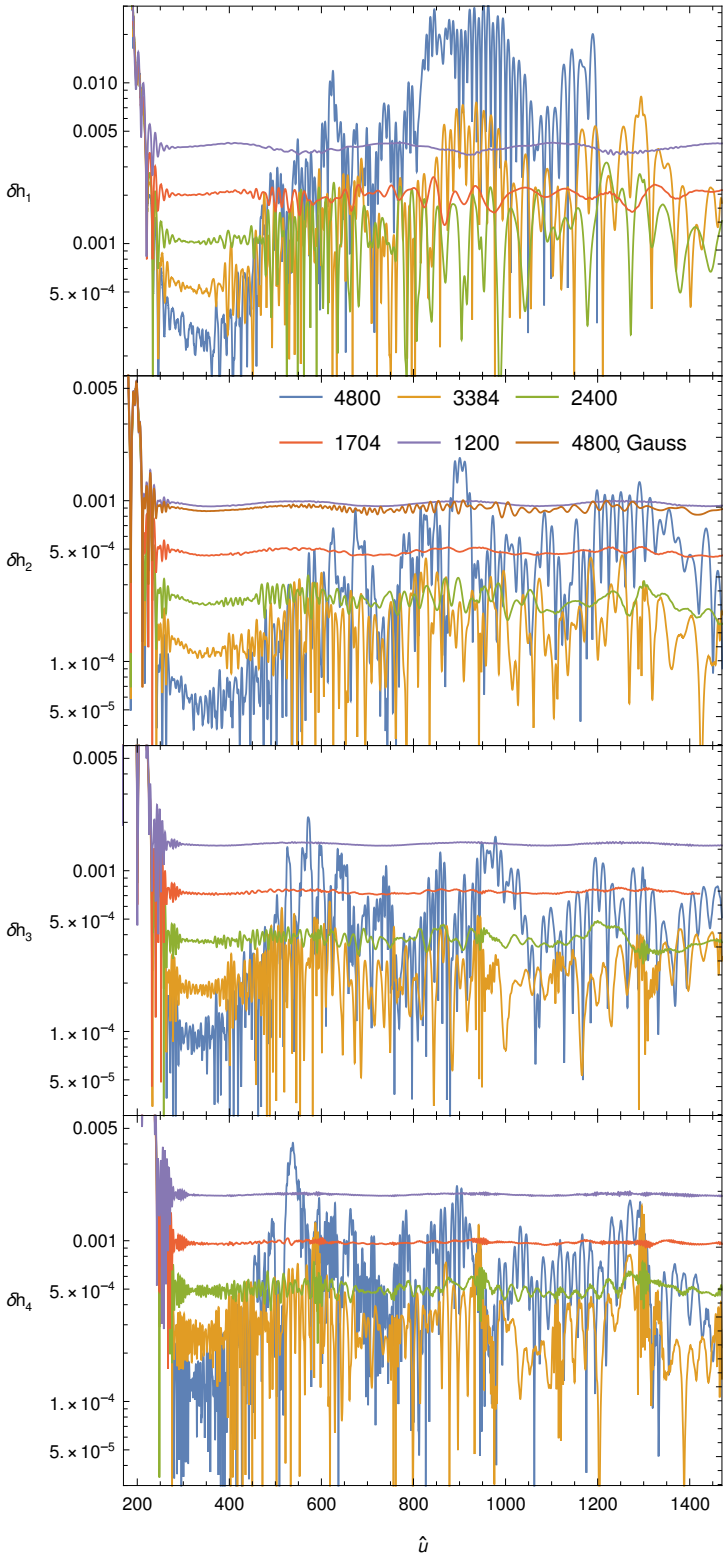

Figure 4.9: Relative difference between time-domain and frequency-domain m-mode of the strain as a function of time for different resolutions in the ρ direction and $m = 1, 2, 3, 4$ from top to bottom. The orbital parameters are $a = 0.9M$, $\sigma = -0.5$, $p = 12$, and $e = 0.2$. The delta function is approximated with piecewise polynomial for all m and resolutions and with Gaussian function for $m = 2$ and resolution 4800. The initial noise is caused by the zero initial data in time domain and decreases around $u = 300M$.

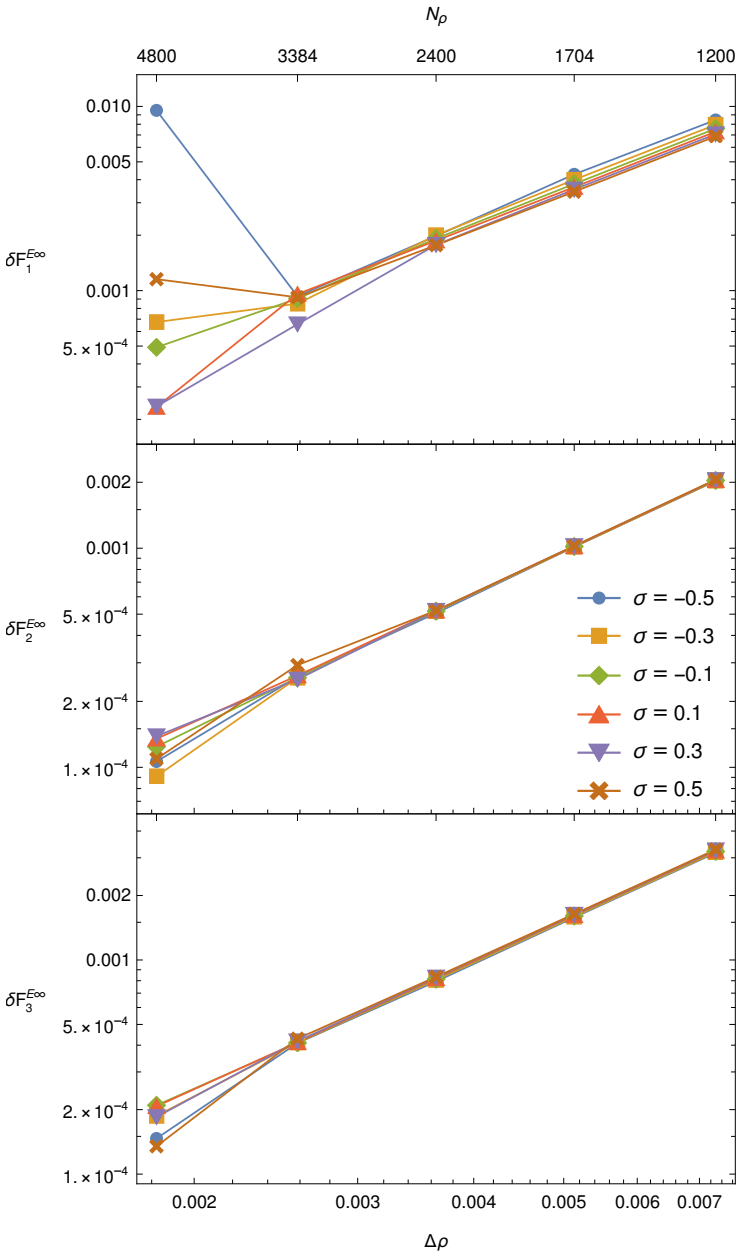

Figure 4.10: Dependence of the relative difference of the time-domain and frequency-domain energy flux on the step length in the ρ direction for $a = 0.9M$, $p = 12$, $e = 0.2$, and different secondary spins σ. The delta function was approximated with piecewise polynomial.

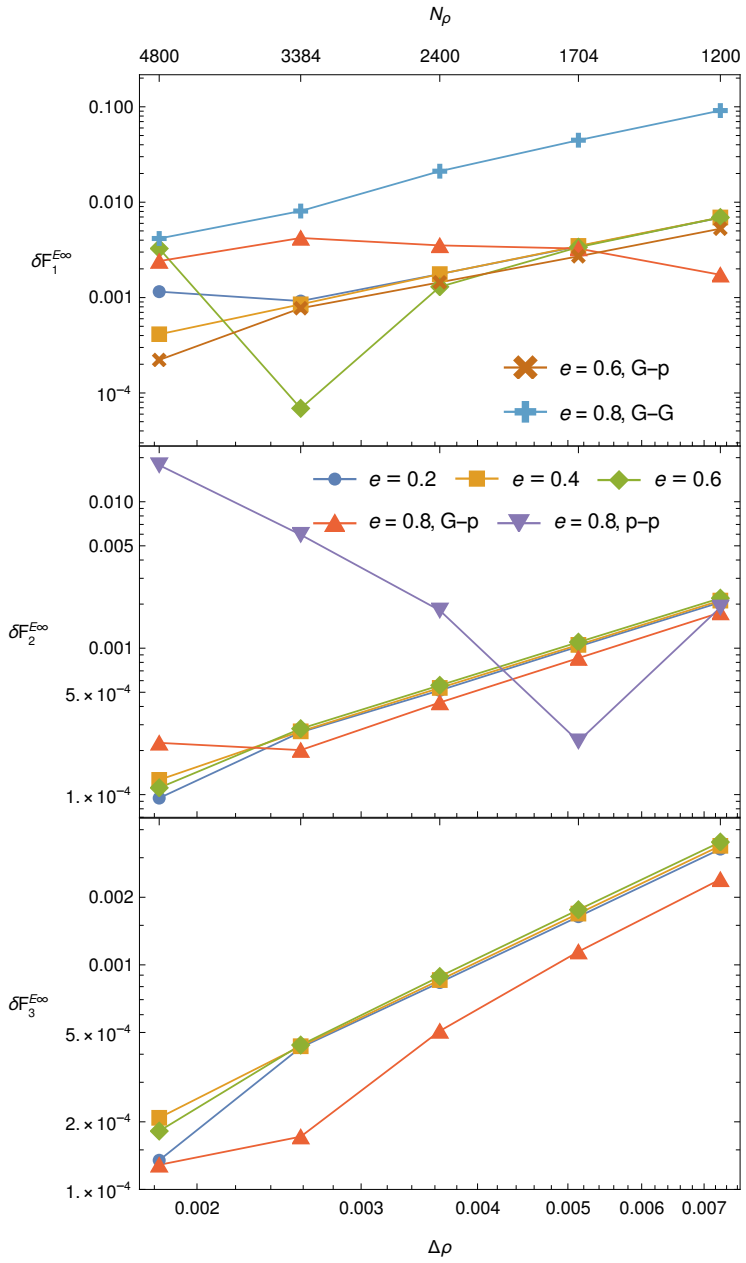

Figure 4.11: Dependence of the relative difference of the time-domain and frequency-domain energy flux on the step length in the ρ direction for $a = 0.9$, $\sigma = 0.5$, $p = 12$, and different eccentricities e. If not specified otherwise, the delta function is approximated as piecewise polynomial in both ρ and θ directions. In some cases we use the Gaussian function in ρ and piecewise polynomial in θ direction (G-p) or Gaussian function in both directions (G-G).

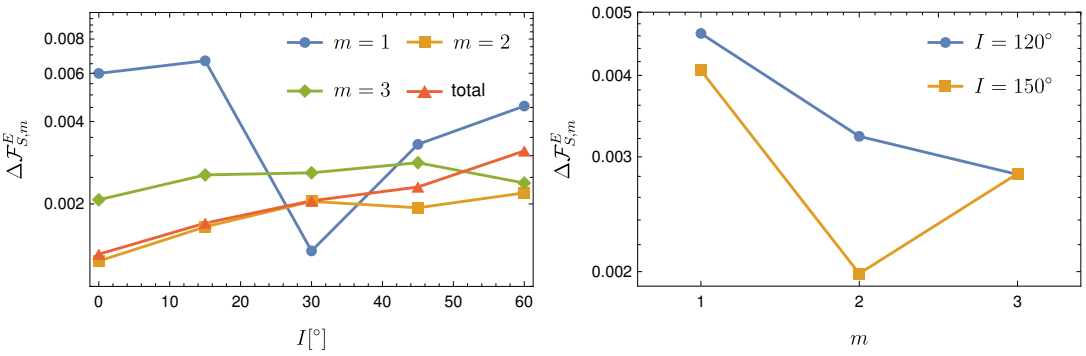

Figure 4.12: Dependence of the relative difference of the time domain and frequency domain energy fluxes on the inclination (left) and on the azimuthal number m (right) for nearly spherical orbits with $a = 0.9M$ and $p = 10$. The plot on the left shows prograde orbits and the plot on the right shows retrograde orbits.

First, using the aforementioned Gauss-Runge-Kuta MPD equations solver we calculate the trajectory which matches the linearized trajectory obtained in frequency domain as follows. For given a, p, e, and I, the conserved energy E and angular momentum J_z along with r, θ, u^r, S^r, and S^θ are calculated using the frequency-domain approach. These values are used as initial conditions together with the other components of u^μ and $S^{\mu\nu}$ determined by numerically solving the constraints (1.7), (1.8), (1.26) and (1.27). These initial conditions ensure that the frequency-domain and time-domain trajectories agree up to linear order in σ. These trajectories for $\sigma = -0.1, -0.05, 0.05, 0.1$ are then used as an input to the Teukode. In this case we used 4800 points in the radial direction and the Gaussian approximation of the delta function to reduce the noise.

Because the energy fluxes calculated in time domain are not constant, we need a procedure to average them. For nearly spherical orbits we average the fluxes over several polar periods $2\pi/\Omega_z$ which are calculated from Eq. (1.67b) using the frequency-domain approach. However, the generic fluxes are not periodic and their spectrum contains all the combinations of the radial and polar frequency $n\Omega_r + k\Omega_z$. Therefore, they cannot be averaged by integrating them over several periods, instead we successively calculate moving averages as follows. The frequency Ω_r has the highest amplitude. Hence we first calculate a moving average with period $2\pi/\Omega_r$. In the resulting time series, the frequency Ω_r and its multiples are eliminated. Next, we calculate moving averages with periods $2\pi/\Omega_z$ and $2\pi/(n\Omega_r + k\Omega_z)$ until the resulting time series is smooth or too short. The result is calculated as an average of this final series.

Having obtained a single value for each time-domain calculation, we calculate the linear part in spin using Eq. (4.11) and the relative difference

$$\Delta\mathcal{F}^E_{S,m} = \left| 1 - \frac{\mathcal{F}^{E\mathrm{td}}_{S,m}}{\mathcal{F}^{E\mathrm{fd}}_{S,m}} \right| . \tag{4.14}$$

The results for nearly spherical orbits can be seen in Fig. (4.12). For all inclinations I and azimuthal numbers m, the error is lower than 7×10^{-3}, which is approximately the error of the *Teukode* (cf. Fig. 4.11). In Table 4.2, we list the values and relative errors of the fluxes from generic orbits for different orbital

p	e	I	m	$\mathcal{F}^E_{S,m}$	$\Delta\mathcal{F}^E_{S,m}$
10	0.1	15°	2	-2.8259×10^{-6}	1×10^{-3}
12	0.2	30°	1	-1.1954×10^{-7}	2×10^{-5}
12	0.2	30°	2	-1.0488×10^{-6}	1×10^{-3}
12	0.2	30°	3	-1.4210×10^{-7}	3×10^{-3}
12	0.2	60°	2	-8.0550×10^{-7}	5×10^{-4}
15	0.5	15°	2	-4.2936×10^{-7}	2×10^{-3}

Table 4.2: Values of the energy flux to infinity and the relative error of the time domain and frequency domain results for generic orbits with given orbital parameters and azimuthal number m.

parameters and azimuthal number m. In this case the relative difference is below 3×10^{-3}.

4.2.4 Summation of the fluxes

Here we describe our approach to the calculation of the total fluxes from eccentric equatorial orbits. In order to get the total equatorial fluxes, they have to be summed over l, m and n with proper bounds determined according to a given accuracy.

The error of the geodesic fluxes must be lower than the mass ratio to calculate the phase to subradian accuracy. Therefore, we set this accuracy to 10^{-7}. The accuracy of the linear parts in spin can be lower, since these parts contribute only to the postadiabatic order. Accordingly, we set the accuracy to 10^{-3}. However, since these linear parts are calculated simultaneously with the geodesic part and the accuracy of the geodesic fluxes is higher, their final error is lower than 10^{-3}.

For these calculations we make use of the following symmetry:

$$\mathcal{F}_{l,-m,-n} = -\mathcal{F}_{l,m,n} \ , \tag{4.15a}$$

$$\omega_{-m,-n} = -\omega_{m,n} \ , \tag{4.15b}$$

where $\mathcal{F}$ stands for the energy and angular momentum fluxes or their linear parts. Therefore, it is possible to sum only the modes with $\omega_{mn} > 0$ and multiply the result by two to obtain the total fluxes. The computed sums have the following structure:

$$\mathcal{F} = 2 \sum_{m=m_{\min}}^{m_{\max}} \mathcal{F}_m \ , \tag{4.16a}$$

$$\mathcal{F}_m = \sum_{l=l_{\min}}^{l_{\max}} \mathcal{F}_{lm} \ , \tag{4.16b}$$

$$\mathcal{F}_{lm} = \sum_{n=n_{\min}}^{n_{\max}} \mathcal{F}_{lmn} \ , \tag{4.16c}$$

where $m_{\min} = -5$, $l_{\min} = \max\{2, |m|\}$ and $n_{\min,\max}$, $m_{\max}$ and $l_{\max}$ are determined during the calculation according to a given error ϵ, which determines the accuracy we wish to achieve.

The procedure starts by calculating $\mathcal{F}_{22}$ mode and summing the $l = m = 2$ fluxes over n from $n_{\min} = \lceil -m\Omega_\phi/\Omega_r \rceil$ to $n = 20$. The lower bound corresponds

to the lowest n for which the frequency is positive. Next, we find the mode with the maximal flux as $\mathcal{F}_{\max} = \max_n \mathcal{F}_{22n}$. In all the studied cases the maximal flux lie within this range. We continue by calculating the fluxes for higher n until three consecutive modes are decreasing and are lower than $\mathcal{F}_{\max}\epsilon/10$. This termination condition is used later in the sums over n for other values of l and m.

Once we obtain the $\mathcal{F}_{22}$ mode, we continue by summing the $m = 2$ mode over l. For $l = 3, 4, \ldots$ we first set n to $n_0 = \lfloor 10me^2 \rfloor$, which is close to the maximum of the flux over n. Having set that, we increase n until the termination condition for n is satisfied. After that, n is decreased until the same termination condition is satisfied or until we reach the last mode with positive frequency. This computational procedure is repeated for higher l until the termination condition for l is satisfied. This termination condition reads $\mathcal{F}_{l_{\max}m} < \mathcal{F}_{22}\epsilon$.

So far, we have described the computation of the $\mathcal{F}_2$ mode. Subsequently, we calculate other m modes from $m_{\min} = -5$ by successively summing the modes over n and l using the termination conditions described in the previous paragraphs. The sum over m is truncated when the estimated error is less than $\epsilon/2$ times the total flux, i.e.

$$\frac{\mathcal{F}_{m_{\max}}}{1 - \mathcal{F}_{m_{\max}}/\mathcal{F}_{m_{\max}-1}} < \frac{\epsilon}{2} \sum_{m=m_{\min}}^{m_{\max}} \mathcal{F}_m \,, \tag{4.17}$$

where the error on the left hand side is calculated from the assumption that the fluxes $\mathcal{F}_m$ decrease exponentially with m. However, for orbits near the separatrix we truncate the series at $m = 20$ even when this condition is not satisfied while knowingly introducing an error. The reason is to save the computational cost. To efficiently calculate the fluxes in this area of the parameter space, further research is needed.

4.2.5 Interpolation of the fluxes

Because the calculation of the fluxes at one point in the parameter space is computationally expensive and can take hours of CPU time, we calculate the fluxes and their linear-in-spin parts on a grid in the $p - e$ plane and interpolate them. In particular, first, at each gridpoint we find the geodesic energy and angular momentum fluxes and their linear-in-spin parts with fixed frequencies $\delta\mathcal{F}|_{\Omega_i}$. The geodesic fluxes are then interpolated. From the linear-in-spin parts $\delta\mathcal{F}|_{\Omega_i}$ and the derivatives of the geodesic fluxes with respect to p and e, we calculate the linear parts with fixed p and e $\delta\mathcal{F}|_{p,e}$ by employing Eq. (2.41). Finally, we calculate $\dot{p}$, $\dot{e}$, $\partial_\sigma\dot{p}$, $\partial_\sigma\dot{e}$, $\partial_p\dot{p}$, $\partial_p\dot{e}$, $\partial_e\dot{p}$, and $\partial_e\dot{e}$ on the $p - e$ grid and interpolate them in order to use them for the calculation of the inspirals.

Prior to the interpolation, we normalize the quantities to factor out the behavior at infinity and near the separatrix. The normalization coefficients are derived from the Newtonian formulas for the fluxes

$$\mathcal{F}^E_{\rm N} = \frac{32}{5} p^{-5} (1 - e^2)^{3/2} \left(1 + \frac{73}{24} e^2 + \frac{37}{96} e^4\right) , \tag{4.18a}$$

$$\mathcal{F}^{J_z}_{\rm N} = \frac{32}{5} p^{-7/2} (1 - e^2)^{3/2} \left(1 + \frac{7}{8} e^2\right) \tag{4.18b}$$

and can be found in Eqs. (91) in Ref. [40].

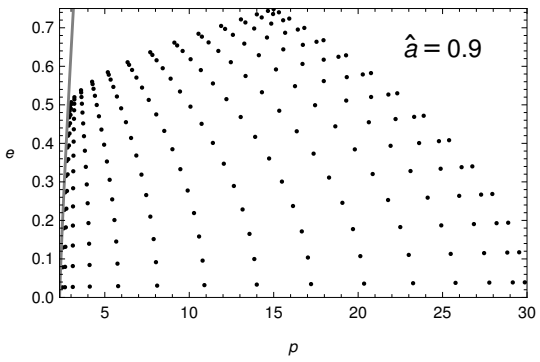

Figure 4.13: Grid in the $p - e$ plane where the fluxes are interpolated.

Instead of constructing the grid on the $p-e$ plane, we transform these variables to different set of coordinated x and y. The reason for this transformation is to make the grid denser near the separatrix and to avoid some regions where the calculation of the fluxes is difficult. The transformation is defined as follows. First, the coordinates p and e are transformed to

$$\tilde{U} = \sqrt{(p - r_{\rm ISCO})^2 - (p_s(e) - r_{\rm ISCO})^2} \,, \tag{4.19a}$$

$$V = e^2 \,, \tag{4.19b}$$

where $p_s(e)$ is the separatrix. This transformation regularizes some diverging quantities for circular orbits ($e = 0$). Next we transform $\tilde{U}$ as

$$U = \frac{c}{\log\left(1 + \frac{c}{\tilde{U}}\right)} \,, \tag{4.20}$$

where c is a parameter controlling the compactness of the grid near the separatrix. In our calculations we set $c = 25$. Then, we perform another transformation in the form

$$U = (U_{11} - U_{10} + U_{00} - U_{01})\mathsf{xy} + (U_{10} - U_{00})\mathsf{x} + (U_{01} - U_{00})\mathsf{y} + U_{00} \,, \tag{4.21a}$$

$$V = (V_{11} - V_{01})\mathsf{xy} + (V_{01} - V_{00})\mathsf{y} \,, \tag{4.21b}$$

where U_{xy} and V_{xy} are chosen according to given boundaries. We calculate the grid for $a = 0, 0.5M, 0.9M$ on Chebyshev nodes in x and y with 15 grid points in each direction. This grid in the $p - e$ plane is shown for $a = 0.9M$ in Fig. 4.13.

The main advantage of the Chebyshev interpolation is the exponential convergence, which allows us to calculate the fluxes at fewer points while maintaining high accuracy. The disadvantages are the slow convergence for non-analytical functions and the propagation of the error at one point across the interpolation domain. When a function is approximated with Chebyshev polynomials as

$$f(x, y) = \sum_{i,j} c_{ij} T_i(x) T_j(y) \,, \tag{4.22}$$

the interpolation error can be estimated as

$$\max_{i=i_{\max} \vee j=j_{\max}} |c_{ij}| \,. \tag{4.23}$$

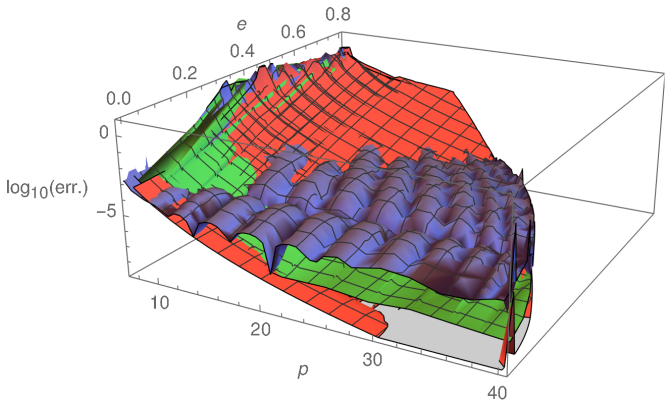

Figure 4.14: Relative interpolation error of the energy flux to infinity (violet) and relative error of the energy flux at individual points (green). The error is estimated from the 9PN series. The error of the PN series is estimated from the last term (red) and it diverges near the separatrix.

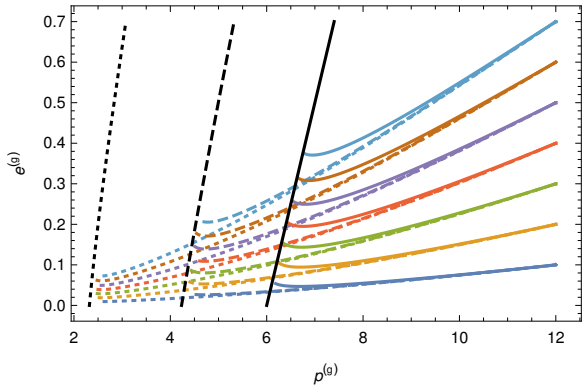

Figure 4.15: Adiabatic inspirals in the $p - e$ plane for $a = 0$ (solid), $a = 0.5M$ (dashed) and $a = 0.9M$ (dotted). The black curves denote the separatrices.

Using this estimate, the relative errors of the interpolated functions are 10^{-4} for the geodesic energy and angular momentum fluxes, 10^{-5} for $\dot{p}^{(\mathrm{g})}$ and $\dot{e}^{(\mathrm{g})}$ and between 10^{-3} and 10^{-2} for the derivatives of $\dot{p}^{(\mathrm{g})}$ and $\dot{e}^{(\mathrm{g})}$.

The achieved accuracy can be seen in Fig. 4.14, where we plot the relative difference between the interpolated energy flux and the 9th order post-Newtonian (PN) series [91] for $a = 0$. This relative difference is around 10^{-4} except for the region near the separatrix, where the PN series fails. In the same figure is plotted also the relative difference between the energy flux at individual points and the PN series, which is around 10^{-7}.

4.3 Calculation of the inspirals

Once we have calculated and interpolated the functions $\dot{p}^{(\mathrm{g})}$, $\dot{e}^{(\mathrm{g})}$ and their derivatives with respect to σ, p and e, we can calculate the inspirals, i.e. the evolution of the functions $p^{(\mathrm{g})}(t)$, $e^{(\mathrm{g})}(t)$, $\delta p(t)$, and $\delta e(t)$, from Eqs. (3.12) and (3.16). For this we employ the *NDSolve* function in *Mathematica* with adaptive-step 7/8th order Runge-Kutta method. Having done this, we can find the adiabatic phase

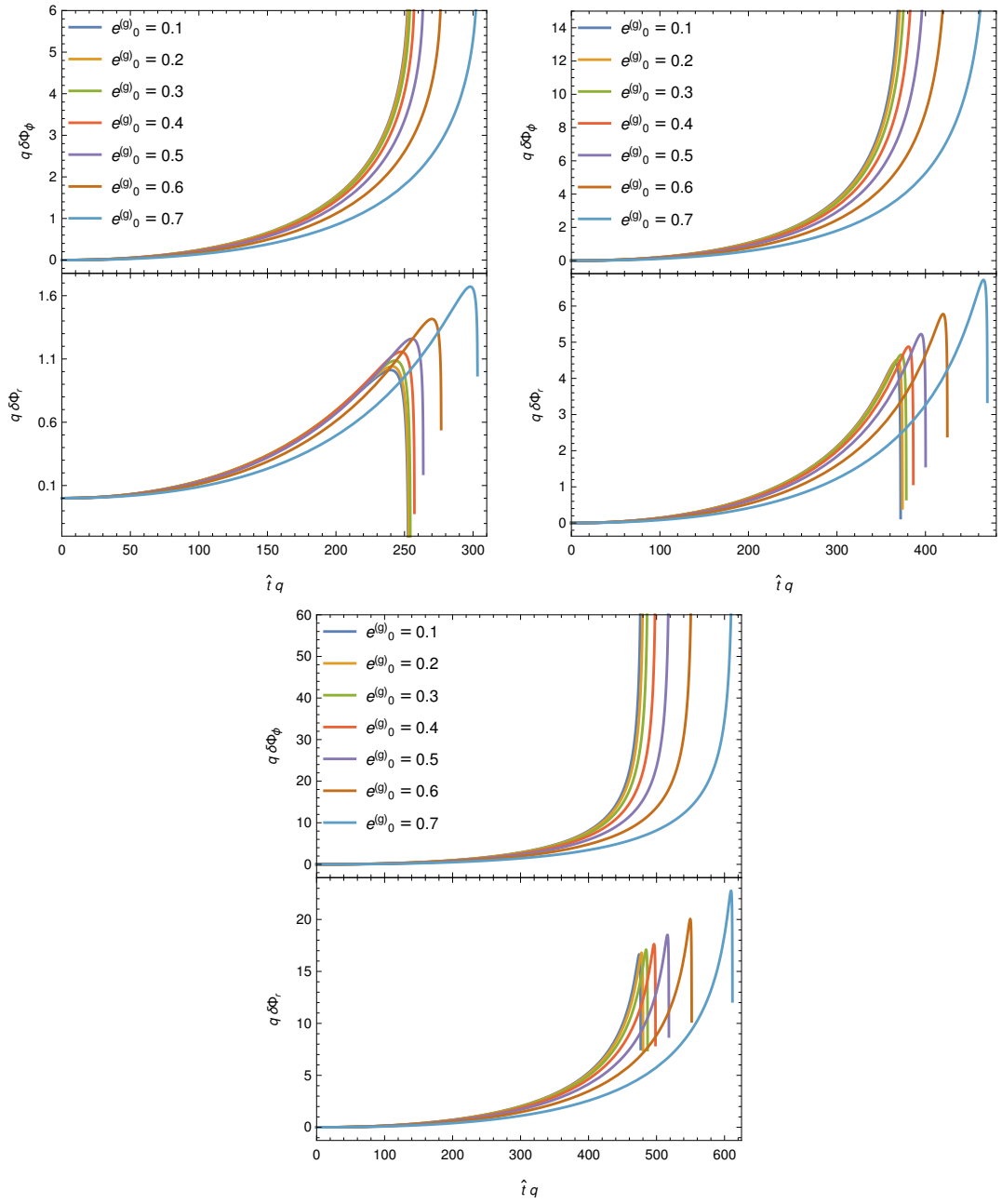

Figure 4.16: Radial and azimuthal phase shifts for the inspirals with $p_0^{(g)} = 12$, $a = 0$ (top left), $a = 0.5M$ (top right) and $a = 0.9M$ (bottom) and different initial eccentricities. The phase shifts are multiplied by q which corresponds to maximally rotating secondary BH.

and the correction due to spin by numerically integrating Eqs. (3.10) and (3.18). We have verified the obtained results by comparing them with the circular limit. This comparison can be found in Ref. [40].

In particular, we calculate the inspirals with matched initial frequencies by choosing the initial conditions for δp and δe from Eqs. (3.20). The inspirals are calculated for initial semi-latus rectum $p = 12$, initial eccentricities from $e = 0.1$ to $e = 0.7$ and three different values of the Kerr parameter $a = 0, 0.5M, 0.9M$. The adiabatic evolution in the $p - e$ plane can be found in Fig. 4.15.

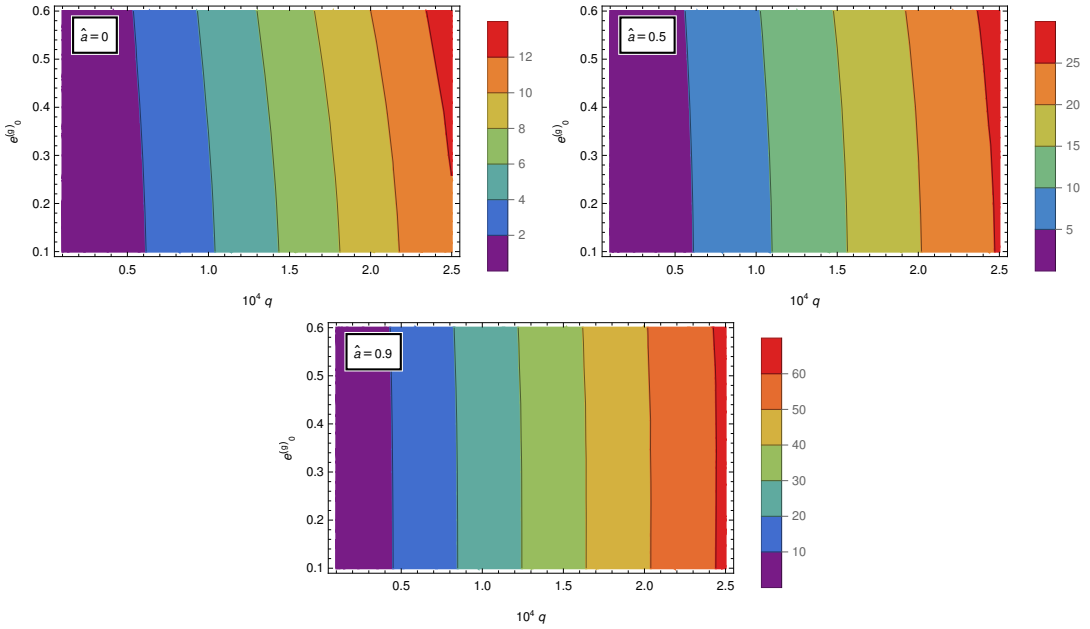

Figure 4.17: Maximal radial phase shifts $\max \delta\Phi_r$ for $\sigma = q$, $M = 10^6 M_\odot$. The duration of the inspiral is 1 year. Different mass ratios q, initial eccentricities $e_0^{(g)}$ and Kerr parameters a are considered in the above plots. The maximal phase shift grows with the mass ratio and the Kerr parameter (note the different scales for each a).

The phase shifts $\delta\Phi_r$ and $\delta\Phi_\phi$ are computed from these inspirals and plotted in Fig. 4.16. We can see that the azimuthal phase shifts are monotonically increasing until the particle reaches the separatrix where they diverge. The radial phase shifts increase at first and after they reach maximal value, they start decreasing and diverge as well. This divergence is caused by the failing of the two timescale approximation and of the linearization in the secondary spin.

To further examine the behavior of the phase shifts, we systematically calculate the inspiral for different initial eccentricities and mass ratios, while keeping the duration of the inspiral fixed at 1 year with the mass of the primary BH being $10^6 M_\odot$. We find the maximum of $\delta\Phi_r$ and plot the result for $\sigma = q$ in Fig. 4.17. We see that the maximal phase shifts increase with q and a reaching values between 20 and 30 for $q = 10^{-4}$ and $a = 0.9M$. The dependence on initial eccentricity is low, however, to study the degeneracies of the resulting waveforms, Bayesian analysis must be performed.

The accuracy of the phase shifts is around 5×10^{-3} which is determined from the comparison with the nonlinearized-in-spin inspirals (see Appendix F in Ref. [40]). In order to use the phase shifts in data analysis, the accuracy must increase. Therefore, we have increased the number of steps in x to 20 in our next work in progress.

Conclusion

The detection of GW signals from EMRIs with LISA and other space-based detectors will allow us to study the strong-field spacetime around massive BHs. To achieve this, waveform templates that include the postadiabatic term are needed. This term contains the effect of the secondary spin that can be calculated by adiabatically evolving the orbital parameters using GW fluxes to infinity and to the horizon of the primary BH. Therefore, we investigated the motion of spinning particles in the Kerr spacetime and calculated GW fluxes from the respective orbits. Then we used the aforementioned fluxes to adiabatically evolve the orbital parameters and to find the phase shift due to the secondary spin.

First, we focused on eccentric equatorial orbits. The only possible orientation of the spin in this setup is such that it is parallel or antiparallel to the symmetry axis of the central BH. Using the equations of motion derived in Ref. [61], we derived analytical formulas for the energy and the angular momentum as functions of the semilatus rectum p and the eccentricity e. Moreover, we found formulas allowing the numerical calculation of the fundamental frequencies with respect to the coordinate time and for the coordinates in Darwin parametrization.

Having the nonlinearized formulas for the coordinates, frequencies and constants of motion, we linearized them in the secondary spin, since this order is sufficient for the first postadiabatic term. We considered two cases with different reference geodesics. In the first case we found the linear-in-spin parts with respect to a geodesic with the same p and e. In the second case the reference geodesics has the same radial and azimuthal frequencies Ω_r and Ω_ϕ.

Next, we moved to generic off-equatorial orbits. Using the approach from Refs. [64, 65], we calculated generic trajectories of spinning particles and the linear-in-spin parts with fixed orbital parameters semi-latus rectum p, eccentricity e, and inclination angle I.

The calculated trajectories were utilized in the calculation of GW fluxes to infinity and to the horizon of the primary BH. This was achieved by solving the Teukolsky equation in the frequency domain with the spinning-particle source term. Because of the discrete frequency spectrum of the trajectory, the frequency spectrum of the fluxes is discrete as well allowing us to calculate the total flux as a sum over multipoles l and m and harmonic indices n and k. The infinity and horizon partial amplitudes of each such mode $C^{\pm}_{lmnk}$ are calculated as integral over the radial and polar phase of a function constructed from the stress-energy tensor of a spinning particle containing the quantities describing the trajectory calculated earlier.

Furthermore, for equatorial fluxes, we calculated the linear-in-spin parts of the amplitudes $\delta C^{\pm}_{lmn}\big|_{\Omega_i}$ and fluxes $\delta\mathcal{F}^{E,J_z}\big|_{\Omega_i}$ with fixed frequencies and found the formula to transform them to the respective linear parts with fixed orbital parameters $\delta C^{\pm}_{lmn}\big|_{p,e}$ and $\delta\mathcal{F}^{E,J_z}\big|_{p,e}$.

The fact that the fluxes $\mathcal{F}_{lmnkj}$ are quadratic in the amplitudes $C^{\pm}_{lmnkj}$ and the amplitudes of the $j = \pm 1$ modes, which correspond to the perpendicular precessing component of the spin, are proportional to σ led us to conclude that the contribution of the perpendicular component of the spin to the fluxes is $\mathcal{O}(\sigma^2)$. Therefore, in the linear-in-spin order only the parallel component is relevant and

measurable.

To verify the the validity of the frequency-domain fluxes computations, we compared them to fluxes obtained from a time-domain TE solver called *Teukode*. For the latter computations, we implemented a piecewise-polynomial approximation of the delta function to improve the efficiency and accuracy of *Teukode*. For equatorial fluxes, we compared the full non-linearized strain at infinity and the energy fluxes for different resolutions of the time-domain grid. Assuming that the error of the frequency-domain result is much lower than the error of the time-domain result, we calculated the error of the time-domain result as relative difference of the time-domain and frequency-domain fluxes. We verified that the relative error decreases with increasing resolution for different values of the secondary spin and eccentricities.

In the generic and nearly spherical case the fluxes are accurate only up to linear order in spin and cannot be directly compared to the nonlinearized time-domain fluxes. Thus, we compared the linear-in-spin parts of the fluxes obtained by numerical derivatives with respect to σ of the frequency domain and time-domain results. Because of the computational costs, which are higher in the generic case, we compared the fluxes only for some orbital parameters without checking the convergence. We found that the frequency-domain and time-domain energy fluxes agree up to the numerical accuracy of *Teukode*.

The obtained equatorial GW fluxes were used to adiabatically evolve the orbital parameters. Because the calculation of the fluxes at each point of the parameter space is computationally expensive, we calculated the fluxes and their linear-in-spin parts on a grid with Chebyshev nodes and interpolated them. Consequently, the grid was used to adiabatically evolve the orbital parameters p, e and the phases Φ_r, Φ_ϕ. Operating in the linear in spin framework allowed us to obtain the radial and azimuthal phase shifts $\delta\Phi_r$ and $\delta\Phi_\phi$ for various parameters of the system.

The natural extension of this work is to calculate adiabatic evolution of the orbital parameters for generic orbits of spinning particles and to find the spin-induced phase shifts. However, for this, the rate of change of the Carter-like constant K_R and the parallel spin $\sigma_\parallel$ are needed. These fluxes have not been derived yet. Another direction is to use the equatorial fluxes to generate the inspirals using the *FastEMRIWaveforms* framework [92] and perform Bayesian analysis of the waveforms to analyze the detactability of the secondary spin, since it was found for quasicircular inspirals [36] that the system is degenerate and the secondary spin is not measurable. The ultimate goal is to include other postadiabatic effects and generate accurate enough waveforms for the detection and parameter analysis of EMRIs.

Bibliography

[1] B. P. Abbott et al. Observation of gravitational waves from a binary black hole merger. *Phys. Rev. Lett.*, 116(6):061102, February 2016.

[2] B. P. Abbott et al. GWTC-1: A gravitational-wave transient catalog of compact binary mergers observed by LIGO and Virgo during the first and second observing runs. *Phys. Rev. X*, 9:031040, September 2019.

[3] R. Abbott et al. GWTC-2: Compact binary coalescences observed by LIGO and Virgo during the first half of the third observing run. *Physical Review X*, 11(2):021053, April 2021.

[4] The LIGO Scientific Collaboration, the Virgo Collaboration, the KAGRA Collaboration, R. Abbott, et al. GWTC-3: Compact binary coalescences observed by LIGO and Virgo during the second part of the third observing run. *arXiv e-prints*, page arXiv:2111.03606, November 2021.

[5] B. P. Abbott et al. GW170817: Observation of gravitational waves from a binary neutron star inspiral. *Phys. Rev. Lett.*, 119:161101, October 2017.

[6] B. P. Abbott et al. GW190425: Observation of a compact binary coalescence with total mass $\sim 3.4\ M_\odot$. *Astrophys. J. Lett.*, 892(1):L3, March 2020.

[7] R. Abbott et al. GW190412: Observation of a binary-black-hole coalescence with asymmetric masses. *Phys. Rev. D*, 102:043015, August 2020.

[8] R. Abbott et al. GW190814: Gravitational waves from the coalescence of a 23 solar mass black hole with a 2.6 solar mass compact object. *The Astrophysical Journal Letters*, 896(2):L44, June 2020.

[9] R. Abbott, Ligo Scientific Collaboration, VIRGO Collaboration, KAGRA Collaboration, et al. Observation of gravitational waves from two neutron star-black hole coalescences. *Astrophys. J. Lett.*, 915(1):L5, July 2021.

[10] Gabriella Agazie, The NANOGrav Collaboration, et al. The NANOGrav 15 yr data set: Evidence for a gravitational-wave background. *The Astrophysical Journal Letters*, 951(1):L8, June 2023.

[11] J. Antoniadis et al. The second data release from the European Pulsar Timing Array III. Search for gravitational wave signals. *arXiv e-prints*, page arXiv:2306.16214, June 2023.

[12] Daniel J. Reardon, Andrew Zic, Ryan M. Shannon, George B. Hobbs, Matthew Bailes, Valentina Di Marco, Agastya Kapur, Axl F. Rogers, Eric Thrane, Jacob Askew, N. D. Ramesh Bhat, Andrew Cameron, Małgorzata Curyło, William A. Coles, Shi Dai, Boris Goncharov, Matthew Kerr, Atharva Kulkarni, Yuri Levin, Marcus E. Lower, Richard N. Manchester, Rami Mandow, Matthew T. Miles, Rowina S. Nathan, Stefan Osłowski, Christopher J. Russell, Renée Spiewak, Songbo Zhang, and Xing-Jiang Zhu. Search for an isotropic gravitational-wave background with the Parkes Pulsar Timing Array. *The Astrophysical Journal Letters*, 951(1):L6, June 2023.

[13] Heng Xu, Siyuan Chen, Yanjun Guo, Jinchen Jiang, Bojun Wang, Jiangwei Xu, Zihan Xue, R. Nicolas Caballero, Jianping Yuan, Yonghua Xu, Jingbo Wang, Longfei Hao, Jingtao Luo, Kejia Lee, Jinlin Han, Peng Jiang, Zhiqiang Shen, Min Wang, Na Wang, Renxin Xu, Xiangping Wu, Richard Manchester, Lei Qian, Xin Guan, Menglin Huang, Chun Sun, and Yan Zhu. Searching for the nano-hertz stochastic gravitational wave background with the Chinese Pulsar Timing Array data release I. *Research in Astronomy and Astrophysics*, 23(7):075024, June 2023.

[14] Pau Amaro-Seoane, Heather Audley, Stanislav Babak, John Baker, Enrico Barausse, Peter Bender, Emanuele Berti, Pierre Binetruy, Michael Born, Daniele Bortoluzzi, Jordan Camp, Chiara Caprini, et al. Laser Interferometer Space Antenna. *arXiv e-prints*, page arXiv:1702.00786, February 2017.

[15] Jun Luo, Li-Sheng Chen, Hui-Zong Duan, Yun-Gui Gong, Shoucun Hu, Jianghui Ji, Qi Liu, Jianwei Mei, Vadim Milyukov, Mikhail Sazhin, Cheng-Gang Shao, Viktor T. Toth, Hai-Bo Tu, Yamin Wang, Yan Wang, Hsien-Chi Yeh, Ming-Sheng Zhan, Yonghe Zhang, Vladimir Zharov, and Ze-Bing Zhou. TianQin: a space-borne gravitational wave detector. *Classical and Quantum Gravity*, 33(3):035010, February 2016.

[16] Wen-Hong Ruan, Zong-Kuan Guo, Rong-Gen Cai, and Yuan-Zhong Zhang. Taiji program: Gravitational-wave sources. *International Journal of Modern Physics A*, 35(17):2050075, June 2020.

[17] Stanislav Babak, Jonathan Gair, Alberto Sesana, Enrico Barausse, Carlos F. Sopuerta, Christopher P. L. Berry, Emanuele Berti, Pau Amaro-Seoane, Antoine Petiteau, and Antoine Klein. Science with the space-based interferometer LISA. V. extreme mass-ratio inspirals. *Phys. Rev. D*, 95(10):103012, May 2017.

[18] Alvin J. K. Chua, Christopher J. Moore, and Jonathan R. Gair. Augmented kludge waveforms for detecting extreme-mass-ratio inspirals. *Phys. Rev. D*, 96(4):044005, August 2017.

[19] Adam Pound and Barry Wardell. *Black Hole Perturbation Theory and Gravitational Self-Force*, pages 1–119. Springer Singapore, Singapore, 2020.

[20] Tanja Hinderer and Éanna É. Flanagan. Two-timescale analysis of extreme mass ratio inspirals in Kerr spacetime: Orbital motion. *Phys. Rev. D*, 78(6):064028, September 2008.

[21] Yasushi Mino. Perturbative approach to an orbital evolution around a supermassive black hole. *Phys. Rev. D*, 67(8):084027, April 2003.

[22] Sarp Akcay, Sam R. Dolan, Chris Kavanagh, Jordan Moxon, Niels Warburton, and Barry Wardell. Dissipation in extreme mass-ratio binaries with a spinning secondary. *Phys. Rev. D*, 102(6):064013, September 2020.

[23] Josh Mathews, Adam Pound, and Barry Wardell. Self-force calculations with a spinning secondary. *Phys. Rev. D*, 105(8):084031, April 2022.

[24] Masaru Shibata. Gravitational waves induced by a particle orbiting around a rotating black hole: Effect of orbital precession. *Progress of Theoretical Physics*, 90(3):595–614, September 1993.

[25] Scott A. Hughes. Evolution of circular, nonequatorial orbits of Kerr black holes due to gravitational-wave emission. *Phys. Rev. D*, 61(8):084004, April 2000.

[26] Curt Cutler, Daniel Kennefick, and Eric Poisson. Gravitational radiation reaction for bound motion around a Schwarzschild black hole. *Phys. Rev. D*, 50:3816–3835, September 1994.

[27] Masaru Shibata. Gravitational waves by compact star orbiting around rotating supermassive black holes. *Phys. Rev. D*, 50:6297–6311, November 1994.

[28] Kostas Glampedakis and Daniel Kennefick. Zoom and whirl: Eccentric equatorial orbits around spinning black holes and their evolution under gravitational radiation reaction. *Phys. Rev. D*, 66:044002, August 2002.

[29] Lee Samuel Finn and Kip S. Thorne. Gravitational waves from a compact star in a circular, inspiral orbit, in the equatorial plane of a massive, spinning black hole, as observed by LISA. *Phys. Rev. D*, 62(12):124021, December 2000.

[30] Scott A. Hughes. Evolution of circular, nonequatorial orbits of Kerr black holes due to gravitational-wave emission. II. Inspiral trajectories and gravitational waveforms. *Phys. Rev. D*, 64(6):064004, September 2001.

[31] Steve Drasco and Scott A. Hughes. Gravitational wave snapshots of generic extreme mass ratio inspirals. *Phys. Rev. D*, 73:024027, January 2006.

[32] Wen-Biao Han. Gravitational radiation from a spinning compact object around a supermassive Kerr black hole in circular orbit. *Phys. Rev. D*, 82(8):084013, October 2010.

[33] Enno Harms, Georgios Lukes-Gerakopoulos, Sebastiano Bernuzzi, and Alessandro Nagar. Asymptotic gravitational wave fluxes from a spinning particle in circular equatorial orbits around a rotating black hole. *Phys. Rev. D*, 93(4):044015, February 2016.

[34] Alessandro Nagar, Francesco Messina, Chris Kavanagh, Georgios Lukes-Gerakopoulos, Niels Warburton, Sebastiano Bernuzzi, and Enno Harms. Factorization and resummation: A new paradigm to improve gravitational wave amplitudes. III. the spinning test-body terms. *Phys. Rev. D*, 100(10):104056, November 2019.

[35] Gabriel Andres Piovano, Andrea Maselli, and Paolo Pani. Extreme mass ratio inspirals with spinning secondary: A detailed study of equatorial circular motion. *Phys. Rev. D*, 102(2):024041, July 2020.

[36] Gabriel Andres Piovano, Richard Brito, Andrea Maselli, and Paolo Pani. Assessing the detectability of the secondary spin in extreme mass-ratio inspirals with fully relativistic numerical waveforms. *Phys. Rev. D*, 104(12):124019, December 2021.

[37] Ryuichi Fujita and Masaru Shibata. Extreme mass ratio inspirals on the equatorial plane in the adiabatic order. *Phys. Rev. D*, 102(6):064005, September 2020.

[38] Scott A. Hughes, Niels Warburton, Gaurav Khanna, Alvin J. K. Chua, and Michael L. Katz. Adiabatic waveforms for extreme mass-ratio inspirals via multivoice decomposition in time and frequency. *Phys. Rev. D*, 103(10):104014, May 2021.

[39] Viktor Skoupý and Georgios Lukes-Gerakopoulos. Spinning test body orbiting around a Kerr black hole: Eccentric equatorial orbits and their asymptotic gravitational-wave fluxes. *Phys. Rev. D*, 103:104045, May 2021.

[40] Viktor Skoupý and Georgios Lukes-Gerakopoulos. Adiabatic equatorial inspirals of a spinning body into a Kerr black hole. *Phys. Rev. D*, 105:084033, April 2022.

[41] Viktor Skoupý, Georgios Lukes-Gerakopoulos, Lisa V. Drummond, and Scott A. Hughes. Asymptotic gravitational-wave fluxes from a spinning test body on generic orbits around a Kerr black hole. *arXiv e-prints*, page arXiv:2303.16798, March 2023.

[42] Myron Mathisson. Neue mechanik materieller systemes. *Acta Phys. Pol.*, 6:163–2900, 1937.

[43] Myron Mathisson. Republication of: New mechanics of material systems. *Gen. Relativ. Gravit.*, 42(4):1011–1048, 2010.

[44] K. Kyrian and O. Semerák. Spinning test particles in a Kerr field – II. *Mon. Not. R. Astron. Soc.*, 382(4):1922–1932, November 2007.

[45] W. G. Dixon. A covariant multipole formalism for extended test bodies in general relativity. *Il Nuovo Cimento*, 34(2):317–339, October 1964.

[46] W.G. Dixon. Isolated gravitating systems in general relativity. *Proceedings of the International School of Physics "Enrico Fermi," Course LXVII, edited by J. Ehlers, North Holland, Amsterdam*, pages 156–219, 1979.

[47] Yasushi Mino, Masaru Shibata, and Takahiro Tanaka. Gravitational waves induced by a spinning particle falling into a rotating black hole. *Phys. Rev. D*, 53:622–634, January 1996.

[48] Takahiro Tanaka, Yasushi Mino, Misao Sasaki, and Masaru Shibata. Gravitational waves from a spinning particle in circular orbits around a rotating black hole. *Phys. Rev. D*, 54(6):3762–3777, September 1996.

[49] Adam Pound. Nonlinear gravitational self-force: Field outside a small body. *Phys. Rev. D*, 86(8):084019, October 2012.

[50] E. Corinaldesi, A. Papapetrou, and Rudolf Ernst Peierls. Spinning test-particles in general relativity. II. *Proc. R. Soc. A*, 209(1097):259–268, 1951.

[51] F. A. E. Pirani. On the physical significance of the Riemann tensor. *Acta Phys. Pol.*, 15:389–405, January 1956.

[52] W Tulczyjew. Motion of multipole particles in general relativity theory. *Acta Phys. Pol.*, 18:393, 1959.

[53] W.G. Dixon. Dynamics of extended bodies in general relativity. I. momentum and angular momentum. *Proc. R. Soc. A*, 314:499–527, 1970.

[54] H. P. Künzle. Canonical dynamics of spinning particles in gravitational and electromagnetic fields. *J. Math. Phys.*, 13(5):739–744, 1972.

[55] Juergen Ehlers and Ekkart Rudolph. Dynamics of extended bodies in general relativity center-of-mass description and quasirigidity. *Gen. Relativ. Gravit.*, 8(3):197–217, 1977.

[56] Vojtěch Witzany, Jan Steinhoff, and Georgios Lukes-Gerakopoulos. Hamiltonians and canonical coordinates for spinning particles in curved space-time. *Class. Quantum Gravity*, 36(7):075003, April 2019.

[57] Ondřej Zelenka, Georgios Lukes-Gerakopoulos, Vojtěch Witzany, and Ondřej Kopáček. Growth of resonances and chaos for a spinning test particle in the Schwarzschild background. *Phys. Rev. D*, 101(2):024037, January 2020.

[58] R Rüdiger. Conserved quantities of spinning test particles in general relativity. I. *Proc. R. Soc. A*, 375:185–193, 1981.

[59] R Rüdiger. Conserved quantities of spinning test particles in general relativity. II. *Proc. R. Soc. A*, 385:229–239, 1981.

[60] Eva Hackmann, Claus Lämmerzahl, Yuri N. Obukhov, Dirk Puetzfeld, and Isabell Schaffer. Motion of spinning test bodies in Kerr spacetime. *Phys. Rev. D*, 90(6):064035, September 2014.

[61] Motoyuki Saijo, Kei-ichi Maeda, Masaru Shibata, and Yasushi Mino. Gravitational waves from a spinning particle plunging into a Kerr black hole. *Phys. Rev. D*, 58:064005, August 1998.

[62] W. Schmidt. Celestial mechanics in Kerr spacetime. *Class. Quantum Gravity*, 19(10):2743, April 2002.

[63] Vojtěch Witzany. Hamilton-Jacobi equation for spinning particles near black holes. *Phys. Rev. D*, 100(10):104030, November 2019.

[64] Lisa V. Drummond and Scott A. Hughes. Precisely computing bound orbits of spinning bodies around black holes. I. General framework and results for nearly equatorial orbits. *Phys. Rev. D*, 105(12):124040, June 2022.

[65] Lisa V. Drummond and Scott A. Hughes. Precisely computing bound orbits of spinning bodies around black holes. II. Generic orbits. *Phys. Rev. D*, 105(12):124041, June 2022.

[66] J.-A. Marck. Solution to the equations of parallel transport in Kerr geometry; tidal tensor. *Proc. R. Soc. A*, 385(1789):431–438, 1983.

[67] Maarten van de Meent. Analytic solutions for parallel transport along generic bound geodesics in Kerr spacetime. *Class. Quantum Gravity*, 37(14):145007, July 2020.

[68] Leor Barack and Adam Pound. Self-force and radiation reaction in general relativity. *Rep. Prog. Phys.*, 82(1):016904, January 2019.

[69] Eric Poisson, Adam Pound, and Ian Vega. The motion of point particles in curved spacetime. *Living Reviews in Relativity*, 14(1):7, September 2011.

[70] Adam Pound. *Motion of Small Objects in Curved Spacetimes: An Introduction to Gravitational Self-Force*, pages 399–486. Springer International Publishing, Cham, 2015.

[71] Abraham I. Harte. Mechanics of extended masses in general relativity. *Class. Quantum Gravity*, 29(5):055012, March 2012.

[72] Adam Pound. Gauge and motion in perturbation theory. *Phys. Rev. D*, 92(4):044021, August 2015.

[73] Yasushi Mino, Misao Sasaki, and Takahiro Tanaka. Gravitational radiation reaction to a particle motion. *Phys. Rev. D*, 55(6):3457–3476, March 1997.

[74] Theodore C. Quinn and Robert M. Wald. Axiomatic approach to electromagnetic and gravitational radiation reaction of particles in curved spacetime. *Phys. Rev. D*, 56(6):3381–3394, September 1997.

[75] N. Sago, T. Tanaka, W. Hikida, K. Ganz, and H. Nakano. Adiabatic evolution of orbital parameters in Kerr spacetime. *Prog. Theor. Phys.*, 115(5):873–907, May 2006.

[76] William Kinnersley. Type D vacuum metrics. *J. Math. Phys.*, 10(7):1195–1203, November 1969.

[77] Saul A. Teukolsky. Perturbations of a rotating black hole. I. Fundamental equations for gravitational, electromagnetic, and neutrino-field perturbations. *Astrophys. J.*, 185:635–648, October 1973.

[78] A. A. Starobinskij and S. M. Churilov. Amplification of electromagnetic and gravitational waves scattered by a rotating black hole. *Zhurnal Eksperimentalnoi i Teoreticheskoi Fiziki*, 65:3–11, January 1973.

[79] S. A. Teukolsky and W. H. Press. Perturbations of a rotating black hole. III. Interaction of the hole with gravitational and electromagnetic radiation. *Astrophys. J.*, 193:443–461, October 1974.

[80] Enno Harms, Sebastiano Bernuzzi, Alessandro Nagar, and Anil Zenginoglu. A new gravitational wave generation algorithm for particle perturbations of the Kerr spacetime. *Class. Quantum Gravity*, 31(24):245004, 2014.

[81] Pranesh A. Sundararajan, Gaurav Khanna, Scott A. Hughes, and Steve Drasco. Towards adiabatic waveforms for inspiral into kerr black holes. II. dynamical sources and generic orbits. *Phys. Rev. D*, 78(2):024022, July 2008.

[82] Johan Waldén. On the approximation of singular source terms in differential equations. *Numerical Methods for Partial Differential Equations*, 15(4):503–520, 1999.

[83] Viktor Skoupý and Georgios Lukes-Gerakopoulos. Gravitational wave templates from extreme mass ratio inspirals. *arXiv e-prints*, page arXiv:2101.04533, January 2021.

[84] Black Hole Perturbation Toolkit. (bhptoolkit.org), 2023.

[85] Seth Hopper, Erik Forseth, Thomas Osburn, and Charles R. Evans. Fast spectral source integration in black hole perturbation calculations. *Phys. Rev. D*, 92(4):044048, August 2015.

[86] Niels Warburton, Barry Wardell, Oliver Long, Sam Upton, Philip Lynch, Zachary Nasipak, and Leo C. Stein. KerrGeodesics, July 2023.

[87] Barry Wardell, Niels Warburton, Kevin Cunningham, Leanne Durkan, Benjamin Leather, Zachary Nasipak, Chris Kavanagh, and TheoTorresV. Teukolsky, July 2023.

[88] Shuhei Mano, Hisao Suzuki, and Eiichi Takasugi. Analytic solutions of the Teukolsky equation and their low frequency expansions. *Prog. Theor. Phys.*, 95:1079–1096, 1996.

[89] Barry Wardell, Niels Warburton, KwintenF, Sam Upton, and Kevin Cunningham. SpinWeightedSpheroidalHarmonics, July 2023.

[90] E. W. Leaver and Subrahmanyan Chandrasekhar. An analytic representation for the quasi-normal modes of Kerr black holes. *Proc. R. Soc. A*, 402(1823):285–298, 1985.

[91] Christopher Munna, Charles R. Evans, Seth Hopper, and Erik Forseth. Determination of new coefficients in the angular momentum and energy fluxes at infinity to 9PN order for eccentric Schwarzschild extreme-mass-ratio inspirals using mode-by-mode fitting. *Phys. Rev. D*, 102(2):024047, July 2020.

[92] Michael L. Katz, Alvin J. K. Chua, Lorenzo Speri, Niels Warburton, and Scott A. Hughes. Fast extreme-mass-ratio-inspiral waveforms: New tools for millihertz gravitational-wave data analysis. *Phys. Rev. D*, 104(6):064047, September 2021.

List of Figures

List of Tables

List of Abbreviations

GW	gravitational wave
BH	black hole
NS	neutron star
EMRI	extreme mass ratio inspiral
MPD	Mathisson-Papapetrou-Dixon
SSC	spin supplementary condition
TE	Teukolsky equation
BHPT	Black Hole Perturbation Toolkit
PN	post-Newtonian

List of publications

1. Viktor Skoupý and Georgios Lukes-Gerakopoulos. Spinning test body orbiting around a Kerr black hole: Eccentric equatorial orbits and their asymptotic gravitational-wave fluxes. *Phys. Rev. D*, 103:104045, May 2021.

2. Viktor Skoupý and Georgios Lukes-Gerakopoulos. Adiabatic equatorial inspirals of a spinning body into a Kerr black hole. *Phys. Rev. D*, 105:084033, April 2022.

3. Viktor Skoupý, Georgios Lukes-Gerakopoulos, Lisa V. Drummond, and Scott A. Hughes. Asymptotic gravitational-wave fluxes from a spinning test body on generic orbits around a Kerr black hole. Accepted to be published in *Phys. Rev. D*

A. Attachments

A.1 Spinning test body orbiting around a Kerr black hole: Eccentric equatorial orbits and their asymptotic gravitational-wave fluxes

This Attachment contains the paper *Spinning test body orbiting around a Kerr black hole: Eccentric equatorial orbits and their asymptotic gravitational-wave fluxes* [39] published in Physical Review D. This version corrects some typos in the published version.

Spinning test body orbiting around a Kerr black hole: Eccentric equatorial orbits and their asymptotic gravitational-wave fluxes

Viktor Skoupý[1,2] and Georgios Lukes-Gerakopoulos[1]
[1] *Astronomical Institute of the Czech Academy of Sciences, Boční II 1401/1a, CZ-141 00 Prague, Czech Republic and*
[2] *Institute of Theoretical Physics, Faculty of Mathematics and Physics, Charles University, 18000 Prague, Czech Republic*

We use the frequency and time domain Teukolsky formalism to calculate gravitational-wave fluxes from a spinning body on a bound eccentric equatorial orbit around a Kerr black hole. The spinning body is represented as a point particle following the pole-dipole approximation of the Mathisson-Papapetrou-Dixon equations. Reformulating these equations we are not only able to find the trajectory of a spinning particle in terms of its constants of motion, but also to provide a method to calculate the azimuthal and the radial frequency of this trajectory. Using these orbital quantities, we introduce the machinery to calculate through the frequency domain Teukolsky formalism the energy and the angular momentum fluxes at infinity, and at the horizon, along with the gravitational strain at infinity. We crosscheck the results obtained from the frequency domain approach with the results obtained from a time domain Teukolsky equation solver called Teukode.

I. INTRODUCTION

An extreme mass ratio inspiral (EMRI) is one of the most promising events expected to be detected with future space-based gravitational wave (GW) detectors like Laser Interferometer Space Antenna (LISA) [1]. An EMRI occurs when a stellar mass compact object such as a black hole (BH) or a neutron star (secondary object) is trapped in the vicinity of a supermassive black hole (SMBH) (primary object). Due to gravitational radiation reaction the secondary is slowly spiralling into the primary while emitting GWs. From these GWs it is possible to extract information about the EMRI system such as the masses of the objects, their spins etc. On a more fundamental physics level, EMRIs detection are expected to allow us to probe the strong gravity regime around a SMBH [2].

Currently in order to extract information from a GW signal, when it is detected by the terrestrial observatories, it has to be uncovered from a dominating noise background. To achieve this, matched filtering is employed, i.e. waveform templates for a wide range of parameters are matched with the detected time series. It is expected that we will have to use matched filtering for GW signal received by LISA as well, but not to uncover the signal from the noise; in LISA's case we will use them to disentangle overlapping GW signals from simultaneously detected sources. Because of this, accurate models of the GW waveform templates are planned to be produced for a wide range of parameters.

To model GWs from an EMRI, first the trajectory of the secondary object must be reproduced. The standard way to do this is to apply the two timescale approximation [3]. In an EMRI the mass ratio $q \equiv \mu/M$ lies between 10^{-7} and 10^{-4}, where μ is the secondary mass and M is the primary mass. The energy changes at rate $\dot{E}/E = \mathcal{O}(q)$ which is very small. The timescale of the inspiral is, thus, of the order $\mathcal{O}(q^{-1})$, i.e, q^{-1} times larger than the orbital timescale. This allows us to break our analysis in two timescales, the fast orbital and the slow adiabatic dissipation in the constants of motion. In the fast one, the trajectory of the secondary over one orbital period is close to a trajectory calculated without a dissipation. The secondary is actually drifting between orbits characterized by a set of constants of motion. In this setup, the azimuthal coordinate of the inspiral can be expanded as $\phi = q^{-1}\phi^{(0)}(qt) + \phi^{(1)}(qt) + \mathcal{O}(q)$. The first term of the expansion is of *adiabatic order* and includes the contribution from the time-averaged dissipative part of the first-order self-force. The second term, which is of the order of radians is called *post-adiabatic* and contains contributions from the conservative part of the first-order self-force, oscillating part of the dissipative part of the first order self-force as well as the time-averaged dissipative part of the second-order self-force. The spin of the secondary contributes to the post-adiabatic term as is of the order of $\mathcal{O}(q)$ [4, 5]. In particular, for the spin magnitude S of a secondary compact object, like a Kerr BH or a neutron star, holds that $S \lesssim \mu^2$, hence the dimensionless spin parameter defined as $\sigma \equiv S/(\mu M) \leq q$ is of the same order as the mass ratio [6]. The phase ϕ is approximately proportional to the phase of the GW. Hence, to accurately model the GW fluxes, all the aforementioned terms must be taken into account.

In this work, we deal with the contribution of the secondary spin to the post-adiabatic term, in the case of bounded equatorial orbits around a Kerr BH. The description of a spinning test body moving on a curved background was for the first time studied in [7–9]. In particular, Mathisson [10] managed to write the stress-energy tensor of an extended test body as a sum of multipolar moments. When the body is sufficiently small and compact, then it is sufficient to take into account only the mass (monopole) and the spin (dipole) leading to what is known as the *pole-dipole approximation*, which essentially reduces the body to a spinning test particle. Later on Papapetrou [11, 12] was able to employ the con-

servation law of the stress energy tensor $\nabla_\mu T^{\mu\nu} = 0$ to derive the equations of motion for a spinning particle. Finally, these equations were rewritten by Tulczyjew [13], Dixon [14–17] and Wald [18] bringing them to their modern form. MPD equations have been studied in several works, see e.g. [6, 19–22]. Particularly, these equations simplify when the particle is confined into the equatorial plane of the Kerr spacetime [23]. In this case, the motion can be determined by the following constants of motion: the energy E, the component of the total angular momentum parallel to the axis of the central BH J_z, the mass of the secondary μ and the magnitude of its spin S.

In the present work, we rederive the equations of motion for a spinning particle in the equatorial plane in a reduced form. This allows us to find analytical formulas for the constants of motion dependence on the eccentricity and the semi-latus rectum and to provide a method to numerically calculate the fundamental frequencies. These results are then used to calculate the GW fluxes. To achieve this, we employ the Teukolsky formalism and solve the GWs perturbatively. Namely, we solve the Teukolsky equation (TE) both in the frequency and in the time domain with a spinning-particle as a source. In the frequency domain, the formulas providing the energy and the angular momentum fluxes to infinity and to the horizon from a spinning particle following equatorial trajectories are novel. While, for the calculations in the time domain, we introduce a new approach to simulate the spinning source making the computations more efficient. Due to the GW flux balance law in an EMRI, these fluxes equal to the rate of change of the constants of motion of an inspiraling spinning particle [5, 24]. Hence, once these fluxes are obtained, then the adiabatic term with the spinning-particle contribution to the post-adiabatic term can be reconstructed.

This paper is organized as follows. Section II briefs the dynamics of a spinning particle moving in a curved spacetime. After covering the basics, the equations of motion of a spinning particle are rederived in a reduced form appropriate for eccentric equatorial orbits in a Kerr BH background. Subsequently, the constants of motion and the frequencies are calculated. Section III reviews the Teukolsky formalism calculating the GW fluxes both in the frequency and the time domain. Finally, the frequency domain results are compared with the time domain results. To make the main text more readable, we have concentrated in a list all the dimensionless quantities we use in Appendix A, Appendix B provides all the explicit formulas for the frequency domain fluxes, while in Appendix C our frequency domain results for a non-spinning object are compared with the ones of [25]. Finally, Appendix D provides tables from the frequency domain calculations aiming to serve as reference for future works.

Throughout this paper, we use geometrized units where the speed of light and the gravitational constant are $c = G = 1$. The Riemann tensor is defined as $R^\mu{}_{\nu\kappa\lambda} = \Gamma^\mu{}_{\nu\lambda,\kappa} - \Gamma^\mu{}_{\nu\kappa,\lambda} + \Gamma^\mu{}_{\rho\kappa}\Gamma^\rho{}_{\nu\lambda} - \Gamma^\mu{}_{\rho\lambda}\Gamma^\rho{}_{\nu\kappa}$ where the comma denotes partial derivative $U_{\mu,\nu} = \partial_\nu U_\mu$. A covariant derivative is denoted by a semicolon $U_{\mu;\nu} = \nabla_\nu U_\mu$ and $\mathrm{D}U^\mu/\mathrm{d}\tau = U^\mu{}_{;\nu}\mathrm{d}x^\nu/\mathrm{d}\tau$. The signature of the metric is $(-,+,+,+)$. Symmetrization of indices is denoted by round brackets $\Phi_{(\mu\nu)} = (\Phi_{\mu\nu} + \Phi_{\nu\mu})/2$. For some quantities we prefer to use their dimensionless counterparts. They are denoted by a hat, e.g. energy $\hat{E} = E/\mu$, radial coordinate $\hat{r} = r/M$ etc (see Appendix A).

II. A POLE-DIPOLE PARTICLE MOVING ON THE EQUATORIAL PLANE OF A KERR BLACK HOLE

The motion of a spinning test object in a curved background is governed by the Mathisson-Papapetrou-Dixon (MPD) equations [9, 11, 14] which read

$$\begin{aligned} \frac{\mathrm{D}P^\mu}{\mathrm{d}\tau} &= -\frac{1}{2}\, R^\mu{}_{\nu\rho\sigma}\, v^\nu\, S^{\rho\sigma}\,, \\ \frac{\mathrm{D}S^{\mu\nu}}{\mathrm{d}\tau} &= P^\mu v^\nu - P^\nu v^\mu\,, \end{aligned} \tag{1}$$

where P^μ is the four-momentum of the particle, $R^\mu{}_{\nu\rho\sigma}$ is the Riemann tensor of the background spacetime, $v^\mu = \mathrm{d}x^\mu/\mathrm{d}\tau$ is the four-velocity, $S^{\mu\nu}$ is the spin tensor of the particle and $\mathrm{D}/\mathrm{d}\tau = v^\mu\nabla_\mu$ is the covariant derivative along the worldline parametrized by the proper time τ.

The stress-energy tensor $T^{\mu\nu}$ for a spinning particle with its trajectory parametrized by the coordinate time t reads [26]

$$T^{\mu\nu} = \frac{P^{(\mu}v^{\nu)}}{v^t}\frac{\delta^3}{\sqrt{-g}} - \nabla_\alpha\left(\frac{S^{\alpha(\mu}v^{\nu)}}{v^t}\frac{\delta^3}{\sqrt{-g}}\right)\,, \tag{2}$$

where for Boyer-Lindquist (BL) coordinates $\delta^3 = \delta(r - r_p(t))\delta(\theta - \theta_p(t))\delta(\phi - \phi_p(t))$ is the delta function located at the particle position $(r_p(t), \theta_p(t), \phi_p(t))$ parametrized by coordinate time. Note that by using the conservation law $T^{\mu\nu}{}_{;\nu} = 0$, it is possible to retrieve the MPD equations.

Actually, the MPD system of equations is underdetermined. The physical implication of the latter fact is that the center of the mass of the spinning object is not defined. To close the system of equations and to define the centre of the mass, a spin supplementary condition (SSC) in the form $S^{\mu\nu}V_\mu = 0$ has to be specified, where V_μ is a timelike vector field. In this work, we use the Tulczyjew-Dixon (TD) SSC [13, 15]

$$S^{\mu\nu}P_\mu = 0\,. \tag{3}$$

Under the TD SSC, the rest mass of the particle with respect to the four-momentun

$$\mu^2 = -P^\mu P_\mu \tag{4}$$

and the magnitude of the spin

$$S^2 = \frac{1}{2}S^{\mu\nu}S_{\mu\nu} \tag{5}$$

are conserved quantities (see e.g. [19]). The conservation of the above quantities is independent of the spacetime background. The symmetries of the spacetime introduce for each Killing vector ξ^μ a specific quantity

$$C = \xi^\mu P_\mu - \frac{1}{2}\xi_{\mu;\nu} S^{\mu\nu} \,, \tag{6}$$

which is conserved upon the evolution of the MPD equations.

Instead of the spin tensor, it is sometimes more convenient to use the spin four-vector

$$S_\mu = -\frac{1}{2}\epsilon_{\mu\nu\rho\sigma}\, u^\nu\, S^{\rho\sigma} \,, \tag{7}$$

where $\epsilon_{\mu\nu\rho\sigma}$ is the Levi-Civita tensor and $u^\nu := P^\nu/\mu$ is the specific four-momentum. The inverse relation of this equation reads

$$S^{\rho\sigma} = -\epsilon^{\rho\sigma\gamma\delta} S_\gamma u_\delta \,. \tag{8}$$

After substituting Eq. (8) into Eq. (5), we can derive the relation for the spin magnitude in terms of the spin four-vector

$$S^2 = S^\mu S_\mu \,. \tag{9}$$

The spin four-vector is from the definition (7) orthogonal to the four-momentum $P_\mu S^\mu = 0$, while from Eq. (8) one sees it is orthogonal also to the spin tensor $S^{\mu\nu} S_\mu = 0$. Finally, from Eq. (10) it can be shown that it is orthogonal to the four-velocity $v_\mu S^\mu = 0$ as well.

Since the MPD equations do not provide an evolution equation for the four-velocity, it is convenient that for the TD SSC exists an explicit relation of the four-velocity in terms of the four-momentum and the spin tensor [27]. This relation reads

$$v^\mu = \frac{\mathsf{m}}{\mu}\left(u^\mu + \frac{2\, S^{\mu\nu} R_{\nu\rho\kappa\lambda} u^\rho S^{\kappa\lambda}}{4\mu^2 + R_{\alpha\beta\gamma\delta} S^{\alpha\beta} S^{\gamma\delta}}\right) \,, \tag{10}$$

where $\mathsf{m} = -P_\mu v^\mu$ is the rest mass with respect to the four-velocity v^μ. This mass m is not conserved under the TD SSC, but it is used to conserve the normalization $v^\mu v_\mu = -1$ during the MPD evolution. This leads to [28]

$$\mathsf{m} = \frac{\mathcal{A}\mu^2}{\sqrt{\mathcal{A}^2\mu^2 - \mathcal{B}S^2}} \,, \tag{11}$$

where

$$\mathcal{A} = 4\mu^2 + R_{\alpha\beta\gamma\delta} S^{\alpha\beta} S^{\gamma\delta} \,, \tag{12}$$

$$\mathcal{B} = 4h^{\kappa\eta} R_{\kappa\iota\lambda\mu} P^\iota S^{\lambda\mu} R_{\eta\nu\omega\pi} P^\nu S^{\omega\pi} \,, \tag{13}$$

$$h^\kappa{}_\eta = \frac{1}{S^2} S^{\kappa\rho} S_{\eta\rho} \,. \tag{14}$$

A. The Kerr spacetime background

Since our work deals with the motion of a spinning in the Kerr spacetime, let us briefly introduce this spacetime. The Kerr geometry in BL coordinates (t, r, θ, ϕ) is described by the metric

$$\begin{aligned} \mathrm{d}s^2 = g_{tt}\, \mathrm{d}t^2 + 2\, g_{t\phi}\, \mathrm{d}t\, \mathrm{d}\phi + g_{\phi\phi}\, \mathrm{d}\phi^2 \\ + g_{rr}\, \mathrm{d}r^2 + g_{\theta\theta}\, \mathrm{d}\theta^2 \,, \end{aligned} \tag{15}$$

where the metric coefficients are

$$\begin{aligned} g_{tt} &= -\left(1 - \frac{2Mr}{\Sigma}\right) \,, \\ g_{t\phi} &= -\frac{2aMr\sin^2\theta}{\Sigma} \,, \\ g_{\phi\phi} &= \frac{(\varpi^4 - a^2\Delta\sin^2\theta)\sin^2\theta}{\Sigma} \,, \\ g_{rr} &= \frac{\Sigma}{\Delta} \,, \\ g_{\theta\theta} &= \Sigma \end{aligned} \tag{16}$$

with

$$\begin{aligned} \Sigma &= r^2 + a^2\cos^2\theta \,, \\ \Delta &= \varpi^2 - 2Mr \,, \\ \varpi^2 &= r^2 + a^2 \,. \end{aligned} \tag{17}$$

The Kerr spacetime is stationary and axisymmetric. This provides two Killing vector fields, the timelike one $\xi^\mu_{(t)}$ and the spacelike one $\xi^\mu_{(\phi)}$. Due to these Killing vector fields, Eq. (6) provides two constants of motion. In particular, thanks to the timelike field, the energy

$$E = -P_t + \frac{1}{2} g_{t\mu,\nu} S^{\mu\nu} \tag{18}$$

is conserved, and thanks to the spacelike field, the component of the total angular momentum parallel to the rotational axis of Kerr (z axis)

$$J_z = P_\phi - \frac{1}{2} g_{\phi\mu,\nu} S^{\mu\nu} \tag{19}$$

is conserved. These two conserved quantities can be used to parametrize the spinning particles orbits as discussed in Sec. II C.

B. Equatorial orbits

We are interested in equatorial orbits, where $\theta = \pi/2$. To constrain the body to the equatorial plane, the v^θ component of the four-velocity must be always zero. The orthogonality of the spin four-vector and the four-velocity $v_\mu S^\mu = 0$ implies that in order to achieve $v^\theta = 0$ for arbitrary equatorial orbit all the components of the spin four vector should be zero except from S^θ, i.e.,

$$S_\mu = S_\theta \delta^\theta_\mu \,. \tag{20}$$

The spin is, therefore, parallel to the z axis. From the orthogonality of the spin four-vector and the four-momentum $P_\mu S^\mu = 0$, it holds that $P^\theta = 0$.

From Eqs. (9) and (20) it can be shown that $S_\theta = -\sqrt{g_{\theta\theta}}S$ where the sign is chosen such that the spin magnitude is positive (negative) when the spin is parallel (antiparallel) to the z axis. Then, from Eq. (8) the only nonzero components of the spin tensor are

$$\begin{aligned} S^{tr} &= -S^{rt} = -S\ u_\phi \sqrt{-\frac{g_{\theta\theta}}{g}} = -\frac{S\ u_\phi}{r}\ , \\ S^{t\phi} &= -S^{\phi t} = S\ u_r \sqrt{-\frac{g_{\theta\theta}}{g}} = \frac{S\ u_r}{r}\ , \\ S^{r\phi} &= -S^{\phi r} = -S\ u_t \sqrt{-\frac{g_{\theta\theta}}{g}} = -\frac{S\ u_t}{r}\ , \end{aligned} \tag{21}$$

where g is determinant of the metric. For Kerr spacetime on equatorial plane, it holds $\sqrt{-g_{\theta\theta}/g} = 1/r$.

Let us recheck the setup for equatorial orbits in a Kerr background. The total derivative with respect to proper time of the θ component of four-momentum can be expressed from Eq. (1)

$$\frac{\mathrm{d}P^\theta}{\mathrm{d}\tau} = -\frac{1}{2}\, R^\theta{}_{\nu\rho\sigma}\ v^\nu\ S^{\rho\sigma} - \Gamma^\theta{}_{\nu\rho} P^\nu v^\rho. \tag{22}$$

The right-hand side (rhs) of this equation is equal to zero on the equatorial plane. Furthermore, Eq. (10) reduces on the equatorial plane to $v^\theta = (\mathsf{m}/\mu^2)P^\theta$. This implies that when $v^\theta = 0$ then P_θ remains zero as well. Thus, the particle stays on the equatorial plane by just demanding that $v^\theta = 0$.

From Eqs. (18), (19) and (21), P_t and P_ϕ can be expressed as functions of E and J_z. These expressions in dimensionless quantities read

$$\begin{aligned} u_t &= \frac{-\hat{E} - \dfrac{\sigma}{\hat{r}^3}(\hat{a}\hat{E} - \hat{J}_z)}{1 - \dfrac{\sigma^2}{\hat{r}^3}}\ , \\ u_\phi &= M\frac{\hat{J}_z - \dfrac{\sigma}{\hat{r}^3}\left[\left(-\hat{a}^2 + \hat{r}^3\right)\hat{E} + \hat{a}\hat{J}_z\right]}{1 - \dfrac{\sigma^2}{\hat{r}^3}}\ . \end{aligned} \tag{23}$$

When we restrict the motion to the equatorial plane, it is possible to reproduce the equations of motion for the spinning particle from Eqs. (10) and (4). In particular, we can express u^r from the normalization (4) as function of E and J_z and thanks to the fact that it holds

$$2S^{r\nu}R_{\nu\rho\kappa\lambda}u^\rho S^{\kappa\lambda} = \frac{12\mu^2\hat{\Delta}\sigma^2 x^2}{\hat{r}^3\Sigma_\sigma^2}u^r \tag{24}$$

we can write the equations of motion as

$$\Sigma_\sigma\Lambda_\sigma\frac{\mathrm{d}\hat{t}}{\mathrm{d}\hat{\tau}} = \frac{\mathsf{m}}{\mu}V^t(\hat{r})\ , \tag{25a}$$

$$\Sigma_\sigma\Lambda_\sigma\frac{\mathrm{d}\hat{r}}{\mathrm{d}\hat{\tau}} = \frac{\mathsf{m}}{\mu}V^r(\hat{r}) = \pm\frac{\mathsf{m}}{\mu}\sqrt{R_\sigma(\hat{r})}\ , \tag{25b}$$

$$\Sigma_\sigma\Lambda_\sigma\frac{\mathrm{d}\phi}{\mathrm{d}\hat{\tau}} = \frac{\mathsf{m}}{\mu}V^\phi(\hat{r})\,, \tag{25c}$$

where

$$\Sigma_\sigma = \hat{r}^2\left(1 - \frac{\sigma^2}{\hat{r}^3}\right)\ , \tag{25d}$$

$$\Lambda_\sigma = 1 - \frac{3\sigma^2\hat{r}x^2}{\Sigma_\sigma^3}\ , \tag{25e}$$

$$V^t = \hat{a}\left(1 + \frac{3\sigma^2}{\hat{r}\Sigma_\sigma}\right)x + \frac{\varpi^2}{\Delta}P_\sigma\ , \tag{25f}$$

$$R_\sigma = P_\sigma^2 - \hat{\Delta}\left(\frac{\Sigma_\sigma^2}{\hat{r}^2} + x^2\right)\ , \tag{25g}$$

$$V^\phi = \left(1 + \frac{3\sigma^2}{\hat{r}\Sigma_\sigma}\right)x + \frac{\hat{a}}{\hat{\Delta}}P_\sigma\ , \tag{25h}$$

$$P_\sigma = \Sigma_\sigma\hat{E} - \left(\hat{a} + \frac{\sigma}{\hat{r}}\right)x\ , \tag{25i}$$

$$x = \hat{J}_z - (\hat{a} + \sigma)\hat{E}\ . \tag{25j}$$

The rest mass with respect to v^μ can be expressed from (11) as

$$\frac{\mathsf{m}}{\mu} = \Lambda_\sigma\sqrt{\frac{1 - \frac{\sigma^2}{\hat{r}^3}}{-1 + 2\Lambda_\sigma - (2 - \Lambda_\sigma)\frac{\sigma^2}{\hat{r}^3}}}\ . \tag{26}$$

This expression is identical to Eq. (49) in [29]. Equations (25) are identical to the equations (2.19)–(2.21) in [23] up to the parametrization with $\mathrm{d}\tilde{\tau}/\mathrm{d}\tau = \mathsf{m}/\mu$ where $\tilde{\tau}$ is the parametrization used in [23]. By dividing Eqs. (25b) and (25c) we obtain Eq. (19) in [30]. Hence, we have checked the validity of the above equations.

To simplify the equations of motion, it is useful to reparametrize Eqs. (25) with a time parameter λ which is similar to the Mino time [24]. Equations (25) and (26) imply that the relation between $\hat{\tau}$ and λ is

$$\frac{\mathrm{d}\hat{\tau}}{\mathrm{d}\lambda} = \hat{r}^2\sqrt{\left(1 - \frac{\sigma^2}{\hat{r}^3}\right)\left(-1 + 2\Lambda_\sigma - (2 - \Lambda_\sigma)\frac{\sigma^2}{\hat{r}^3}\right)}\ . \tag{27}$$

Then it holds $\mathrm{d}\hat{x}^\mu/\mathrm{d}\lambda = V^\mu$ where $\hat{x}^\mu = (\hat{t}, \hat{r}, \theta, \phi)$ with $V^\theta = 0$. V^μ can be interpreted as dimensionless four-velocity with respect to λ.

C. Constants of motion as orbital parameters

Let us see how we can use the constants of motion E, J_z to parametrize bounded equatorial orbits. To do that we have to find first the roots of Eq. (25b), which will lead us to the turning points of an equatorial eccentric orbit. The function $\hat{r}^4 R_\sigma(\hat{r})$ is an eighth order polynomial, hence it has generally 8 roots. At least four of these roots are real as in the nonspinning case, while four additional roots, which come from the secondary spin's terms, can be complex or real. From these roots the two outermost ones $0 < \hat{r}_1 \leq \hat{r}_2$ are the candidates for being the turning points we are seeking. Obviously for these two roots it has to hold that

$$R_\sigma(\hat{r}_1) = 0\ , \qquad R_\sigma(\hat{r}_2) = 0\ . \tag{28}$$

To have a bound equatorial orbit between these two roots, Eq. (25b) implies that $R_\sigma(\hat{r}) > 0$ for $\hat{r}_1 < \hat{r} < \hat{r}_2$. The latter can be true only if for the derivative of $R_\sigma(\hat{r})$ with respect to $\hat{r}$ it holds that

$$R'_\sigma(\hat{r}_1) \geq 0 \,, \qquad R'_\sigma(\hat{r}_2) < 0 \,. \tag{29}$$

When the conditions (28), (29) are satisfied, then $\hat{r}_1$ is the pericenter and $\hat{r}_2$ is the apocenter of an equatorial eccentric orbit, and it also holds that $\hat{E}^2 < 1$.

Having found the turning points of an equatorial eccentric orbit, we can parametrize each eccentric equatorial orbit by its semi-latus rectum p and its eccentricity e, which relate to the turning points as follows

$$\hat{r}_1 = \frac{p}{1+e} \,, \qquad \hat{r}_2 = \frac{p}{1-e} \,. \tag{30}$$

The inverse relations read

$$p = \frac{2\hat{r}_1\hat{r}_2}{\hat{r}_1+\hat{r}_2} \,, \qquad e = \frac{\hat{r}_2-\hat{r}_1}{\hat{r}_1+\hat{r}_2} \,. \tag{31}$$

Equation (28) can be written as two quadratic equations in terms of $\hat{E}$ and $\hat{J}_z$. Using the same method as in Appendix B of [31] we can rearrange the formulas (28) for energy and angular momentum to arrive at

$$f_i\hat{E}^2 - 2g_i\hat{E}\hat{J}_z - h_i\hat{J}_z^2 - d_i = 0 \qquad i = 1,2 \tag{32}$$

where $f_1 = f(\hat{r}_1)$, $f_2 = f(\hat{r}_2)$ etc. and

$$\begin{aligned} f(\hat{r}) =& \hat{a}^2(\hat{r}+2)\hat{r} + \hat{r}^4 + \\ &+ \sigma\left(\frac{\hat{a}^2\sigma}{\hat{r}^2} + \frac{2\hat{a}^2(\hat{a}+\sigma)}{\hat{r}} + 6\hat{a}\hat{r} - (\hat{r}-2)\hat{r}\sigma\right) \\ g(\hat{r}) =& 2\hat{a}\hat{r} + \sigma\left(\frac{\hat{a}\sigma}{\hat{r}^2} + \frac{\hat{a}(2\hat{a}+\sigma)}{\hat{r}} - (\hat{r}-3)\hat{r}\right) \\ h(\hat{r}) =& \hat{\Delta} - \left(\hat{a}+\frac{\sigma}{\hat{r}}\right)^2 \\ d(\hat{r}) =& \frac{\hat{\Delta}(\hat{r}^3-\sigma^2)^2}{\hat{r}^4} \end{aligned} \tag{33}$$

These functions for $\sigma = 0$ are identical to the functions (B.6) – (B.9) in [31] with $z_- = 0$. By manipulating Eq. (32) properly, we arrive at

$$\hat{E}^2 = \frac{\kappa\rho + 2\epsilon\tilde{\sigma} \pm 2\sqrt{\tilde{\sigma}(\tilde{\sigma}\epsilon^2 + \rho\epsilon\kappa - \eta\kappa^2)}}{\rho^2 + 4\eta\tilde{\sigma}} \,, \tag{34}$$

$$\hat{J}_z = \frac{\rho\hat{E}^2 - \kappa}{2\sigma\hat{E}} \,, \tag{35}$$

where

$$\begin{aligned} \kappa &= d_1h_2 - d_2h_1 \,, \\ \epsilon &= d_1g_2 - d_2g_1 \,, \\ \rho &= f_1h_2 - f_2h_1 \,, \\ \eta &= f_1g_2 - f_2g_1 \,, \\ \tilde{\sigma} &= g_1h_2 - g_2h_1 \end{aligned} \tag{36}$$

are the determinants appearing in [31]. Thanks to the identity $\epsilon\rho - \kappa\eta = \tilde{\sigma}\zeta$, where

$$\zeta = d_1f_2 - d_2f_1 \,, \tag{37}$$

we can rearrange Eq. (34) as

$$\hat{E}^2 = \frac{\kappa\rho + 2\epsilon\tilde{\sigma} - 2\,\mathrm{sgn}\,(\hat{J}_z)\,\tilde{\sigma}\sqrt{\epsilon^2+\kappa\zeta}}{\rho^2 + 4\eta\tilde{\sigma}} \,. \tag{38}$$

Since for $\hat{a} = \sigma = 0$ the determinant $\tilde{\sigma} = 0$ and the Eq. (35) is singular, it is better to substitute $\hat{E}^2$ into Eq. (35) and rearrange it as follows

$$\hat{J}_z = \frac{\epsilon\rho - 2\kappa\eta - \mathrm{sgn}\,(\hat{J}_z)\,\rho\sqrt{\epsilon^2+\kappa\zeta}}{(\rho^2 + 4\eta\tilde{\sigma})\hat{E}} \,. \tag{39}$$

The signs of $\hat{J}_z$ appearing in Eqs. (38) and (39) have been numerically verified for spin values $|\sigma| \leq 1$.

The constants of motion $\hat{E}$ and J_z for given p and e have two solutions corresponding to the corotating orbit and the counterrotating orbit. We can choose the coordinates such that the z axis is parallel to the total angular momentum, i.e. $\hat{J}_z > 0$. This convention implies that $\hat{a} > 0$ corresponds to corotating orbits and $\hat{a} < 0$ to counterrotating orbits. The spins of the secondary particle and of the central black hole are parallel when $\hat{a}\,\sigma > 0$ and antiparallel when $\hat{a}\,\sigma < 0$.

For $e = 0$, both the numerator and the denominator of Eq. (38) become zero. This inconvenience can be avoided by noticing that a coefficient e can be factored out from the determinants (36) and canceled out in Eq. (38). In this fashion, the solution (38) is valid even for $e = 0$. Actually, this allows us to verify that for $e = 0$ Eqs. (38) and (39) are identical to Eqs. (59) and (60) given in [29].

There is a limit between the bounded and unbounded equatorial orbits defined by a separatrix. The term unbounded orbits includes orbits escaping to infinity and orbits plunging to the central black hole. In the case the separatrix splits plunging and bounded orbits, it holds that $R'_\sigma(\hat{r}_1) = 0$ and $R'_\sigma(\hat{r}_2) < 0$. The orbit with $R'_\sigma(\hat{r}_1) = 0$ is an unstable circular orbit, while a trajectory originating from $\hat{r}_2$ with energy and angular momentum satisfying Eqs. (38) and (39) will asymptotically approach the circular orbit at $\hat{r}_1$ either evolved forward or backward in time.[1] For a given Kerr parameter $\hat{a}$ and spin σ the effective potential R_σ depends on $\hat{E}(p,e)$ and $\hat{J}_z(p,e)$, therefore the separatrices can be plotted on the $p-e$ plane splitting it into two parts. In one part of the plane lie the bounded orbits, while in the other part lie unbounded orbits or initial conditions, which do not correspond to an orbit (Fig. 1). We can see that for given e

[1] In the limiting case that $\hat{r}_1 = \hat{r}_2$ the orbit is circular ($e = 0$) and marginally stable, since it holds that $R_\sigma(\hat{r}_1) = R'_\sigma(\hat{r}_1) = R''_\sigma(\hat{r}_1) = 0$. This orbit is often called the innermost stable circular orbit (ISCO).

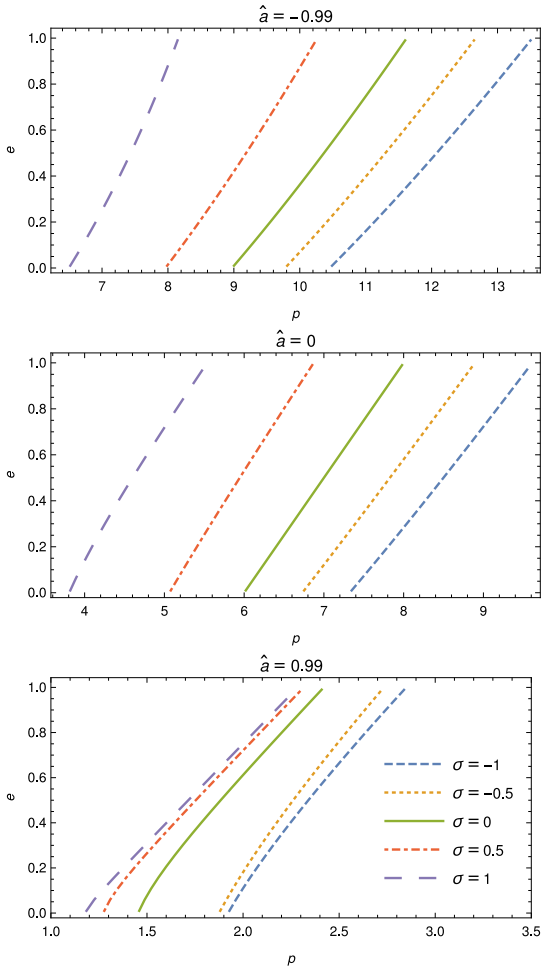

FIG. 1. Separatrices for different Kerr parameters and spins. Points $(p,\ e)$ on the depicted lines correspond to orbits asymptotically approaching the unstable circular orbit lying at $\hat{r} = p/(1+e)$. For given e the semi-latus rectum p of the separatrix decreases with increasing spin. Therefore, for a spinning particle it is possible to approach the horizon closer than a nonspinning particle. Note that even though the EMRI relevant values of the secondary spin are $\sigma \leq q \ll 1$, we use much higher spin values to make the differences between the separatrices more prominent and visible. All plots are for $\hat{J}_z > 0$.

the semi-latus rectum p of the separatrix decreases with increasing spin.

Figure 2 shows two cases of a separatrix on the $\hat{J}_z - \hat{E}$ plane along with a grid of constant p and e lines. Note that the intersection point between the separatrix and the line $e = 0$ lying at the left lower corner of both panels of Fig. 2 represents ISCO.

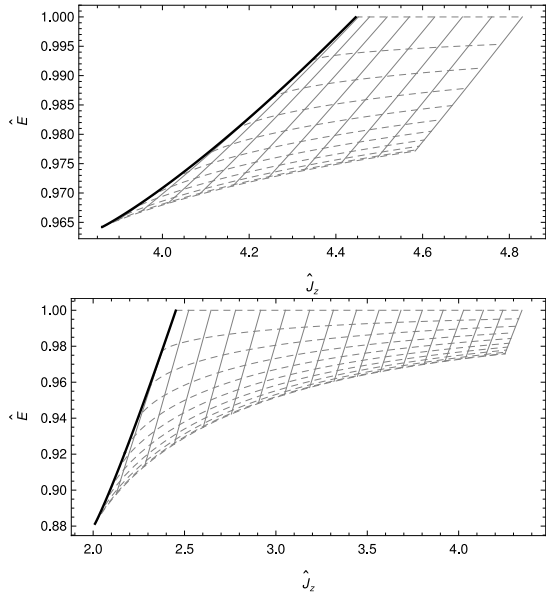

FIG. 2. Separatrices (black thick solid) in the $\hat{J}_z - \hat{E}$ plane along with lines of constant semi-latus rectum (grey solid) and eccentricity (grey dashed) for Kerr parameter $\hat{a} = -0.5$ (top panel) and $\hat{a} = 0.5$ (bottom panel). In both case the secondary spin is $\sigma = 0.5$. The eccentricity lines start at $e = 0$ for lower energies and reach $e = 1$ when $\hat{E} = 1$ with step 0.1. The semi-latus rectum ranges from $p = 10$ to $p = 20$ for $\hat{a} = -0.5$ and from $p = 3$ to $p = 20$ for $\hat{a} = 0.5$ with step 1 in both plots. At a separatrix the semi-latus rectum is the lowest and is increasing with increasing $\hat{J}_z$.

D. Frequencies of eccentric equatorial orbits

The radial motion of a particle in the equatorial plane parametrized by the time parameter λ has a period Λ_r. This period can be defined as the time needed to go from the apocenter to the pericenter and back. Hence, Λ_r can be found by integrating the inversion of Eq. (25b), i.e.,

$$\frac{\mathrm{d}\lambda}{\mathrm{d}\hat{r}} = \frac{1}{\sqrt{R_\sigma(\hat{r})}}\,, \tag{40}$$

over the above two branches (first from $\hat{r}_1$ to $\hat{r}_2$ and then from $\hat{r}_2$ to $\hat{r}_1$) with respect to the radius $\hat{r}$. However, the integration over one branch is equal to the integration over the other. Hence, we can find the Λ_r by integrating Eq. (25b) over the first branch to obtain the time elapsed during the first branch and multiply the result by two [32], i.e.,

$$\Lambda_r = 2\int_{\hat{r}_1}^{\hat{r}_2} \frac{\mathrm{d}\hat{r}}{\sqrt{R_\sigma(\hat{r})}}\,. \tag{41}$$

The radial frequency can be defined as $\Upsilon_r = 2\pi/\Lambda_r$. If we set the initial radius to $r(\lambda = 0) = r_1$, then the radius

$r(\lambda)$ is an even function and can be written as

$$r(\lambda) = r^{(0)} + \sum_{n=1}^{\infty} r^{(n)} \cos(n\Upsilon_r \lambda) \ . \tag{42}$$

After substituting Eq. (42) to Eqs. (25a) and (25c) and integrating them, we obtain

$$\begin{aligned} \hat{t}(\lambda) &= \Gamma\lambda + \Delta\hat{t}(\lambda) \ , \\ \phi(\lambda) &= \Upsilon_\phi \lambda + \Delta\phi(\lambda) \ , \end{aligned} \tag{43}$$

where Γ and Υ are frequencies with respect to λ and functions $\Delta\hat{t}(\lambda)$ and $\Delta\phi(\lambda)$ are periodic with period Λ_r. Note that since the function $\hat{r}(\lambda)$ is even, the functions $V^t(\hat{r}(\lambda))$ and $V^\phi(\hat{r}(\lambda))$ are even in λ as well. Hence, after the aforementioned integration and the subtraction of the linear term $\Gamma\lambda$ or $\Upsilon_\phi\lambda$, respectively in Eq. (43), the functions $\Delta\hat{t}(\lambda)$ and $\Delta\phi(\lambda)$ are odd and can be written as series of sines.

The average rate of change of the azimuthal coordinate and time with respect to λ is

$$\Upsilon_\phi = \frac{2}{\Lambda_r} \int_{\hat{r}_1}^{\hat{r}_2} \frac{V^\phi(\hat{r})}{\sqrt{R_\sigma(\hat{r})}} \mathrm{d}\hat{r} \ , \tag{44}$$

$$\Gamma = \frac{2}{\Lambda_r} \int_{\hat{r}_1}^{\hat{r}_2} \frac{V^t(\hat{r})}{\sqrt{R_\sigma(\hat{r})}} \mathrm{d}\hat{r} \ . \tag{45}$$

These integrals can be solved in terms of Lauricella's hypergeometric functions [33]. However, for achieving this, the exact values of the roots of the radial potential $\hat{r}^4 R_\sigma(\hat{r})$, which is eighth order polynomial in $\hat{r}$, must be found. This task can be only performed numerically. Thus, instead the integrals (41), (44) and (45) were calculated directly numerically. These integrals have singular points at $\hat{r}_1$ and $\hat{r}_2$, but this difficulty can be overcome. Namely, first we factor out the roots

$$R_\sigma(\hat{r}) = (\hat{r} - \hat{r}_1)(\hat{r}_2 - \hat{r}) Q(\hat{r}) \ , \tag{46}$$

where $\hat{r}^4 Q(\hat{r})$ is sixth order polynomial. To remove the singularities, an angle like coordinate $\chi \in [0, \pi)$ is used by applying the transformation

$$\hat{r} = \frac{p}{1 + e\cos\chi} \ . \tag{47}$$

Then, the integrals take the form

$$\Lambda_r = \frac{2\sqrt{1-e^2}}{p} \int_0^\pi \frac{1}{\sqrt{J(\chi)}} \mathrm{d}\chi \ , \tag{48}$$

$$\Upsilon_\phi = \frac{2\sqrt{1-e^2}}{\Lambda_r p} \int_0^\pi V^\phi\left(\frac{p}{1+e\cos\chi}\right) \frac{1}{\sqrt{J(\chi)}} \mathrm{d}\chi \ , \tag{49}$$

$$\Gamma = \frac{2\sqrt{1-e^2}}{\Lambda_r p} \int_0^\pi V^t\left(\frac{p}{1+e\cos\chi}\right) \frac{1}{\sqrt{J(\chi)}} \mathrm{d}\chi \ , \tag{50}$$

where

$$J(\chi) = \sum_{k=0}^{6} (1 + e\cos\chi)^k \sum_{l=0}^{k} \frac{j_l^{(p)} j_{k-l}^{(e)}}{(1-e^2)^{k-l} p^l} \tag{51}$$

is a polynomial in $\cos\chi$ with coefficients

$$\begin{aligned} j_0^{(p)} &= 1 - \hat{E}^2 \ , \\ j_1^{(p)} &= -2 \ , \\ j_2^{(p)} &= \hat{a}^2 + 2\hat{a}\hat{E}x + x^2 \ , \\ j_3^{(p)} &= -2((1-\hat{E}^2)\sigma^2 - \hat{E}\sigma x + x^2) \ , \\ j_4^{(p)} &= 4\sigma^2 \ , \\ j_5^{(p)} &= -2\hat{a}\sigma(\hat{a}\sigma + x(\hat{E}\sigma + x)) \ , \\ j_6^{(p)} &= \sigma^2((1-\hat{E})\sigma - x)((1+\hat{E})\sigma + x) \end{aligned}$$

and

$$\begin{aligned} j_0^{(e)} &= 1 \ , \\ j_1^{(e)} &= 2 \ , \\ j_2^{(e)} &= e^2 + 3 \ , \\ j_3^{(e)} &= 4(e^2+1) \ , \\ j_4^{(e)} &= e^4 + 10e^2 + 5 \ , \\ j_5^{(e)} &= 2(e^2+3)(3e^2+1) \ , \\ j_6^{(e)} &= e^6 + 21e^4 + 35e^2 + 7 \ . \end{aligned}$$

The polynomial $J(\chi)$ for $\sigma = 0$ is identical to the polynomial (40) in [31] with Carter constant $Q = 0$ up to the factor $1 - e^2$ due to a different definition of $J(\chi)$ used in [31].

We can define the frequencies with respect to the coordinate time as

$$\hat{\Omega}_r = \frac{\Upsilon_r}{\Gamma} = \frac{\pi p}{\sqrt{1-e^2}\int_0^\pi V^t(\hat{r}(\chi))/\sqrt{J(\chi)}\mathrm{d}\chi} \ , \tag{52}$$

$$\hat{\Omega}_\phi = \frac{\Upsilon_\phi}{\Gamma} = \frac{\int_0^\pi V^\phi(\hat{r}(\chi))/\sqrt{J(\chi)}\mathrm{d}\chi}{\int_0^\pi V^t(\hat{r}(\chi))/\sqrt{J(\chi)}\mathrm{d}\chi} \ . \tag{53}$$

We have numerically verified the above frequency formulas by comparing them with frequencies obtained by a direct integration of the MPD equations for the respective eccentric orbits. To integrate the MPD equations an implicit Gauss-Runge-Kutta integrator was used as described in [34].

The equatorial plane equations of motion (25) given in t, r and ϕ can be rewritten in λ, t and ϕ parametrized by χ, i.e.

$$\frac{\mathrm{d}\lambda}{\mathrm{d}\chi} = \sqrt{\frac{1-e^2}{p^2 J(\chi)}} \tag{54}$$

$$\frac{\mathrm{d}\hat{t}}{\mathrm{d}\chi} = V^t\left(\frac{p}{1+e\cos\chi}\right)\sqrt{\frac{1-e^2}{p^2 J(\chi)}} \tag{55}$$

$$\frac{\mathrm{d}\phi}{\mathrm{d}\chi} = V^\phi\left(\frac{p}{1+e\cos\chi}\right)\sqrt{\frac{1-e^2}{p^2 J(\chi)}} \tag{56}$$

These equations will be used later on, when the energy and angular momentum fluxes are calculated.

III. GRAVITATIONAL WAVE FLUXES

A. Teukolsky formalism

To calculate the GW fluxes we employ the Teukolsky formalism. The GWs are described perturbatively using the Weyl curvature scalar

$$\Psi_4 = -C_{\alpha\beta\gamma\delta} n^\alpha \overline{m}^\beta n^\gamma \overline{m}^\delta \,, \tag{57}$$

where n^μ and $\overline{m}^\mu$ are components of the Kinnersley tetrad

$$n^\mu = \frac{1}{2\Sigma}\left(\varpi^2, -\Delta, 0, a\right) \,, \tag{58}$$

$$\overline{m}^\mu = \frac{\rho}{\sqrt{2}}\left(ia\sin\theta, 0, -1, i\csc\theta\right) \,, \tag{59}$$

where $\rho = -(r - ia\cos\theta)^{-1}$. The Weyl scalar Ψ_4 is zero for the Kerr spacetime and its perturbation is governed by the TE

$${}_s\mathcal{O}\,{}_s\psi(t, r, \theta, \phi) = 4\pi\Sigma T \tag{60}$$

with spin weight $s = -2$ for ${}_{-2}\psi = \rho^{-4}\Psi_4$ in the case of the GWs [35].

1. Frequency domain approach

This partial differential equation can be separated into ordinary differential equations after a Fourier transform in t and ϕ

$${}_{-2}\psi = \sum_{l,m}^{\infty} \frac{1}{2\pi} \int_{-\infty}^{\infty} \mathrm{d}\omega e^{-i\omega t} \psi_{lm\omega}(r) {}_{-2}S^{a\omega}_{lm}(\theta, \phi) \,, \tag{61}$$

where ${}_{-2}S^{a\omega}_{lm}(\theta, \phi)$ is spin weighted spheroidal harmonic function with spin weight -2 normalized as

$$\int \mathrm{d}\Omega \, |{}_{-2}S^{a\omega}_{lm}(\theta, \phi)| = 1 \,. \tag{62}$$

For simplicity we use the notation $S^{a\omega}_{lm}(\theta) = {}_{-2}S^{a\omega}_{lm}(\theta, 0)$ for the angular part henceforth. To calculate the angular function the *Black Hole Perturbation Toolkit* [36] has been employed.

After the separation, an ordinary differential equation

$$\mathcal{D}\psi_{lm\omega}(r) = \mathcal{T}_{lm\omega} \tag{63}$$

is obtained for the radial part $\psi_{lm\omega}(r)$, where $\mathcal{D}$ is a differential operator that can be found, e.g., in [35] and $\mathcal{T}_{lm\omega}$ is a source term discussed below. The asymptotic behavior of the homogeneous solutions $R_{lm\omega}(r)$ of Eq. (63) is discussed in [4, 25]. To satisfy physical boundary conditions, the solution must be purely outgoing at infinity and purely ingoing at the horizon; in other words, we are dealing with a retarded solution. We will denote a homogeneous solution satisfying the first condition as $R^+_{lm\omega}$ and a solution satisfying the second condition as $R^-_{lm\omega}$.[2] An inhomogeneous solution satisfying boundary conditions can be found using the Green function formalism as

$$\psi_{lm\omega}(r) = C^+_{lm\omega}(r) R^+_{lm\omega}(r) + C^-_{lm\omega}(r) R^-_{lm\omega}(r) \,, \tag{64}$$

where the amplitudes are

$$C^\pm_{lm\omega}(r) = \frac{1}{W} \int_{r_+}^{\infty} \Theta^\pm(r, r') \frac{R^\mp_{lm\omega}(r') \mathcal{T}_{lm\omega}(r')}{\Delta^2(r')} \mathrm{d}r' \tag{65}$$

with the invariant Wronskian

$$W = \frac{R^+_{lm\omega}(r)\partial_r R^-_{lm\omega}(r) - (\partial_r R^+_{lm\omega}(r)) R^-_{lm\omega}(r)}{\Delta(r)} \tag{66}$$

and the Heaviside step functions defined as

$$\Theta^+(r, r') = \Theta(r' - r) \,, \qquad \Theta^-(r, r') = \Theta(r - r') \,. \tag{67}$$

Since we are interested in GW fluxes at the horizon and at infinity, we will denote the relevant amplitudes as $C^-_{lm\omega} \equiv C^-_{lm\omega}(r \to r_+)$ and $C^+_{lm\omega} \equiv C^+_{lm\omega}(r \to \infty)$ respectively. In fact, the amplitudes are constant for $r < r_1$ and $r > r_2$.

The source term in (63) can be written as

$$\mathcal{T}_{lm\omega} = \int \mathrm{d}t \, \mathrm{d}\theta \, \mathrm{d}\phi \, \Delta^2 (\mathcal{T}_{nn} + \mathcal{T}_{n\overline{m}} + \mathcal{T}_{\overline{m}\overline{m}}) e^{i\omega t - im\phi} \,, \tag{68}$$

where

$$\begin{aligned}
\mathcal{T}_{nn} &= f^{(0)}_{nn}(r, \theta)\sqrt{-g} T_{nn} \,, \\
\mathcal{T}_{n\overline{m}} &= \partial_r (f^{(1)}_{n\overline{m}}(r, \theta)\sqrt{-g} T_{n\overline{m}}) \\
&\quad + f^{(0)}_{n\overline{m}}(r, \theta)\sqrt{-g} T_{n\overline{m}} \,, \\
\mathcal{T}_{\overline{m}\overline{m}} &= \partial_{rr} (f^{(2)}_{\overline{m}\overline{m}}(r, \theta)\sqrt{-g} T_{\overline{m}\overline{m}}) + \\
&\quad \partial_r (f^{(1)}_{\overline{m}\overline{m}}(r, \theta)\sqrt{-g} T_{\overline{m}\overline{m}}) + f^{(0)}_{\overline{m}\overline{m}}(r, \theta)\sqrt{-g} T_{\overline{m}\overline{m}} \,.
\end{aligned} \tag{69}$$

The functions $f^{(i)}_{ab}(r, \theta)$ can be found in [29]. Projections of the stress energy tensor onto a tetrad $e^{(a)}_\mu$ read

$$\begin{aligned}
T_{ab} &= \frac{1}{\sqrt{-g}} \left(C^0_{ab} - C^\sigma_{ab}\right) \delta^3 \\
&\quad - \frac{1}{\sqrt{-g}} \partial_\rho \left((v^t)^{-1} S^{\rho(\mu} v^{\nu)} \delta^3 \right) e^{(a)}_\mu e^{(b)}_\nu \,,
\end{aligned} \tag{70}$$

where

$$\begin{aligned}
C^0_{ab} &= (v^t)^{-1} P^{(\mu} v^{\nu)} e^{(a)}_\mu e^{(b)}_\nu \,, \\
C^\sigma_{ab} &= (v^t)^{-1} S^{\rho(\mu} \Gamma^{\nu)}{}_{\rho\lambda} v^\lambda e^{(a)}_\mu e^{(b)}_\nu \,.
\end{aligned} \tag{71}$$

The four-vectors P^μ and v^μ as well as the spin tensor $S^{\mu\nu}$ are functions of time, the Christoffel symbols are

[2] These functions are often denoted $R^\infty_{lm\omega}$ and $R^{\rm H}_{lm\omega}$ or $R^{\rm Up}_{lm\omega}$ and $R^{\rm In}_{lm\omega}$.

evaluated at the coordinates of the particle $r_p(t), \theta_p(t)$, the delta functions are functions of both the space coordinates r, θ, ϕ and the coordinate time t and the square root of the determinant $\sqrt{-g}$, the functions $f^{(i)}_{ab}$ and the tetrad legs $e^{(a)}_\mu$ are functions of r and θ. In our case, $e^{(a)}_\mu$, $e^{(b)}_\mu$ are the Kinnersley tetrad components n_μ and $\overline{m}_\mu$.

After integrating Eq. (68) over θ and ϕ and Eq. (65) over r using rules for integrating delta function, we obtain a relation for the amplitudes

$$C^{\pm}_{lm\omega} = \int_{-\infty}^{\infty} \mathrm{d}t e^{i\omega t - im\phi_p(t)} I^{\pm}_{lm\omega}(r_p(t), \theta_p(t)) \tag{72}$$

where

$$I^{\pm}_{lm\omega}(r,\theta) = \frac{1}{W}\left(A_0 - (A_1 + B_1)\frac{\mathrm{d}}{\mathrm{d}r} + (A_2 + B_2)\frac{\mathrm{d}^2}{\mathrm{d}r^2} - B_3\frac{\mathrm{d}^3}{\mathrm{d}r^3}\right) R^{\mp}_{lm\omega}(r)\,. \tag{73}$$

The coefficients A_i in their general form can be found in Appendix B.

Up to this point the derivation of GW fluxes holds for a generic orbit of a spinning particle. In the following part, we confine it to equatorial orbits with the spin parallel to the z axis as described in Sec. II B.

Thanks to the fact that the quantity $I^{\pm}_{lm\omega}(r_p(t), \pi/2)e^{im(\Omega_\phi t - \phi_p(t))}$ is periodic in time with frequency Ω_r (see eg. [37] for details), we can write the amplitude as a sum over discrete frequencies

$$C^{\pm}_{lm\omega} = \sum_{n=-\infty}^{\infty} C^{\pm}_{lmn}\delta(\omega - \omega_{mn})\,, \tag{74}$$

$$\omega_{mn} = m\Omega_\phi + n\Omega_r\,. \tag{75}$$

The partial amplitudes can be calculated as Fourier coefficients by integrating over one period $T_r = 2\pi/\Omega_r$

$$C^{\pm}_{lmn} = \Omega_r \int_0^{T_r} \mathrm{d}t I^{\pm}_{lm\omega_{mn}}(r_p(t), \pi/2) \times \exp(i\omega_{mn}t - im\phi_p(t))\,. \tag{76}$$

However, it is more convenient to integrate over the time parameter λ

$$C^{\pm}_{lmn} = \Omega_r \int_0^{\Lambda_r} \mathrm{d}\lambda \frac{\mathrm{d}t}{\mathrm{d}\lambda} I^{\pm}_{lm\omega_{mn}}(r_p(t(\lambda)), \pi/2) \times \exp(i\omega_{mn}t(\lambda) - im\phi_p(\lambda))\,. \tag{77}$$

The integration over the two branches of the motion (from r_1 to r_2 which correspond to λ from 0 to $\Lambda_r/2$ and from r_2 to r_1 which correspond to λ from $\Lambda_r/2$ to Λ_r) differs only by the sign of the radial velocity. Therefore, we can break the integral to two integrals, the first from 0 to $\Lambda_r/2$ and the second from Λ_r to $\Lambda_r/2$ (note the reverse direction of integration). Using the identities (43) we can write

$$\omega_{mn}t(\lambda) - m\phi(\lambda) = n\Upsilon_r\lambda + \omega_{mn}\Delta t - m\Delta\phi\,. \tag{78}$$

From the fact that Δt and $\Delta\phi$ are series of sines with period Λ_r, it holds $\Delta t(\Lambda_r - \lambda) = -\Delta t(\lambda)$ and $\Delta\phi(\Lambda_r - \lambda) = -\Delta\phi(\lambda)$. After changing the integration variable to χ, we can write the integral as a sum over the sign $D_r = \pm$ of the radial velocity, on which the coefficients A_i depend, i.e.

$$C^{\pm}_{lmn} = \Omega_r \int_0^{\pi} \mathrm{d}\chi \frac{\mathrm{d}\lambda}{\mathrm{d}\chi} \sum_{D_r=\pm} \frac{\mathrm{d}t}{\mathrm{d}\lambda} I^{\pm}_{lm\omega_{mn}}(r(\chi), \pi/2, D_r) \times \exp(iD_r(\omega_{mn}t(\chi) - m\phi(\chi)))\,, \tag{79}$$

where $\mathrm{d}\lambda/\mathrm{d}\chi$ comes from Eq. (54), $I^{\pm}_{lm\omega_{mn}}$ comes from Eq. (73) and $t(\chi)$, $\phi(\chi)$ are calculated from Eqs. (55), (56).

The metric perturbation $h_{\mu\nu} = \mathcal{O}(q)$ which can be defined as $g^{\mathrm{exact}}_{\mu\nu} = g_{\mu\nu} + h_{\mu\nu} + \mathcal{O}(q^2)$, can be calculated from the Weyl scalar Ψ_4 [38]. GWs consist of two polarizations and the metric perturbation can be written as $h_{\mu\nu} = h_+ e^+_{\mu\nu} + h_\times e^\times_{\mu\nu}$ where $e^+_{\mu\nu}$ and $e^\times_{\mu\nu}$ are the polarization tensors. At infinity, the relation between the strain $h = h_+ - ih_\times$ and the Weyl scalar is

$$\Psi_4(r\to\infty) = \ddot{h}/2\,, \tag{80}$$

where the dots denote derivative with respect to the BL coordinate time t. From Eqs. (61), (64), (74) and the asymptotic behavior of $R^+_{lm\omega}$ it holds

$$h = -\frac{2}{r}\sum_{lmn}\frac{C^+_{lmn}}{\omega^2_{mn}} S^{a\omega_{mn}}_{lm}(\theta) e^{-i\omega_{mn}(t-r^*)+im\phi}\,, \tag{81}$$

where r^* is tortoise coordinate defined as $\mathrm{d}r^*/\mathrm{d}r = \varpi^2/\Delta$. The stress-energy tensor of the GW can be reconstructed from the strain which yields the energy and angular momentum fluxes at infinity

$$\left\langle \frac{\mathrm{d}E^\infty}{\mathrm{d}t} \right\rangle = \sum_{l=2}^{\infty}\sum_{m=-l}^{l}\sum_{n=-\infty}^{\infty} \frac{\left|C^+_{lmn}\right|^2}{4\pi\omega^2_{mn}}\,, \tag{82}$$

$$\left\langle \frac{\mathrm{d}J^\infty_z}{\mathrm{d}t} \right\rangle = \sum_{l=2}^{\infty}\sum_{m=-l}^{l}\sum_{n=-\infty}^{\infty} \frac{m\left|C^+_{lmn}\right|^2}{4\pi\omega^3_{mn}} \tag{83}$$

where the brackets denote time averaging. In the equatorial case, the average can be calculated over one period T_r. Similar derivation can be made for the fluxes at the horizon [39]

$$\left\langle \frac{\mathrm{d}E^\mathrm{H}}{\mathrm{d}t} \right\rangle = \sum_{l=2}^{\infty}\sum_{m=-l}^{l}\sum_{n=-\infty}^{\infty} \alpha_{lmn}\frac{\left|C^-_{lmn}\right|^2}{4\pi\omega^2_{mn}}\,, \tag{84}$$

$$\left\langle \frac{\mathrm{d}J^\mathrm{H}_z}{\mathrm{d}t} \right\rangle = \sum_{l=2}^{\infty}\sum_{m=-l}^{l}\sum_{n=-\infty}^{\infty} \alpha_{lmn}\frac{m\left|C^-_{lmn}\right|^2}{4\pi\omega^3_{mn}}\,, \tag{85}$$

where

$$\alpha_{lmn} = \frac{256(2Mr_+)^5 P(P^2+4\epsilon^2)(P^2+16\epsilon^2)\omega_{mn}^3}{\left|\mathscr{C}_{lm\omega_{mn}}\right|^2} \quad (86)$$

with $\epsilon = \sqrt{M^2-a^2}/(4Mr_+)$, $P = \omega_{mn} - ma/(2Mr_+)$ and the Teukolsky-Starobinsky constant is

$$\begin{aligned}\left|\mathscr{C}_{lm\omega}\right|^2 = &\Big((\lambda_{lm\omega}+2)^2 + 4a\omega(m-a\omega)\Big)\\ &\times\left(\lambda_{lm\omega}^2 + 36a\omega(m-a\omega)\right)\\ &-\left(2\lambda_{lm\omega}+3\right)\left(48a\omega(m-2a\omega)\right)\\ &+144\omega^2\left(M^2-a^2\right)\ . \end{aligned} \quad (87)$$

The partial amplitudes $C^{\pm}_{lmn}$ are proportional to the secondary mass μ and therefore, if we use dimensionless quantities on the rhs, we obtain

$$\left\langle \frac{\mathrm{d}E^{\infty}}{\mathrm{d}t} \right\rangle = q^2 \sum_{l,m,n} \frac{\left|\hat{C}^{+}_{lmn}\right|^2}{4\pi\hat{\omega}_{mn}^2} \equiv q^2 \sum_{l,m,n} \mathcal{F}^{E\infty}_{lmn}\ , \quad (88)$$

$$\left\langle \frac{\mathrm{d}J_z^{\infty}}{\mathrm{d}t} \right\rangle = Mq^2 \sum_{l,m,n} \frac{m\left|\hat{C}^{+}_{lmn}\right|^2}{4\pi\hat{\omega}_{mn}^3} \equiv Mq^2 \sum_{l,m,n} \mathcal{F}^{J_z\infty}_{lmn}\ , \quad (89)$$

where we have defined the dimensionless fluxes $\mathcal{F}^{E\infty}_{lmn}$ and $\mathcal{F}^{J_z\infty}_{lmn}$ that do not depend on the mass ratio q. The horizon fluxes $\mathcal{F}^{E\mathrm{H}}_{lmn}$ and $\mathcal{F}^{J_z\mathrm{H}}_{lmn}$ can be defined in a similar fashion. We can write the dimensionless energy and angular momentum loss as

$$\left\langle \frac{\mathrm{d}\hat{E}^{\infty}}{\mathrm{d}\hat{t}} \right\rangle = q \sum_{l,m,n} \mathcal{F}^{E\infty}_{lmn}\ , \quad (90)$$

$$\left\langle \frac{\mathrm{d}\hat{J}_z^{\infty}}{\mathrm{d}\hat{t}} \right\rangle = q \sum_{l,m,n} \mathcal{F}^{J_z\infty}_{lmn}\ . \quad (91)$$

These fluxes can be used for calculating the evolution of the orbital parameters p and e during an adiabatic approximation of an inspiral.

2. *Time domain approach*

To verify the frequency domain calculations, we numerically solved the TE (60) in the time domain. For this, we have employed the time domain solver `Teukode` which is described in [40–42]. `Teukode` uses the method of lines, i.e. finite differences in space and Runge-Kutta for evolution in time. Instead of using Kinnersley tetrad and BL coordinates, it solves TE using Campanelli tetrad [43] and hyperboloidal horizon-penetrating (HH) coordinates[3] $(\tau, \rho, \theta, \varphi)$ (for their definition see Eq. (10) in [41]). These coordinates reach future null infinity $\mathscr{I}^+$ ("scri") and horizon at finite radial coordinate ρ_S so no extrapolation is needed to extract GW fluxes at infinity. Another advantage is that the coordinate light speed at the boundaries vanishes, therefore, no numerical boundary condition must be imposed. After the decomposition into azimuthal m-modes $\psi = \sum_m \psi_m e^{im\varphi}$ the equation in $(2+1)$-dimensional form reads

$$\begin{aligned}\big(&C_{\tau\tau}\partial_\tau^2 + C_{\tau\rho}\partial_\tau\partial_\rho + C_{\rho\rho}\partial_\rho^2 + C_{\theta\theta}\partial_\theta^2\\ &+C_\tau\partial_\tau + C_\rho\partial_\rho + C_\theta\partial_\theta + C_0\big)\,\psi_m = S_s\ , \end{aligned} \quad (92)$$

where the coefficients $C_{\tau\tau}, C_{\tau\rho}, \ldots$ are functions of ρ and θ and S_s is the source term for spinning particle discussed in [30].

The source term consists of derivatives of delta functions up to third order. For accurate results proper representation of delta functions must be used. Approximation as Gaussian function and piecewise polynomials as described in [44] were implemented to the `Teukode`. According to [41], piecewise polynomial approximation is more accurate for circular equatorial orbits and faster to calculate than Gaussian approximation, whereas calculations with Gaussian approximation are more stable when the particle is moving in ρ or θ direction. The third derivative of the delta function, which is needed for spinning particle, was implemented only as Gaussian approximation in the previous works. In our work we introduced to `Teukode` an approach suggested in [45], which describes slightly different formulas for piecewise polynomial approximation to construct delta function and its derivatives. `Teukode` has been tested extensively on circular equatorial orbits of a spinning particle in [29, 30, 46–48], but in this work it is tested for the first time on eccentric equatorial orbits of a spinning particle.

B. Numerical results

This Section discusses our numerical calculations of GW fluxes in the frequency domain (as described in Sec. III A 1) and compare them with time domain results obtained from the `Teukode` (Sec. III A 2).

First we present our approach to calculate quantities related to an orbit for given parameters $\hat{a}$, σ, p and e. These quantities include the energy and the angular momentum from Eqs. (38) and (39) respectively, the orbital frequencies $\hat{\Omega}_r$ and $\hat{\Omega}_\phi$ from Eqs. (52) and (53) respectively and the functions $\hat{t}(\chi)$ and $\phi(\chi)$ from Eqs. (55) and (56) respectively. The integrals (52) and (53) were calculated numerically using methods built-in to *Mathematica*. We used extended precision to 48 places, because high precision of the parameters a and $\omega = m\Omega_\phi + n\Omega_r$ is needed for the calculation of the radial function $R^{\pm}_{lm\omega}$.

To calculate the energy and angular momentum fluxes and the strain at infinity, one has to find the partial amplitudes $\hat{C}^{\pm}_{lmn}$ and Eq. (79) implies integration over

[3] In this section ρ denotes the radial HH-coordinate.

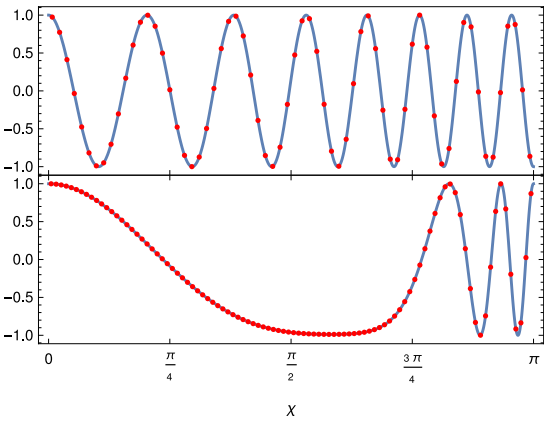

FIG. 3. The real part of $\exp(iD_r(\omega_{mn}t(\chi) - m\phi(\chi)))$ for orbital parameters $\hat{a} = 0.9$, $\sigma = -0.5$, $p = 12$, $e = 0.2$ and $m = 2$, $n = 15$ (top panel) and for orbital parameters $\hat{a} = 0.9$, $\sigma = -0.5$, $p = 12$, $e = 0.8$ and $m = 2$, $n = 4$ (bottom panel). The red dots indicate the values at which the function is calculated during the numerical integration.

χ. The numerical integration errors depend on the employed integration method and the number of points at which the function is enumerated. For our purposes, a fractional accuracy of the order of 10^{-6} is sufficient. Therefore, we used the midpoint rule inducing an error of the order $\mathcal{O}(N^{-2})$ to the integration, where N is the number of points. The advantage of the midpoint rule is that for given accuracy, this method minimizes the number of points N needed for the calculation. However, more complex method can be implemented in the future to improve the accuracy of this integration. The main oscillatory part of Eq. (79) is contained in the exponential term $\exp(iD_r(\omega_{mn}t(\chi) - m\phi(\chi)))$. Figure 3 shows the behavior of this oscillatory part for certain setups. The higher the value of n is, the more the exponential function oscillates. High frequency oscillations are present especially around $\chi = \pi$ in high eccentricity cases. The number of the points N needed for the integration is calculated from the maximum of the derivative of the function $\omega_{mn}t(\chi) - m\phi(\chi)$ with respect to χ, which in dimensionless quantities reads $(\hat{\omega}_{mn}V^t(\hat{r}(\chi)) - mV^\phi(\hat{r}(\chi)))\sqrt{(1-e^2)/J(\chi)}/p$.

The radial functions $R^{\pm}_{lmn}$ were calculated using the BHPToolkit [36], which employs the Mano-Suzuki-Takasugi (MST) method [49] or a numerical integration of the radial TE. The angular functions $S^{\hat{a}\hat{\omega}}_{lm}$ were also calculated using the BHPToolkit which employs the Leaver's method [50].

The strain is calculated from Eq. (81) and the fluxes are calculated from Eqs. (88). The range of l and n for given m-mode was found in the following way. First we calculate the coefficient $\hat{C}^{+}_{lmn}$ for $l = \max(|m|, 2)$ for a range of n to find the mode with the maximal $\left|\hat{C}^{+}_{lmn}\right|$. Then, we calculate other l and n modes until the absolute value is less than a chosen accuracy times the maximal mode. In our calculations, we have chosen accuracy 10^{-6}. However, in some cases the absolute value $\left|\hat{C}^{+}_{lmn}\right|$ is not monotonous in n and it drops suddenly for some n. Because of this, after such a sudden decrease, amplitudes for more n must be calculated. In Fig. 4, the absolute values of the coefficients $\left|\hat{C}^{+}_{lmn}\right|$ are plotted for an orbit with $\hat{a} = 0.9$, $\sigma = -0.5$, $p = 12$, $e = 0.2$ and azimuthal number $m = 2$ for different l and n. We can see that, for given accuracy, only limited number of modes is needed (for $l = m = 2$ it is 21 n-modes) and the absolute value of the amplitudes is decreasing exponentially with $|n|$ for sufficiently high $|n|$. Note that although the astrophysical relevant value of the spin σ is of the same order as the mass ratio $q \ll 1$, it is possible to calculate the GW fluxes for higher spins and then linearize the result in σ to find the contribution of spin $\sigma \ll 1$. We use also these large values to make any deficiencies in our calculations prominent.

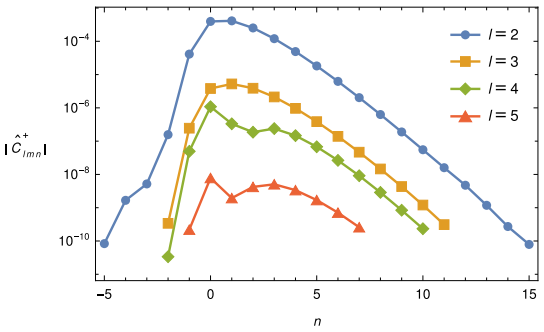

FIG. 4. Absolute values of the partial amplitudes $\left|\hat{C}^{+}_{lmn}\right|$ for orbital parameters $\hat{a} = 0.9$, $\sigma = -0.5$, $p = 12$, $e = 0.2$ and azimuthal number $m = 2$

In Appendix C we compare our coefficients $\hat{C}^{\pm}_{lmn}$ and fluxes $\mathcal{F}^{E\infty}_{lmn}$ and $\mathcal{F}^{\mathrm{EH}}_{lmn}$ with that of [25]. A simplified version of our code calculating GW fluxes from circular equatorial orbit of a spinning particle around a Kerr BH was used to independently verify the results of [29]. These results are discussed in detail in [51]. Tables of the values of the partial amplitudes $\hat{C}^{\pm}_{lmn}$ for future references are in Appendix D.

1. *Comparison of frequency domain and time domain*

To compare the time domain and the frequency domain results, we have calculated the coefficients $\hat{C}^{+}_{lmn}$ for some range of l and n in the frequency domain for different values of the spin σ and of the eccentricity e. We have used these coefficients to find the respective strains and

energy fluxes at infinity. Then, these results have served as reference values in our comparison with the azimuthal m-mode of the strain at infinity multiplied by the radial coordinate $\hat{r}\, h_m$ and the energy fluxes at infinity $\mathcal{F}_m^{E\infty}$ obtained in the time domain. Because of the fact that the space discretization applied in `Teukode` induces numerical errors to the time domain calculations, we have run the time domain calculations for several resolutions and tested the convergence of the code.

To calculate the strains and the fluxes with in the time domain with `Teukode`, we need to approximate the delta functions representing the secondary body in the ρ and θ directions. To do that we have used different combinations of Gaussian functions and piecewise polynomials in these directions. The accuracy appears to be higher when the piecewise polynomial are used in both ρ and θ direction or Gaussian function in ρ direction and piecewise polynomial in θ direction, than in the other two possible settings, i.e., Gaussian in both directions and Gaussian in θ direction with piecewise polynomial in ρ direction. When the piecewise polynomial is used in both directions, calculations are faster and, therefore, we have used this approximation in most cases. In our calculations, the strain has been extracted at $r = \infty$ and $\theta = \pi/2$ and the energy flux has been averaged over two periods T_r starting at the retarded coordinate around $u = 350M$, where $u = t - r^*$.

In order to provide a first comparison of the frequency and the time domain results, we use the relative difference of the azimuthal mode m of the strain at $r = \infty$ and $\theta = \pi/2$

$$\delta h_m = \left| 1 - \frac{h_m^{\rm td}}{h_m^{\rm fd}} \right| , \tag{93}$$

where $h_m^{\rm td}$ is the strain calculated using `Teukode` and $h_m^{\rm fd}$ is m-mode of the strain calculated in frequency domain using Eq. (81) without the sum over m. Figure 5 shows the relative difference of the azimuthal modes $m = 1, 2, 3, 4$ of the strain as function of the retarded coordinate $\hat{u}$. In this plot, the strain calculated in the frequency domain (the denominator of δh_m) remains fixed, while each time domain calculated evolution of the strain is performed for different number of points in the ρ direction N_ρ (resolution). The delta function is approximated by a piecewise polynomial for five resolutions (N_ρ=1200,1704,2400,3384,4800), while in one case is approximated by a Gaussian function for $N_\rho = 4800$. We can see that the relative difference δh_m tends to decrease as the resolution increases, but for the highest resolution $N_\rho = 4800$ the numerical noise becomes significant. Though the Gaussian approximation is less accurate, the amplitude of its noise is relatively smaller than the amplitude of the noise for the piecewise polynomial approximation with the same resolution. We speculate that the cause of this numerical noise comes from the fact that as the resolution increases, the approximation becomes less smooth. Namely, we have used a 12th order approximation of the delta function, which is 12 points wide, for each resolution; therefore, the higher the resolution is, the narrower and higher is the delta function. Note that

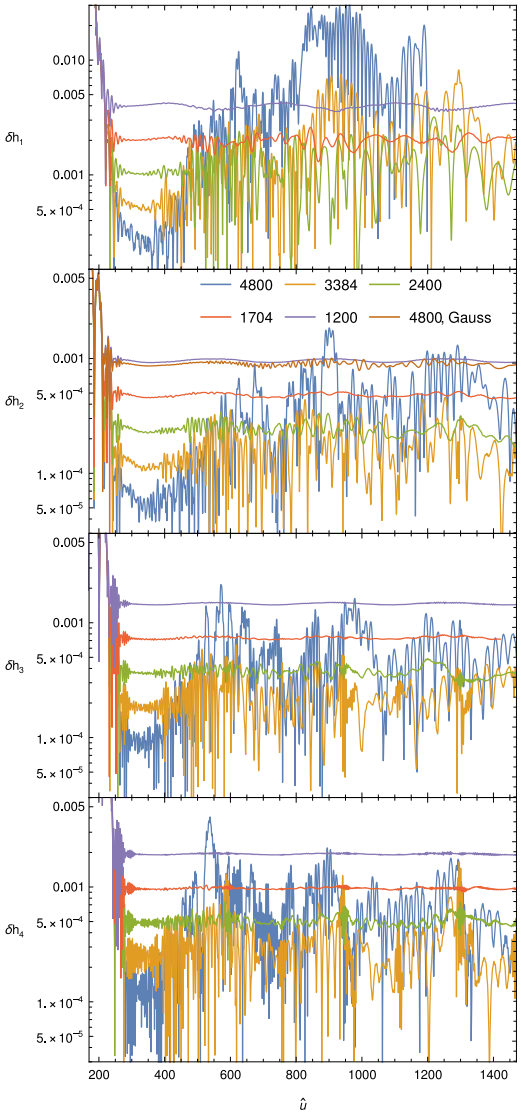

FIG. 5. The relative difference of the strain δh_m from the $m = 1$ mode (top panel) to the $m = 4$ mode (bottom panel) as a function of the retarded coordinate $\hat{u}$ at $r = \infty$ and $\theta = \pi/2$. Each plotted curve represents a case with different number of points in the ρ direction N_ρ. The piecewise polynomial approximation of the delta function was used for all cases apart from one, for which the Gaussian approximation with resolution 4800 was employed. The parameters of the orbit are $\hat{a} = 0.9$, $\sigma = -0.5$, $p = 12$, $e = 0.2$. The initial noise is caused by zero initial data in time domain.

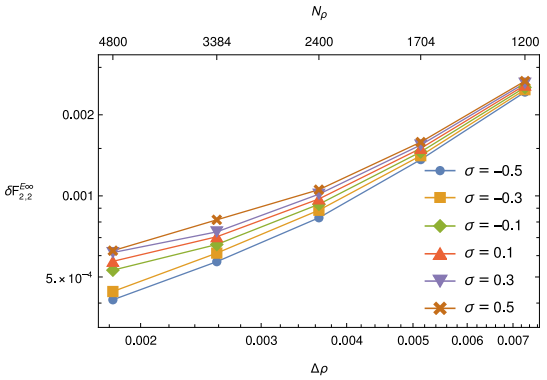

FIG. 6. The relative difference of the energy flux $\delta\mathcal{F}^{E\infty}_{lm}$ of the $l = m = 2$ mode as function of the grid length in the ρ direction of the time domain calculations. Note that the time domain calculations have been projected on the Y_{lm} basis, while the frequency domain ones on the $S^{a\omega}_{lm}$. Each curve represents a different value of the secondary spin, while the Kerr parameter $\hat{a} = 0.9$, semi-latus rectum $p = 12$ and eccentricity $e = 0.2$ remain fixed.

the $m = 1$-mode has very small value and the noise has relatively higher amplitude than in $m = 2, 3, 4$ modes. The $m = 0$-mode, which is not shown here, although nonzero, has extremely small value allowing the numerical noise to be dominant.

To further check our results, we have calculated the relative difference of the energy fluxes

$$\delta\mathcal{F}^{E\infty}_{lm} = \left|1 - \frac{\mathcal{F}^{E\infty}_{lm,\mathrm{td}}}{\mathcal{F}^{E\infty}_{lm,\mathrm{fd}}}\right|, \tag{94}$$

where $\mathcal{F}^{E\infty}_{lm,\mathrm{td}}$ is the value calculated using `Teukode` and $\mathcal{F}^{E\infty}_{lm,\mathrm{fd}}$ is the value calculated with the frequency domain approach summed over n. Figure 6 shows how the time domain calculations of the dominant $l = m = 2$ mode of the energy fluxes converges to the frequency ones as the resolution increases. For this plot we have kept fixed the Kerr parameter $\hat{a} = 0.9$, the semi-latus rectum $p = 12$ and the eccentricity $e = 0.2$, while we have used for each curve a different value of the secondary spin σ spanning from -0.5 to 0.5. The relative difference in the fluxes should converge to zero as the grid length $\Delta\rho = (\rho_S - \rho_+)/N_\rho$ decreases (increasing resolution). However, the relative differences do not converge to zero, because in the frequency domain calculations we use the projection to spin-weighted spheroidal harmonics $S^{a\omega}_{lm}$ and `Teukode` projects the strain to the spin-weighted spherical harmonics $Y_{lm} = S^0_{lm}$. For the dominant mode the difference between the projections to these functions is low because for low $a\omega$, the spheroidal functions $S^{a\omega}_{lm}$ can be approximated by the spherical functions Y_{lm}.

Because of the aforementioned projection issue, for a proper comparison of the time and frequency domain results, we must calculate the sum of the fluxes over l. The relative difference

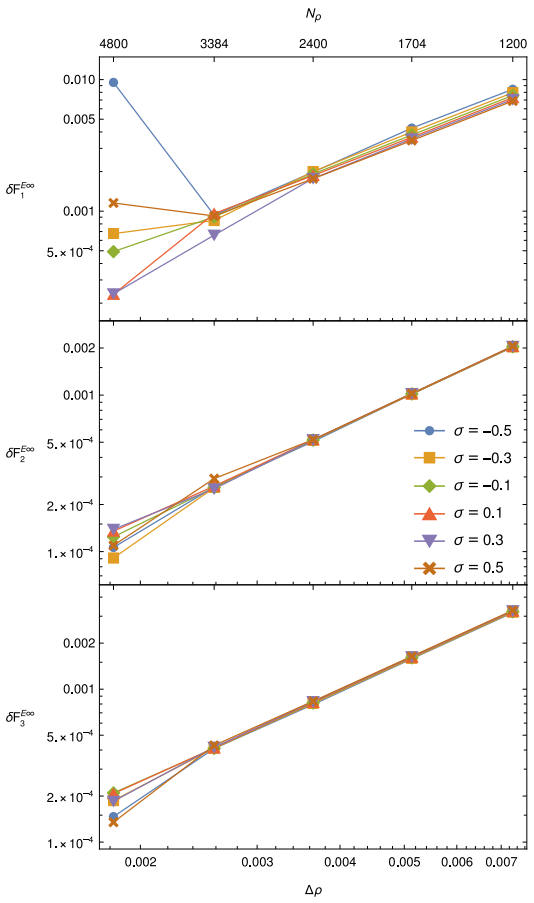

FIG. 7. Comparison of frequency domain and time domain results. The relative difference $\delta\mathcal{F}^{E\infty}_{m=1}$ (top panel), $\delta\mathcal{F}^{E\infty}_{m=2}$ (middle panel) and $\delta\mathcal{F}^{E\infty}_{m=3}$ (bottom panel) is plotted for different values of the secondary spins σ spanning from -0.5 to 0.5. The Kerr parameter $\hat{a} = 0.9$, the semi-latus rectum $p = 12$ and the eccentricity 0.2 are kept fixed for all the cases.

$$\delta\mathcal{F}^{E\infty}_{m} = \left|1 - \frac{\mathcal{F}^{E\infty}_{m,\mathrm{td}}}{\mathcal{F}^{E\infty}_{m,\mathrm{fd}}}\right|, \tag{95}$$

for $m = 1, 2, 3$ has been calculated for different secondary spins σ in the frequency domain and in time domain we used different resolutions ($N_\rho = 1200, 1704, 2400, 3384, 4800$). We can see in Fig. 7 that the relative differences converge to zero as we expected. The lowest step $\Delta\rho$ corresponding to the highest resolution $N_\rho = 4800$ shows variance in the relative differences. This is caused by the fact that the noise amplitude is the highest for the highest resolution, which can be seen in

Fig. 5. Especially in the case $m = 1$ where the energy flux is significantly lower than for $m = 2$, the variance in the relative differences is clearly visible. For the highest resolution, the relative difference is higher for higher values of spin $|\sigma|$. This can be caused by the numerical noise in time domain calculations induced by the non-smoothness of the piecewise polynomial approximation of the third derivative of the delta function. Namely, the term with the third derivative is proportional to the spin σ. For negative σ the noise is relatively higher because the value of energy flux for $\sigma < 0$ is lower than the flux for $\sigma > 0$ and thus the noise is more dominant.

To check the dependence of our calculations on the value of eccentricity, we have calculated the energy fluxes for fixed Kerr parameter $\hat{a} = 0.9$, secondary spin $\sigma = 0.5$ and semi-latus rectum $p = 12$, while the eccentricity e value spans from 0.2 to 0.8. For each eccentricity we have calculated the relative difference in the energy fluxes $\delta\mathcal{F}_m^{E\infty}$ for $m = 1, 2, 3$. Then, we have compared the dependence of the relative difference on the resolution for different eccentricities as in the case with the changing secondary spin. This comparison is shown in Fig. 8. First, we have calculated the dominant $m = 2$ mode in time domain with piecewise polynomial approximation of the delta function in both ρ and θ direction (p-p), but for $e = 0.8$ the noise is increasing with the resolution and $\delta\mathcal{F}_2^{E\infty}$ does not converge to zero (purple line in the middle panel of Fig. 8). Therefore, for $m = 2$ and other modes, we performed the time domain calculations for $e = 0.8$ using the Gaussian approximation in ρ direction and the piecewise polynomial approximation in θ direction (G-p, red line in all panels of Fig. 8). However, the $m = 1$ mode has low amplitude and the noise is therefore more significant and the p-p approximation for $e = 0.6$ and the G-p approximation for $e = 0.8$ fails. Because of this, for $m = 1$ mode we repeated the calculation for $e = 0.6$ with G-p approximation and for $e = 0.8$ with Gaussian approximation in both directions (G-G).

The fact that for the piecewise polynomial approximation the noise has greater impact on higher eccentricities can be explained as follows. The shape of the delta function depends on the distance between the delta function and the two grid points around it. Since the distance between these grid points changes rapidly on a highly eccentric orbit, the shape of the delta function changes rapidly as well. The greater is the change in the shape, the greater is the noise. Thus, the piecewise polynomial approximation is optimal for circular trajectories. Moreover, higher eccentricities imply longer periods of motion and thus longer runtime, which allows the exponentially growing noise to reach higher values. For the Gaussian approximation noise grows more slowly.

Figure 8 indicates that by choosing a proper delta function approximation the relative difference $\delta\mathcal{F}_m^{E\infty}$ would converge to zero for all m-modes and eccentricities e. This choice currently seems to depend on the orbital parameters and modes. For example, the piecewise polynomial approximation appears to be in general more efficient than the Gaussian approximation, however its own limitation in our example became prominent for high eccentricities and modes corresponding to small flux or strain absolute values, i.e. in modes that the numerical noise is dominant.

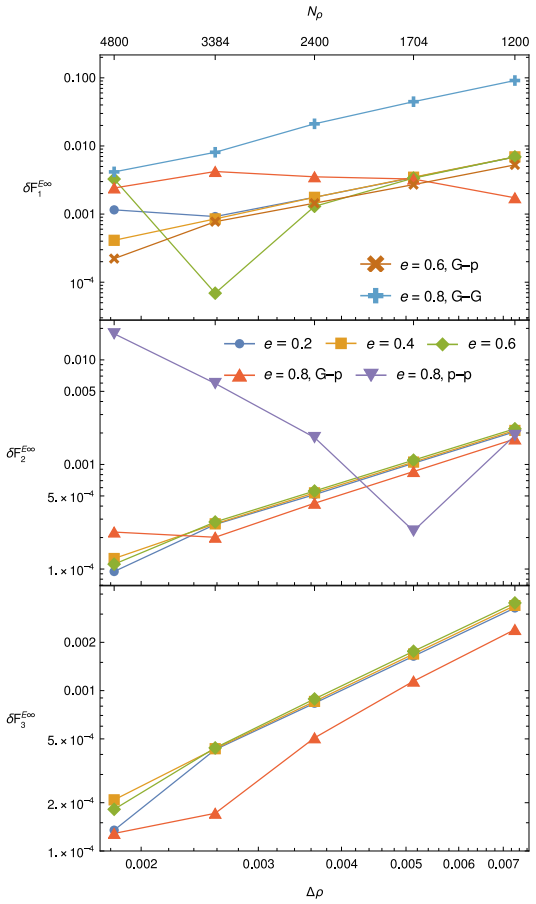

FIG. 8. Comparison of frequency domain and time domain results. The relative difference $\delta\mathcal{F}_{m=1}^{E\infty}$ (top panel), $\delta\mathcal{F}_{m=2}^{E\infty}$ (middle panel) and $\delta\mathcal{F}_{m=3}^{E\infty}$ (bottom panel) is plotted for different values of the eccentricity e spanning from 0.2 to 0.8. The Kerr parameter $\hat{a} = 0.9$, the secondary spin $\sigma = 0.5$ and the semi-latus rectum $p = 12$ are kept fixed for all the cases. If not specified, the delta function is approximated by a piecewise polynomial in both ρ and θ direction. For $m = 1$, $e = 0.6$ and $m = 2$, $e = 0.8$ the delta function is approximated as Gaussian function in ρ direction and piecewise polynomial in θ direction. For $m = 1$, $e = 0.8$ the delta function is approximated as Gaussian function in both ρ and θ directions.

IV. SUMMARY

In this work, we have studied the motion of a spinning particle in the equatorial plane of a Kerr black hole and the GW fluxes from these orbits. The only possible configuration of the spins in this setup is the spins to be parallel or antiparallel. In this framework, we have derived a reduced set of equations of motion equivalent to the MPD equations with TD SSC. Taking advantage of the fact that an orbit can be characterized by its constants of motion, namely the energy E and the z component of the total angular momentum J_z, we have provided explicit formulas for the energy and the angular momentum in terms of the eccentricity e and semi-latus rectum p. Furthermore, through the reduced equations of motion and by introducing a Mino-like time parameter λ, we were able to find expressions allowing the numerical calculation of the frequencies of the radial and azimuthal motion. These expressions provide the frequencies with respect to λ or the BL time.

The orbital findings were then implemented in the calculation of the GW fluxes from the equatorial orbits in the frequency domain. Namely, this work introduces the formulas giving the strain h, the energy fluxes and the angular momentum fluxes at infinity and at the horizon from a spinning secondary moving on the equatorial plane of a Kerr black hole. For this purpose, we have developed a *Mathematica* code calculating the amplitudes $C^{\pm}_{lmn}$ on which the frequency domain GW fluxes depend. We plan to make this code publicly available through the *Black Hole Perturbation Toolkit* repository. The frequency domain results were, then, compared with time domain results obtained from a TE solver called `Teukode`. To improve the efficiency of `Teukode`, we have implemented a piecewise polynomial to approximate the delta functions and its derivatives in the spinning-particle source term. The comparison has shown good agreement between the frequency domain results with the time domain ones.

To check the discretization error in the time domain calculations introduced by the piecewise polynomial, we have calculated the fluxes in time domain for different resolutions and compared them with the respective frequency domain results. The difference between the results from these two approaches tend to consistently decrease with increasing resolution. However, for the highest resolution, which we have implemented, the numerical noise in the time domain calculations becomes significant. This behavior occurs for different calculation setups. Namely, we have checked our calculations by varying the secondary spin while keeping the other parameters fixed and by varying the eccentricities while keeping the other parameters fixed.

These calculations are part of the on-going effort to build post-adiabatic gravitational waveforms modelling gravitational waves emitted by extreme mass ratio inspirals. In a future work, the frequency domain fluxes will be used to find the adiabatic evolution of the orbit on the equatorial plane under the influence of radiation reaction. The influence of the secondary spin on the change of the orbital parameters and phase of the GW will be studied.

ACKNOWLEDGMENTS

The authors have been supported by the fellowship Lumina Quaeruntur No. LQ100032102 of the Czech Academy of Sciences. The authors would like to acknowledge networking support by the GWverse COST Action CA16104, “Black holes, gravitational waves and fundamental physics”. V.S. would also like to express gratitude for the hospitality of the Theoretical Physics Institute at the University of Jena. We would like to thank Sebastiano Bernuzzi, Enno Harms, Vojtěch Witzany and Tomáš Ledvinka for useful discussions and comments. This work makes use of the Black Hole Perturbation Toolkit. Computational resources were supplied by the project ”e-Infrastruktura CZ” (e-INFRA LM2018140) provided within the program Projects of Large Research, Development and Innovations Infrastructures.

Appendix A: List of dimensionless quantities

Throughout this work, we use several quantities both in their full form and dimensionless form. The dimensionless form is denoted by a hat. Their list with relation between the full and dimensionless form is in Table I. Some quantities such as the time parameter λ or x are defined only as dimensionless whereas other quantities are used only in their full form.

TABLE I. List of dimensionless quantities

$\hat{t} = t/M$	BL time
$\hat{r} = r/M$	BL radial coordinate
$\hat{a} = a/M$	Kerr parameter
$\sigma = S/(\mu M)$	Secondary spin
$\hat{E} = E/\mu$	Energy
$\hat{J}_z = J_z/(\mu M)$	Angular momentum
$\hat{\tau} = \tau/M$	Proper time
$\hat{\Delta} = \Delta/M^2$	
$\hat{\varpi}^2 = \varpi^2/M^2$	
$\hat{\Omega}_r = \Omega_r M$	Radial BL frequency
$\hat{\Omega}_\phi = \Omega_\phi M$	Orbital BL frequency
$\hat{\omega} = \omega M$	Frequency
$\hat{C}^0_{ab} = C^0_{ab}/\mu$	
$\hat{C}^\sigma_{ab} = C^\sigma_{ab}/\mu$	
$\hat{C}^{\pm}_{lmn} = C^{\pm}_{lmn} M^2/\mu$	Partial amplitudes
$\hat{u} = u/M$	Retarded coordinate

Appendix B: Formulas for GW fluxes

In this Appendix we derive the coefficients $A_i = A_i(r,\theta)$ and $B_{i+1} = B_{i+1}(r,\theta)$, $i = 0,1,2$, in Eq. (73) for calculation of partial amplitudes of GWs from general bound orbits of a spinning particle around a Kerr black hole. Then we list explicit formulas for equatorial orbits with secondary spin parallel to the z axis.

To find the form of the coefficients A_i and B_{i+1} in Eq. (73), the integrals (68) and (65) must be evaluated using rules for integrating delta functions. We can classify the parts of the coefficients A_i according to term from which they originate:

$$A_0 = \sum_{ab=nn,n\overline{m},\overline{m}\overline{m}} \left(A^0_{ab0} + A^{t\phi}_{ab0} + A^r_{ab0} + A^\theta_{ab0}\right) , \quad \text{(B1)}$$

$$A_1 = \sum_{ab=n\overline{m},\overline{m}\overline{m}} \left(A^0_{ab1} + A^{t\phi}_{ab1} + A^r_{ab1} + A^\theta_{ab1}\right) , \quad \text{(B2)}$$

$$A_2 = A^0_{\overline{m}\overline{m}0} + A^{t\phi}_{\overline{m}\overline{m}0} + A^r_{\overline{m}\overline{m}1} + A^\theta_{\overline{m}\overline{m}1} . \quad \text{(B3)}$$

The terms A^0_{abi} originate from the first term of the stress-energy tensor (70) containing the nonspinning part of $T^{\mu\nu}$ and parts containing Christoffel symbols. The terms $A^{t\phi}_{abi}$ originate from the second term of (70) containing t and ϕ derivative. Similarly, the terms A^r_{abi} or A^θ_{abi} originate from the second term of Eq. (70) containing r or θ derivative respectively. The subscripts ab denote the tetrad legs in Eq. (69).

A^0_{abi} can be found by integrating θ and ϕ after substituting the first term of Eq. (70) into Eq. (68) by replacing $\theta \to \theta_p(t)$, $\phi \to \phi_p(t)$ and then using integration by parts in Eq. (65), where the derivatives with respect to r in (69) are shifted to the radial function $R^\pm_{lmn}$ to obtain

$$A^0_{abi} = \left(C^0_{ab} - C^\sigma_{ab}\right) f^{(i)}_{ab} , \quad \text{(B4)}$$

where C^0_{ab} and C^σ_{ab} are defined in Eq. (71).

To find the form of $A^{t\phi}_{abi}$, we must perform integration by parts in Eq. (68) where the t or ϕ derivative in the second term of Eq. (70) are shifted to $\exp(i\omega - im\phi)$ because no other functions depend on t and ϕ. From this, we get terms multiplied by $i\omega$ and $-im\phi$. After that, an integration over r of Eq. (65) is done similarly as in the previous case and we obtain

$$A^{t\phi}_{abi} = \frac{\mathrm{d}\tau}{\mathrm{d}t}(i\omega S^{t\mu} - imS^{\phi\mu})v^\nu e^{(a}_{(\mu} e^{b)}_{\nu)} f^{(i)}_{ab} . \quad \text{(B5)}$$

The term A^θ_{abi} is derived in similar way. The derivative with respect to θ in the second term in (70) is shifted to the functions $f^{(i)}_{ab}$ and the tetrad legs. The boundary term vanishes because $f^{(i)}_{ab}(r,0) = f^{(i)}_{ab}(r,\pi) = 0$. The final term has the form

$$A^\theta_{abi} = \frac{\mathrm{d}\tau}{\mathrm{d}t} S^{\theta(\mu}v^{\nu)} f^{(i)}_{ab} \partial_\theta (e^{(a}_\mu e^{b)}_\nu) + \frac{\mathrm{d}\tau}{\mathrm{d}t} S^{\theta(\mu}v^{\nu)} e^{(a}_\mu e^{b)}_\nu \partial_\theta f^{(i)}_{ab} . \quad \text{(B6)}$$

Now let us focus on the term containing the r derivative in Eq. (70). After substituting the stress-energy tensor (70) into Eq. (69), the derivative of the delta function can be shifted to the function $f^{(i)}_{ab}$ and the tetrad legs. For example, from the first term of $\mathcal{T}_{n\overline{m}}$ we obtain

$$\begin{aligned}\partial_r \left(f^{(1)}_{n\overline{m}}(r,\theta) n_\mu \overline{m}_\nu \partial_r \left((v^t)^{-1} S^{r(\mu}v^{\nu)}\delta^3\right)\right) = \\ \partial_r^2 \left(f^{(1)}_{n\overline{m}}(r,\theta) n_\mu \overline{m}_\nu (v^t)^{-1} S^{r(\mu}v^{\nu)}\delta^3\right) \\ - \partial_r \left(\partial_r \left(f^{(1)}_{n\overline{m}}(r,\theta) n_\mu \overline{m}_\nu\right)(v^t)^{-1} S^{r(\mu}v^{\nu)}\delta^3\right) \quad \text{(B7)}\end{aligned}$$

After substituting Eq. (68) into Eq. (65) we can change the order of the t and r integrals and integrate by parts. From the second term in Eq. (B7) we obtain a term with derivatives with respect to r of $f^{(i)}_{ab}$ and the tetrad legs

$$A^r_{abi} = \frac{\mathrm{d}\tau}{\mathrm{d}t} S^{r(\mu}v^{\nu)} f^{(i)}_{ab} \partial_r (e^{(a}_\mu e^{b)}_\nu) + \frac{\mathrm{d}\tau}{\mathrm{d}t} S^{r(\mu}v^{\nu)} e^{(a}_\mu e^{b)}_\nu \partial_r f^{(i)}_{ab} . \quad \text{(B8)}$$

From the second term in Eq. (B7) we obtain terms with one order higher derivatives of the radial function $R^\pm_{lm\omega}$, of which the integration by parts we can perform to obtain the coefficients

$$B_1 = \sum_{ab=nn,n\overline{m},\overline{m}\overline{m}} B_{ab1} , \quad \text{(B9)}$$

$$B_2 = \sum_{ab=n\overline{m},\overline{m}\overline{m}} B_{ab2} , \quad \text{(B10)}$$

$$B_3 = B_{\overline{m}\overline{m}3} , \quad \text{(B11)}$$

where

$$B_{ab(i+1)} = -\frac{\mathrm{d}\tau}{\mathrm{d}t} S^{r(\mu}v^{\nu)} e^{(a}_\mu e^{b)}_\nu f^{(i)}_{ab} . \quad \text{(B12)}$$

The functions $f^{(i)}_{ab} = f^{(i)}_{ab}(r,\theta)$ in the equatorial plane are given by

$$f^{(0)}_{nn}\left(r,\frac{\pi}{2}\right) = -\frac{2r^2}{\Delta^2}\left(\mathscr{L}^\dagger_1\mathscr{L}^\dagger_2 - \frac{2ia}{r}\mathscr{L}^\dagger_2\right) S^{a\omega}_{lm}(\theta)\Big|_{\theta\to\frac{\pi}{2}} , \quad \text{(B13)}$$

$$f^{(0)}_{n\overline{m}}\left(r,\frac{\pi}{2}\right) = \frac{2\sqrt{2}r}{\Delta}\left(\frac{iK}{\Delta} + \frac{2}{r}\right)\mathscr{L}^\dagger_2 S^{a\omega}_{lm}(\theta)\Big|_{\theta\to\frac{\pi}{2}} , \quad \text{(B14)}$$

$$f^{(1)}_{n\overline{m}}\left(r,\frac{\pi}{2}\right) = \frac{2\sqrt{2}r}{\Delta}\mathscr{L}^\dagger_2 S^{a\omega}_{lm}(\theta)\Big|_{\theta\to\frac{\pi}{2}} , \quad \text{(B15)}$$

$$f^{(0)}_{\overline{m}\overline{m}}\left(r,\frac{\pi}{2}\right) = \left(i\partial_r\left(\frac{K}{\Delta}\right) - 2i\frac{K}{\Delta r} + \frac{K^2}{\Delta^2}\right) S^{a\omega}_{lm}\left(\frac{\pi}{2}\right) , \quad \text{(B16)}$$

$$f^{(1)}_{\overline{m}\overline{m}}\left(r,\frac{\pi}{2}\right) = -2\left(\frac{1}{r} + i\frac{K}{\Delta}\right) S^{a\omega}_{lm}\left(\frac{\pi}{2}\right) , \quad \text{(B17)}$$

$$f^{(2)}_{\overline{m}\overline{m}}\left(r,\frac{\pi}{2}\right) = -S^{a\omega}_{lm}\left(\frac{\pi}{2}\right) , \quad \text{(B18)}$$

where

$$K = (r^2 + a^2)\omega - am \ , \tag{B19}$$

$$\mathscr{L}_n^\dagger = \partial_\theta - m\csc\theta + a\omega\sin\theta + n\cot\theta \ . \tag{B20}$$

Up to this point the analysis holds for generic orbits of a spinning particle. When we constrain the particle on equatorial orbits with its spin set parallel to the z axis, then $S^{\theta\mu} = 0$ for all μ and, therefore, $A^\theta_{abi} = 0$. For the presentation of the equatorial case, we prefer to use the dimensionless quantities.

In the definition of C^0_{ab} and C^σ_{ab} (71) we can replace the derivative with respect to τ in v^μ with derivative with respect to λ and use the fact that $V^t = \mathrm{d}\hat{t}/\mathrm{d}\lambda$, $V^r = \mathrm{d}\hat{r}/\mathrm{d}\lambda$ and $V^\phi = \mathrm{d}\phi/\mathrm{d}\lambda$. From Eqs. (23) and (25) we obtain

$$\hat{C}^0_{nn} = \frac{\mathrm{d}\lambda}{\mathrm{d}\hat{t}}\frac{V_n^2}{\Sigma_\sigma} \ , \tag{B21}$$

$$\hat{C}^0_{n\overline{m}} = \frac{\mathrm{d}\lambda}{\mathrm{d}\hat{t}}\frac{V_{\overline{m}}V_n\left(2\hat{r}^3+\sigma^2\right)}{2\Sigma_\sigma\left(\hat{r}^3+2\sigma^2\right)} \ , \tag{B22}$$

$$\hat{C}^0_{\overline{m}\overline{m}} = \frac{\mathrm{d}\lambda}{\mathrm{d}\hat{t}}\frac{\hat{r}V_{\overline{m}}^2}{\left(\hat{r}^3+2\sigma^2\right)} \ , \tag{B23}$$

$$\hat{C}^\sigma_{nn} = \frac{\mathrm{d}\lambda}{\mathrm{d}\hat{t}}\frac{\sigma}{2\hat{r}^2\Sigma_\sigma}\left(2\hat{a}V_n^2 - \frac{\hat{\Delta}(\hat{r}^3+2\sigma^2)}{\hat{r}^3-\sigma^2}V_n x + (\hat{a}^2-\hat{r})V^r x\right) \ , \tag{B24}$$

$$\hat{C}^\sigma_{n\overline{m}} = \frac{\mathrm{d}\lambda}{\mathrm{d}\hat{t}}\frac{i\sigma}{2\sqrt{2}\hat{r}\Sigma_\sigma}\left(-\frac{\hat{a}^2-\hat{r}}{\Delta}\left(2V_n^2+(V^r)^2\right) - \frac{\hat{a}^2-\hat{r}^2}{\hat{\Delta}}V_nV^r + \frac{3\hat{a}\sigma^2}{\hat{r}\Sigma_\sigma}V_n x - \hat{a}V^r x + \frac{\hat{\Delta}(\hat{r}^3+2\sigma^2)}{2\hat{r}\Sigma_\sigma}x^2\right) \ , \tag{B25}$$

$$\hat{C}^\sigma_{\overline{m}\overline{m}} = \frac{\mathrm{d}\lambda}{\mathrm{d}\hat{t}}\frac{\sigma}{\Sigma_\sigma}\left(-\frac{\hat{a}}{\hat{\Delta}}\left(2V_n^2+2V_nV^r+(V^r)^2\right) + \frac{i}{\hat{r}\sqrt{2}}\left(2V_n+V^r\right)V_{\overline{m}}\right) \ , \tag{B26}$$

where

$$V_n = V^t n_t + V^r n_r + V^\phi\frac{n_\phi}{M} = -\frac{P_\sigma(\hat{r})+V^r}{2} \ , \tag{B27}$$

$$V_{\overline{m}} = V^t\overline{m}_t + V^\phi\frac{\overline{m}_\phi}{M} = -\frac{ix\left(\hat{r}^3+2\sigma^2\right)}{\sqrt{2}\Sigma_\sigma} \ . \tag{B28}$$

We can rewrite the expressions for $A^{t\phi}_{abi}$, A^r_{abi}, and $B_{ab(i+1)}$ into dimensionless quantities as

$$\hat{A}^{t\phi}_{abi} = \frac{\mathrm{d}\lambda}{\mathrm{d}\hat{t}}\left(i\hat{\omega}\hat{S}^t{}_{(a} - im\hat{S}^\phi{}_{(a}\right)V_{b)}\hat{f}^{(i)}_{ab}\left(\hat{r},\frac{\pi}{2}\right) \ , \tag{B29}$$

$$\hat{A}^r_{abi} = \frac{\mathrm{d}\lambda}{\mathrm{d}\hat{t}}(\hat{S}^r{}_{(\partial_{\hat{r}}a}V_{b)} + \hat{S}^r{}_{(b}V_{\partial_{\hat{r}}a)})\hat{f}^{(i)}_{ab}\left(\hat{r},\frac{\pi}{2}\right) + \frac{\mathrm{d}\lambda}{\mathrm{d}\hat{t}}\hat{S}^r{}_{(a}V_{b)}\partial_{\hat{r}}\hat{f}^{(i)}_{ab}\left(\hat{r},\frac{\pi}{2}\right) \ , \tag{B30}$$

$$\hat{B}_{ab(i+1)} = -\frac{\mathrm{d}\lambda}{\mathrm{d}\hat{t}}\hat{S}^r{}_{(a}V_{b)}\hat{f}^{(i)}_{ab}\left(\hat{r},\frac{\pi}{2}\right) \ , \tag{B31}$$

where we used the dimensionless projections of $S^{\mu\nu}$ into the tetrad

$$\hat{S}^t{}_n = \frac{1}{\mu M}\left(S^{tr}n_r + S^{r\phi}n_\phi\right) = \frac{\sigma\left(x\hat{\varpi}^2 - 2\hat{a}V_n\right)}{2\hat{r}\Sigma_\sigma} \ , \tag{B32}$$

$$\hat{S}^r{}_n = \frac{1}{\mu M}\left(-S^{tr}n_t + S^{r\phi}n_\phi\right) = -\frac{\sigma x\hat{\Delta}}{2\hat{r}\Sigma_\sigma} \ , \tag{B33}$$

$$\hat{S}^\phi{}_n = \frac{1}{\mu}\left(-S^{t\phi}n_t - S^{r\phi}n_r\right) = \frac{\sigma(\hat{a}x - 2V_n)}{2\hat{r}\Sigma_\sigma} \ , \tag{B34}$$

$$\hat{S}^t{}_{\overline{m}} = \frac{1}{\mu M}S^{t\phi}\overline{m}_\phi = -\frac{i\sigma\hat{\varpi}^2V^r}{\sqrt{2}\hat{\Delta}\Sigma_\sigma} \ , \tag{B35}$$

$$\hat{S}^r{}_{\overline{m}} = \frac{1}{\mu M}\left(-S^{tr}\overline{m}_t + S^{r\phi}\overline{m}_\phi\right) = -\frac{i\sigma P_\sigma(\hat{r})}{\sqrt{2}\Sigma_\sigma} \ , \tag{B36}$$

$$\hat{S}^\phi{}_{\overline{m}} = -\frac{1}{\mu}S^{t\phi}\overline{m}_t = -\frac{i\sigma\hat{a}V^r}{\sqrt{2}\hat{\Delta}\Sigma_\sigma} \ . \tag{B37}$$

The quantities $V_{\partial_{\hat{r}}a}$ and $\hat{S}^r{}_{\partial_{\hat{r}}a}$ can be understood as dimensionless projections on the differentiated tetrad $\partial_r e^\mu_{(a)}$

$$V_{\partial_{\hat{r}}n} = M\left(V^t\partial_r n_t + V^r\partial_r n_r + V^\phi\frac{\partial_r n_\phi}{M}\right) = \frac{(\hat{a}^2-\hat{r})P_\sigma(\hat{r})}{\hat{r}\hat{\Delta}} \ , \tag{B38}$$

$$V_{\partial_{\hat{r}}\overline{m}} = M\left(V^t\partial_r\overline{m}_t + V^\phi\frac{\partial_r\overline{m}_\phi}{M}\right) = \frac{V_{\overline{m}}}{\hat{r}} - \frac{i\sqrt{2}\hat{a}P_\sigma(\hat{r})}{\hat{\Delta}} \ , \tag{B39}$$

$$\hat{S}^r{}_{\partial_{\hat{r}}n} = \frac{1}{\mu}\left(-S^{tr}\partial_r n_t + S^{r\phi}\partial_r n_\phi\right) = \frac{\sigma(\hat{a}^2-\hat{r})x}{\hat{r}^2\Sigma_\sigma} \ , \tag{B40}$$

$$\hat{S}^r{}_{\partial_{\hat{r}}\overline{m}} = \frac{1}{\mu}\left(-S^{tr}\partial_r\overline{m}_t + S^{r\phi}\partial_r\overline{m}_\phi\right) = -\frac{i\sigma(2\hat{a}x + P_\sigma(\hat{r}))}{\sqrt{2}\hat{r}\Sigma_\sigma} \ , \tag{B41}$$

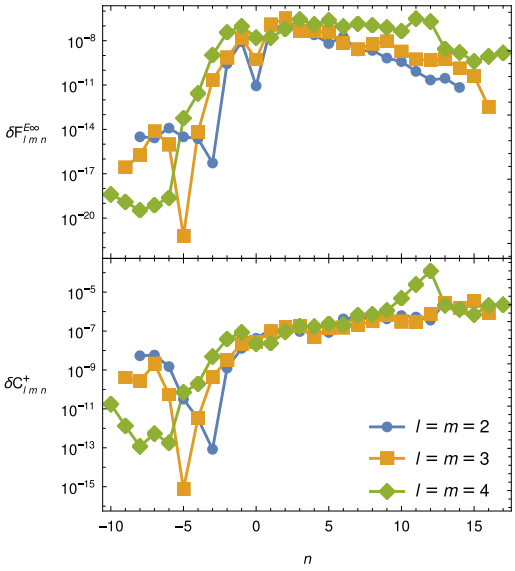

FIG. 9. Differences between our frequency domain results and the results obtained in [25]. Top panel: the difference $\delta\mathcal{F}^{E\infty}_{lmn}$ between the fluxes normalized by $\max_{n_{\min}\le n\le n_{\max}}\left|\mathcal{F}^{E\infty}_{lmn}\right|$. Bottom panel: the difference $\delta\hat{C}^{+}_{lmn}$ between the coefficients normalized by $\max_{n_{\min}\le n\le n_{\max}}\left|\hat{C}^{+}_{lmn}\right|$.

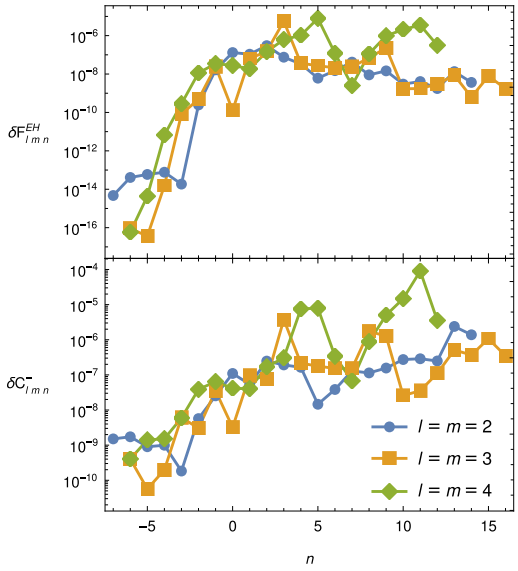

FIG. 10. Differences between our frequency domain results and the results obtained in [25]. Top panel: the difference $\delta\mathcal{F}^{\rm EH}_{lmn}$ between the fluxes normalized by $\max_{n_{\min}\le n\le n_{\max}}\left|\mathcal{F}^{\rm EH}_{lmn}\right|$. Bottom panel: the difference $\delta\hat{C}^{-}_{lmn}$ between the coefficients normalized by $\max_{n_{\min}\le n\le n_{\max}}\left|\hat{C}^{-}_{lmn}\right|$.

where the covariant components of the tetrad are

$$n_\mu = \frac{1}{2\Sigma}\left(-\Delta, -\Sigma, 0, a\Delta\sin^2\theta\right)\ , \tag{B42}$$

$$\overline{m}_\mu = -\frac{\rho}{\sqrt{2}}\left(ia\sin\theta, 0, \Sigma, -i\varpi^2\sin\theta\right)\ . \tag{B43}$$

Appendix C: Comparison with [Phys. Rev. D 73, 024027 (2006)]

This section compares our frequency domain calculations for a nonspinning particle with results obtained in [25]. In that work, the GW fluxes were calculated from generic orbits of a nonspinning particle moving around a Kerr black hole using Teukolsky formalism with the fractional accuracy of the energy flux l, m-modes set to 10^{-6}.

We have compared our data with theirs for an equatorial orbit around a Kerr black hole with $\hat{a} = 0.3$, $p = 8.463649 = 1.7\hat{r}_{\rm ISCO}$ and $e = 0.3$. In particular, we have compared our energy fluxes $\mathcal{F}^{E\infty}_{lmn}$, $\mathcal{F}^{E\rm H}_{lmn}$ and amplitudes $\hat{C}^{\pm}_{lmn}$ with their data. In the top panel of Fig. 9, we plot the difference between our calculated fluxes $\mathcal{F}^{E\infty}_{lmn}$ and the fluxes $\mathcal{F}^{E\infty}_{lmn\rm DH}$ calculated in [25] normalized by the maximum of $\mathcal{F}^{E\infty}_{lmn}$ over n for each lm-mode

$$\delta\mathcal{F}^{E\infty}_{lmn} = \frac{\left|\mathcal{F}^{E\infty}_{lmn} - \mathcal{F}^{E\infty}_{lmn\rm DH}\right|}{\max\limits_{n_{\min}\le n\le n_{\max}}\mathcal{F}^{E\infty}_{lmn}}\ . \tag{C1}$$

We can see that for each lmn-mode the error is less than 10^{-6} of the maximal value for given l and m. In a similar way, we have compared the coefficients $\hat{C}^{+}_{lmn}$ using the quantity

$$\delta C^{+}_{lmn} = \frac{\left|\hat{C}^{+}_{lmn} - \hat{C}^{+}_{lmn\rm DH}\right|}{\max\limits_{n_{\min}\le n\le n_{\max}}\left|\hat{C}^{+}_{lmn}\right|}\ . \tag{C2}$$

The result of this comparison is shown in the bottom panel of Fig. 9. The normalized difference for the coefficients $\hat{C}^{+}_{lmn}$ is higher than in the flux comparison, because the flux is calculated from the second power of $\hat{C}^{+}_{lmn}$ and the error is thus relatively smaller. Similar comparison was calculated for the horizon fluxes $\mathcal{F}^{E\rm H}_{lmn}$ and $\hat{C}^{\pm}_{lmn}$. The result is shown in Fig. 10. Although the accuracy is less than 10^{-6} for some modes, the contribution from the horizon fluxes is smaller than from the fluxes to infinity and the overall accuracy remains higher.

Appendix D: Data tables

In this appendix we present data tables of the partial amplitudes $C^{\pm}_{lmn}$ (Tables II to V) for an orbit with orbital parameters $\hat{a} = 0.9$, $\sigma = -0.5$, $p = 12$, $e = 0.2$. The constants of motion and the fundamental frequencies calculated from the Eqs. (38), (39), (53) and (52) are

$$\hat{E} = 0.96191874964251768013472945840123336898 9\ldots$$
$$\hat{J}_z = 3.32224435878881667018396018111005668645 7\ldots$$
$$\hat{\Omega}_\phi = 0.02267178737574754852309392793191780 7$$
$$\hat{\Omega}_r = 0.01774444809231338856885032860919001 0$$

Only modes with $\left|C^{+}_{lmn}\right| > 10^{-9}$ are listed for $1 \leq m \leq 4$. The accuracy of the dominant modes should be at six significant digits, but for lower modes, the accuracy drops. This accuracy depends mostly on the accuracy of the radial function $R^{\pm}_{lmn}$ and the coordinates $t(\chi)$ and $\phi(\chi)$.

[1] P. Amaro-Seoane, H. Audley, S. Babak, J. Baker, E. Barausse, P. Bender, E. Berti, P. Binetruy, M. Born, D. Bortoluzzi, J. Camp, C. Caprini, *et al.*, Laser Interferometer Space Antenna, arXiv e-prints , arXiv:1702.00786 (2017), arXiv:1702.00786 [astro-ph.IM].

[2] S. Babak, J. Gair, A. Sesana, E. Barausse, C. F. Sopuerta, C. P. L. Berry, E. Berti, P. Amaro-Seoane, A. Petiteau, and A. Klein, Science with the space-based interferometer LISA. V. Extreme mass-ratio inspirals, Phys. Rev. D **95**, 103012 (2017).

[3] T. Hinderer and E. E. Flanagan, Two-timescale analysis of extreme mass ratio inspirals in Kerr spacetime: Orbital motion, Phys. Rev. D **78**, 064028 (2008).

[4] Y. Mino, M. Sasaki, M. Shibata, H. Tagoshi, and T. Tanaka, Black hole perturbation: Chapter 1, Prog.Theor.Phys.Suppl. **128**, 1 (1997), arXiv:gr-qc/9712057 [gr-qc].

[5] S. Akcay, S. R. Dolan, C. Kavanagh, J. Moxon, N. Warburton, and B. Wardell, Dissipation in extreme mass-ratio binaries with a spinning secondary, Phys. Rev. D **102**, 064013 (2020), arXiv:1912.09461 [gr-qc].

[6] M. D. Hartl, Dynamics of spinning test particles in Kerr space-time, Phys. Rev. **D67**, 024005 (2003), arXiv:gr-qc/0210042 [gr-qc].

[7] J. Frenkel, Die elektrodynamik des rotierenden elektrons, Zeitschrift fuer Physik **37**, 243 (1926).

[8] C. Lanczos, Ueber eine invariante formulierung der erhaltungssaetze in der allgemeinen relativitaetstheorie, Zeitschrift fuer Physik **59**, 514 (1930).

[9] M. Mathisson, Neue mechanik materieller systemes, Acta Phys.Polon. **6**, 163 (1937).

[10] M. Mathisson, Republication of: New mechanics of material systems, General Relativity and Gravitation **42**, 1011 (2010).

[11] A. Papapetrou, Spinning test particles in general relativity. 1., Proc.Roy.Soc.Lond. **A209**, 248 (1951).

[12] E. Corinaldesi and A. Papapetrou, Spinning test particles in general relativity. 2., Proc. Roy. Soc. Lond. **A209**, 259 (1951).

[13] W. Tulczyjew, Motion of multipole particles in general relativity theory, Acta Phys. Pol **18**, 393 (1959).

[14] W. Dixon, A covariant multipole formalism for extended test bodies in general relativity, Il Nuovo Cimento **34**, 317 (1964).

[15] W. Dixon, Dynamics of extended bodies in general relativity. II. Moments of the charge-current vector, Proc.Roy.Soc.Lond. **A319**, 509 (1970).

[16] W. Dixon, Dynamics of extended bodies in general relativity. I. Momentum and angular momentum, Proc.Roy.Soc.Lond. **A314**, 499 (1970).

[17] W. G. Dixon, Dynamics of extended bodies in general relativity. III. Equations of motion, Philosophical Transactions of the Royal Society of London A: Mathematical, Physical and Engineering Sciences **277**, 59 (1974).

[18] R. M. Wald, Gravitational spin interaction, Phys.Rev. **D6**, 406 (1972).

[19] O. Semerák, Spinning test particles in a Kerr field. 1., Mon.Not.Roy.Astron.Soc. **308**, 863 (1999).

[20] K. Kyrian and O. Semerák, Spinning test particles in a Kerr field, Mon.Not.Roy.Astron.Soc. **382**, 1922 (2007).

[21] D. Bini, G. Gemelli, and R. Ruffini, Spinning test particles in general relativity: Nongeodesic motion in the Reissner-Nordstrom space-time, Phys.Rev. **D61**, 064013 (2000).

[22] M. D. Hartl, A Survey of spinning test particle orbits in Kerr space-time, Phys. Rev. **D67**, 104023 (2003), arXiv:gr-qc/0302103 [gr-qc].

[23] M. Shibata and Y. Mino, Gravitational waves from a spinning particle plunging into a Kerr black hole, Physical Review D - Particles, Fields, Gravitation and Cosmology **58**, 3 (1998).

[24] Y. Mino, Perturbative approach to an orbital evolution around a supermassive black hole, Phys. Rev. D **67**, 084027 (2003).

[25] S. Drasco and S. A. Hughes, Gravitational wave snapshots of generic extreme mass ratio inspirals, Phys.Rev. **D73**, 024027 (2006), arXiv:gr-qc/0509101 [gr-qc].

[26] G. Faye, L. Blanchet, and A. Buonanno, Higher-order spin effects in the dynamics of compact binaries. I. Equations of motion, Phys.Rev. **D74**, 104033 (2006), arXiv:gr-qc/0605139 [gr-qc].

[27] J. Ehlers and E. Rudolph, Dynamics of extended bodies in general relativity center-of-mass description and quasirigidity, General Relativity and Gravitation **8**, 197 (1977).

TABLE II. List of partial amplitudes $C^{\pm}_{l1n}$ for an orbit with orbital parameters $\hat{a} = 0.9$, $\sigma = -0.5$, $p = 12$, $e = 0.2$.

l	m	n	$\mathrm{Re}\{C^{+}_{lmn}\}$	$\mathrm{Im}\{C^{+}_{lmn}\}$	$\mathrm{Re}\{C^{-}_{lmn}\}$	$\mathrm{Im}\{C^{-}_{lmn}\}$
2	1	-6	5.167891×10^{-10}	-1.467715×10^{-9}	4.763386×10^{-9}	7.282975×10^{-8}
2	1	-5	1.335467×10^{-9}	-4.271458×10^{-9}	9.287132×10^{-9}	3.018417×10^{-7}
2	1	-4	2.722364×10^{-9}	-1.043309×10^{-8}	-5.859804×10^{-10}	1.237186×10^{-6}
2	1	-3	3.539058×10^{-9}	-1.824696×10^{-8}	-1.435506×10^{-7}	5.014982×10^{-6}
2	1	-2	1.292175×10^{-9}	-1.244299×10^{-8}	-1.084857×10^{-6}	2.011327×10^{-5}
2	1	-1	2.025147×10^{-10}	4.098935×10^{-9}	-6.110857×10^{-6}	7.974254×10^{-5}
2	1	0	-8.063520×10^{-7}	-5.100353×10^{-6}	-4.159829×10^{-5}	4.294392×10^{-4}
2	1	1	-1.456843×10^{-6}	-6.201949×10^{-6}	-3.035062×10^{-5}	2.643207×10^{-4}
2	1	2	-1.100808×10^{-6}	-3.735099×10^{-6}	-1.503776×10^{-5}	1.150093×10^{-4}
2	1	3	-5.586369×10^{-7}	-1.633602×10^{-6}	-6.182375×10^{-6}	4.266183×10^{-5}
2	1	4	-2.230519×10^{-7}	-5.891306×10^{-7}	-2.272133×10^{-6}	1.441687×10^{-5}
2	1	5	-7.504175×10^{-8}	-1.849669×10^{-7}	-7.750262×10^{-7}	4.582582×10^{-6}
2	1	6	-2.190751×10^{-8}	-5.168866×10^{-8}	-2.508722×10^{-7}	1.395109×10^{-6}
2	1	7	-5.569707×10^{-9}	-1.283265×10^{-8}	-7.819832×10^{-8}	4.114092×10^{-7}
2	1	8	-1.192995×10^{-9}	-2.742169×10^{-9}	-2.371637×10^{-8}	1.184135×10^{-7}
3	1	-6	4.142460×10^{-10}	-9.135246×10^{-10}	1.272727×10^{-8}	1.107665×10^{-8}
3	1	-5	9.739033×10^{-10}	-2.513096×10^{-9}	4.917854×10^{-8}	4.243317×10^{-8}
3	1	-4	1.677799×10^{-9}	-5.375419×10^{-9}	1.880053×10^{-7}	1.599580×10^{-7}
3	1	-3	1.428809×10^{-9}	-6.372160×10^{-9}	7.093426×10^{-7}	5.919756×10^{-7}
3	1	-2	-3.968943×10^{-10}	3.427931×10^{-9}	2.633559×10^{-6}	2.144669×10^{-6}
3	1	0	-1.196768×10^{-7}	-6.663590×10^{-7}	4.292987×10^{-5}	3.279176×10^{-5}
3	1	1	2.815396×10^{-7}	1.022378×10^{-6}	2.784472×10^{-5}	2.044711×10^{-5}
3	1	2	3.393782×10^{-7}	9.521505×10^{-7}	1.277421×10^{-5}	8.974092×10^{-6}
3	1	3	1.975341×10^{-7}	4.622740×10^{-7}	4.983533×10^{-6}	3.333072×10^{-6}
3	1	4	8.151849×10^{-8}	1.663691×10^{-7}	1.766440×10^{-6}	1.119246×10^{-6}
3	1	5	2.659713×10^{-8}	4.876757×10^{-8}	5.874042×10^{-7}	3.508458×10^{-7}
3	1	6	7.014470×10^{-9}	1.180811×10^{-8}	1.866093×10^{-7}	1.045302×10^{-7}
3	1	7	1.392344×10^{-9}	2.201409×10^{-9}	5.728150×10^{-8}	2.993285×10^{-8}
4	1	0	-6.611595×10^{-10}	-3.354890×10^{-9}	1.778200×10^{-6}	-9.269538×10^{-7}
4	1	1	3.327272×10^{-9}	1.078814×10^{-8}	1.293272×10^{-6}	-7.573044×10^{-7}
4	1	2	5.489708×10^{-9}	1.347987×10^{-8}	6.508828×10^{-7}	-4.275336×10^{-7}
4	1	3	3.989895×10^{-9}	8.004271×10^{-9}	2.704943×10^{-7}	-1.991900×10^{-7}
4	1	4	1.899103×10^{-9}	3.250073×10^{-9}	9.959920×10^{-8}	-8.225436×10^{-8}
4	1	5	6.514413×10^{-10}	9.782216×10^{-10}	3.367305×10^{-8}	-3.122972×10^{-8}
5	1	1	2.035370×10^{-9}	6.185810×10^{-9}	-1.963261×10^{-8}	-1.023901×10^{-7}
5	1	3	-1.411206×10^{-9}	-2.593480×10^{-9}	-8.203217×10^{-9}	-2.319941×10^{-8}
5	1	4	-1.152085×10^{-9}	-1.783264×10^{-9}	-3.940505×10^{-9}	-8.863485×10^{-9}

[28] V. Witzany, J. Steinhoff, and G. Lukes-Gerakopoulos, Hamiltonians and canonical coordinates for spinning particles in curved space-time, Classical and Quantum Gravity **36**, 075003 (2019), arXiv:1808.06582 [gr-qc].

[29] G. A. Piovano, A. Maselli, and P. Pani, Extreme mass ratio inspirals with spinning secondary: A detailed study of equatorial circular motion, Physical Review D **102**, 10.1103/PhysRevD.102.024041 (2020), arXiv:2004.02654.

[30] E. Harms, G. Lukes-Gerakopoulos, S. Bernuzzi, and A. Nagar, Asymptotic gravitational wave fluxes from a spinning particle in circular equatorial orbits around a rotating black hole, Phys. Rev. **D93**, 044015 (2016), arXiv:1510.05548 [gr-qc].

[31] W. Schmidt, Celestial mechanics in Kerr spacetime, Classical and Quantum Gravity **19**, 2743 (2002), arXiv:0202090 [gr-qc].

[32] R. Fujita and W. Hikida, Analytical solutions of bound timelike geodesic orbits in Kerr spacetime, Classical and Quantum Gravity **26**, 135002 (2009), arXiv:0906.1420 [gr-qc].

[33] E. Hackmann, C. Laemmerzahl, Y. N. Obukhov, D. Puetzfeld, and I. Schaffer, Motion of spinning test bodies in Kerr spacetime, Phys.Rev. **D90**, 064035 (2014), arXiv:1408.1773 [gr-qc].

[34] G. Lukes-Gerakopoulos, J. Seyrich, and D. Kunst, Investigating spinning test particles: spin supplementary conditions and the Hamiltonian formalism, Phys.Rev. **D90**, 104019 (2014), arXiv:1409.4314 [gr-qc].

[35] S. A. Teukolsky, Perturbations of a rotating black hole. 1. Fundamental equations for gravitational electromagnetic and neutrino field perturbations, Astrophys. J. **185**, 635 (1973).

[36] Black Hole Perturbation Toolkit, (bhptoolkit.org).

[37] K. Glampedakis and D. Kennefick, Zoom and whirl: Eccentric equatorial orbits around spinning black holes and their evolution under gravitational radiation reaction, Phys.Rev. **D66**, 044002 (2002), arXiv:gr-qc/0203086 [gr-

TABLE III. List of partial amplitudes $C^{\pm}_{l2n}$ for the same orbit as in Table II.

l	m	n	Re$\{C^{+}_{lmn}\}$	Im$\{C^{+}_{lmn}\}$	Re$\{C^{-}_{lmn}\}$	Im$\{C^{-}_{lmn}\}$
2	2	-4	-1.646357×10^{-9}	-2.613368×10^{-10}	2.350051×10^{-8}	1.728856×10^{-9}
2	2	-3	-5.171809×10^{-9}	-3.499305×10^{-10}	1.187803×10^{-7}	1.441103×10^{-8}
2	2	-2	1.563190×10^{-7}	-1.253110×10^{-8}	2.380182×10^{-6}	3.978260×10^{-7}
2	2	-1	-4.066035×10^{-5}	6.801245×10^{-6}	-9.742181×10^{-5}	-2.076711×10^{-5}
2	2	0	3.858210×10^{-4}	-8.824264×10^{-5}	5.307355×10^{-4}	1.379732×10^{-4}
2	2	1	3.970205×10^{-4}	-1.089118×10^{-4}	4.287891×10^{-4}	1.314682×10^{-4}
2	2	2	2.406528×10^{-4}	-7.404687×10^{-5}	2.175548×10^{-4}	7.698517×10^{-5}
2	2	3	1.138352×10^{-4}	-3.764006×10^{-5}	8.960040×10^{-5}	3.602218×10^{-5}
2	2	4	4.644175×10^{-5}	-1.599176×10^{-5}	3.266409×10^{-5}	1.474535×10^{-5}
2	2	5	1.715753×10^{-5}	-5.997531×10^{-6}	1.098058×10^{-5}	5.516737×10^{-6}
2	2	6	5.901325×10^{-6}	-2.047506×10^{-6}	3.482534×10^{-6}	1.934221×10^{-6}
2	2	7	1.922706×10^{-6}	-6.480880×10^{-7}	1.056831×10^{-6}	6.456290×10^{-7}
2	2	8	6.002221×10^{-7}	-1.923652×10^{-7}	3.097499×10^{-7}	2.073768×10^{-7}
2	2	9	1.810496×10^{-7}	-5.403652×10^{-8}	8.825836×10^{-8}	6.461080×10^{-8}
2	2	10	5.321319×10^{-8}	-1.460369×10^{-8}	2.456752×10^{-8}	1.967628×10^{-8}
2	2	11	1.545017×10^{-8}	-3.880442×10^{-9}	6.695307×10^{-9}	5.913216×10^{-9}
2	2	12	4.635476×10^{-9}	-9.455299×10^{-10}	1.752615×10^{-9}	1.779985×10^{-9}
2	2	13	1.168229×10^{-9}	-1.713718×10^{-10}	4.702090×10^{-10}	4.920492×10^{-10}
3	2	-1	-2.396250×10^{-7}	5.060581×10^{-8}	1.890430×10^{-6}	-9.847625×10^{-7}
3	2	0	3.649975×10^{-6}	-1.111405×10^{-6}	3.187469×10^{-5}	-1.653879×10^{-5}
3	2	1	4.889631×10^{-6}	-1.883465×10^{-6}	3.015258×10^{-5}	-1.566972×10^{-5}
3	2	2	3.536010×10^{-6}	-1.615521×10^{-6}	1.793053×10^{-5}	-9.383274×10^{-6}
3	2	3	1.888741×10^{-6}	-9.843758×10^{-7}	8.495665×10^{-6}	-4.500460×10^{-6}
3	2	4	8.370027×10^{-7}	-4.845333×10^{-7}	3.503785×10^{-6}	-1.888329×10^{-6}
3	2	5	3.260656×10^{-7}	-2.055320×10^{-7}	1.314468×10^{-6}	-7.241796×10^{-7}
3	2	6	1.154284×10^{-7}	-7.798475×10^{-8}	4.601592×10^{-7}	-2.603261×10^{-7}
3	2	7	3.790759×10^{-8}	-2.708873×10^{-8}	1.527743×10^{-7}	-8.912589×10^{-8}
3	2	8	1.170216×10^{-8}	-8.743846×10^{-9}	4.863519×10^{-8}	-2.937305×10^{-8}
3	2	9	3.415775×10^{-9}	-2.649605×10^{-9}	1.496262×10^{-8}	-9.389021×10^{-9}
3	2	10	9.324112×10^{-10}	-7.609938×10^{-10}	4.474358×10^{-9}	-2.926757×10^{-9}
4	2	-1	-4.819515×10^{-8}	1.102927×10^{-8}	1.244599×10^{-7}	-4.205354×10^{-7}
4	2	0	1.025155×10^{-6}	-3.437785×10^{-7}	1.114267×10^{-6}	-4.056764×10^{-6}
4	2	1	3.046028×10^{-7}	-1.313240×10^{-7}	9.753818×10^{-7}	-3.881701×10^{-6}
4	2	2	-1.647969×10^{-7}	8.570891×10^{-8}	5.323946×10^{-7}	-2.357344×10^{-6}
4	2	3	-2.043076×10^{-7}	1.234177×10^{-7}	2.267391×10^{-7}	-1.142665×10^{-6}
4	2	4	-1.208388×10^{-7}	8.265904×10^{-8}	8.153936×10^{-8}	-4.822614×10^{-7}
4	2	5	-5.386171×10^{-8}	4.095780×10^{-8}	2.551314×10^{-8}	-1.851227×10^{-7}
4	2	6	-2.029400×10^{-8}	1.691104×10^{-8}	6.938177×10^{-9}	-6.628891×10^{-8}
4	2	7	-6.788401×10^{-9}	6.130268×10^{-9}	1.566483×10^{-9}	-2.250158×10^{-8}
4	2	8	-2.068407×10^{-9}	2.005378×10^{-9}	2.389387×10^{-10}	-7.319933×10^{-9}
5	2	0	7.342146×10^{-9}	-2.652971×10^{-9}	-9.489133×10^{-8}	-1.219765×10^{-7}
5	2	1	1.759299×10^{-9}	-8.273581×10^{-10}	-1.010641×10^{-7}	-1.194663×10^{-7}
5	2	2	-3.657312×10^{-9}	2.102053×10^{-9}	-7.026352×10^{-8}	-7.612572×10^{-8}
5	2	3	-4.181570×10^{-9}	2.831232×10^{-9}	-3.875359×10^{-8}	-3.833430×10^{-8}
5	2	4	-2.657863×10^{-9}	2.069513×10^{-9}	-1.841952×10^{-8}	-1.655902×10^{-8}
5	2	5	-1.274114×10^{-9}	1.121653×10^{-9}	-7.882070×10^{-9}	-6.404217×10^{-9}

qc].

[38] P. L. Chrzanowski, Vector potential and metric perturbations of a rotating black hole, Physical Review D **11**, 2042 (1975).

[39] S. Teukolsky and W. Press, Perturbations of a rotating black hole. III - Interaction of the hole with gravitational and electromagnetic radiation, Astrophys.J. **193**, 443 (1974).

[40] E. Harms, S. Bernuzzi, and B. Brügmann, Numerical solution of the 2+1 Teukolsky equation on a hyperboloidal and horizon penetrating foliation of Kerr and application to late-time decays, Class.Quant.Grav. **30**, 115013 (2013), arXiv:1301.1591 [gr-qc].

[41] E. Harms, S. Bernuzzi, A. Nagar, and A. Zenginoglu, A new gravitational wave generation algorithm for particle perturbations of the Kerr spacetime, Class. Quant. Grav. **31**, 245004 (2014), arXiv:1406.5983 [gr-qc].

TABLE IV. List of partial amplitudes $C^{\pm}_{l3n}$ for the same orbit as in Table II.

l	m	n	Re$\{C^{+}_{lmn}\}$	Im$\{C^{+}_{lmn}\}$	Re$\{C^{-}_{lmn}\}$	Im$\{C^{-}_{lmn}\}$
3	3	-3	-1.004997×10^{-9}	-7.760638×10^{-9}	3.558851×10^{-9}	1.588115×10^{-8}
3	3	-2	4.716853×10^{-7}	2.003985×10^{-6}	-3.882412×10^{-7}	-1.922022×10^{-6}
3	3	-1	-1.300363×10^{-5}	-4.030524×10^{-5}	4.310309×10^{-6}	2.366988×10^{-5}
3	3	0	5.305191×10^{-5}	1.331426×10^{-4}	-9.633994×10^{-6}	-5.865711×10^{-5}
3	3	1	8.900651×10^{-5}	1.911136×10^{-4}	-1.135235×10^{-5}	-7.650771×10^{-5}
3	3	2	7.612663×10^{-5}	1.447861×10^{-4}	-7.199807×10^{-6}	-5.358218×10^{-5}
3	3	3	4.744130×10^{-5}	8.189333×10^{-5}	-3.482019×10^{-6}	-2.851315×10^{-5}
3	3	4	2.434203×10^{-5}	3.884905×10^{-5}	-1.438478×10^{-6}	-1.289482×10^{-5}
3	3	5	1.092213×10^{-5}	1.635785×10^{-5}	-5.363338×10^{-7}	-5.227212×10^{-6}
3	3	6	4.438184×10^{-6}	6.316315×10^{-6}	-1.863735×10^{-7}	-1.957612×10^{-6}
3	3	7	1.670164×10^{-6}	2.283624×10^{-6}	-6.164127×10^{-8}	-6.902951×10^{-7}
3	3	8	5.909836×10^{-7}	7.840535×10^{-7}	-1.969217×10^{-8}	-2.321446×10^{-7}
3	3	9	1.988825×10^{-7}	2.581659×10^{-7}	-6.141824×10^{-9}	-7.513658×10^{-8}
3	3	10	6.409344×10^{-8}	8.217920×10^{-8}	-1.884840×10^{-9}	-2.356231×10^{-8}
3	3	11	2.020696×10^{-8}	2.531856×10^{-8}	-5.716907×10^{-10}	-7.198380×10^{-9}
3	3	12	6.131692×10^{-9}	7.692513×10^{-9}	-1.717137×10^{-10}	-2.149742×10^{-9}
3	3	13	1.679868×10^{-9}	2.245018×10^{-9}	-5.246898×10^{-11}	-6.287407×10^{-10}
4	3	-2	2.685489×10^{-9}	1.028336×10^{-8}	-2.488432×10^{-8}	-2.373154×10^{-8}
4	3	-1	-1.147948×10^{-7}	-3.145041×10^{-7}	1.950153×10^{-7}	1.857823×10^{-7}
4	3	0	6.392598×10^{-7}	1.390373×10^{-6}	-2.124982×10^{-6}	-2.014665×10^{-6}
4	3	1	1.316270×10^{-6}	2.399175×10^{-6}	-2.891155×10^{-6}	-2.717792×10^{-6}
4	3	2	1.323400×10^{-6}	2.090102×10^{-6}	-2.242899×10^{-6}	-2.082785×10^{-6}
4	3	3	9.395536×10^{-7}	1.315492×10^{-6}	-1.324312×10^{-6}	-1.210354×10^{-6}
4	3	4	5.364249×10^{-7}	6.771760×10^{-7}	-6.609932×10^{-7}	-5.923846×10^{-7}
4	3	5	2.629183×10^{-7}	3.032417×10^{-7}	-2.939162×10^{-7}	-2.573399×10^{-7}
4	3	6	1.149548×10^{-7}	1.224621×10^{-7}	-1.200513×10^{-7}	-1.023073×10^{-7}
4	3	7	4.595850×10^{-8}	4.564687×10^{-8}	-4.593515×10^{-8}	-3.795772×10^{-8}
4	3	8	1.708722×10^{-8}	1.595567×10^{-8}	-1.668689×10^{-8}	-1.331898×10^{-8}
4	3	9	5.977998×10^{-9}	5.284213×10^{-9}	-5.810556×10^{-9}	-4.462024×10^{-9}
4	3	10	1.986521×10^{-9}	1.675756×10^{-9}	-1.953240×10^{-9}	-1.437145×10^{-9}
5	3	-2	7.907117×10^{-10}	2.853014×10^{-9}	-6.478361×10^{-9}	-3.587094×10^{-10}
5	3	-1	-4.398249×10^{-8}	-1.123248×10^{-7}	1.317613×10^{-8}	5.278265×10^{-10}
5	3	0	3.218695×10^{-7}	6.453677×10^{-7}	-3.389273×10^{-7}	-7.785256×10^{-9}
5	3	1	3.455801×10^{-7}	5.738309×10^{-7}	-4.536955×10^{-7}	-1.859315×10^{-9}
5	3	2	1.711208×10^{-7}	2.430505×10^{-7}	-3.512562×10^{-7}	5.820222×10^{-9}
5	3	3	3.896109×10^{-8}	4.837181×10^{-8}	-2.071569×10^{-7}	8.090550×10^{-9}
5	3	4	-1.094717×10^{-8}	-1.206677×10^{-8}	-1.031213×10^{-7}	6.536982×10^{-9}
5	3	5	-1.726012×10^{-8}	-1.709111×10^{-8}	-4.563110×10^{-8}	4.089656×10^{-9}
5	3	6	-1.143495×10^{-8}	-1.026788×10^{-8}	-1.850203×10^{-8}	2.179864×10^{-9}
5	3	7	-5.747543×10^{-9}	-4.714943×10^{-9}	-7.009564×10^{-9}	1.037791×10^{-9}
5	3	8	-2.468744×10^{-9}	-1.860621×10^{-9}	-2.514576×10^{-9}	4.537261×10^{-10}
5	3	9	-9.509418×10^{-10}	-6.710533×10^{-10}	-8.623420×10^{-10}	1.854954×10^{-10}
6	3	0	2.515496×10^{-9}	4.721206×10^{-9}	-8.984566×10^{-9}	9.229790×10^{-9}
6	3	1	3.001379×10^{-9}	4.619049×10^{-9}	-1.151088×10^{-8}	1.262076×10^{-8}
6	3	2	1.275195×10^{-9}	1.660290×10^{-9}	-9.081402×10^{-9}	1.067007×10^{-8}
6	3	4	-7.270147×10^{-10}	-7.155788×10^{-10}	-2.769497×10^{-9}	3.789745×10^{-9}

[42] A. Nagar, E. Harms, S. Bernuzzi, and A. Zenginoglu, The antikick strikes back: recoil velocities for nearly-extremal binary black hole mergers in the test-mass limit, Phys.Rev. **D90**, 124086 (2014), arXiv:1407.5033 [gr-qc].

[43] M. Campanelli, G. Khanna, P. Laguna, J. Pullin, and M. P. Ryan, Perturbations of the Kerr space-time in horizon penetrating coordinates, Class.Quant.Grav. **18**, 1543 (2001), arXiv:gr-qc/0010034 [gr-qc].

[44] P. A. Sundararajan, G. Khanna, and S. A. Hughes, Towards adiabatic waveforms for inspiral into Kerr black holes: I. A new model of the source for the time domain perturbation equation, Phys. Rev. **D76**, 104005 (2007), arXiv:gr-qc/0703028.

[45] J. Waldén, On the approximation of singular source terms in differential equations, Numerical Methods for Partial Differential Equations **15**, 503 (1999).

TABLE V. List of partial amplitudes $C^{\pm}_{l4n}$ for the same orbit as in Table II.

l	m	n	Re$\{C^{+}_{lmn}\}$	Im$\{C^{+}_{lmn}\}$	Re$\{C^{-}_{lmn}\}$	Im$\{C^{-}_{lmn}\}$
4	4	-3	1.030232×10^{-7}	-2.987138×10^{-8}	2.594938×10^{-8}	-1.364431×10^{-8}
4	4	-2	-3.167459×10^{-6}	1.235891×10^{-6}	-5.564356×10^{-7}	2.832212×10^{-7}
4	4	-1	2.493681×10^{-5}	-1.203041×10^{-5}	3.475072×10^{-6}	-1.718247×10^{-6}
4	4	0	-3.730632×10^{-5}	2.123841×10^{-5}	-4.314063×10^{-6}	2.079650×10^{-6}
4	4	1	-8.092430×10^{-5}	5.277164×10^{-5}	-9.355450×10^{-6}	4.413471×10^{-6}
4	4	2	-7.619630×10^{-5}	5.574275×10^{-5}	-8.650047×10^{-6}	4.008745×10^{-6}
4	4	3	-5.089773×10^{-5}	4.112353×10^{-5}	-5.704990×10^{-6}	2.607445×10^{-6}
4	4	4	-2.773635×10^{-5}	2.444478×10^{-5}	-3.087320×10^{-6}	1.397110×10^{-6}
4	4	5	-1.316378×10^{-5}	1.252512×10^{-5}	-1.461746×10^{-6}	6.575647×10^{-7}
4	4	6	-5.647802×10^{-6}	5.750074×10^{-6}	-6.277339×10^{-7}	2.818301×10^{-7}
4	4	7	-2.243064×10^{-6}	2.424266×10^{-6}	-2.501089×10^{-7}	1.125120×10^{-7}
4	4	8	-8.381942×10^{-7}	9.546192×10^{-7}	-9.388208×10^{-8}	4.248119×10^{-8}
4	4	9	-2.980940×10^{-7}	3.554223×10^{-7}	-3.356380×10^{-8}	1.533473×10^{-8}
4	4	10	-1.020168×10^{-7}	1.261960×10^{-7}	-1.152115×10^{-8}	5.334443×10^{-9}
4	4	11	-3.378335×10^{-8}	4.299271×10^{-8}	-3.820558×10^{-9}	1.799074×10^{-9}
4	4	12	-1.082123×10^{-8}	1.416903×10^{-8}	-1.229874×10^{-9}	5.909993×10^{-10}
4	4	13	-2.922436×10^{-9}	4.787284×10^{-9}	-3.860830×10^{-10}	1.899575×10^{-10}
4	4	14	-1.034014×10^{-9}	1.406801×10^{-9}	-1.182908×10^{-10}	5.976449×10^{-11}
5	4	-2	-1.875445×10^{-8}	7.933698×10^{-9}	-3.023775×10^{-9}	5.361340×10^{-9}
5	4	-1	1.928140×10^{-7}	-1.021033×10^{-7}	3.348964×10^{-8}	-5.960966×10^{-8}
5	4	0	-3.581359×10^{-7}	2.267803×10^{-7}	-1.071155×10^{-7}	1.920896×10^{-7}
5	4	1	-8.885218×10^{-7}	6.538335×10^{-7}	-2.097613×10^{-7}	3.803623×10^{-7}
5	4	2	-9.357029×10^{-7}	7.847094×10^{-7}	-2.025645×10^{-7}	3.727819×10^{-7}
5	4	3	-6.840485×10^{-7}	6.445750×10^{-7}	-1.413811×10^{-7}	2.650546×10^{-7}
5	4	4	-4.007050×10^{-7}	4.196831×10^{-7}	-8.077376×10^{-8}	1.548634×10^{-7}
5	4	5	-2.013663×10^{-7}	2.324005×10^{-7}	-4.013179×10^{-8}	7.900370×10^{-8}
5	4	6	-9.029619×10^{-8}	1.140120×10^{-7}	-1.795737×10^{-8}	3.645112×10^{-8}
5	4	7	-3.705473×10^{-8}	5.087027×10^{-8}	-7.399921×10^{-9}	1.555748×10^{-8}
5	4	8	-1.416211×10^{-8}	2.102079×10^{-8}	-2.851190×10^{-9}	6.238100×10^{-9}
5	4	9	-5.102297×10^{-9}	8.148365×10^{-9}	-1.038250×10^{-9}	2.376195×10^{-9}
5	4	10	-1.757070×10^{-9}	2.997933×10^{-9}	-3.601133×10^{-10}	8.670269×10^{-10}
5	4	11	-5.830642×10^{-10}	1.054002×10^{-9}	-1.196530×10^{-10}	3.049759×10^{-10}
6	4	-2	-8.666245×10^{-9}	3.877093×10^{-9}	1.065444×10^{-10}	7.051137×10^{-10}
6	4	-1	1.052404×10^{-7}	-5.945050×10^{-8}	-9.799602×10^{-10}	-5.966157×10^{-9}
6	4	0	-2.657233×10^{-7}	1.812153×10^{-7}	4.508872×10^{-9}	2.519233×10^{-8}
6	4	1	-3.867479×10^{-7}	3.097707×10^{-7}	9.373712×10^{-9}	4.799473×10^{-8}
6	4	2	-2.693825×10^{-7}	2.488393×10^{-7}	9.932362×10^{-9}	4.656984×10^{-8}
6	4	3	-1.291963×10^{-7}	1.359028×10^{-7}	7.665334×10^{-9}	3.290682×10^{-8}
6	4	4	-4.680907×10^{-8}	5.556090×10^{-8}	4.860330×10^{-9}	1.910878×10^{-8}
6	4	5	-1.257609×10^{-8}	1.673105×10^{-8}	2.686650×10^{-9}	9.678828×10^{-9}
6	4	6	-1.863538×10^{-9}	2.764762×10^{-9}	1.340226×10^{-9}	4.427345×10^{-9}
6	4	7	4.381872×10^{-10}	-7.223455×10^{-10}	6.169229×10^{-10}	1.870247×10^{-9}
6	4	8	5.248114×10^{-10}	-9.583384×10^{-10}	2.660845×10^{-10}	7.408825×10^{-10}
7	4	0	-1.681887×10^{-9}	1.221218×10^{-9}	8.419294×10^{-10}	6.223333×10^{-10}
7	4	1	-2.629027×10^{-9}	2.263383×10^{-9}	1.494752×10^{-9}	1.045267×10^{-9}
7	4	2	-1.825947×10^{-9}	1.832837×10^{-9}	1.524851×10^{-9}	1.004491×10^{-9}
7	4	3	-7.525698×10^{-10}	8.711420×10^{-10}	1.156468×10^{-9}	7.142646×10^{-10}

[46] E. Harms, G. Lukes-Gerakopoulos, S. Bernuzzi, and A. Nagar, Spinning test body orbiting around a Schwarzschild black hole: Circular dynamics and gravitational-wave fluxes, Phys. Rev. **D94**, 104010 (2016), arXiv:1609.00356 [gr-qc].

[47] G. Lukes-Gerakopoulos, E. Harms, S. Bernuzzi, and A. Nagar, Spinning test body orbiting around a Kerr black hole: Circular dynamics and gravitational-wave fluxes, Phys.Rev. D **96**, 064051 (2017), arXiv:1707.07537 [gr-qc].

[48] A. Nagar, F. Messina, C. Kavanagh, G. Lukes-Gerakopoulos, N. Warburton, S. Bernuzzi, and E. Harms, Factorization and resummation: A new paradigm to improve gravitational wave amplitudes. III. The spinning test-body terms, Phys. Rev. D **100**, 104056 (2019).

[49] M. Sasaki and H. Tagoshi, Analytic black hole perturbation approach to gravitational radiation, Living Rev.Rel. **6**, 6 (2003), arXiv:gr-qc/0306120 [gr-qc].

[50] E. W. Leaver, An Analytic representation for the quasi normal modes of Kerr black holes, Proc. Roy. Soc. Lond. **A402**, 285 (1985).

[51] V. Skoupý and G. Lukes-Gerakopoulos, Gravitational wave templates from Extreme Mass Ratio Inspirals, arXiv e-prints , arXiv:2101.04533 (2021), arXiv:2101.04533 [gr-qc].

A.2 Adiabatic equatorial inspirals of a spinning body into a Kerr black hole

This Attachment contains the paper *Adiabatic equatorial inspirals of a spinning body into a Kerr black hole* [40] published in Physical Review D. This version corrects some typos in the published version.

Adiabatic equatorial inspirals of a spinning body into a Kerr black hole

Viktor Skoupý[1,2] and Georgios Lukes-Gerakopoulos[1]
[1] *Astronomical Institute of the Czech Academy of Sciences, Boční II 1401/1a, CZ-141 00 Prague, Czech Republic and*
[2] *Institute of Theoretical Physics, Faculty of Mathematics and Physics, Charles University, CZ-180 00 Prague, Czech Republic*

The detection of gravitational waves from extreme mass ratio inspirals (EMRIs) by the future space-based gravitational-wave detectors demands the generation of accurate enough waveform templates. Since the spin of the smaller secondary body cannot be neglected for the detection and parameter estimation of EMRIs, we study its influence on the phase of the gravitational waves from EMRIs with a spinning secondary. We focus on generic eccentric equatorial orbits around a Kerr black hole. To model the spinning secondary object, we use the Mathisson-Papapetrou-Dixon equations in the pole-dipole approximation. Furthermore, we linearize in spin the orbital variables and the gravitational-wave fluxes from the respective orbits. We obtain these fluxes by using the Teukolsky formalism in the frequency domain. We derive the evolution equations for the spin-induced corrections to the adiabatic evolution of an inspiral. Finally, through their numerical integration we find the gravitational-wave phase shift between an inspiral of a spinning and a nonspinning body.

I. INTRODUCTION

Extreme mass ratio inspirals (EMRIs) are promising sources for future space-based gravitational-wave (GW) detectors such as the Laser Interferometer Space Antenna (LISA) [1, 2]. These systems consist of a primary supermassive black hole and a secondary, much lighter compact object such as a neutron star or a black hole. In an EMRI, the mass ratio $q = \mu/M$ of the secondary mass μ and the primary mass M is expected to lie between 10^{-7} and 10^{-4}. Because of the gravitational radiation reaction, the secondary object is slowly inspiraling into the primary while it radiates gravitational waves. The detection of EMRIs will provide the opportunity to study strong gravitational fields around supermassive black holes lying at the center of galaxies and to test general relativity.

The millihertz GW bandwidth that EMRIs are emitting is expected to be rich in GW sources. To overcome the fact that signals from various sources will overlap during their detection by LISA, matched filtering is planned to be employed; i.e., the detected signal will be compared with a large number of GW templates covering the estimated parameter space [1]. The use of templates will not only allow the detection of EMRI signals, but it will also be employed for the parameter estimation of these systems. To get these estimations adequately enough, we need to generate waveform templates whose phases are accurate up to fractions of radians.

To achieve such accuracy, a series of techniques can be employed. The backbone of them is that the system is treated as the motion of a secondary object in the background spacetime of the primary object. Hence, to model the GW phase, we need first to find the trajectory of the secondary z^μ. The secondary is perturbing the background spacetime, and the gravitational self-force drives the secondary away from the trajectory which it would follow without this perturbation.[1] To find this self-force, perturbation theory is used. Namely, the exact metric is expanded in the terms of the mass ratio as

$$g^{\text{exact}}_{\mu\nu} = g_{\mu\nu} + h^{(1)}_{\mu\nu} + h^{(2)}_{\mu\nu} + \mathcal{O}\left(q^3\right) , \tag{1}$$

where $g_{\mu\nu}$ is the background metric, which in our case is the Kerr one, $h^{(1)}_{\mu\nu} = \mathcal{O}(q)$ is the first-order perturbation and $h^{(2)}_{\mu\nu} = \mathcal{O}(q)^2$ is the second-order perturbation. $h^{(n)}_{\mu\nu}$ are found by expanding the Einstein equations in the mass ratio with the source constructed from the secondary body and solving order by order [3, 4]. The parts of the metric perturbation are then used to construct the first- and second-order self-force

$$\frac{\mathrm{D}^2 z^\mu}{\mathrm{d}\tau^2} = q f^\mu_{(1)} + q^2 f^\mu_{(2)} + \mathcal{O}\left(\sigma^3\right) , \tag{2}$$

where τ is the proper time and $f^\mu_{(1)}$ is constructed from $h^{(1)}_{\mu\nu}$ and the secondary's spin-curvature coupling, while $f^\mu_{(2)}$ is constructed from $h^{(2)}_{\mu\nu}$ [4–6].

Because the radiation reaction is of the order $\mathcal{O}(q)$, its effects act on a much larger timescale than is the orbital timescale. Actually, the secondary makes $\mathcal{O}\left(q^{-1}\right)$ cycles around the primary due to the radiation reaction, before it plunges into the primary. Thanks to this timescale difference, we can use the so-called *two-timescale approximation* [7]. In this approximation, the coordinates are transformed to anglelike variables q_μ, which can be ex-

[1] This unperturbed trajectory is a geodesic orbit for a nonspinning secondary, while for a spinning secondary, the trajectory can be provided by the Mathisson-Papapetrou-Dixon equations.

panded in the mass ratio as[2]

$$q_\mu(t) = \frac{1}{q} q_\mu^{(0)}(q\,t) + q_\mu^{(1)}(q\,t) + \mathcal{O}(q)\,, \tag{3}$$

where t is the evolution parameter. The first term $q_\mu^{(0)}(q\,t)$ is called the *adiabatic* term and can be calculated only from the time-averaged dissipative part of the first-order self-force. The second term $q_\mu^{(1)}(q\,t)$, which is called the first-order *postadiabatic* term, is constructed from the oscillating dissipative and conservative parts of the first-order self-force, the averaged dissipative part of the second-order self-force and the contribution from the spin of the secondary body. These angle variables are directly related to the phases of the GW. The adiabatic term for generic orbits around a Kerr black hole was calculated only recently [8–11], and, so far, the postadiabatic term with the first-order self-force was calculated for a spinning secondary only for quasicircular orbits in the Schwarzschild spacetime [12] and for a nonspinning secondary for equatorial orbits in the Schwarzschild [13] and Kerr [14] spacetime, while the full first- and second-order self-force for quasicircular orbits in the Schwarzschild spacetime was calculated in Ref. [15].

The error in the adiabatic term must be less than the mass ratio to obtain subradian precision. It has been proven for a nonspinning secondary [16, 17], but also for a spinning secondary [18], that the time-averaged dissipative part of the self-force can be reconstructed from the time-averaged energy and angular momentum fluxes calculated at infinity and at the horizon of the primary black hole. Therefore, for the calculations in the adiabatic order, we do not need to calculate the perturbation $h_{\mu\nu}^{(1)}$ in the vicinity of the secondary body, but we need only to find the aforementioned GW fluxes. These fluxes were calculated for generic orbits of non-spining bodies around a Kerr black hole in Ref. [19], for circular orbits of spinning bodies around a Schwarzschild and a Kerr black hole in Refs. [18, 20–24], and, finally, for eccentric equatorial orbits of spinning particles around a Kerr black hole [25].

A postadiabatic term is of the order of radians and, thus, cannot be neglected. Hence, since the spin of the secondary contributes to the postadiabatic term, we have to take it into account. In the case of compact objects, like black holes and neutron stars, a pole-dipole approximation is considered to be sufficient, and all the higher multipoles of the body can be ignored. The scalars describing a pole-dipole secondary are its mass μ and the measure of its spin S. In the EMRI framework, instead of S we can gain more insight about the contribution of the secondary spin by defining its dimensionless counterpart $\sigma = S/(\mu M)$. For example, if we consider the secondary black hole as an extreme Kerr black hole, we have that $S = \mu^2$ leading to $\sigma = q$, which suggests that σ is of the order of the mass ratio, i.e., $\sigma \lesssim q \ll 1$. This fact, actually, allows us to ignore all the terms with higher powers in σ and focus on the linearized in spin contributions to the inspiral.[3] Additionally, it is easier to fill the parameter space with precomputed EMRI waveform templates by linearizing in spin, since the spin contribution appears in this case as σ times a coefficient independent of the exact value of the spin. This implies that we avoid the calculation of each quantity for several values of the spin. Moreover, there are evidence [27, 28] suggesting that the pole-dipole approximation breaks down for higher than the quadratic order in spin.

Hence, this work focuses on the influence of the secondary spin on the evolution of an inspiral moving on the equatorial plane of a Kerr black hole, when the calculations are restricted to the linear order in spin. Having confined our study on the equatorial plane of a Kerr black hole allows us to parametrize the orbital evolution by the energy E and the z component of the angular momentum J_z of the system. The energy and the angular momentum fluxes, which reach infinity and the horizon, were already derived in Ref. [25]. In this work, we linearize these fluxes to calculate the adiabatic inspiral and the linear in spin part of the GW phase, i.e., the phase shift between the adiabatic inspiral of a spinning secondary and a nonspinning secondary. In particular, this phase shift $\delta\Phi_\mu$ can be found by linearizing in spin of the phase, i.e.,

$$\Phi_\mu = \frac{1}{q}\Phi_\mu^{(0)} + \frac{\sigma}{q}\delta\Phi_\mu + \mathcal{O}\big(\sigma^2/q\big)\,. \tag{4}$$

Note that in this work we neglect the other postadiabatic terms, the evolution of the primary mass and its spin due to the absorption of the GWs through the horizon as well as the evolution of the spin magnitude σ.

The rest of this paper is organized as follows. Section II describes the dynamics of a spinning body in a Kerr spacetime and introduces the orbital variables linearized in the spin of the secondary. Section III focuses on GW fluxes from spinning bodies moving on eccentric equatorial orbits around a Kerr black hole with these fluxes linearized in spin. Section IV presents the equations driving the adiabatic evolution of the orbital parameters and the phases. By linearization in spin, this section provides the equations governing the phase shifts. Section V first discusses the numerical methods and then provides the respective results. Finally, Section VI summarizes the main findings of our work.

[2] In fact, the expansion contains also a term proportional to $q^{-1/2}$ caused by the orbital resonances, but here we neglect it for simplicity.

[3] This reasoning holds away from the resonances, since the resonances are governed by the $\mathcal{O}(S^2)$ [26], which implies a contribution to the phase of order of radians.

A. Notation

In this work, we use geometrized units where $c = G = 1$. A partial derivative is denoted with a comma as $U_{\mu,\nu} = \partial_\nu U_\mu$, whereas a covariant derivative is denoted by a semicolon as $U_{\mu;\nu} = \nabla_\nu U_\mu$. The Riemann tensor is defined as $R^\mu{}_{\nu\kappa\lambda} = \Gamma^\mu{}_{\nu\lambda,\kappa} - \Gamma^\mu{}_{\nu\kappa,\lambda} + \Gamma^\mu{}_{\rho\kappa}\Gamma^\rho{}_{\nu\lambda} - \Gamma^\mu{}_{\rho\lambda}\Gamma^\rho{}_{\nu\kappa}$, and the signature of the metric is $(-,+,+,+)$. For convenience, we use some quantities in their dimensionless form, which is denoted by a hat. A list with these quantities and their dimensionless counterparts can be found in Appendix A.

II. MOTION OF A SPINNING PARTICLE

Following Mathisson's gravitational skeleton approach [29, 30] and truncating the expansion up to the second term, the stress-energy tensor of a spinning test body in a curved spacetime can be written as

$$T^{\mu\nu} = \frac{P^{(\mu}v^{\nu)}}{v^t}\frac{\delta^3}{\sqrt{-g}} - \nabla_\alpha\left(\frac{S^{\alpha(\mu}v^{\nu)}}{v^t}\frac{\delta^3}{\sqrt{-g}}\right) , \quad (5)$$

where P^μ is the four-momentum, $v^\mu = \mathrm{d}x^\mu/\mathrm{d}\tau$ is the four-velocity, $S^{\alpha\beta}$ is the spin tensor, $\delta^3 \equiv \delta^3(x^i - x^i_{\mathrm{p}}(t))$ is the Dirac delta function located at the particle position $x^i_{\mathrm{p}}(t)$ parametrized by the coordinate time t and g is the determinant of the metric. In this so-called pole-dipole approximation the stress-energy tensor consists of a monopole (first term) and a dipole (second term).

Applying the stress-energy conservation law $T^{\mu\nu}{}_{;\nu} = 0$ on the stress-energy tensor (5), the Mathisson-Papapetrou-Dixon (MPD) equations [30–32]

$$\frac{\mathrm{D}P^\mu}{\mathrm{d}\tau} = -\frac{1}{2}R^\mu{}_{\nu\rho\sigma}\,v^\nu\,S^{\rho\sigma} , \quad (6a)$$

$$\frac{\mathrm{D}S^{\mu\nu}}{\mathrm{d}\tau} = P^\mu v^\nu - P^\nu v^\mu \quad (6b)$$

can be derived, where $R^\mu{}_{\nu\rho\sigma}$ is the Riemann tensor and τ is the proper time.

The MPD system of equations is underdetermined, because for the 14 independent components $(x^\mu, P^\mu, S^{\mu\nu})$ only ten independent equations are available. This ambiguity is related to the freedom we have to choose the center of mass of the spinning body. Thus, additional conditions must be imposed to fix the center of mass and close the system. One such condition is the Tulczyjew-Dixon spin supplementary condition (TD SSC) [33, 34]

$$S^{\mu\nu}P_\mu = 0 , \quad (7)$$

which introduces three independent constraints to the system. The fourth constraint comes from the fact we have chosen the proper time as the evolution parameter in Eq. (6) and, hence,

$$v^\mu v_\mu = -1. \quad (8)$$

Note that, in order to follow the evolution of the body, we actually track the worldline along the center of the mass, which is the reason why a spinning body is often called a spinning particle. We will use both terms interchangeably throughout the rest of the paper.

Under the TD SSC, the mass of the spinning particle with respect to the four-momentum

$$\mu = \sqrt{-P^\mu P_\mu} \quad (9)$$

and the magnitude of the particle's spin

$$S = \sqrt{\frac{S^{\mu\nu}S_{\mu\nu}}{2}} \quad (10)$$

are conserved along the trajectory. Often, it is convenient to use the dimensionless spin parameter σ

$$\sigma = \frac{S}{\mu M} , \quad (11)$$

instead of the spin magnitude S and the spin four-vector

$$S_\mu = -\frac{1}{2}\epsilon_{\mu\nu\rho\sigma}\,u^\nu\,S^{\rho\sigma} \quad (12)$$

instead of the spin tensor, where $u^\mu = P^\mu/\mu$. It can be checked then that the spin magnitude can be expressed as $S = \sqrt{S^\mu S_\mu}$.

Thanks to the TD SSC, it is possible to derive a relation between the four-momentum and the four-velocity [35]:

$$v^\mu = \frac{\mathsf{m}}{\mu}\left(u^\mu + \frac{2\,S^{\mu\nu}R_{\nu\rho\kappa\lambda}u^\rho S^{\kappa\lambda}}{4\mu^2 + R_{\alpha\beta\gamma\delta}S^{\alpha\beta}S^{\gamma\delta}}\right) , \quad (13)$$

where $\mathsf{m} \equiv -p^\mu v_\mu$ is the rest mass with respect to the four-velocity. The value of this mass is not conserved under TD SSC; however, it is constrained by Eq. (8).

A. Motion on a Kerr background

We are interested in the motion of a spinning particle in Kerr spacetime background. This spacetime describes a spinning black hole at vacuum. The nonzero components of the Kerr metric in Boyer-Lindquist (BL) coordinates

$$\mathrm{d}s^2 = g_{tt}\,\mathrm{d}t^2 + 2\,g_{t\phi}\,\mathrm{d}t\,\mathrm{d}\phi + g_{\phi\phi}\,\mathrm{d}\phi^2 + g_{rr}\,\mathrm{d}r^2 + g_{\theta\theta}\,\mathrm{d}\theta^2 \quad (14)$$

read

$$\begin{aligned} g_{tt} &= -\left(1 - \frac{2Mr}{\Sigma}\right) , \\ g_{t\phi} &= -\frac{2aMr\sin^2\theta}{\Sigma} , \\ g_{\phi\phi} &= \frac{(\varpi^4 - a^2\Delta\sin^2\theta)\sin^2\theta}{\Sigma} , \\ g_{rr} &= \frac{\Sigma}{\Delta} , \\ g_{\theta\theta} &= \Sigma \end{aligned} \quad (15)$$

with

$$\begin{aligned}\Sigma &= r^2 + a^2\cos^2\theta\ ,\\ \Delta &= \varpi^2 - 2Mr\ ,\\ \varpi^2 &= r^2 + a^2\ ,\end{aligned} \tag{16}$$

where M is the mass of the black hole and a is the Kerr parameter.

The outer horizon of a Kerr black hole is located at $r_+ = M + \sqrt{M^2 - a^2}$ and the spacetime is equipped with two killing vectors, one timelike $\xi^\mu_{(t)} = \delta^\mu_t$ and one spacelike $\xi^\mu_{(\phi)} = \delta^\mu_\phi$. The existence of these Killing vectors provides the conservation of two additional quantities, namely, of the energy measured at infinity:

$$E = -P_t + \frac{1}{2} g_{t\mu,\nu} S^{\mu\nu} \tag{17}$$

and of the total angular momentum projected onto the symmetry axis of the black hole measured at infinity:

$$J_z = P_\phi - \frac{1}{2} g_{\phi\mu,\nu} S^{\mu\nu}\ . \tag{18}$$

B. Equatorial motion

In our work we focus on the equatorial motion; hence, $v^\theta = 0$. It can be shown that in this case the particle stays in the equatorial plane [25] and it holds that $p^\theta = 0$ and

$$S_\mu = -rS\,\delta^\theta_\mu\ . \tag{19}$$

Bounded equatorial orbits can be characterized by their semilatus rectum p and their eccentricity e, which are defined as

$$p = \frac{2\hat{r}_1\hat{r}_2}{\hat{r}_1 + \hat{r}_2}\ , \qquad e = \frac{\hat{r}_2 - \hat{r}_1}{\hat{r}_1 + \hat{r}_2}\ , \tag{20}$$

where $\hat{r}_1$ is the pericenter and $\hat{r}_2$ is the apocenter. For the orbital description, we introduce dimensionless counterparts of the involved quantities (for details, see Table I).

The radial coordinate of the particle periodically oscillates between $\hat{r}_1$ and $\hat{r}_2$. Because of this fact, we can change the parametrization of the trajectory from proper time τ to the anglelike relativistic anomaly χ defined as

$$\hat{r} = \frac{p}{1 + e\cos(\chi + \chi_0)}\ , \tag{21}$$

where χ_0 determines the initial radial position. For $\chi + \chi_0 = 0$ and 2π the particle is at the pericenter, and for $\chi + \chi_0 = \pi$ the particle is at the apocenter. The equations of motion for t and ϕ in this so-called Darwin parametrization then read

$$\frac{\mathrm{d}\hat{t}}{\mathrm{d}\chi} = V^t\left(\frac{p}{1 + e\cos(\chi + \chi_0)}\right)\sqrt{\frac{1 - e^2}{p^2 J(\chi + \chi_0)}}\ , \tag{22a}$$

$$\frac{\mathrm{d}\phi}{\mathrm{d}\chi} = V^\phi\left(\frac{p}{1 + e\cos(\chi + \chi_0)}\right)\sqrt{\frac{1 - e^2}{p^2 J(\chi + \chi_0)}}\ , \tag{22b}$$

where the functions V^t, V^ϕ, and J can be found in Appendix B.

By integrating over χ, the functions $\hat{t}(\chi)$ and $\phi(\chi)$ read

$$\hat{t}(\chi) = \int_0^\chi \frac{\mathrm{d}\hat{t}}{\mathrm{d}\chi}(\chi')\mathrm{d}\chi'\ , \tag{23a}$$

$$\phi(\chi) = \phi_0 + \int_0^\chi \frac{\mathrm{d}\phi}{\mathrm{d}\chi}(\chi')\mathrm{d}\chi'\ , \tag{23b}$$

respectively, where we set the initial time $t(0) = 0$.

Since it is possible to express the energy and the angular momentum as $\hat{E}(p, e, \sigma)$ and $\hat{J}_z(p, e, \sigma)$, i.e., as functions of p, e, and σ [4] [25] (see Appendix B), to uniquely identify a trajectory, one needs four parameters p, e, χ_0, and ϕ_0. However, many quantities are independent of the initial angles χ_0 and ϕ_0. Therefore, we can define a fiducial trajectory with $\chi_0 = 0$ and $\phi_0 = 0$. The coordinates of this trajectory as well as all the quantities calculated from it are denoted with a check mark as $\check{\hat{t}}(\chi)$, $\check{\hat{r}}(\chi)$, and $\check{\phi}(\chi)$. After the substitution $\chi = v - \chi_0$, Eq. (23a) can be written as

$$\hat{t}(\chi) = \int_{\chi_0}^{\chi+\chi_0} \frac{\mathrm{d}\check{\hat{t}}}{\mathrm{d}\chi}(v)\mathrm{d}v = \check{\hat{t}}(\chi + \chi_0) - \check{\hat{t}}(\chi_0)\ , \tag{24}$$

where $\mathrm{d}\check{\hat{t}}\big/\mathrm{d}\chi$ comes from Eq. (22a) when $\chi_0 = 0$. An analogous relation holds for $\phi(\chi)$, and, therefore, a general trajectory can be expressed using a fiducial trajectory as

$$\hat{t}(\chi) = \check{\hat{t}}(\chi + \chi_0) - \check{\hat{t}}(\chi_0)\ , \tag{25a}$$

$$\hat{r}(\chi) = \check{\hat{r}}(\chi + \chi_0)\ , \tag{25b}$$

$$\phi(\chi) = \phi_0 + \check{\phi}(\chi + \chi_0) - \check{\phi}(\chi_0)\ . \tag{25c}$$

Trajectory-dependent quantities such as the frequencies or the GW fluxes, which are independent of χ_0 and ϕ_0, can be calculated using the fiducial trajectory.

The radial period, i.e., the time between two successive passages through the pericenter can be expressed as

$$\begin{aligned}\hat{T}_r &= \frac{\sqrt{1 - e^2}}{p}\int_0^{2\pi} V^t\left(\frac{p}{1 + e\cos\chi}\right)\frac{1}{\sqrt{J(\chi)}}\mathrm{d}\chi\\ &= 2\frac{\sqrt{1 - e^2}}{p}\int_0^{\pi} V^t\left(\frac{p}{1 + e\cos\chi}\right)\frac{1}{\sqrt{J(\chi)}}\mathrm{d}\chi\ ,\end{aligned} \tag{26}$$

where we can integrate from 0 to π, because the integrand is even around π. Similarly, the accumulated phase of the azimuthal coordinate can be written as

$$\Delta\phi = 2\frac{\sqrt{1 - e^2}}{p}\int_0^{\pi} V^\phi\left(\frac{p}{1 + e\cos\chi}\right)\frac{1}{\sqrt{J(\chi)}}\mathrm{d}\chi\ . \tag{27}$$

[4] They also depend on the Kerr parameter a, but we will treat it only as a parameter.

The frequencies with respect to the BL time can be then calculated as

$$\hat{\Omega}_r = \frac{2\pi}{\hat{T}_r} \,, \tag{28a}$$

$$\hat{\Omega}_\phi = \frac{\Delta\phi}{\hat{T}_r} \,. \tag{28b}$$

C. Linearization in the secondary spin

Because of the fact that the dimensionless spin σ is of the same order as the mass ratio q, i.e., $\sigma \ll 1$, it is reasonable to linearize the expressions for the frequencies (28) in σ to obtain

$$\hat{\Omega}_i(p,e,\sigma) = \hat{\Omega}_i^{(\mathrm{g})}(p,e) + \sigma\,\delta\hat{\Omega}_i(p,e) + \mathcal{O}\big(\sigma^2\big) \,, \tag{29a}$$

where $i = r, \phi$ and

$$\hat{\Omega}_i^{(\mathrm{g})}(p,e) = \hat{\Omega}(p,e,\sigma=0) \,, \tag{29b}$$

$$\delta\hat{\Omega}_i(p,e) = \left(\frac{\partial\hat{\Omega}_i}{\partial\sigma}\right)_{\sigma=0} \,. \tag{29c}$$

Note that the index (g) in the above quantities refers to a geodesic orbit, i.e., for $\sigma = 0$.

However, for the calculation of GW fluxes it is convenient to linearize the quantities, such as energy and angular momentum fluxes, with respect to a reference geodesic with the same orbital frequencies (see Sec. III A). In other words, we must linearize the functions parametrized by the frequencies, i.e., $f(p(\hat{\Omega}_i,\sigma), e(\hat{\Omega}_i,\sigma), \sigma)$. For this, one must find the linear part of the functions

$$p(\hat{\Omega}_i,\sigma) = p^{(\mathrm{g})}(\hat{\Omega}_i) + \sigma\,\delta p(\hat{\Omega}_i) + \mathcal{O}\big(\sigma^2\big) \,, \tag{30a}$$

$$e(\hat{\Omega}_i,\sigma) = e^{(\mathrm{g})}(\hat{\Omega}_i) + \sigma\,\delta e(\hat{\Omega}_i) + \mathcal{O}\big(\sigma^2\big) \,, \tag{30b}$$

where δp and δe correspond to the change of the orbital parameters after a geodesic with frequencies $\hat{\Omega}_i$ is perturbed by a secondary spin σ while keeping the frequencies same. Because the relations $p(\Omega_i,\sigma)$ and $e(\Omega_i,\sigma)$ are not known, we cannot simply take the derivative of $p(\Omega_i,\sigma)$ and $e(\Omega_i,\sigma)$ with respect to σ to find $\delta p(\Omega_i)$ and $\delta e(\Omega_i)$; instead, we have to use the derivatives of the implicit functions

$$\hat{\Omega}_r = \hat{\Omega}_r(p(\hat{\Omega}_r,\hat{\Omega}_\phi,\sigma), e(\hat{\Omega}_r,\hat{\Omega}_\phi,\sigma),\sigma) \,, \tag{31a}$$

$$\hat{\Omega}_\phi = \hat{\Omega}_\phi(p(\hat{\Omega}_r,\hat{\Omega}_\phi,\sigma), e(\hat{\Omega}_r,\hat{\Omega}_\phi,\sigma),\sigma) \tag{31b}$$

with respect to σ to find them. In these functions, the lhs is constant and the rhs are functions defined in Eqs. (28). After differentiating them with respect to σ, substituting $\sigma = 0$, and solving for $\delta p = \partial p/\partial\sigma$ and $\delta e = \partial e/\partial\sigma$, we obtain

$$\delta p = \frac{\dfrac{\partial\hat{\Omega}_\phi^{(\mathrm{g})}}{\partial e}\delta\hat{\Omega}_r - \dfrac{\partial\hat{\Omega}_r^{(\mathrm{g})}}{\partial e}\delta\hat{\Omega}_\phi}{\left|J_{(\hat{\Omega}_i)}\right|} \,, \tag{32a}$$

$$\delta e = \frac{-\dfrac{\partial\hat{\Omega}_\phi^{(\mathrm{g})}}{\partial p}\delta\hat{\Omega}_r + \dfrac{\partial\hat{\Omega}_r^{(\mathrm{g})}}{\partial p}\delta\hat{\Omega}_\phi}{\left|J_{(\hat{\Omega}_i)}\right|} \,, \tag{32b}$$

where all the derivatives are evaluated at $\sigma = 0$ and the determinant of the Jacobian matrix is

$$\left|J_{(\hat{\Omega}_i)}\right| = \frac{\partial\hat{\Omega}_r^{(\mathrm{g})}}{\partial p}\frac{\partial\hat{\Omega}_\phi^{(\mathrm{g})}}{\partial e} - \frac{\partial\hat{\Omega}_r^{(\mathrm{g})}}{\partial e}\frac{\partial\hat{\Omega}_\phi^{(\mathrm{g})}}{\partial p} \,. \tag{33}$$

Since $\delta p(p,e)$ and $\delta e(p,e)$ were derived through the above procedure, they are functions of p and e. Actually, they can be interpreted as shifts of p and e when a geodesic originally with semilatus rectum p and eccentricity e is perturbed by a spin σ, while keeping the frequencies constant. Explicit formulas for the calculation of δp, δe and the derivatives of Ω_i can be found in a *Mathematica* notebook in the Supplemental Material [36].

As was proven in Ref. [37] for the Schwarzschild spacetime and in Ref. [38] for the Kerr spacetime, bound geodesics cannot be uniquely parametrized by the frequencies $\Omega_i^{(\mathrm{g})}$ and there exists a region of the parameter space near the separatrix with pairs of orbits with identical frequencies Ω_r and Ω_ϕ. This implies that there exists a curve in the $p-e$ plane separating these pairs, on which the determinant (33) is zero. Therefore quantities linearized with respect to a geodesic with the same frequencies cannot be calculated on this curve.

The constants of motion $\hat{E}$ and $\hat{J}_z$ from Eqs. (B1) and (B2) are functions of p, e, and σ; hence, the linear part in σ with respect to a geodesic with the same frequencies can be found using the chain rule as

$$\delta\hat{E}\Big|_{\Omega_i} = \left.\frac{\partial\hat{E}}{\partial\sigma}\right|_{\sigma=0} + \frac{\partial\hat{E}^{(\mathrm{g})}}{\partial p}\delta p + \frac{\partial\hat{E}^{(\mathrm{g})}}{\partial e}\delta e \,, \tag{34a}$$

$$\delta\hat{J}_z\Big|_{\Omega_i} = \left.\frac{\partial\hat{J}_z}{\partial\sigma}\right|_{\sigma=0} + \frac{\partial\hat{J}_z^{(\mathrm{g})}}{\partial p}\delta p + \frac{\partial\hat{J}_z^{(\mathrm{g})}}{\partial e}\delta e \,, \tag{34b}$$

where δp and δe come from Eqs. (32) and the subscript Ω_i denotes that the quantity is linearized with respect to a geodesic with the same frequencies. We have, thus, introduced the operator $\delta f\big|_{\Omega_i}$ acting on a function $f(p,e,\sigma)$ as

$$\delta f\Big|_{\Omega_i} = \left.\frac{\partial f}{\partial\sigma}\right|_{\sigma=0} + \frac{\partial f^{(\mathrm{g})}}{\partial p}\delta p + \frac{\partial f^{(\mathrm{g})}}{\partial e}\delta e \,. \tag{35}$$

Using the above linearized quantities, the coordinate functions $(\hat{t}(\chi), \hat{r}(\chi), \phi(\chi))$ can be linearized as well. When an equatorial geodesic parametrized by χ with frequencies $\hat{\Omega}_i$ is perturbed by a spin σ, the change of the coordinate time and the azimuthal coordinate can be described as

$$\hat{t}(\chi) = \hat{t}^{(\mathrm{g})}(\chi) + \sigma\ \delta\hat{t}\Big|_{\Omega_i}(\chi) + \mathcal{O}\big(\sigma^2\big) \,, \tag{36a}$$

$$\phi(\chi) = \phi^{(\mathrm{g})}(t) + \sigma\ \delta\phi\Big|_{\Omega_i}(\chi) + \mathcal{O}\big(\sigma^2\big) \,, \tag{36b}$$

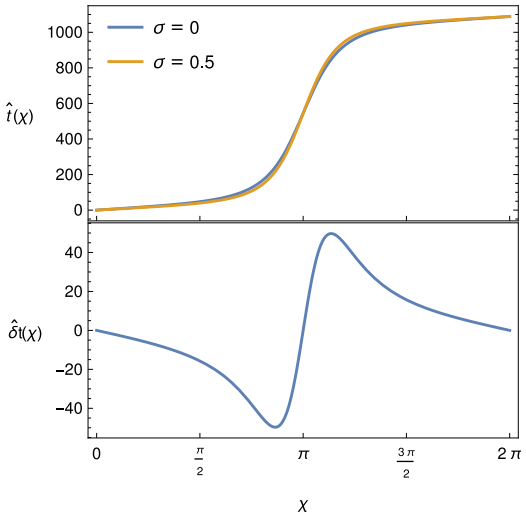

FIG. 1. Top: the evolution of $\hat{t}^{(\mathrm{g})}(\chi)$ for a geodesic orbit with $\hat{a}=0$, $\hat{\Omega}_r=0.00577033$, and $\hat{\Omega}_\phi=0.00942436$, which corresponds to $p^{(\mathrm{g})}=10$, $e^{(\mathrm{g})}=0.8$, and $t(\chi)$ for a trajectory of a spinning particle with $\sigma=0.5$ and the same frequencies as the geodesic orbit, which corresponds to $p=8.6538$ and $e=0.831688$. Bottom: difference $\delta\hat{t}(\chi)=(\hat{t}(\chi)-\hat{t}^{(\mathrm{g})}(\chi))/\sigma$. We can see that if the initial difference is $\hat{t}(0)-\hat{t}^{(\mathrm{g})}(0)=0$, then at the end of the period $\hat{t}(2\pi)-\hat{t}^{(\mathrm{g})}(2\pi)=0$ as well. The spin value has been chosen to be unphysically large to make the difference visible.

respectoively, where $\hat{t}^{(\mathrm{g})}(\chi)$ and $\phi^{(\mathrm{g})}(\chi)$ are calculated from Eqs. (22) for $\sigma=0$ and equations for $\delta\hat{t}\big|_{\Omega_i}(\chi)$ and $\delta\phi\big|_{\Omega_i}(\chi)$ are derived by linearizing Eqs. (22) in σ with respect to a geodesic with the same frequencies, i.e.,

$$\frac{\mathrm{d}\delta\hat{t}}{\mathrm{d}\chi}=\frac{\partial}{\partial\sigma}\left(\frac{\mathrm{d}\hat{t}}{\mathrm{d}\chi}\right)\bigg|_{\sigma=0}+\frac{\partial}{\partial p}\left(\frac{\mathrm{d}\hat{t}^{(\mathrm{g})}}{\mathrm{d}\chi}\right)\delta p+\frac{\partial}{\partial e}\left(\frac{\mathrm{d}\hat{t}^{(\mathrm{g})}}{\mathrm{d}\chi}\right)\delta e\,, \tag{37a}$$

$$\frac{\mathrm{d}\delta\phi}{\mathrm{d}\chi}=\frac{\partial}{\partial\sigma}\left(\frac{\mathrm{d}\phi}{\mathrm{d}\chi}\right)\bigg|_{\sigma=0}+\frac{\partial}{\partial p}\left(\frac{\mathrm{d}\phi^{(\mathrm{g})}}{\mathrm{d}\chi}\right)\delta p+\frac{\partial}{\partial e}\left(\frac{\mathrm{d}\phi^{(\mathrm{g})}}{\mathrm{d}\chi}\right)\delta e\,. \tag{37b}$$

For the fiducial trajectory, the initial conditions can be chosen such that the linear corrections δt and $\delta\phi$ are zero at the pericenter, namely $\delta\check{t}(0)=0=\delta\check{\phi}(0)$. Thanks to the frequency matching, it holds that $\delta\check{t}(2\pi)=0=\delta\check{\phi}(2\pi)$, because the radial period and accumulated phase in ϕ are the same for both the perturbed and the unperturbed trajectory. This can be seen in Fig. 1, where we plot the evolution of $\hat{t}(\chi)$ for a geodesic orbit ($\sigma=0$) with $p=10$, $e=0.8$, and for a trajectory of a spinning particle with $\sigma=0.5$, which frequencies were matched to the same as the frequencies of the geodesic orbit.

The linear correction to the radial coordinate can be calculated as

$$\begin{aligned}\delta\hat{r}(\chi)&=\frac{\partial\hat{r}}{\partial p}\delta p+\frac{\partial\hat{r}}{\partial e}\delta e\\&=\frac{\delta p}{1+e\cos\chi}-\frac{p\,\delta e\cos\chi}{(1+e\cos\chi)^2}\,.\end{aligned} \tag{37c}$$

III. GRAVITATIONAL-WAVE FLUXES

For the calculation of the GW fluxes, we use Teukolsky formalism where the GWs are treated as perturbations of the background spacetime. To obtain the GW fluxes to infinity and to the horizon, we calculate perturbation of the Weyl curvature scalar

$$\Psi_4=-C_{\alpha\beta\gamma\delta}n^\alpha\overline{m}^\beta n^\gamma\overline{m}^\delta\,, \tag{38}$$

where $C_{\alpha\beta\gamma\delta}$ is the Weyl tensor and

$$n^\mu=\frac{1}{2\Sigma}\left(\varpi^2,-\Delta,0,a\right)\,, \tag{39}$$

$$\overline{m}^\mu=-\frac{1}{\sqrt{2}\zeta}\left(ia\sin\theta,0,-1,i\csc\theta\right) \tag{40}$$

are two legs of the Kinnersley null tetrad with

$$\zeta=r-ia\cos\theta.$$

The Weyl scalar is related to the gravitational radiation at infinity as

$$\Psi_4(r\to\infty)=\frac{1}{2}\frac{\mathrm{d}^2h}{\mathrm{d}t^2}\,, \tag{41}$$

where $h=h_+-ih_\times$ is the strain, which is defined as $h_{\mu\nu}=h_+e^+_{\mu\nu}+h_\times e^\times_{\mu\nu}$ with the metric perturbation $h_{\mu\nu}$ and polarization tensors $e^{+,\times}_{\mu\nu}$. The Weyl scalar Ψ_4 encodes the gravitational radiation emitted to infinity; however, by using the Teukolsky-Starobinsky identities, it is possible to infer from Ψ_4 the fluxes at the horizon as well.

Teukolsky in Ref. [39] introduced the master equation for the field in the form[5]

$${}_s\mathcal{O}\,{}_s\psi(t,r,\theta,\phi)=4\pi\Sigma T\,, \tag{42}$$

where ${}_s\mathcal{O}$ is a second-order partial differential operator and T is a source term calculated as a certain differential operator acting on projections of the stress-energy tensor (the interested reader is referred to Ref. [39] for more details). In the case of GWs, the calculated quantity from Eq. (42) is ${}_{-2}\psi=\zeta^4\Psi_4$.

[5] In this section, the coordinates (t,r,θ,ϕ) denote an event in the spacetime in which the field is measured, while the trajectory of the particle is denoted by $(t_\mathrm{p},r_\mathrm{p},\theta_\mathrm{p},\phi_\mathrm{p})$.

In this paper, we use frequency domain solutions of the Teukolsky equation (TE), for which the field is written using Fourier modes

$$ {}_{-2}\psi = \sum_{l,m}^{\infty} \frac{1}{2\pi} \int_{-\infty}^{\infty} \mathrm{d}\omega \, \psi_{lm\omega}(r) {}_{-2}S_{lm}^{a\omega}(\theta) e^{-i\omega t + im\phi} \, . \tag{43} $$

Having done that, Eq. (42) can be separated into two ordinary differential equations: one for the radial part $\psi_{lm\omega}(r)$ and one for the angular part ${}_{-2}S_{lm}^{a\omega}(\theta)$, which is called the spin-weighted spheroidal harmonic.

The asymptotic behavior of the radial part at infinity and at the horizon can be written as [9]

$$ \psi_{lm\omega}(r) \approx C^{+}_{lm\omega} r^3 e^{i\omega r^*} \qquad r \to \infty \, , \tag{44a} $$

$$ \psi_{lm\omega}(r) \approx C^{-}_{lm\omega} \Delta e^{-ik_{\mathcal{H}} r^*} \qquad r \to r_+ \, , \tag{44b} $$

respectively, where $k_{\mathcal{H}} = \omega - m\Omega_{\mathcal{H}}$ is the frequency at the horizon, $\Omega_{\mathcal{H}} = a/(2Mr_+)$ is the horizon's angular velocity and r^* is the tortoise coordinate defined as $\mathrm{d}r^*/\mathrm{d}r = \varpi^2/\Delta$.

The amplitudes $C^{\pm}_{lm\omega}$ can be calculated using Green function formalism as

$$ C^{\pm}_{lm\omega} = \int_{-\infty}^{\infty} \mathrm{d}t \, e^{i\omega t - im\phi_p(t)} I^{\pm}_{lm\omega}(r_{\mathrm{p}}(t), \theta_{\mathrm{p}}(t)) \tag{45} $$

with

$$ I^{\pm}_{lm\omega}(r,\theta) = \frac{1}{W} \left(A_0 - (A_1 + B_1) \frac{\mathrm{d}}{\mathrm{d}r} + (A_2 + B_2) \frac{\mathrm{d}^2}{\mathrm{d}r^2} - B_3 \frac{\mathrm{d}^3}{\mathrm{d}r^3} \right) R^{\mp}_{lm\omega}(r) \, , \tag{46} $$

where $R^{\pm}_{lm\omega}(r)$ are homogeneous solutions of the radial equation satisfying boundary conditions at infinity "+" or at the horizon "−," respectively, W is the invariant Wronskian, and A_i and B_i are functions of the orbital quantities. These quantities can be found in Appendix B in Ref. [25].

After we confine the particle trajectory into the equatorial plane, it can be shown, that thanks to the periodicity of the radial motion, the frequency spectrum is discrete, and the amplitudes can be written as a sum over individual n modes:

$$ C^{\pm}_{lm\omega} = \sum_{n=-\infty}^{\infty} C^{\pm}_{lmn} \delta(\omega - \omega_{mn}) \tag{47} $$

with frequencies

$$ \omega_{mn} = m\Omega_\phi + n\Omega_r \, , \tag{48} $$

where n is an integer.

After reparametrization of the orbit with χ, the partial amplitudes can be calculated as

$$ C^{\pm}_{lmn} = \Omega_r \int_0^{\pi} \mathrm{d}\chi \sum_{D_r = \pm} \frac{\mathrm{d}t}{\mathrm{d}\chi} I^{\pm}_{lmn}(r_{\mathrm{p}}(\chi), \pi/2, D_r) \times \exp(i D_r \varphi_{mn}(\chi)) \, , \tag{49} $$

where $I^{\pm}_{lmn} = I^{\pm}_{lm\omega_{mn}}$, $\varphi_{mn}(\chi) = \omega_{mn} t_{\mathrm{p}}(\chi) - m\phi_{\mathrm{p}}(\chi)$, and D_r is the sign of the radial velocity.

After Eqs. (25) are substituted into the above equation and the integration variable $\chi \to \chi - \chi_0$ is changed, the partial amplitudes from an equatorial orbit with $\chi_0 \neq 0$, $\phi_0 \neq 0$ can be expressed using partial amplitudes from the fiducial trajectory $\check{C}^{\pm}_{lmn}$ and a phase factor as

$$ C^{\pm}_{lmn} = e^{i\xi_{mn}} \check{C}^{\pm}_{lmn} \, , \tag{50} $$

where the phase factor reads

$$ \xi_{mn} = -\omega_{mn} \check{t}_{\mathrm{p}}(\chi_0) + m\big(\check{\phi}_{\mathrm{p}}(\chi_0) - \phi_0\big) \, . \tag{51} $$

This factor agrees with Eq. (3.19) in Ref. [9] for equatorial motion.

From Eqs. (41), (43), and (44a), the strain at infinity can be expressed as

$$ h = -\frac{2}{r} \sum_{lmn} \frac{C^{+}_{lmn}}{\omega^2_{mn}} S_{lm}^{a\omega_{mn}}(\theta) e^{-i\omega_{mn}(t - r^*) + im\phi} \, . \tag{52} $$

The effective stress energy of a GW can be reconstructed from the strain. From it, the orbit-averaged energy and angular momentum fluxes to the future null infinity $\mathcal{J}^+$ can be derived as

$$ \left\langle \mathcal{F}^{E\mathcal{J}^+} \right\rangle = \sum_{l=2}^{\infty} \sum_{m=-l}^{l} \sum_{n=-\infty}^{\infty} \frac{\left| \check{\dot{C}}^{+}_{lmn} \right|^2}{4\pi \hat{\omega}^2_{mn}} \, , \tag{53a} $$

$$ \left\langle \mathcal{F}^{J_z\mathcal{J}^+} \right\rangle = \sum_{l=2}^{\infty} \sum_{m=-l}^{l} \sum_{n=-\infty}^{\infty} \frac{m \left| \check{\dot{C}}^{+}_{lmn} \right|^2}{4\pi \hat{\omega}^3_{mn}} \, , \tag{53b} $$

respectively, where the brackets denote averaging over the radial period. Similar relations can be derived for the fluxes through the future horizon $\mathcal{H}^+$:

$$ \left\langle \mathcal{F}^{E\mathcal{H}^+} \right\rangle = \sum_{l=2}^{\infty} \sum_{m=-l}^{l} \sum_{n=-\infty}^{\infty} \alpha_{lmn} \frac{\left| \check{\dot{C}}^{-}_{lmn} \right|^2}{4\pi \hat{\omega}^2_{mn}} \, , \tag{53c} $$

$$ \left\langle \mathcal{F}^{J_z\mathcal{H}^+} \right\rangle = \sum_{l=2}^{\infty} \sum_{m=-l}^{l} \sum_{n=-\infty}^{\infty} \alpha_{lmn} \frac{m \left| \check{\dot{C}}^{-}_{lmn} \right|^2}{4\pi \hat{\omega}^3_{mn}} \, , \tag{53d} $$

where $\alpha_{lmn} = \alpha_{lm\omega_{mn}}$ can be found in Ref. [25]. These fluxes are defined from the dimensionless quantities in accordance with [25]. Note that thanks to the absolute value of the partial amplitudes in Eqs. (53), the phase correction in Eq. (50) is canceled and, thus, the averaged fluxes can be computed from the fiducial trajectory.

A. Linearization in the secondary spin

The partial amplitudes $C^{\pm}_{lmn}$ calculated above depend on p, e, and σ, but, since the formula contains the dependence on the frequencies $\Omega_i(p,e,\sigma)$, the partial amplitudes can be written as $C^{\pm}_{lmn}(p,e,\Omega_i(p,e,\sigma),\sigma)$. In

this form, they can be linearized in σ as

$$C^{\pm}_{lmn}(p,e,\sigma) = C^{(\mathrm{g})\pm}_{lmn}(p,e) + \sigma\, \delta C^{\pm}_{lmn}\Big|_{p,e}(p,e) + \mathcal{O}\big(\sigma^2\big)\,, \tag{54}$$

where

$$\delta C^{\pm}_{lmn}\Big|_{p,e}(p,e) = \frac{\partial C^{\pm}_{lmn}}{\partial\sigma}\Big|_{\sigma=0} + \frac{\partial C^{(\mathrm{g})\pm}_{lmn}}{\partial\Omega_i}\frac{\partial\Omega_i}{\partial\sigma}\,, \tag{55}$$

in which we use the convention that all repeated indices are summed over and $|_{p,e}$ denotes that the quantity is calculated with respect to reference geodesic with fixed p and e. The partial amplitudes $C^{\pm}_{lmn}$ depend on the frequencies Ω_i, since the functions giving it, like the homogeneous solutions $R^{\pm}_{lm\omega}(r)$ and $S^{a\omega}_{lm}(\theta)$, depend on ω_{mn}. Thus, for the calculation of $\delta C^{\pm}_{lmn}\big|_{p,e}(p,e)$, one needs the derivatives of $R_{lm\omega}(r)$ and $S^{a\omega}_{lm}(\theta)$ with respect to ω. To find these derivatives, the radial and angular TE must be differentiated with respect to ω, and then this system of equation must be solved. Rather than developing a code for finding these derivatives, we were able to achieve our goal by calculating slightly different quantities, for which the ω derivative of the homogeneous solutions is not needed. In this alternative procedure, we can use the TE solver implemented in the Black Hole Perturbation Toolkit. In particular, we calculate the linear part of the partial amplitudes with respect to a reference geodesic with the same frequencies. Formally, the dependence of the partial amplitudes on Ω_i can be written as $C^{\pm}_{lmn}(p(\Omega_i,\sigma),e(\Omega_i,\sigma),\Omega_i,\sigma)$, which can be linearized as

$$C^{\pm}_{lmn}(\Omega_i,\sigma) = C^{(\mathrm{g})\pm}_{lmn}(\Omega_i) + \sigma\ \delta C^{\pm}_{lmn}\Big|_{\Omega_i}(\Omega_i) + \mathcal{O}\big(\sigma^2\big)\,, \tag{56}$$

where

$$\delta C^{\pm}_{lmn}\Big|_{\Omega_i}(\Omega_i) = \frac{\partial C^{\pm}_{lmn}}{\partial\sigma}\Big|_{\sigma=0} + \frac{\partial C^{(\mathrm{g})\pm}_{lmn}}{\partial p}\delta p + \frac{\partial C^{(\mathrm{g})\pm}_{lmn}}{\partial e}\delta e \tag{57}$$

and δp and δe are defined in Eqs. (32). All the above derivatives are calculated for $\sigma = 0$, i.e., for a geodesic, and we can use the fact that $\Omega_i = \Omega^{(\mathrm{g})}_i(p,e)$ to obtain these linear parts as functions of p and e.

The linearized expression for $\delta C^{\pm}_{lmn}(p,e)$ from Eqs. (49) and (57) reads

$$\delta C^{\pm}_{lmn}\Big|_{\Omega_i} = \Omega_r \int_0^{\pi} \mathrm{d}\chi \sum_{D_r} \exp(iD_r\varphi_{mn}(\chi)) \times \left(\delta\tilde{I}^{\pm}_{lmn}\Big|_{\Omega_i} + \tilde{I}^{\pm}_{lmn} iD_r\delta\varphi_{mn}(\chi)\right) \tag{58}$$

where $\tilde{I}^{\pm}_{lmn} = \mathrm{d}t/\mathrm{d}\chi\ I^{\pm}_{lmn}$ and

$$\delta\varphi_{mn}(\chi) = \omega_{mn}\delta t(\chi) - m\delta\phi(\chi)\,. \tag{59}$$

From Eqs. (53), we can find the linear in σ part of the fluxes $\mathcal{F}(\Omega_i,\sigma) = \mathcal{F}^{(\mathrm{g})}(\Omega_i) + \sigma\,\delta\mathcal{F}(\Omega_i) + \mathcal{O}\big(\sigma^2\big)$, where $\mathcal{F}$ stands for $\mathcal{F}^{E\mathcal{J}^+}$, $\mathcal{F}^{E\mathcal{H}^+}$, $\mathcal{F}^{J_z\mathcal{J}^+}$, and $\mathcal{F}^{J_z\mathcal{H}^+}$. The result is

$$\delta\mathcal{F}^{\mathcal{C}\mathcal{I}^+,\mathcal{H}^+}\Big|_{\Omega_i} = \sum_{lmn}\left(\mathrm{Re}\left\{\delta\hat{C}^{\pm}_{lmn}\Big|_{\Omega_i}\right\}\mathrm{Re}\left\{\hat{C}^{(\mathrm{g})\pm}_{lmn}\right\} + \mathrm{Im}\left\{\delta\hat{C}^{\pm}_{lmn}\Big|_{\Omega_i}\right\}\mathrm{Im}\left\{\hat{C}^{(\mathrm{g})\pm}_{lmn}\right\}\right)\frac{\hat{\beta}^{\pm}_{\mathcal{C}lmn}}{2\pi\hat{\omega}^3_{mn}} \tag{60}$$

where $\mathcal{C}$ stands for E or J_z and $\hat{\beta}^{+}_{Elmn} = \hat{\omega}_{mn}$, $\hat{\beta}^{+}_{J_zlmn} = m$, $\hat{\beta}^{-}_{Elmn} = \alpha_{lmn}\hat{\omega}_{mn}$, and $\beta^{-}_{J_zlmn} = \alpha_{lmn}m$. All the linear parts above are with respect to geodesic with the same frequencies.

When the geodesic fluxes and their linear corrections are calculated on a grid in the $p-e$ plane, it is possible to find the linear part $\delta\mathcal{F}\big|_{p,e}$ from $\delta\mathcal{F}\big|_{\Omega_i}$ and the derivatives of $\mathcal{F}^{(\mathrm{g})}$ with respect to p and e. Namely,

$$\delta\mathcal{F}\Big|_{p,e} = \delta\mathcal{F}\Big|_{\Omega_i} - \frac{\mathrm{d}\mathcal{F}^{(\mathrm{g})}}{\mathrm{d}p}\delta p - \frac{\mathrm{d}\mathcal{F}^{(\mathrm{g})}}{\mathrm{d}e}\delta e\,, \tag{61}$$

where $\delta\mathcal{F}\big|_{\Omega_i}$ is computed using Eq. (60), δp and δe are from Eqs. (32), and the derivatives with respect to p and e are understood as

$$\frac{\mathrm{d}\mathcal{F}^{(\mathrm{g})}}{\mathrm{d}p,e} = \frac{\partial\mathcal{F}^{(\mathrm{g})}}{\partial p,e} + \frac{\partial\mathcal{F}^{(\mathrm{g})}}{\partial\hat{\Omega}_i}\frac{\partial\hat{\Omega}_i}{\partial p,e}\,, \tag{62}$$

although, in our scheme, they are directly calculated numerically on the grid in the $p-e$ plane.

Let us now prove that Eq. (61) holds. The linear part $\delta\mathcal{F}\big|_{\Omega_i}$ reads

$$\delta\mathcal{F}\Big|_{\Omega_i} = \frac{\partial\mathcal{F}}{\partial\sigma}\Big|_{\sigma=0} + \frac{\partial\mathcal{F}^{(\mathrm{g})}}{\partial p}\delta p + \frac{\partial\mathcal{F}^{(\mathrm{g})}}{\partial e}\delta e\,, \tag{63}$$

since $\hat{\Omega}_i(p,e,\sigma)$. Replacing the above along with the total derivatives with respect to p and e (Eq. (62)) into Eq. (61) reduces Eq. (61) to

$$\delta\mathcal{F}\Big|_{p,e} = \frac{\partial\mathcal{F}}{\partial\sigma}\Big|_{\sigma=0} - \frac{\partial\mathcal{F}^{(\mathrm{g})}}{\partial\hat{\Omega}_i}\left(\frac{\partial\hat{\Omega}^{(\mathrm{g})}_i}{\partial p}\delta p + \frac{\partial\hat{\Omega}^{(\mathrm{g})}_i}{\partial e}\delta e\right) \tag{64}$$

By substituting Eqs. (32) into the latter, it can be proven that the term in brackets equals to $-\,\partial\hat{\Omega}_i\big/\partial\sigma$, and we, thus, obtain

$$\delta\mathcal{F}\Big|_{p,e} = \frac{\partial\mathcal{F}}{\partial\sigma}\Big|_{\sigma=0} + \frac{\partial\mathcal{F}^{(\mathrm{g})}}{\partial\hat{\Omega}_i}\frac{\partial\hat{\Omega}_i}{\partial\sigma}\,, \tag{65}$$

which is the definition of $\delta\mathcal{F}\big|_{p,e}$ similar to Eq. (55).

Note that, though the linear part $\delta\mathcal{F}\big|_{\Omega_i}$ is singular for some points on the $p-e$ plane due to a vanishing $\big|J_{(\Omega_i)}\big|$ (Eq. (33)), the linear part $\delta\mathcal{F}\big|_{p,e}$ is regular in the whole parameter space for which the semilatus rectum p is larger than the separatrix one p_{s}. This is caused by the cancellation of the diverging terms in $\delta\mathcal{F}\big|_{\Omega_i}$, δp and δe in Eq. (61). However, due to numerical errors arising in the calculation of $\mathrm{d}\mathcal{F}^{(\mathrm{g})}\big/\mathrm{d}p,e$, the result is not reliable near these diverging points and the error may be high.

IV. ADIABATIC EVOLUTION OF THE ORBITS

During an equatorial inspiral, the orbital parameters p and e are slowly evolving due to gravitational radiation reaction. Using the adiabatic approximation in the framework of the two-timescale approximation, thanks to the balance law, the evolution of an inspiral can be calculated from the energy and angular momentum fluxes to infinity and to the horizon [18]. In particular, the evolution of the constants of motion is related to the averaged fluxes as

$$\left\langle \dot{\hat{E}} \right\rangle \equiv \left\langle \frac{\mathrm{d}\hat{E}}{\mathrm{d}\hat{t}} \right\rangle = -q\Big(\left\langle \mathcal{F}^{E\mathcal{I}^+} \right\rangle + \left\langle \mathcal{F}^{E\mathcal{H}^+} \right\rangle \Big) \,, \tag{66a}$$

$$\left\langle \dot{\hat{J}}_z \right\rangle \equiv \left\langle \frac{\mathrm{d}\hat{J}_z}{\mathrm{d}\hat{t}} \right\rangle = -q\Big(\left\langle \mathcal{F}^{J_z\mathcal{I}^+} \right\rangle + \left\langle \mathcal{F}^{J_z\mathcal{H}^+} \right\rangle \Big) \,, \tag{66b}$$

Using the chain rule, the derivatives of E and J_z can be calculated from the derivatives of p and e as

$$\begin{pmatrix} \dfrac{\mathrm{d}\hat{E}}{\mathrm{d}\hat{t}} \\ \dfrac{\mathrm{d}\hat{J}_z}{\mathrm{d}\hat{t}} \end{pmatrix} = \begin{pmatrix} \dfrac{\partial\hat{E}}{\partial p} & \dfrac{\partial\hat{E}}{\partial e} \\ \dfrac{\partial\hat{J}_z}{\partial p} & \dfrac{\partial\hat{J}_z}{\partial e} \end{pmatrix} \begin{pmatrix} \dfrac{\mathrm{d}p}{\mathrm{d}\hat{t}} \\ \dfrac{\mathrm{d}e}{\mathrm{d}\hat{t}} \end{pmatrix} . \tag{67}$$

By inverting the Jacobian matrix, we obtain the equations for $\dot{p}$ and $\dot{e}$ in the form

$$\frac{\mathrm{d}p}{\mathrm{d}\hat{t}} = \frac{\dfrac{\partial\hat{J}_z}{\partial e}\dot{\hat{E}} - \dfrac{\partial\hat{E}}{\partial e}\dot{\hat{J}}_z}{\left|J_{(\hat{E},\hat{J}_z)}\right|} \equiv \dot{p}(p(\hat{t}),e(\hat{t}),\sigma) \,, \tag{68a}$$

$$\frac{\mathrm{d}e}{\mathrm{d}\hat{t}} = \frac{-\dfrac{\partial\hat{J}_z}{\partial p}\dot{\hat{E}} + \dfrac{\partial\hat{E}}{\partial p}\dot{\hat{J}}_z}{\left|J_{(\hat{E},\hat{J}_z)}\right|} \equiv \dot{e}(p(\hat{t}),e(\hat{t}),\sigma) \,, \tag{68b}$$

respectively, where we have omitted the angle brackets for simplicity and where the Jacobian determinant is

$$\left|J_{(\hat{E},\hat{J}_z)}\right| = \frac{\partial\hat{E}}{\partial p}\frac{\partial\hat{J}_z}{\partial e} - \frac{\partial\hat{E}}{\partial e}\frac{\partial\hat{J}_z}{\partial p} \,. \tag{69}$$

Thanks to Eq. (68), the evolution of p and e can be computed using the fluxes which, in fact, depend on p and e.

Once we have the evolution of $p(\hat{t})$ and $e(\hat{t})$, the waveform at infinity can be computed from Eq. (52) as [4]

$$\hat{r}h(\hat{u}) = \sum_{lmn} \hat{A}_{lmn}(\hat{u}) S_{lm}^{\hat{a}\hat{\omega}_{lm}(p(\hat{u}),e(\hat{u}))}(\theta) e^{-i\Phi_{mn}(\hat{u})+im\phi} \,, \tag{70}$$

where $\hat{u} = \hat{t} - \hat{r}^*$ is the retarded coordinate and the amplitudes and phases read, respectively,

$$\hat{A}_{lmn}(\hat{u}) = -2q\frac{\hat{C}^+_{lmn}(p(\hat{u}),e(\hat{u}))}{\hat{\omega}^2_{mn}(p(\hat{u}),e(\hat{u}))} \,, \tag{71}$$

$$\Phi_{mn}(\hat{u}) = \int_0^{\hat{u}} \hat{\omega}_{lm}(p(\hat{u}'),e(\hat{u}'))\mathrm{d}\hat{u}' \,. \tag{72}$$

From Eq. (48), the phase can be written as $\Phi_{mn} = m\Phi_\phi + n\Phi_r$, where the particular phases

$$\Phi_i(\hat{u}) = \int_0^{\hat{u}} \hat{\Omega}_i(p(\hat{u}'),e(\hat{u}'))\mathrm{d}\hat{u}' \tag{73}$$

can be calculated separately. The partial amplitudes $C^+_{lmn}(p(\hat{u}),e(\hat{u}))$ can be calculated from the fiducial partial amplitude $\hat{C}^+_{lmn}$ and the phase factor $\xi_{mn}(p(\hat{u}),e(\hat{u}))$, which evolves over time. This correction changes slowly and remains at the order of unity [9].

Note that the above amplitudes (71) and phases (72) are part of the two-timescale expansion in the first-order perturbation theory [4]. However, with modifications, this scheme can be used even in the calculations of second-order perturbations [40].

A. Linearization in the secondary spin

The evolution equations (68) of p and e depend on p, e, and σ. Therefore, the evolution can be linearized in σ as

$$p(\hat{t},\sigma) = p^{(\mathrm{g})}(\hat{t}) + \sigma\,\delta p(\hat{t}) + \mathcal{O}\big(\sigma^2\big) \tag{74a}$$

$$e(\hat{t},\sigma) = e^{(\mathrm{g})}(\hat{t}) + \sigma\,\delta e(\hat{t}) + \mathcal{O}\big(\sigma^2\big) \tag{74b}$$

where $p^{(\mathrm{g})}(\hat{t})$ and $e^{(\mathrm{g})}(\hat{t})$ describe inspirals with a nonspinning secondary and $\delta p(\hat{t})$ and $\delta e(\hat{t})$ are corrections to the evolution due to the secondary spin.[6]

Functions $p^{(\mathrm{g})}(\hat{t})$ and $e^{(\mathrm{g})}(\hat{t})$ are calculated from Eqs. (68) for $\sigma = 0$:

$$\frac{\mathrm{d}p^{(\mathrm{g})}}{\mathrm{d}\hat{t}} = \dot{p}(p^{(\mathrm{g})}(\hat{t}),e^{(\mathrm{g})}(\hat{t}),0) \,, \tag{75a}$$

$$\frac{\mathrm{d}e^{(\mathrm{g})}}{\mathrm{d}\hat{t}} = \dot{e}(p^{(\mathrm{g})}(\hat{t}),e^{(\mathrm{g})}(\hat{t}),0) \,, \tag{75b}$$

and $\delta p(t)$ and $\delta e(t)$ are calculated from the linear part of Eqs. (68):

$$\frac{\mathrm{d}\delta p}{\mathrm{d}\hat{t}} = \left.\frac{\mathrm{d}\dot{p}}{\mathrm{d}\sigma}\right|_{\sigma=0} \equiv \delta\dot{p}(p^{(\mathrm{g})}(\hat{t}),e^{(\mathrm{g})}(\hat{t}),\delta p(\hat{t}),\delta e(\hat{t})) \,, \tag{76a}$$

$$\frac{\mathrm{d}\delta e}{\mathrm{d}\hat{t}} = \left.\frac{\mathrm{d}\dot{e}}{\mathrm{d}\sigma}\right|_{\sigma=0} \equiv \delta\dot{e}(p^{(\mathrm{g})}(\hat{t}),e^{(\mathrm{g})}(\hat{t}),\delta p(\hat{t}),\delta e(\hat{t})) \,, \tag{76b}$$

where the total derivatives are defined as

$$\left.\frac{\mathrm{d}f}{\mathrm{d}\sigma}\right|_{\sigma=0} = \left.\frac{\partial f}{\partial\sigma}\right|_{\sigma=0} + \frac{\partial f^{(\mathrm{g})}}{\partial p}\delta p + \frac{\partial f^{(\mathrm{g})}}{\partial e}\delta e \,. \tag{77}$$

More explicit formulas can be found in Appendix C.

[6] Note that these quantities are different from the quantities in Eqs. (32), which denote the change in the orbital parameters when a geodesic is perturbed with secondary spin while keeping the frequencies constant.

The linear parts of $\dot{\hat{E}}$ and $\dot{\hat{J}}_z$ in Eqs. (76) are calculated from the linearized fluxes with respect to geodesic with the same p and e, i.e., from $\delta\mathcal{F}\big|_{p,e}$, which is computed from Eq. (61). This equation as well as Eqs. (76) contains derivatives of the geodesic fluxes $\mathcal{F}^{(\mathrm{g})}$ with respect to p and e which must be calculated numerically.

After we expand the phase in the secondary spin as

$$\Phi_i(\hat{u},\sigma) = \Phi_i^{(\mathrm{g})}(\hat{u}) + \sigma\delta\Phi_i(\hat{u}) + \mathcal{O}\big(\sigma^2\big)\,, \tag{78}$$

we get the leading adiabatic term $\Phi_i^{(\mathrm{g})}$, which is $\mathcal{O}\big(q^{-1}\big)$, and the linear in spin term together with the spin value $\sigma\delta\Phi_i$, which is $\mathcal{O}(\sigma/q) = \mathcal{O}(1)$. Since for LISA data analysis the GW phase is needed with precision to fractions of radians, apart from the former dominant term, also the latter term must be included. In this work, we call $\sigma\,\delta\Phi_i$ a *phase shift*. The linear in spin term can be calculated by the linearization of Eq. (73) as

$$\delta\Phi_i = \int_0^{\hat{u}} \left(\left.\frac{\partial\hat{\Omega}_i}{\partial\sigma}\right|_{\sigma=0} + \frac{\partial\hat{\Omega}_i^{(\mathrm{g})}}{\partial p}\delta p(\hat{u}') + \frac{\partial\hat{\Omega}_i^{(\mathrm{g})}}{\partial e}\delta e(\hat{u}') \right) \mathrm{d}\hat{u}'\,, \tag{79}$$

where the derivatives of Ω_i are evaluated at $p^{(\mathrm{g})}(\hat{u}')$ and $e^{(\mathrm{g})}(\hat{u}')$.

The evolution of the phase factor $\xi_{mn}(p(\hat{u}), e(\hat{u}))$ also changes when the secondary spin is included. The linear in spin part of the phase factor,

$$\delta\xi_{mn} = \left.\frac{\partial\xi_{mn}}{\partial\sigma}\right|_{\sigma=0} + \frac{\partial\xi_{mn}}{\partial p}\delta p + \frac{\partial\xi_{mn}}{\partial e}\delta e\,, \tag{80}$$

evaluated at $p^{(\mathrm{g})}(\hat{u})$ and $e^{(\mathrm{g})}(\hat{u})$ contributes to the phase as $\sigma\,\delta\xi_{mn} \ll 1$. This contribution is of the same order as the second postadiabatic term and can be neglected in the framework of a first-order postadiabatic analysis. Note, however, when the inspiral approaches the separatrix, our approximation fails because δp and δe diverge (see Sec. V B), and a different scheme must be employed.

V. NUMERICAL IMPLEMENTATION AND RESULTS

In this section we discuss how we implemented the results from the previous sections in order to calculate an inspiral of a spinning particle into a Kerr black hole in the linearized in spin approximation. Moreover, we present the phase shifts $\sigma\delta\Phi_i$ between the phase of an inspiral with a spinning secondary and an inspiral with a nonspinning secondary. All the calculations were done in *Mathematica* and we have used the *Black Hole Perturbation Toolkit* (BHPT) [41].

A. Implementation

Let us now discuss our approach to the numerical calculations of the adiabatic inspirals and of the phase shift in steps.

1. For given p and e, we calculate conservative trajectories; i.e., we find $\hat{E}$, $\hat{J}_z$, $\hat{\Omega}_i$, $\check{\hat{t}}(\chi)$, $\check{\hat{r}}(\chi)$, and $\check{\hat{\phi}}(\chi)$;
2. we find the linear in σ parts of the trajectory, i.e., δp, δe, $\delta\hat{E}$, $\delta\hat{J}_z$, $\delta\hat{t}(\chi)$, $\delta\hat{r}(\chi)$, and $\delta\hat{\phi}(\chi)$;
3. we compute the partial amplitudes $\hat{C}^{(\mathrm{g})\pm}_{lmn}$ and $\delta\hat{C}^{\pm}_{lmn}$ over a range of l, m, and n;
4. we repeat the steps 1–3 for many points in the $p-e$ plane, and then we interpolate the total energy and angular momentum fluxes;
5. we calculate the evolution of $p^{(\mathrm{g})}(\hat{t})$, $e^{(\mathrm{g})}(\hat{t})$, $\delta p(\hat{t})$, and $\delta e(\hat{t})$ for given initial parameters using the interpolated fluxes;
6. using $p^{(\mathrm{g})}(\hat{t})$, $e^{(\mathrm{g})}(\hat{t})$, $\delta p(\hat{t})$, and $\delta e(\hat{t})$, we find the linear parts of the phases $\delta\Phi_i$.

The above steps are described in detail in the following sections.

1. *Trajectories*

Before we calculate the amplitudes $\hat{C}^{\pm}_{lmn}$, we have to precompute the orbital quantities. For given $\hat{a}$, p, and e, we calculate the geodesic quantities $\hat{\Omega}_i$, $\hat{E}$, $\hat{J}_z$, $\check{\hat{t}}(\chi)$, $\check{\hat{r}}(\chi)$, and $\check{\hat{\phi}}(\chi)$ and the linear corrections due to the secondary spin with respect to this geodesic for the same frequencies. In particular, we obtain δp and δe from Eqs. (32), $\delta\hat{E}$ and $\delta\hat{J}_z$ we get from Eqs. (34), and, finally, $\delta\hat{t}(\chi)$, $\delta\hat{r}(\chi)$, and $\delta\hat{\phi}(\chi)$ are calculated from Eqs. (37). Moreover, the geodesic quantities $\check{t}(\chi)$ and $\check{\phi}(\chi)$ are calculated through the BHPT, which uses the discrete cosine transform (DCT) [42]. This method numerically transforms the integrand in Eqs. (23) into a series of cosines which is trivial to integrate. Actually, the linear in spin part of the trajectory, i.e., $\delta t(\chi)$ and $\delta\phi(\chi)$, is derived by employing DCT on 50 points obtained from Eqs. (37). With this number of points, the error is less than 10^{-6} for all the calculated orbital configurations; however, note that this error is much lower for orbits far from the separatrix and for orbits with lower eccentricity.

2. *Gravitational-wave fluxes*

The obtained orbital parameters can now be used for the calculation of the partial amplitudes. The description of how to calculate the non-linearized in spin amplitudes $\check{\hat{C}}^{\pm}_{lmn}$ can be found in Ref. [25]. In this work, we discuss the procedure allowing us to calculate the geodesic partial amplitude $\check{\hat{C}}^{(\mathrm{g})\pm}_{lmn}$ from Eq. (49) for $\sigma = 0$ and the linear in spin part $\delta\hat{C}^{\pm}_{lmn}\big|_{\Omega_i}$ according to Eq. (58). In particular, the integral in Eq. (58) is evaluated using

the midpoint rule, which should have exponential convergence [42], while for the calculation of the homogeneous solutions $R^{\pm}_{lm\omega}$ and $S^{a\omega}_{lm}$ the BHPT has been employed. More details about the calculation of the partial amplitudes and tests of their validity can be found in Appendix D.

To obtain an adequately accurate energy or angular momentum flux, we need to calculate the amplitudes $\mathcal{F}_{l,m,n}$ for a range of l, m, and n values. Thanks to the symmetry

$$\mathcal{F}_{l,m,n} = \mathcal{F}_{l,-m,-n}\,, \tag{81}$$
$$\hat{\omega}_{m,n} = -\hat{\omega}_{-m,-n}\,, \tag{82}$$

we decided to calculate only the modes with $\hat{\omega}_{mn} > 0$, and the total sum $\mathcal{F}$ can be found as double of the sum of calculated modes.[7] The structure of the summation is

$$\mathcal{F} = 2\sum_{m=m_{\min}}^{m_{\max}} \mathcal{F}_m\,, \tag{83a}$$
$$\mathcal{F}_m = \sum_{l=l_{\min}}^{l_{\max}} \mathcal{F}_{lm}\,, \tag{83b}$$
$$\mathcal{F}_{lm} = \sum_{n=n_{\min}}^{n_{\max}} \mathcal{F}_{lmn}\,, \tag{83c}$$

where $m_{\min} = -5$, $l_{\min} = \max\{2, |m|\}$ and $m_{\max}$, $l_{\max}$, $n_{\min}$, and $n_{\max}$ are chosen dynamically according to a given accuracy ϵ, i.e., the maximal allowed error. This error for the geodesic fluxes should be lower than the mass ratio; otherwise, it will be larger than the contribution from the postadiabatic terms, notably the secondary spin. In our calculations, we set the accuracy of the geodesic fluxes to $\epsilon = 10^{-6}$ and the accuracy of the linear corrections to the fluxes to $\epsilon = 10^{-3}$.

Our first step in our computation scheme is to calculate the modes with $m = l = 2$, $\lceil -m\hat{\Omega}_\phi/\hat{\Omega}_r\rceil \le n \le 20$, where the lower bound corresponds to the mode with minimal n, for which $\hat{\omega}_{mn} > 0$. In all the cases we treated, the mode with maximal flux $\max_{l,m,n}\mathcal{F}_{lmn}$ lays in this range. Then we continue the summation in n until the stopping condition for $n_{\max}$ is reached. This stopping condition is that the magnitude of three successive modes drops below $(\epsilon/10)\max\mathcal{F}_{lmn}$. This condition must be satisfied for three consecutive modes, because the modes are not monotonic in n, as has been reported already in other papers [9, 19].

At this point, we have obtained the dominant $\mathcal{F}_{l=2,m=2}$ mode. Similarly, we calculate the other $\mathcal{F}_{l,m=2}$ modes until the stopping condition for $l_{\max}$, i.e., $\mathcal{F}_{l_{\max}m} < \epsilon\mathcal{F}_{2,2}$, is satisfied. The magnitude of $\mathcal{F}_{lm}$ drops quickly with l, and usually for given m no more than four l modes are needed. In this way, we obtain the dominant $\mathcal{F}_{m=2}$ mode. After that, we calculate other m modes. For high m, modes with low n can be neglected. Therefore, we start the sum over n at $n_0 = \lfloor 10me^2\rfloor$, which is close to the maximal value of $\mathcal{F}_{lmn}$ for given l and m as we found empirically. Then we increase n until the stopping condition for $n_{\max}$ is satisfied. Finally, we decrease n until the condition for $n_{\min}$ is satisfied or until we reach $n = \lceil -m\hat{\Omega}_\phi/\hat{\Omega}_r\rceil$.

The above procedure is repeated for other values of m. The stopping condition for $m_{\max}$ is

$$\frac{\mathcal{F}_{m_{\max}}}{1-\mathcal{F}_{m_{\max}}/\mathcal{F}_{m_{\max}-1}} < \frac{\epsilon}{2}\sum_{m=m_{\min}}^{m_{\max}}\mathcal{F}_m\,. \tag{84}$$

If we assume that for high m the modes $\mathcal{F}_m$ decrease exponentially, the lhs of Eq. (84) corresponds to the terms neglected by the truncation of the sum over m at $m_{\max}$. For orbits with low p around a Kerr black hole with $\hat{a} = 0.9$ the number of m modes required for an accuracy $\epsilon = 10^{-6}$ is very high, so we truncate the sum at $m_{\max} = 25$ consciously knowing that we lose in accuracy.

The amplitudes were calculated in *Mathematica* using extended precision. For lower $\hat{a}$, l, and m, the input parameters are given to 48 places. However, for modes with higher $\hat{\omega}$ and $\hat{a}$, the calculation returns a wrong result due to the loss of precision during the calculation of $R^{\pm}_{lmn}$. Therefore, we check if the result lays orders of magnitudes away from the Newtonian amplitudes for circular orbits in Eq. (B3) in Ref. [23], and, when it does, we repeat the calculation with higher precision. The maximal precision is 112 places for higher $\hat{a}$, l, m and n, and lower p.

The calculation of individual modes with low eccentricity and n takes around one second, but for high eccentricities and n the computation time can be up to tens of seconds. All the modes in one grid point are calculated in around 1 h (1 day) for lower (higher) eccentricity. The calculation of the whole grid takes hundreds of CPU hours.

3. *Interpolation in the $p-e$ plane*

Because of the high computational cost, instead of calculating the fluxes during the evolution of the orbital parameters, they are precalculated on a grid in the $p-e$ plane and then interpolated. The grid is chosen to reflect the behavior near the separatrix and to avoid some problematic regions. Actually, this grid is not in the p and e coordinates, but in a new set of variables x and y which are obtained after several transformations from p and e.

The first transformation reads

$$\tilde{U} = \sqrt{(p-\hat{r}_{\rm ISCO})^2 - (p_{\rm s}(e)-\hat{r}_{\rm ISCO})^2}\,, \tag{85}$$
$$V = e^2\,, \tag{86}$$

[7] All formulas in this subsection are valid both for the fluxes $\mathcal{F}$ and their linear parts $\delta\mathcal{F}$. We demonstrate the formulas with $\mathcal{F}$ for brevity.

where $p_{\rm s}(e)$ is the location of the separatrix. The purpose of this transformation is to make the quantities and their derivatives finite for circular orbits, i.e., for $e = 0$. Namely, since the fluxes depend only on even powers of e, their derivative with respect to e vanishes for $e = 0$. The inverse relation of Eq. (85) reads

$$p = \hat{r}_{ISCO} + \sqrt{\tilde{U}^2 + (p_{\rm s}(\sqrt{V}) - \hat{r}_{ISCO})^2}\,. \tag{87}$$

Next, we transform from $\tilde{U}$ to

$$U = \frac{c}{\log\left(1 + c/\tilde{U}\right)} \tag{88}$$

to regularize the quantities near the separatrix. c is a parameter controlling the grid density near the separatrix. For higher c, the grid points are more dense near the separatrix, while for $c \to 0$ it holds that $U \to \tilde{U}$. We have chosen the value $c = 25$ in our calculations. The asymptotic behavior of these transformations is

1. $U \to p$, when $p \to \infty$, and
2. $U \to -1/\log(p - p_{\rm s})$, when $p \to p_{\rm s}$,

which is proportional to the behavior of the radial frequency $\hat{\Omega}_r$ near the separatrix [38, 43].

We made one additional transformation to avoid two areas with high eccentricity: (a) an area with high p, for which the total time of the inspiral is very long, and (b) an area close to the separatrix, for which the inspiral must start with very high eccentricity. This transformation to $\mathsf{x} \in (0,1)$, $\mathsf{y} \in (0,1)$ is given by

$$\begin{aligned} U = {} & (U_{11} - U_{10} + U_{00} - U_{01})\mathsf{xy} + (U_{10} - U_{00})\mathsf{x} \\ & + (U_{01} - U_{00})\mathsf{y} + U_{00}\,, \end{aligned} \tag{89}$$

$$V = (V_{11} - V_{01})\mathsf{xy} + (V_{01} - V_{00})\mathsf{y}\,, \tag{90}$$

where the parameters U_{xy} and V_{xy} are chosen according to the boundaries described in the following paragraph.

The GW fluxes were calculated on a grid in Chebyshev nodes in the x, y coordinates. We used 15 grid points in both directions. The boundaries were chosen for each value of $\hat{a}$ separately. In all $\hat{a}$ cases, the coordinates of the lower left corners are $(p, e) = (\hat{r}_{\rm ISCO}(\hat{a}) + 0.15, 0)$. For $\hat{a} = 0$, the upper left corner is at $(p_{\rm s}(0.6) + 0.1, 0.6)$ and at $(p_{\rm s}(0.5) + 0.1, 0.5)$ for $\hat{a} = 0.5, 0.9$. The lower right corner is located at $(40, 0)$ or $(30, 0)$ for $\hat{a} = 0$ or $\hat{a} = 0.5, 0.9$, respectively. The coordinates of the upper right corner are $(20, 0.8)$ for $\hat{a} = 0$, $(15, 0.8)$ for $\hat{a} = 0.5$ and $(15, 0.75)$ for $\hat{a} = 0.9$. These grids are depicted in Fig. 2.

On the grid, we interpolated the total energy and angular momentum fluxes $\mathcal{F}^{E(\rm g)}$ and $\mathcal{F}^{J_z(\rm g)}$ with their linear in spin counterparts $\delta\mathcal{F}^E$ and $\delta\mathcal{F}^{J_z}$, respectively, the time derivatives of the orbital parameters $\dot{p}^{(\rm g)}$ and $\dot{e}^{(\rm g)}$, and the derivatives of $\dot{p}$ and $\dot{e}$ with respect to σ, p, and e for the calculation of $\delta\dot{p}$ and $\delta\dot{e}$ using Eq. (76). Each

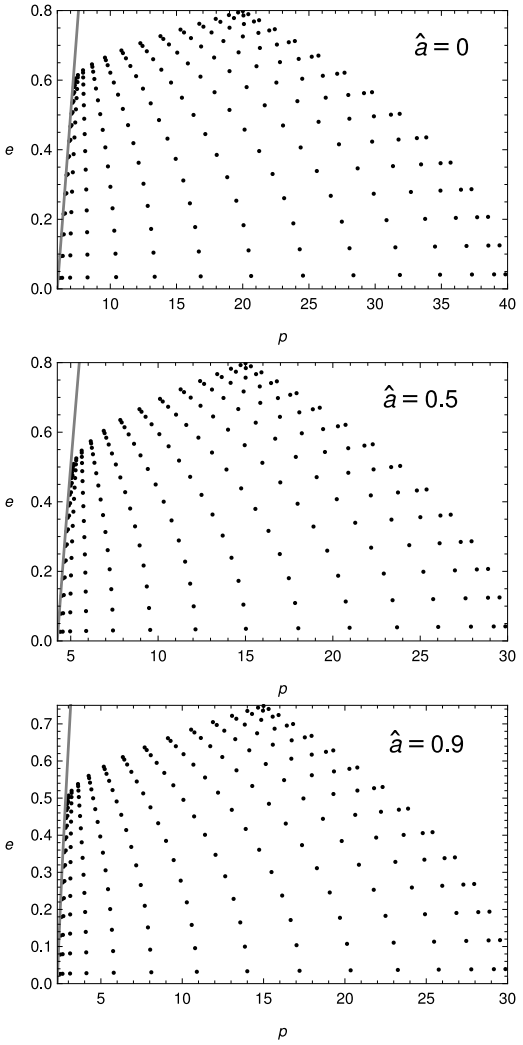

FIG. 2. Grids for the interpolation in $p - e$ plane. The grid points are at Chebyshev nodes in $\mathsf{x} - \mathsf{y}$ plane.

function was divided by the following normalization factors to regularize the behavior near the separatrix, for high p and for low e:

$$N_{\mathcal{F}^E} = \frac{32}{5} p^{-5} \left(1 - e^2\right)^{3/2} \left(1 + \frac{73}{24} e^2 + \frac{37}{96} e^4\right), \tag{91a}$$

$$N_{\mathcal{F}^{J_z}} = \frac{32}{5} p^{-7/2} \left(1 - e^2\right)^{3/2} \left(1 + \frac{7}{8} e^2\right), \tag{91b}$$

$$N_{\delta\mathcal{F}^E} = -\frac{25}{4} p^{-3/2} N_{\mathcal{F}^E} \frac{p^2}{\tilde{U}^2}\,, \tag{91c}$$

$$N_{\delta\mathcal{F}^{J_z}} = -\frac{25}{4}p^{-3/2}N_{\mathcal{F}^{J_z}}\frac{p^2}{\tilde{U}^2}\,, \tag{91d}$$

$$N_{\dot{p}^{(\mathrm{g})}} = \frac{8}{5}p^{-3}\left(1-e^2\right)^{3/2}\left(8+7e^2\right)\frac{p^2}{\tilde{U}^2}\,, \tag{91e}$$

$$N_{\dot{e}^{(\mathrm{g})}} = \frac{1}{15}ep^{-4}\left(1-e^2\right)^{3/2}\left(304+121e^2\right)\frac{p^2}{\tilde{U}^2}\,, \tag{91f}$$

$$N_{\partial_\sigma \dot{p}} = \frac{1}{\tilde{U}^4}\left(1-e^2\right)^{3/2}, \tag{91g}$$

$$N_{\partial_\sigma \dot{e}} = e\frac{1}{p\tilde{U}^4}\left(1-e^2\right)^{3/2}, \tag{91h}$$

$$N_{\partial_p \dot{p}} = \frac{p}{\tilde{U}^4}\left(1-e^2\right)^{3/2}, \tag{91i}$$

$$N_{\partial_e \dot{p}} = e\frac{p^2}{\tilde{U}^4}\,, \tag{91j}$$

$$N_{\partial_p \dot{e}} = e\frac{1}{\tilde{U}^4}\left(1-e^2\right)^{3/2}, \tag{91k}$$

$$N_{\partial_e \dot{e}} = \frac{p}{\tilde{U}^4}\,. \tag{91l}$$

The behavior of $N_{\mathcal{F}^E}$ and $N_{\mathcal{F}^{J_z}}$ comes from Ref. [44], where they derived the fluxes from a Keplerian orbit, which represents the large p limit. On the other hand, the behavior of $N_{\delta\mathcal{F}^E}$ and $N_{\delta\mathcal{F}^{J_z}}$ for large p is derived from the post-Newtonian GW fluxes of spinning particles on circular equatorial orbits [45]. The accuracy of the interpolation is discussed in Appendix E.

4. *Evolution of the orbital parameters*

Uusing the interpolated functions obtained in the previous section multiplied by the normalization factors allows the calculation of the evolution of the geodesic orbital parameters $p^{(\mathrm{g})}(\hat{t})$ and $e^{(\mathrm{g})}(\hat{t})$ and the respective corrections $\delta p(\hat{t})$ and $\delta e(\hat{t})$. For given initial parameters $p_0^{(\mathrm{g})}$ and $e_0^{(\mathrm{g})}$, we numerically solved Eqs. (75) in *Mathematica* using the 7/8th-order Runge-Kutta method with adaptive step size. The calculation was terminated when the orbital parameters reached the boundary at $\mathsf{x} = 0$.

These results were then used to evolve Eqs. (76) for given initial conditions $\delta p_0^{(\mathrm{g})}$ and $\delta e_0^{(\mathrm{g})}$. These initial conditions specify the trajectory of a spinning particle, which is then compared with the geodesic starting at $p_0^{(\mathrm{g})}$ and $e_0^{(\mathrm{g})}$. The case $\delta p_0 = 0 = \delta e_0$ corresponds to a trajectory of a spinning particle compared with a geodesic which starts at the same $p_0^{(\mathrm{g})}$ and $e_0^{(\mathrm{g})}$.

However, δp_0 and δe_0 can be chosen such that we compare a trajectory of a spinning particle with a geodesic with the same initial orbital frequencies $\hat{\Omega}_r$ and $\hat{\Omega}_\phi$. In this case, we set δp_0 and δe_0 to

$$\delta p_0 = \delta p(p_0^{(\mathrm{g})}, e_0^{(\mathrm{g})})\,, \tag{92a}$$

$$\delta e_0 = \delta e(p_0^{(\mathrm{g})}, e_0^{(\mathrm{g})})\,, \tag{92b}$$

respectively, where the functions δp and δe have been defined in Eq. (32).

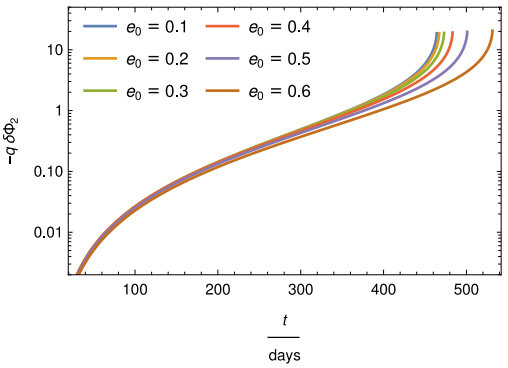

FIG. 3. The phase shift $q\delta\Phi_m = qm\delta\Phi_\phi$ of the dominant $m = 2$ mode for properly matched initial azimuthal frequency Ω_ϕ and eccentricity e. The inspirals of a spinning particle with $\mu = 30M_\odot$ into a Kerr black hole with $M = 10^6 M_\odot$, $\hat{a} = 0.9$, start from $p_0^{(\mathrm{g})} = 10.1$.

We have also calculated the case where the trajectory of a spinning particle is compared with a geodesic with the same initial eccentricity e and azimuthal frequency $\hat{\Omega}_\phi$. This choice was used in previous works [24, 46] when calculating quasicircular inspirals. In this case, we set

$$\delta p_0 = -\frac{\frac{\partial\hat{\Omega}_\phi}{\partial\sigma}}{\frac{\partial\hat{\Omega}_\phi}{\partial p}} \tag{93a}$$

$$\delta e_0 = 0 \tag{93b}$$

evaluated at $p_0^{(\mathrm{g})}$, $e_0^{(\mathrm{g})}$, and $\sigma = 0$.

5. *Evolution of the phase shifts*

After the calculation of the orbital parameters, we calculated the linear parts of the phases $\delta\Phi_i$ using Eq. (79) with the default solver `NDSolve` in *Mathematica*. The results were compared with nonlinearized inspiral to verify them. Details are given in Appendix F.

B. Results

1. *Matched eccentricity and azimuthal frequency*

When the phase shift $\delta\Phi_\phi$ is calculated for circular orbits, the phase from an inspiral with a nonspinning secondary is compared with an inspiral with a spinning secondary which has the same initial azimuthal frequency Ω_ϕ and initial eccentricity $e = 0$ as the inspiral with a nonspinning secondary. Obviously, the radial frequency Ω_r is not relevant for circular orbits; in fact, the partial amplitudes C^0_{lmn} vanish for $n \neq 0$, and only the modes with frequency $m\Omega_\phi$ remain. However, we can extend

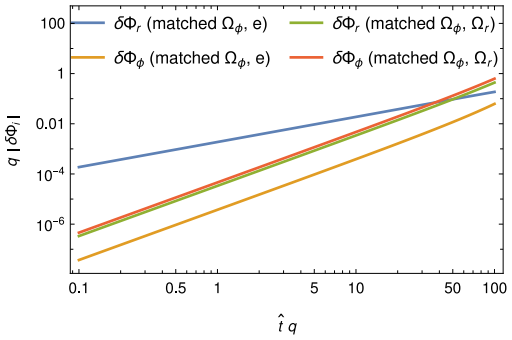

FIG. 4. Phase shifts $q\delta\Phi_i$ for different initial conditions. The inspirals are around a Kerr black hole with $\hat{a} = 0.9$ and start at $p_0^{(\mathrm{g})} = 10.1$ and $e_0^{(\mathrm{g})} = 0.2$. For matched Ω_ϕ and e, $\delta\Phi_\phi$ grows as $\hat{t}^2$ and $\delta\Phi_r$ grows as $\hat{t}$ for low t, while for matched Ω_r and Ω_ϕ both $\delta\Phi_r$ and $\delta\Phi_\phi$ grow as $\hat{t}^2$.

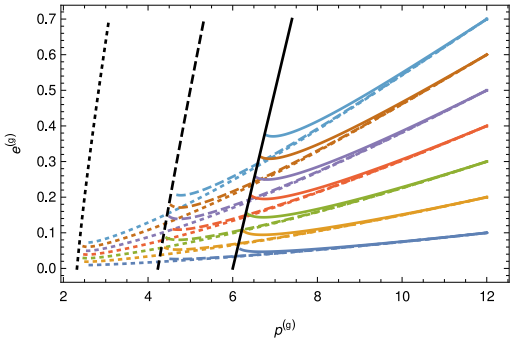

FIG. 5. Adiabatic evolution of $p^{(\mathrm{g})}$ and $e^{(\mathrm{g})}$ for $\hat{a} = 0$ (solid line), $\hat{a} = 0.5$ (dashed line), and $\hat{a} = 0.9$ (dotted line), while the respective black lines denote the separatrices, where the evolution ends.

this approach to the calculation of the phase shift from eccentric inspirals by choosing properly the initial conditions as given in Eq. (93). The corresponding numerical examples are given in Fig. 3, which shows the phase shift $\delta\Phi_{2,0}$ for the dominant $m = 2$ mode. Fig. 3 is consistent with Fig. 2 from Ref. [46] and Fig. 3 from Ref. [24]. Note that, since we examine the phase at constant distance from the central black hole, i.e., at constant $\hat{r}$, we can use t as the time variable instead of u.

When the initial azimuthal frequency and eccentricity are properly matched, the phase shift $\delta\Phi_\phi$ grows as $\hat{t}^2$, whereas $\delta\Phi_r$ grows as $\hat{t}$ for low $\hat{t}$, as can be seen in Fig. 4. The reason for this behavior is that the initial value for

$$\delta\hat{\Omega}_i = \left.\frac{\partial\hat{\Omega}_i}{\partial\sigma}\right|_{\sigma=0} + \frac{\partial\hat{\Omega}_i^{(\mathrm{g})}}{\partial p}\delta p + \frac{\partial\hat{\Omega}_i^{(\mathrm{g})}}{\partial e}\delta e\,, \qquad (94)$$

which appears in the integral (79), is zero for $\delta\hat{\Omega}_\phi$, but it is nonzero for $\delta\hat{\Omega}_r$. Thus, the phase shift $\delta\Phi_r$ grows linearly in $\hat{t}$ after the integration for low $\hat{t}$.

2. *Matched frequencies*

Since for eccentric orbits both frequencies are observable, we prefer to match the initial frequencies according to Eqs. (92) than as discussed in Sec. V B 1. For this initial setting, both $\delta\Phi_\phi$ and $\delta\Phi_r$ grow as $\hat{t}^2$ for low t, as can be seen in Fig. 4. In the numerical example given in Fig. 5, we have calculated the inspiral providing the evolution of $p^{(\mathrm{g})}(\hat{t})$ and $e^{(\mathrm{g})}(\hat{t})$ for initial semilatus rectum $p_0^{(\mathrm{g})} = 12$ and different initial eccentricities. The respective phase shifts for $\hat{a} = 0$, $\hat{a} = 0.5$, and $\hat{a} = 0.9$ are shown in Figs. 6–8. The linear in spin part of the azimuthal phase $\delta\Phi_\phi$ is increasing and is positive as opposed to the case with matched initial Ω_ϕ and e in Sec. V B 1, where it is negative (see Fig. 3). The linear part of the radial

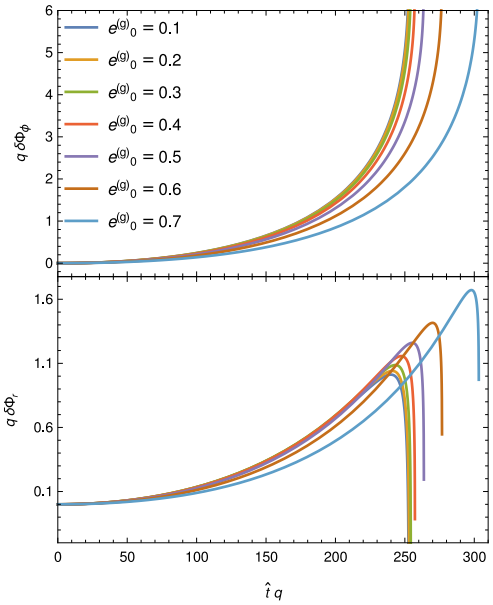

FIG. 6. The azimuthal (top) and the radial (bottom) phase shift for orbits around a Schwarzschild black hole with initial semilatus rectum $p_0^{(\mathrm{g})} = 12$ and different initial eccentricities. This plot shows the phase shift when the particle has spin $\sigma = q$, i.e., the secondary corresponds to an extremal Kerr black hole.

phase $\delta\Phi_r$ is increasing and positive for the majority of the inspiral; however, right before the trajectory reaches the separatrix, $\delta\Phi_r$ starts to decrease. Both $\delta\Phi_\phi$ and $\delta\Phi_r$ diverge when the trajectory is approaching the separatrix, because both the linearization in spin and the two-scale approximation break at the separatrix.

In Ref. [47], where they compared eccentric equato-

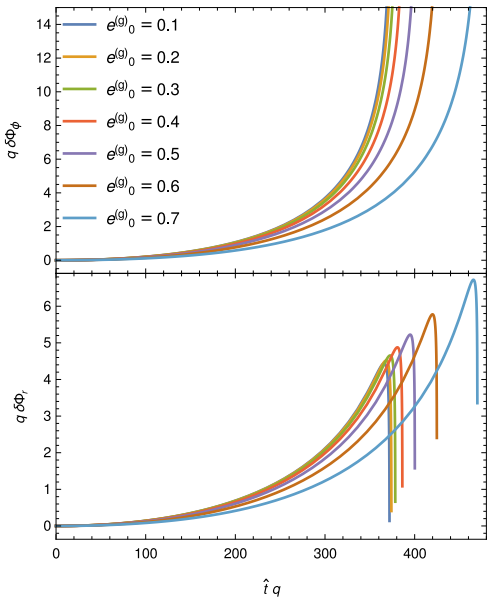

FIG. 7. The same as Fig. 6, but for a Kerr black hole with $\hat{a} = 0.5$

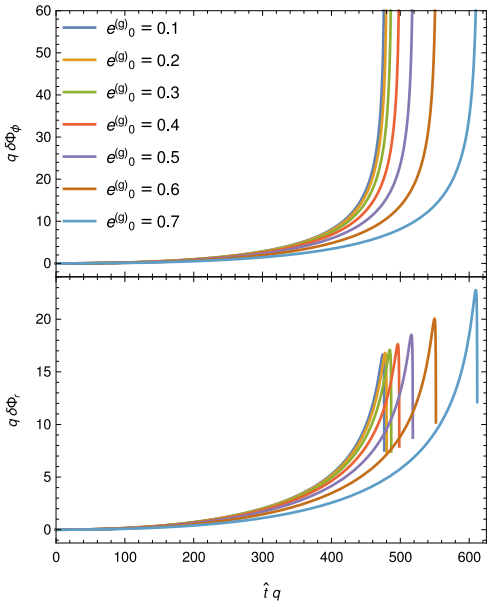

FIG. 8. The same as Fig. 6, but for a Kerr black hole with $\hat{a} = 0.9$

rial inspirals of spinning particles into a Schwarzschild black hole using the osculating geodesics method, they

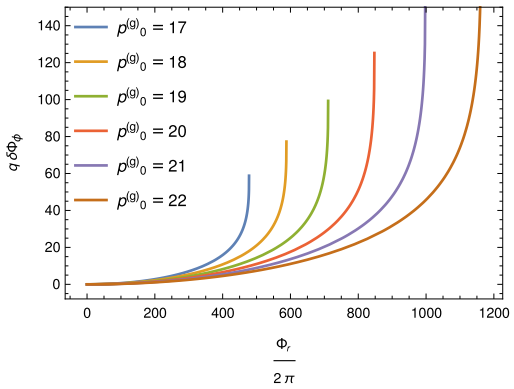

FIG. 9. The phase shift for inspirals around a Schwarzschild black hole with initial eccentricity $e^{(g)}_0 = 0.75$ and $\sigma = q$. The horizontal axis corresponds to the number of passages through the pericenter.

found initial parameters for which the difference $\Delta\phi = \phi_{\sigma=q} - \phi_{\sigma=0}$ between the azimuthal coordinates $\phi_{\sigma=q}$ of a spinning body and $\phi_{\sigma=0}$ of a nonspinning body changes its sign during the inspiral (Fig. 2 in Ref. [47]). However, that work included only the MPD force into the equations of motion and did not take into account the correction to the self-force caused by the body's spin. We have calculated the phase shift $q\delta\Phi_\phi$, which should correspond to $\Delta\phi$ when the particle passes the pericenter, for the same initial parameters as Ref. [47] and found no change in the sign of $\Delta\phi$ (see Fig. 9). However, note that we have not included the conservative and oscillating dissipative parts of the self-force, and, thus, these results are not directly comparable. Also, the accumulated phase shift is higher in our Fig. 9, where the secondary's spin contribution is incorporated to the fluxes, than in Fig. 2 in Ref. [47], where this contribution has not been taken into account.

To systematically probe the parameter space, we have calculated the inspirals for various initial parameters, and for each inspiral we have found the maximum of the radial phase shift $\max q\delta\Phi_r$.[8] Then we have plotted this maximum against the initial eccentricity $e^{(g)}_0$ and the mass ratio q, assuming that the duration of the inspiral is 1 yr while the mass of the central black hole is $M = 10^6 M_\odot$. At each point in the $q - e^{(g)}_0$ plane, the inspirals start at different initial semilatus rectum $p^{(g)}_0$. The calculation was repeated for $\hat{a} = 0, 0.5, 0.9$, and the results are shown in Fig. 10. We can see that for a higher mass ratio the maximal phase shift is higher, which corresponds to higher $p^{(g)}_0$. For higher $\hat{a}$, the maximal phase shift is almost independent of the initial eccentricity, but, to find

[8] In Appendix F we verify that the accuracy of the phase shift is high and the approximations are valid at this point.

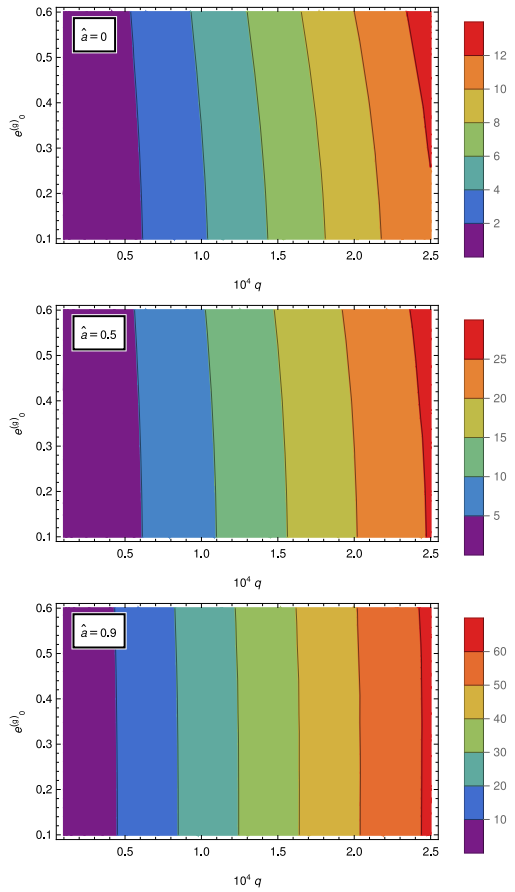

FIG. 10. The maximal radial phase shift $\max q\delta\Phi_r$ for different initial eccentricities, mass ratios, and Kerr parameters. The mass of the central black hole is $M = 10^6 M_\odot$ and the duration of the inspirals is 1 yr. This phase shift corresponds to a particle with spin $\sigma = q$.

the degeneracies in the parameter space and to assess the detectability of the initial eccentricity or the secondary spin, proper analysis must be done, which is out of the scope of the present technical work.

VI. CONCLUSIONS

We studied the influence of the spin σ of a secondary body on the phase of a GW from an EMRI moving on the equatorial plane of a Kerr black hole. Thanks to the fact that the spin σ is of the same order as the mass ratio q, we worked in the linear order in σ, neglecting higher-order terms. We emphasize that our results are not sufficient for the generation of the waveform templates for the detection, since they must be accurately and rapidly generated in the whole parameter space. The purpose of this work is to provide the technical background needed to calculate the secondary's spin contributions to the waveform.

The first step to achieve our goal was to derive the linear in σ parts of the orbital parameters p and e, constants of motion E and J_z and the coordinate functions $t(\chi)$, $r(\chi)$, and $\phi(\chi)$ in the Darwin parametrization. The linearization was done with respect to a reference geodesic with the same frequencies Ω_r and Ω_ϕ. Then we used these quantities to linearize the GW fluxes to infinity and through the horizon. We provided the linear parts $\delta\mathcal{F}^E$ and $\delta\mathcal{F}^{J_z}$ of the total energy and angular momentum flux using the Teukolsky formalism in the frequency domain. Again, we calculated the linear part with respect to a geodesic with the same frequencies. We also found the relation between the latter type of linearization and the linearization with respect to a geodesic with the same orbital parameters p and e.

The fluxes were calculated on a grid in the $p-e$ plane and interpolated, since the calculation at one point is computationally expensive. Once we have calculated the energy and angular momentum fluxes linearized in σ, we derived the evolution equations for the orbital parameters $p^{(\mathrm{g})}(t)$ and $e^{(\mathrm{g})}(t)$ for a nonspinning secondary and for corrections due to the spin $\delta p(t)$ and $\delta e(t)$. After that, we have evolved these quantities numerically. From the evolution of the orbital parameters and their corrections, we then constructed the evolution of the phase shifts $\delta\Phi_r(t)$ and $\delta\Phi_\phi(t)$, which is the difference between the GW phase from an inspiral with a spinning and a nonspinning secondary. We tested the results against nonlinearized evolution obtained from the fluxes, that were derived in Ref. [25]. We found that the error of the phase shifts, i.e., the relative difference between linearized and non-linearized phase shifts, is around 10^{-3}.

The phase shifts were computed using two different types of initial conditions. First we set the initial conditions such that we compared inspirals with a spinning and a nonspinning secondary which start with the same azimuthal frequency Ω_ϕ and eccentricity e. This was done to validate the results against quasicircular inspirals. We have found the expected behavior where the azimuthal phase shift grows as t^2 for low t and the radial phase shift grows as t. After that, we set the initial condition such that we compare inspirals with the same initial radial frequency Ω_r and azimuthal frequency Ω_ϕ. We found that the azimuthal phase shift is positive, as opposed to the previous choice of initial condition, and that the radial phase shift is positive and increasing up to a point before it reaches the separatrix, where it becomes decreasing. Both the azimuthal and radial phase shift diverge when the inspiral reaches the separatrix, and, thus, a different method must be employed for the waveform generation near the plunge in the future.

To systematically probe the parameter space and find the general behavior of the phase shifts, we calculated

the maximal value of the radial phase shift for different initial eccentricities, mass ratios, and Kerr parameters while fixing the masses of the bodies and the observation time. We found that the maximal radial phase shift grows with the mass ratio and the Kerr parameter and almost does not depend on the eccentricity.

In the future, this work can be extended to off-equatorial orbits with precessing spin, which is significantly more complex since the equations of motion are not separable, even in the linear in spin order [48]. We are also planing to generate the waveforms using the *FastEMRIWaveforms* package [11] to find the degeneracies in the parameter space and to assess the detectability, since in Ref. [49] it was claimed that for quasicircular orbits the secondary spin should not be detectable, while in Ref. [50] it was claimed that effects of spin-induced quadrupolar deformation, which are of $\mathcal{O}(\sigma^2)$, are strong enough for the detection.

ACKNOWLEDGMENTS

The authors have been supported by the fellowship Lumina Quaeruntur No. LQ100032102 of the Czech Academy of Sciences. V.S. acknowledges support by the project "Grant schemes at CU" (reg.no. CZ.02.2.69/0.0/0.0/19_073/0016935). We would like to thank Tomáš Ledvinka and Maarten van de Meent for useful discussions and comments. This work makes use of the Black Hole Perturbation Toolkit. Computational resources were supplied by the project "e-Infrastruktura CZ" (e-INFRA CZ LM2018140) supported by the Ministry of Education, Youth and Sports of the Czech Republic.

Appendix A: List of dimensionless quantities

In this work, we define some quantities in their dimensionless form. However, since we use these quantities often in both full and dimensionless form, we present the respective relations in Table I.

Note that some quantities such as x or the fluxes $\mathcal{F}$ have been defined solely as dimensionless; quantities derived from others, e.g., by linearization in σ, have the same relation between their dimensionless and full form as the original quantities.

Appendix B: Eccentric equatorial orbits of spinning particles

This appendix briefs some formulas describing the motion of spinning particles on bound eccentric equatorial orbits around a Kerr black hole. Details regarding these formulas can be found in Refs. [25, 51].

Bound equatorial orbits of a spinning particle moving around a Kerr black hole can be parametrized by

TABLE I. List of dimensionless quantities

$\sigma = S/(\mu M)$	Secondary spin
$\hat{t} = t/M$	BL time
$\hat{r} = r/M$	BL radial coordinate
$\hat{E} = E/\mu$	Energy
$\hat{J}_z = J_z/(\mu M)$	Angular momentum
$\hat{a} = a/M$	Kerr parameter
$\hat{T}_r = T_r/M$	Radial period
$\hat{\Omega}_r = \Omega_r M$	Radial BL frequency
$\hat{\Omega}_\phi = \Omega_\phi M$	Azimuthal BL frequency
$\hat{\omega} = \omega M$	Frequency
$\hat{C}^{\pm}_{lmn} = C^{\pm}_{lmn} M^2/\mu$	Partial amplitudes
$\hat{A}^{\pm}_{lmn} = A^{\pm}_{lmn}/M$	Waveform amplitudes
$\hat{u} = u/M$	Retarded coordinate
$\hat{\Delta} = \Delta/M^2$	
$\hat{\varpi}^2 = \varpi^2/M^2$	

the eccentricity e and the semilatus rectum p. This parametrization is in one-to-one correspondence to the parametrization with respect to the energy $\hat{E}$ and the z component of total angular momentum $\hat{J}_z$. The expressions of $\hat{E}$ and $\hat{J}_z$ as functions of p and e read

$$\hat{E}^2 = \frac{\kappa\rho + 2\epsilon\tilde{\sigma} - 2\,\mathrm{sgn}\,(\hat{J}_z)\,\tilde{\sigma}\sqrt{\epsilon^2 + \kappa\zeta}}{\rho^2 + 4\eta\tilde{\sigma}}\,, \tag{B1}$$

$$\hat{J}_z = \frac{\epsilon\rho - 2\kappa\eta - \mathrm{sgn}\,(\hat{J}_z)\,\rho\sqrt{\epsilon^2 + \kappa\zeta}}{(\rho^2 + 4\eta\tilde{\sigma})\hat{E}}\,, \tag{B2}$$

respectively, where the coefficients

$$\begin{aligned}
\kappa &= d_1 h_2 - d_2 h_1\,,\\
\epsilon &= d_1 g_2 - d_2 g_1\,,\\
\rho &= f_1 h_2 - f_2 h_1\,,\\
\eta &= f_1 g_2 - f_2 g_1\,,\\
\tilde{\sigma} &= g_1 h_2 - g_2 h_1\,,\\
\zeta &= d_1 f_2 - d_2 f_1
\end{aligned}$$

are calculated from the functions

$$\begin{aligned}
f(\hat{r}) =& \hat{a}^2(\hat{r}+2)\hat{r} + \hat{r}^4 + \\
&+ \sigma\left(\frac{\hat{a}^2\sigma}{\hat{r}^2} + \frac{2\hat{a}^2(\hat{a}+\sigma)}{\hat{r}} + 6\hat{a}\hat{r} - (\hat{r}-2)\hat{r}\sigma\right)\,,\\
g(\hat{r}) =& 2\hat{a}\hat{r} + \sigma\left(\frac{\hat{a}\sigma}{\hat{r}^2} + \frac{\hat{a}(2\hat{a}+\sigma)}{\hat{r}} - (\hat{r}-3)\hat{r}\right)\,,\\
h(\hat{r}) =& \hat{\Delta} - \left(\hat{a} + \frac{\sigma}{\hat{r}}\right)^2\,,\\
d(\hat{r}) =& \frac{\hat{\Delta}(\hat{r}^3 - \sigma^2)^2}{\hat{r}^4}\,.
\end{aligned}$$

at the pericenter $f_1 = f(p/(1+e))$ and at the apocenter $f_2 = f(p/(1-e))$, etc.

The trajectories in Darwin parametrization can then

be calculated from the evolution equations (22) with

$$V^t = \hat{a}\left(1+\frac{3\sigma^2}{\hat{r}\Sigma_\sigma}\right)x + \frac{\varpi^2}{\Delta}P_\sigma \,, \tag{B3}$$

$$V^\phi = \left(1+\frac{3\sigma^2}{\hat{r}\Sigma_\sigma}\right)x + \frac{\hat{a}}{\hat{\Delta}}P_\sigma \,, \tag{B4}$$

$$P_\sigma = \Sigma_\sigma \hat{E} - \left(\hat{a}+\frac{\sigma}{\hat{r}}\right)x \,, \tag{B5}$$

$$\Sigma_\sigma = \hat{r}^2\left(1-\frac{\sigma^2}{\hat{r}^3}\right) \,, \tag{B6}$$

$$x = \hat{J}_z - (\hat{a}+\sigma)\hat{E} \tag{B7}$$

and

$$J(\chi) = \sum_{k=0}^{6}(1+e\cos\chi)^k \sum_{l=0}^{k}\frac{j_l^{(p)} j_{k-l}^{(e)}}{(1-e^2)^{k-l}p^l} \tag{B8}$$

with

$$\begin{aligned}
j_0^{(p)} &= 1-\hat{E}^2 \,,\\
j_1^{(p)} &= -2 \,,\\
j_2^{(p)} &= \hat{a}^2 + 2\hat{a}\hat{E}x + x^2 \,,\\
j_3^{(p)} &= -2((1-\hat{E}^2)\sigma^2 - \hat{E}\sigma x + x^2) \,,\\
j_4^{(p)} &= 4\sigma^2 \,,\\
j_5^{(p)} &= -2\hat{a}\sigma(\hat{a}\sigma + x(\hat{E}\sigma + x)) \,,\\
j_6^{(p)} &= \sigma^2((1-\hat{E}^2)\sigma^2 - 2\hat{E}\sigma x - x^2)
\end{aligned}$$

and

$$\begin{aligned}
j_0^{(e)} &= 1 \,,\\
j_1^{(e)} &= 2 \,,\\
j_2^{(e)} &= e^2+3 \,,\\
j_3^{(e)} &= 4(e^2+1) \,,\\
j_4^{(e)} &= e^4+10e^2+5 \,,\\
j_5^{(e)} &= 2(e^2+3)(3e^2+1) \,,\\
j_6^{(e)} &= e^6+21e^4+35e^2+7 \,.
\end{aligned}$$

Appendix C: Linearized evolution of the orbital parameters

In this appendix we provide formulas for the evolution of the corrections δp and δe in Sec. IV A. The evolution of the linear parts δp and δe is governed by Eqs. (76) where the functions $\delta\dot{p}$ and $\delta\dot{e}$ are, respectively,

$$\delta\dot{p} = \left.\frac{\partial\dot{p}}{\partial\sigma}\right|_{\sigma=0} + \frac{\partial\dot{p}^{(\mathrm{g})}}{\partial p}\delta p + \frac{\partial\dot{p}^{(\mathrm{g})}}{\partial e}\delta e \,, \tag{C1}$$

$$\delta\dot{e} = \left.\frac{\partial\dot{e}}{\partial\sigma}\right|_{\sigma=0} + \frac{\partial\dot{e}^{(\mathrm{g})}}{\partial p}\delta p + \frac{\partial\dot{e}^{(\mathrm{g})}}{\partial e}\delta e \,. \tag{C2}$$

After substitution from Eqs. (68), the σ derivatives read

$$\begin{aligned}
\frac{\partial\dot{p}}{\partial\sigma} &= \frac{\dfrac{\partial^2\hat{J}_z}{\partial e\partial\sigma}\dot{\hat{E}} + \dfrac{\partial\hat{J}_z}{\partial e}\delta\dot{\hat{E}} - \dfrac{\partial^2\hat{E}}{\partial e\partial\sigma}\dot{\hat{J}}_z - \dfrac{\partial\hat{E}}{\partial e}\delta\dot{\hat{J}}_z}{\left|J_{(\hat{E},\hat{J}_z)}\right|}\\
&\quad - \frac{\dfrac{\partial\hat{J}_z}{\partial e}\dot{\hat{E}} - \dfrac{\partial\hat{E}}{\partial e}\dot{\hat{J}}_z}{\left|J_{(\hat{E},\hat{J}_z)}\right|^2}\frac{\partial\left|J_{(\hat{E},\hat{J}_z)}\right|}{\partial\sigma} \,,
\end{aligned} \tag{C3}$$

$$\begin{aligned}
\frac{\partial\dot{e}}{\partial\sigma} &= \frac{-\dfrac{\partial^2\hat{J}_z}{\partial p\partial\sigma}\dot{\hat{E}} - \dfrac{\partial\hat{J}_z}{\partial p}\delta\dot{\hat{E}} + \dfrac{\partial^2\hat{E}}{\partial p\partial\sigma}\dot{\hat{J}}_z + \dfrac{\partial\hat{E}}{\partial p}\delta\dot{\hat{J}}_z}{\left|J_{(\hat{E},\hat{J}_z)}\right|}\\
&\quad - \frac{-\dfrac{\partial\hat{J}_z}{\partial p}\dot{\hat{E}} + \dfrac{\partial\hat{E}}{\partial p}\dot{\hat{J}}_z}{\left|J_{(\hat{E},\hat{J}_z)}\right|^2}\frac{\partial\left|J_{(\hat{E},\hat{J}_z)}\right|}{\partial\sigma} \,,
\end{aligned} \tag{C4}$$

$$\frac{\partial|J|}{\partial\sigma} = \frac{\partial^2\hat{E}}{\partial p\partial\sigma}\frac{\partial\hat{J}_z}{\partial e} + \frac{\partial\hat{E}}{\partial p}\frac{\partial^2\hat{J}_z}{\partial e\partial\sigma} - \frac{\partial^2\hat{E}}{\partial e\partial\sigma}\frac{\partial\hat{J}_z}{\partial p} - \frac{\partial\hat{E}}{\partial e}\frac{\partial^2\hat{J}_z}{\partial p\partial\sigma} \,, \tag{C5}$$

where $\delta\dot{E}$ and $\delta\dot{J}_z$ are given by the linear parts of the fluxes

$$\delta\dot{\hat{E}} = -q\;\delta\mathcal{F}^E\Big|_{p,e} \,, \tag{C6}$$

$$\delta\dot{\hat{J}}_z = -q\;\delta\mathcal{F}^{J_z}\Big|_{p,e} \,. \tag{C7}$$

The derivatives of $\dot{p}$ and $\dot{e}$ with respect to p and e are calculated similarly, while the derivatives of the constants of motion with respect to p, e, and σ can be calculated from Eqs. (B1) and (B2). The exact formulas of the latter are not presented here, because, even if they are straightforward to calculate, they have long complex forms. Interested readers can find them in the Supplemental Material [36].

Appendix D: Linearized partial amplitudes

Here, we give more details about the calculation of the linearized in spin partial amplitudes $\delta C^{\pm}_{lmn}$ (Eq. (58)). The linear part of $I^{\pm}_{lmn}$ from Eq. (46) reads

$$\begin{aligned}
\frac{\mathrm{d}I^{\pm}_{lmn}}{\mathrm{d}\sigma} &= \frac{1}{W}\Bigg(\delta A_0 - (\delta A_1 + \delta B_0 - A_0\delta r)\frac{\mathrm{d}}{\mathrm{d}r}\\
&+ (\delta A_2 + \delta B_2 - A_1\delta r)\frac{\mathrm{d}^2}{\mathrm{d}r^2} - (\delta B_3 - A_2\delta r)\frac{\mathrm{d}^3}{\mathrm{d}r^3}\Bigg)R^{\mp}_{lm\omega} \,,
\end{aligned} \tag{D1}$$

where the coefficients δA_i and δB_i are calculated by the linearization in spin of the expressions in Eqs. (B1)–(B3)

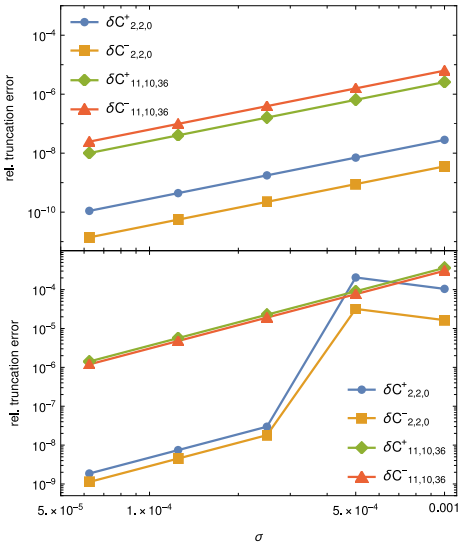

FIG. 11. The relative truncation errors (D5) for $\hat{a} = 0.9$, $p^{(\mathrm{g})} = 12$, and $e^{(\mathrm{g})} = 0.6$ (top) and $\hat{a} = 0.9$, $p^{(\mathrm{g})} = 4$, and $e^{(\mathrm{g})} = 0.4$ (bottom). These errors tend to zero for sufficiently small σ, and the calculation of $\delta C^{\pm}_{lmn}$ is, therefore, correct.

and (B9)–(B11) of Appendix B in Ref. [25]. Particularly, the linear part of A^{0}_{abi} is calculated as

$$\delta A^{0}_{abi} = \left(\delta C^{0}_{ab} - \delta C^{\sigma}_{ab}\right) f^{(i)}_{ab} + C^{0(\mathrm{g})}_{ab} \frac{\mathrm{d} f^{(i)}_{ab}}{\mathrm{d}r} \delta r \,, \tag{D2}$$

and the calculation of $\delta A^{t\phi}_{abi}$, δA^{r}_{abi}, and δB_i is trivial, because these functions are proportional to σ.

The linear parts of the partial amplitudes $\delta C^{\pm}_{lmn}$ are calculated simultaneously with the geodesic amplitudes $C^{\pm(\mathrm{g})}_{lmn}$. We have tested the results against nonlinearized partial amplitudes $C^{\pm}_{lmn}$ by comparing them with numerical σ derivatives of $C^{\pm}_{lmn}$ with respect to a reference geodesic with the same frequencies. To find the orbital parameters of a trajectory of a spinning particle with the same frequencies as those of a geodesic with $p^{(\mathrm{g})}$ and $e^{(\mathrm{g})}$, we numerically calculated $p^{\pm}$ and $e^{\pm}$ satisfying

$$\Omega_i(p^{\pm}, e^{\pm}, \pm\sigma) = \Omega^{(\mathrm{g})}_i(p^{(\mathrm{g})}, e^{(\mathrm{g})}) \tag{D3}$$

Then we numerically calculated the derivative

$$\delta C^{\pm\mathrm{Num}}_{lmn} = \frac{C^{\pm}_{lmn}(p^{+}, e^{+}, \sigma) - C^{\pm}_{lmn}(p^{-}, e^{-}, -\sigma)}{2\sigma} \tag{D4}$$

and the relative difference

$$\left| 1 - \frac{\delta C^{\pm\mathrm{Num}}_{lmn}}{\delta C^{\pm}_{lmn}} \right| \tag{D5}$$

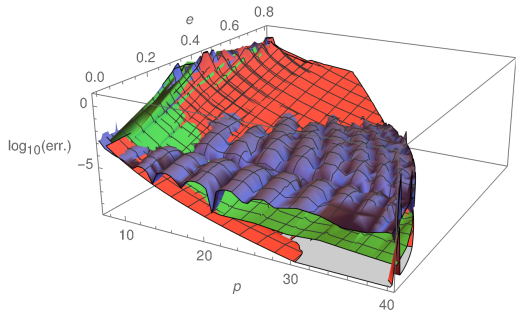

FIG. 12. The relative error of the interpolated energy flux to infinity compared to a 9PN series (purple), the relative error at individual grid points (green), and the relative error of the 9PN series deducted from the last term (red). We can see that the relative interpolation error is around 10^{-4}. In the area near the separatrix or with high eccentricity, the 9PN series loses accuracy.

If the calculation of $\delta C^{\pm}_{lmn}$ from Eq. (58) is correct, then the relative difference equals the relative truncation error of second-order finite difference formula and behaves as $\mathcal{O}(\sigma^2)$.

We have calculated the relative difference for two orbits, namely, with $p^{(\mathrm{g})} = 12$, $e^{(\mathrm{g})} = 0.6$ and $p^{(\mathrm{g})} = 4$, $e^{(\mathrm{g})} = 0.4$ for $\hat{a} = 0.9$ and for two modes with $l = 2$, $m = 2$, $n = 0$ and $l = 11$, $m = 10$, $n = 36$. The results are plotted in Fig. 11. We can see that for sufficiently small σ the relative error tends to zero and, therefore, the linear parts $\delta C^{\pm}_{lmn}$ are correct.

Appendix E: Accuracy of the interpolation

In this appendix we discus the interpolation error originated when interpolating the fluxes and other quantities in the $p - e$ plane in Sec. V A 3.

We use global interpolation on the Chebyshev nodes. The advantage of this method is that the convergence is exponential and the interpolation error is bounded and uniform. The disadvantage is that the convergence is slow, when the function is not analytical, and the errors in the evaluation at individual points spread across the whole domain.

The interpolation error of the Chebyshev interpolation can be easily estimated. Namely, when a function f is expanded into the Chebyshev polynomials as

$$f(x, y) = \sum_{i=1}^{i_{\max}} \sum_{j=1}^{j_{\max}} c_{ij} T_i(x) T_j(y) \,, \tag{E1}$$

where $T_i(x)$ are Chebyshev polynomials and c_{ij} are the coefficients, then the error can be estimated as

$$\max_{i=i_{\max} \vee j=j_{\max}} |c_{ij}| \,. \tag{E2}$$

Using this approach, we have found that the relative error of the interpolated geodesic fluxes $\mathcal{F}^{(\mathrm{g})}$ is around 10^{-4}, the relative error of $\dot{p}^{(\mathrm{g})}$ and $\dot{e}^{(\mathrm{g})}$ is around 10^{-5}, and the relative error of the derivatives of $\dot{p}$ and $\dot{e}$ is between 10^{-3} and 10^{-2}. Since the functions $\delta\dot{p}$ and $\delta\dot{e}$ are calculated from these derivatives, their precision is also between 10^{-3} and 10^{-2}.

To verify the geodesic energy flux to infinity for the Schwarzschild black hole, we compared the data with 9PN series [41]. Fig. 12 shows both relative difference between the PN series and the interpolated function and the value of the flux at individual points. It also shows the error of the PN series estimated by its last term. We can see that the interpolation error is dominant for higher p and lower e, and its value is around 10^{-4}. The error of the fluxes at individual grid points is between 10^{-8} and 10^{-7}, but the error of the PN series grows with decreasing p and increasing e, and, therefore, the fluxes near the separatrix cannot be verified using the PN series.

Appendix F: Accuracy of the phase shifts

In this appendix we compare the linearized phase shifts $\delta\Phi_i(t)$ obtained in Sec. IV A with the phases computed using nonlinearized formula (73). The purpose of this section is to test the validity and accuracy of the calculation.

First, we have computed the nonlinearized fluxes on a grid in the $p-e$ plane for $\sigma = 10^{-3}$ and $\hat{a} = 0$. The grid is similar to the grid for $\hat{a} = 0$ in Fig. 2, but the separatrix is located at different position fulfilling $p_{\mathrm{s}}(\sigma) = 6 + 2e + \mathcal{O}(\sigma)$, i.e., around 10^{-3} away from the geodetic separatrix. The calculation of the nonlinearized fluxes was equivalent to the calculation of linearized fluxes in Sec. V A. Because the numerical error in the non-linearized fluxes is around 10^{-4}, we have chosen such a high value of σ to prevent the loss of the spin contribution in the noise. Note that we tested the linearized results against only the aforementioned value of the spin in the nonlinearized case, because the calculation of the fluxes on the whole grid is computationally expensive.

We have computed the evolution of the orbital parameters $p(t)$ and $e(t)$ using Eqs. (68), and from $p(t)$ and $e(t)$ we calculated the phases (73). The initial orbital parameters p_0 and e_0 were chosen to match the initial frequencies of a geodesic with initial parameters $p_0^{(\mathrm{g})}$ and $e_0^{(\mathrm{g})}$. Similarly, we have calculated the phase for $\sigma = 0$. We have compared the phase shift

$$\Delta\Phi_i = \frac{\Phi_i(\sigma) - \Phi_i(\sigma = 0)}{\sigma} \tag{F1}$$

with the linear part of the phase $\delta\Phi_i$ as

$$\left| 1 - \frac{\delta\Phi_i}{\Delta\Phi_i} \right|. \tag{F2}$$

This relative difference is plotted in Fig. 13 for initial semilatus rectum $p_0^{(\mathrm{g})} = 12$ and different initial eccentricities $e_0^{(\mathrm{g})}$. We can see that the relative difference is below 5×10^{-3} for the majority of the inspiral. Before the particle reaches the separatrix, the relative difference diverges, because the linearization in σ breaks here. This is caused by the fact that the linear parts $\delta p(t)$ and $\delta e(t)$ diverge here and the functions as $\dot{p}(p^{(\mathrm{g})}(t)+\sigma\delta p(t), e^{(\mathrm{g})}(t)+\sigma\delta e(t), \sigma)$ cannot be linearized. The relative difference diverges also for $t = 0$, because both $\delta\Phi_i$ and $\Delta\Phi_i$ are close to zero; i.e., we divide two very small inaccurate quantities.

Since the quantity $\Delta\Phi_i$ is nonlinearized, it contains $\mathcal{O}(\sigma)$ contribution to the phase which should be around 10^{-3}. However, since the accuracy of the non-linearized calculations is around 10^{-3}, the relative difference shows this numerical error.

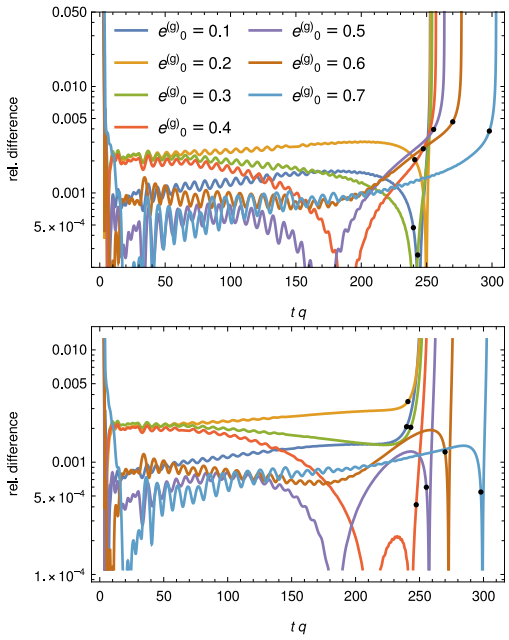

FIG. 13. The relative difference between the nonlinearized phase shift $\Delta\Phi_i$ and the linearized phase shift $\delta\Phi_i$ for $i = \phi$ (top) and $i = r$ (bottom). It can be seen that the relative difference is below 5×10^{-3} for the majority of the inspiral. At the end of the inspiral, the relative difference grows rapidly, because the linearization in σ breaks. The black dots show points where $\delta\Phi_r$ changes from an increasing to a decreasing function of t and it has maximal value. The error at these points is below 5×10^{-3}.

[1] P. Amaro-Seoane, H. Audley, S. Babak, J. Baker, E. Barausse, P. Bender, E. Berti, P. Binetruy, M. Born, D. Bortoluzzi, J. Camp, C. Caprini, *et al.*, Laser Interferometer Space Antenna, arXiv e-prints , arXiv:1702.00786 (2017), arXiv:1702.00786 [astro-ph.IM].

[2] S. Babak, J. Gair, A. Sesana, E. Barausse, C. F. Sopuerta, C. P. L. Berry, E. Berti, P. Amaro-Seoane, A. Petiteau, and A. Klein, Science with the space-based interferometer LISA. V. Extreme mass-ratio inspirals, Phys. Rev. D **95**, 103012 (2017), arXiv:1703.09722 [gr-qc].

[3] L. Barack and A. Pound, Self-force and radiation reaction in general relativity, Reports on Progress in Physics **82**, 016904 (2019), arXiv:1805.10385 [gr-qc].

[4] A. Pound and B. Wardell, Black hole perturbation theory and gravitational self-force (2021), arXiv:2101.04592 [gr-qc].

[5] S. E. Gralla and R. M. Wald, A rigorous derivation of gravitational self-force, Classical and Quantum Gravity **25**, 205009 (2008), arXiv:0806.3293 [gr-qc].

[6] A. Pound, Self-consistent gravitational self-force, Phys. Rev. D **81**, 024023 (2010), arXiv:0907.5197 [gr-qc].

[7] T. Hinderer and É. É. Flanagan, Two-timescale analysis of extreme mass ratio inspirals in Kerr spacetime: Orbital motion, Phys. Rev. D **78**, 064028 (2008), arXiv:0805.3337 [gr-qc].

[8] R. Fujita and M. Shibata, Extreme mass ratio inspirals on the equatorial plane in the adiabatic order, Phys. Rev. D **102**, 064005 (2020), arXiv:2008.13554 [gr-qc].

[9] S. A. Hughes, N. Warburton, G. Khanna, A. J. K. Chua, and M. L. Katz, Adiabatic waveforms for extreme mass-ratio inspirals via multivoice decomposition in time and frequency, Phys. Rev. D **103**, 104014 (2021), arXiv:2102.02713 [gr-qc].

[10] A. J. K. Chua, M. L. Katz, N. Warburton, and S. A. Hughes, Rapid Generation of Fully Relativistic Extreme-Mass-Ratio-Inspiral Waveform Templates for LISA Data Analysis, Phys. Rev. Lett. **126**, 051102 (2021), arXiv:2008.06071 [gr-qc].

[11] M. L. Katz, A. J. K. Chua, L. Speri, N. Warburton, and S. A. Hughes, Fast extreme-mass-ratio-inspiral waveforms: New tools for millihertz gravitational-wave data analysis, Phys. Rev. D **104**, 064047 (2021), arXiv:2104.04582 [gr-qc].

[12] J. Mathews, A. Pound, and B. Wardell, Self-Force Calculations with a Spinning Secondary, arXiv e-prints , arXiv:2112.13069 (2021), arXiv:2112.13069 [gr-qc].

[13] T. Osburn, N. Warburton, and C. R. Evans, Highly eccentric inspirals into a black hole, Phys. Rev. D **93**, 064024 (2016), arXiv:1511.01498 [gr-qc].

[14] P. Lynch, M. van de Meent, and N. Warburton, Eccentric self-forced inspirals into a rotating black hole, arXiv e-prints , arXiv:2112.05651 (2021), arXiv:2112.05651 [gr-qc].

[15] B. Wardell, A. Pound, N. Warburton, J. Miller, L. Durkan, and A. Le Tiec, Gravitational waveforms for compact binaries from second-order self-force theory, arXiv e-prints , arXiv:2112.12265 (2021), arXiv:2112.12265 [gr-qc].

[16] Y. Mino, Perturbative approach to an orbital evolution around a supermassive black hole, Phys. Rev. D **67**, 084027 (2003), arXiv:gr-qc/0302075 [gr-qc].

[17] S. Isoyama, R. Fujita, H. Nakano, N. Sago, and T. Tanaka, "Flux-balance formulae" for extreme mass-ratio inspirals, Progress of Theoretical and Experimental Physics **2019**, 013E01 (2019), arXiv:1809.11118 [gr-qc].

[18] S. Akcay, S. R. Dolan, C. Kavanagh, J. Moxon, N. Warburton, and B. Wardell, Dissipation in extreme mass-ratio binaries with a spinning secondary, Phys. Rev. D **102**, 064013 (2020), arXiv:1912.09461 [gr-qc].

[19] S. Drasco and S. A. Hughes, Gravitational wave snapshots of generic extreme mass ratio inspirals, Phys.Rev. **D73**, 024027 (2006), arXiv:gr-qc/0509101 [gr-qc].

[20] E. Harms, G. Lukes-Gerakopoulos, S. Bernuzzi, and A. Nagar, Asymptotic gravitational wave fluxes from a spinning particle in circular equatorial orbits around a rotating black hole, Phys. Rev. D **93**, 044015 (2016), arXiv:1510.05548 [gr-qc].

[21] E. Harms, G. Lukes-Gerakopoulos, S. Bernuzzi, and A. Nagar, Spinning test body orbiting around a Schwarzschild black hole: Circular dynamics and gravitational-wave fluxes, Phys. Rev. D **94**, 104010 (2016), arXiv:1609.00356 [gr-qc].

[22] G. Lukes-Gerakopoulos, E. Harms, S. Bernuzzi, and A. Nagar, Spinning test body orbiting around a Kerr black hole: Circular dynamics and gravitational-wave fluxes, Phys. Rev. D **96**, 064051 (2017), arXiv:1707.07537 [gr-qc].

[23] A. Nagar, F. Messina, C. Kavanagh, G. Lukes-Gerakopoulos, N. Warburton, S. Bernuzzi, and E. Harms, Factorization and resummation: A new paradigm to improve gravitational wave amplitudes. III. The spinning test-body terms, Phys. Rev. D **100**, 104056 (2019), arXiv:1907.12233 [gr-qc].

[24] G. A. Piovano, A. Maselli, and P. Pani, Extreme mass ratio inspirals with spinning secondary: A detailed study of equatorial circular motion, Phys. Rev. D **102**, 024041 (2020), arXiv:2004.02654 [gr-qc].

[25] V. Skoupý and G. Lukes-Gerakopoulos, Spinning test body orbiting around a Kerr black hole: Eccentric equatorial orbits and their asymptotic gravitational-wave fluxes, Phys. Rev. D **103**, 104045 (2021), arXiv:2102.04819 [gr-qc].

[26] O. Zelenka, G. Lukes-Gerakopoulos, V. Witzany, and O. Kopáček, Growth of resonances and chaos for a spinning test particle in the Schwarzschild background, Phys. Rev. D **101**, 024037 (2020), arXiv:1911.00414 [gr-qc].

[27] L. F. O. Costa, G. Lukes-Gerakopoulos, and O. Semerák, Spinning particles in general relativity: Momentum-velocity relation for the Mathisson-Pirani spin condition, Phys. Rev. D **97**, 084023 (2018), arXiv:1712.07281 [gr-qc].

[28] I. Timogiannis, G. Lukes-Gerakopoulos, and T. A. Apostolatos, Spinning test body orbiting around a Schwarzschild black hole: Comparing spin supplementary conditions for circular equatorial orbits, Phys. Rev. D **104**, 024042 (2021), arXiv:2104.11183 [gr-qc].

[29] M. Mathisson, Neue mechanik materieller systemes, Acta Phys. Polon. **6**, 163 (1937).

[30] M. Mathisson, Republication of: New mechanics of material systems, Gen. Relativ. Gravit. **42**, 1011 (2010).

[31] A. Papapetrou, Spinning test particles in general relativity. 1., Proc.Roy.Soc.Lond. **A209**, 248 (1951).

[32] W. Dixon, A covariant multipole formalism for extended test bodies in general relativity, Il Nuovo Cimento **34**, 317 (1964).
[33] W. Tulczyjew, Motion of multipole particles in general relativity theory, Acta Phys. Pol. **18**, 393 (1959).
[34] W. Dixon, Dynamics of extended bodies in general relativity. I. Momentum and angular momentum, Proc. R. Soc. A **314**, 499 (1970).
[35] J. Ehlers and E. Rudolph, Dynamics of extended bodies in general relativity center-of-mass description and quasirigidity, Gen. Relativ. Gravit. **8**, 197 (1977).
[36] Derivatives of the constants of motion and orbital frequencies, Mathematica notebook.
[37] L. Barack and N. Sago, Beyond the geodesic approximation: Conservative effects of the gravitational self-force in eccentric orbits around a Schwarzschild black hole, Phys. Rev. D **83**, 084023 (2011), arXiv:1101.3331 [gr-qc].
[38] N. Warburton, L. Barack, and N. Sago, Isofrequency pairing of geodesic orbits in Kerr geometry, Phys. Rev. D **87**, 084012 (2013), arXiv:1301.3918 [gr-qc].
[39] S. A. Teukolsky, Perturbations of a rotating black hole. 1. Fundamental equations for gravitational electromagnetic and neutrino field perturbations, Astrophys. J. **185**, 635 (1973).
[40] J. Miller and A. Pound, Two-timescale evolution of extreme-mass-ratio inspirals: Waveform generation scheme for quasicircular orbits in Schwarzschild spacetime, Phys. Rev. D **103**, 064048 (2021), arXiv:2006.11263 [gr-qc].
[41] Black Hole Perturbation Toolkit, (bhptoolkit.org) (2021).
[42] S. Hopper, E. Forseth, T. Osburn, and C. R. Evans, Fast spectral source integration in black hole perturbation calculations, Phys. Rev. D **92**, 044048 (2015), arXiv:1506.04742 [gr-qc].
[43] K. Glampedakis and D. Kennefick, Zoom and whirl: Eccentric equatorial orbits around spinning black holes and their evolution under gravitational radiation reaction, Phys.Rev. **D66**, 044002 (2002), arXiv:gr-qc/0203086 [gr-qc].
[44] P. C. Peters and J. Mathews, Gravitational radiation from point masses in a keplerian orbit, Phys. Rev. **131**, 435 (1963).
[45] T. Tanaka, Y. Mino, M. Sasaki, and M. Shibata, Gravitational waves from a spinning particle in circular orbits around a rotating black hole, Phys. Rev. D **54**, 3762 (1996), arXiv:gr-qc/9602038 [gr-qc].
[46] V. Skoupý and G. Lukes-Gerakopoulos, Gravitational wave templates from Extreme Mass Ratio Inspirals, arXiv e-prints , arXiv:2101.04533 (2021), arXiv:2101.04533 [gr-qc].
[47] N. Warburton, T. Osburn, and C. R. Evans, Evolution of small-mass-ratio binaries with a spinning secondary, Phys. Rev. D **96**, 084057 (2017), arXiv:1708.03720 [gr-qc].
[48] V. Witzany, Hamilton-Jacobi equation for spinning particles near black holes, Phys. Rev. D **100**, 104030 (2019), arXiv:1903.03651 [gr-qc].
[49] G. A. Piovano, R. Brito, A. Maselli, and P. Pani, Assessing the detectability of the secondary spin in extreme mass-ratio inspirals with fully relativistic numerical waveforms, Phys. Rev. D **104**, 124019 (2021), arXiv:2105.07083 [gr-qc].
[50] M. Rahman and A. Bhattacharyya, The prospect of distinguishing astrophysical objects with LISA, arXiv e-prints , arXiv:2112.13869 (2021), arXiv:2112.13869 [gr-qc].
[51] M. Saijo, K.-I. Maeda, M. Shibata, and Y. Mino, Gravitational waves from a spinning particle plunging into a Kerr black hole, Phys. Rev. D **58**, 064005 (1998).

A.3 Asymptotic gravitational-wave fluxes from a spinning test body on generic orbits around a Kerr black hole

This Attachment contains the paper *Asymptotic gravitational-wave fluxes from a spinning test body on generic orbits around a Kerr black hole* [41] accepted to to be published in Physical Review D. This version corrects some typos in the published version.

Asymptotic gravitational-wave fluxes from a spinning test body on generic orbits around a Kerr black hole

Viktor Skoupý[1, 2], Georgios Lukes-Gerakopoulos[1], Lisa V. Drummond[3], and Scott A. Hughes[3]
[1] *Astronomical Institute of the Czech Academy of Sciences, Boční II 1401/1a, CZ-141 00 Prague, Czech Republic*
[2] *Institute of Theoretical Physics, Faculty of Mathematics and Physics, Charles University, CZ-180 00 Prague, Czech Republic and*
[3] *Department of Physics and MIT Kavli Institute, MIT, Cambridge, MA 02139 USA*

This work provides gravitational-wave energy and angular momentum asymptotic fluxes from a spinning body moving on generic orbits in a Kerr spacetime up to linear-in-spin approximation. To achieve this, we have developed a new frequency-domain Teukolsky equation solver that calculates asymptotic amplitudes from generic orbits of spinning bodies with their spin aligned with the total orbital angular momentum. However, the energy and angular momentum fluxes from these orbits in the linear-in-spin approximation are appropriate for adiabatic models of extreme mass ratio inspirals even for spins nonaligned to the orbital angular momentum. To check the newly obtained fluxes, they are compared with already known frequency-domain results for equatorial orbits and with results from a time-domain Teukolsky equation solver called *Teukode* for off-equatorial orbits. The spinning-body framework of our work is based on the Mathisson-Papapetrou-Dixon equations under the Tulczyjew-Dixon spin supplementary condition.

I. INTRODUCTION

Future space-based gravitational-wave (GW) detectors, like the Laser Interferometer Space Antenna (LISA) [1], TianQin [2], and Taiji [3], are designed to detect GWs from sources emitting in the mHz bandwidth like the extreme mass ratio inspirals (EMRI). An EMRI consists of a primary supermassive black hole and a secondary compact object, like a stellar-mass black hole or a neutron star, which is orbiting in close vicinity around the primary. Due to gravitational radiation reaction, the secondary slowly inspirals into the primary, while the EMRI system is emitting GWs to infinity. Since signals from EMRIs are expected to overlap with other systems concurrently emitting GWs in the mHz bandwidth [1], matched filtering will be employed for the detection and parameter estimation of the received GW signals. This method relies on comparison of the signal with GW waveform templates and, thus, these templates must be calculated in advance and with an accuracy of the GW phases up to fractions of radians [4]. With this level of accuracy, it is anticipated that the detection of GWs from EMRIs will provide an opportunity to probe in detail the strong gravitational field near a supermassive black hole [4].

Several techniques have been employed to model an EMRI system and the GWs it is emitting. The backbone of these techniques is the perturbation theory [5–7] in which the secondary body is treated as a point particle moving in a background spacetime. Such an approach is justified, because the mass ratio $q = \mu/M$ between the mass of the secondary μ and the mass of the primary M lies between 10^{-7} and 10^{-4}. The particle acts as a source to a gravitational perturbation to the background spacetime and conversely the perturbation exerts a force on the particle [7]. After the expansion of the perturbation in q, the first-order perturbation is the source of the first-order self-force and both first and second-order perturbations are sources of the second-order self-force. These parts of the self-force are expected to be sufficient to reach the expected accuracy needed to model an EMRI [6].

Another technique, which is widely used in EMRI modeling, is the *two-timescale approximation* [8, 9]. This approximation relies on the separation between the orbital timescale and the inspiral timescale. In an EMRI the rate of energy loss $\dot{E}$ over the energy E is $\dot{E}/E = \mathcal{O}(q)$, which implies that the time an inspiral lasts is $\mathcal{O}(q^{-1})$. Hence, the inspiraling time is much longer than the orbital timescale $\mathcal{O}(q^0)$. Moreover, since the mass ratio q is very small, the deviation from the trajectory, which the secondary body would follow without the self-force, is very small as well. Hence, an EMRI can be modeled as a secondary body moving on an orbit in a given spacetime background with slowly changing orbital parameters; this type of modeling is called the *adiabatic approximation* [10–13].

For a nonspinning body inspiraling into a Kerr black hole the phases of the GW can be expanded in the mass ratio [8] as

$$\Phi_\mu(t) = \frac{1}{q}\Phi^0_\mu(qt) + \Phi^1_\mu(qt) + \mathcal{O}(q)\,, \tag{1}$$

where the first term on the right hand side is called adiabatic and the second postadiabatic term. The adiabatic term can be calculated from the averaged dissipative part of the first-order self-force, while the postadiabatic term is calculated from several other parts of the self-force. Namely, from the rest of the first-order self-force, i.e., the oscillating dissipative part and the conservative part, and from the averaged dissipative part of the second-order self-force [6]. To accurately model the inspiral up to radians, the postadiabatic term cannot be neglected.

So far we have discussed the case of a nonspinning secondary body, however, to accurately calculate wave-

forms for an EMRI, one must also include the spin of the secondary. To understand why, it is useful to normalize the spin magnitude of the secondary $S = \mathcal{O}(\mu^2)$ as $\sigma = S/(\mu M) = \mathcal{O}(q)$ [14]. For example, if the spinning body is set to be an extremal Kerr black hole, i.e. $S = \mu^2$, then $\sigma = q$. Thus, the contribution of the spin of the secondary to an EMRI evolution is of postadiabatic order.

The adiabatic term in the nonspinning case can be found from the asymptotic GW fluxes to infinity and to the horizon of the central back hole. This stems from the flux-balance laws which have been proven for the evolution of energy, angular momentum and the Carter constant for nonspinning particle in Ref. [15]. For spinning bodies in the linear-in-spin approximation the flux-balance laws have been proven just for the energy and angular momentum fluxes in Refs. [16, 17]. In the nonlinear-in-spin case the motion of a spinning body in a Kerr background is non-integrable [14], i.e. there are more degrees of freedom than constants of motion. Ref. [18] has been shown that the motion of a spinning particle in a curved spacetime can be expressed by a Hamiltonian with at least 5 degrees of freedom. Hence, since this Hamiltonian system is autonomous, i.e. the Hamiltonian itself is a constant of motion, four other constants of motion are needed to achieve integrability. In the Kerr case, there is the energy and the angular momentum along the symmetry axis for the full equations, while in the linear-in-spin approximation Rüdiger [19, 20] found two quasiconserved constants of motion [21]. These quasiconserved constants can be interpreted as a projection of the spin to the orbital angular momentum and a quantity similar to the Carter constant [22]. If the evolution of these quantities could be calculated from asymptotic fluxes, then one could calculate the influence of the secondary spin on the asymptotic GW fluxes. This, in turn, would allow us to capture the influence of the secondary spin on the GW phase for generic inspirals.

Fully relativistic GW fluxes from orbits of nonspinning particles along with the evolution of the respective inspirals were first calculated in Ref [23] for eccentric orbits around a Schwarzschild black hole and in Ref. [24] for circular equatorial orbits around a Kerr black hole. Fluxes from eccentric orbits in the Kerr spacetime were calculated in Refs. [25, 26], while the adiabatic evolution of the inspirals was presented in Ref. [10]. Fully generic fluxes from a nonspinning body were calculated in Ref. [27] and were employed in Ref. [11] to adiabatically evolve the inspirals. The spin of the secondary was included to the fluxes in Refs. [16, 28–31] from circular orbits in a black hole spacetime and to the quasicircular adiabatic evolution of the orbits in Refs. [32–35]. In Ref. [17] the first-order self-force was calculated for circular orbits in the Schwarzschild spacetime. Finally, the fluxes from spinning bodies on eccentric equatorial orbits around a Kerr black hole were calculated in Ref. [36] and the adiabatic evolution in linear-in-spin approximation was calculated in Ref. [12].

In this work, we follow the frequency-domain method to calculate generic orbits of spinning bodies around a Kerr black hole developed in Refs. [37, 38] and use it to find asymptotic GW fluxes from these orbits in the case when the spin is aligned with the orbital angular momentum. The results are valid up to linear order in the secondary spin, since the orbits are calculated only up to this order.

The rest of our paper is organized as follows. Section II introduces the motion of spinning test bodies in the Kerr spacetime and describes the calculation of the linear-in-spin part of the motion in the frequency domain. Section III presents the computation of GW fluxes from the orbits calculated in Section II. Section IV describes the numerical techniques we have employed to calculate the aforementioned orbits and fluxes, and it presents comparisons of the new results with previously known equatorial limit results and with time domain results for generic off-equatorial orbits. Finally, Section V summarizes our work and provides an outlook for possible extensions.

In this work, we use geometrized units where $c = G = 1$. Spacetime indices are denoted by Greek letters and go from 0 to 3, null-tetrad indices are denoted by lowercase Latin letters $a, b, c, \ldots$ and go from 1 to 4 and indices of the Marck tetrad are denoted by uppercase Latin letters $A, B, C, \ldots$ and go from 0 to 3. A partial derivative is denoted with a comma as $U_{\mu,\nu} = \partial_\nu U_\mu$, whereas a covariant derivative is denoted by a semicolon as $U_{\mu;\nu} = \nabla_\nu U_\mu$. The Riemann tensor is defined as $R^\mu{}_{\nu\kappa\lambda} = \Gamma^\mu{}_{\nu\lambda,\kappa} - \Gamma^\mu{}_{\nu\kappa,\lambda} + \Gamma^\mu{}_{\rho\kappa}\Gamma^\rho{}_{\nu\lambda} - \Gamma^\mu{}_{\rho\lambda}\Gamma^\rho{}_{\nu\kappa}$, and the signature of the metric is $(-,+,+,+)$. Levi-Civita tensor $\epsilon^{\alpha\beta\gamma\delta}$ is defined as $\epsilon^{0123} = 1/\sqrt{-g}$ for rational polynomial coordinates[1].

II. MOTION OF A SPINNING TEST BODY

The motion of an extended test body in the general relativity framework was first addressed by Mathisson in [39, 40] where he introduced the concept of a "gravitational skeleton", i.e., an expansion of an extended body using its multipoles. If we wish to describe the motion of a compact object, like a black hole or a neutron star, then we can restrict ourselves to the pole-dipole approximation [14], where the aforementioned expansion is truncated to the dipole term and all the higher multipoles are ignored. In this way, the extended test body is reduced to a body with spin and the respective stress-energy tensor

[1] Note that for Boyer-Lindquist (BL) coordinates the sign is opposite since the coordinate frame in BL coordinates is right-handed whereas the coordinate frame in rational polynomial coordinates is left-handed.

can be written as [41]

$$T^{\mu\nu} = \int \mathrm{d}\tau \Bigg(P^{(\mu} v^{\nu)} \frac{\delta^4(x^\rho - z^\rho(\tau))}{\sqrt{-g}} - \nabla_\alpha \Bigg(S^{\alpha(\mu} v^{\nu)} \frac{\delta^4(x^\rho - z^\rho(\tau))}{\sqrt{-g}} \Bigg) \Bigg) \tag{2}$$

where τ is the proper time, P^μ is the four-momentum, $v^\mu = \mathrm{d}z^\mu/\mathrm{d}\tau$ is the four-velocity, $S^{\mu\nu}$ is the spin tensor and g is the determinant of the metric. Note that x^μ denotes arbitrary point of the spacetime and $z^\mu(\tau)$ denotes the position of the body parametrized by the proper time.

From the conservation law $T^{\mu\nu}{}_{;\nu} = 0$ the Mathisson-Papapetrou-Dixon (MPD) equations [40, 42, 43] can be derived as

$$\frac{\mathrm{D}P^\mu}{\mathrm{d}\tau} = -\frac{1}{2}\, R^\mu{}_{\nu\rho\sigma}\, v^\nu\, S^{\rho\sigma}\,, \tag{3a}$$

$$\frac{\mathrm{D}S^{\mu\nu}}{\mathrm{d}\tau} = P^\mu v^\nu - P^\nu v^\mu \tag{3b}$$

where $R^\mu{}_{\nu\rho\sigma}$ is the Riemann tensor. However, this system of equations is underdetermined because one has the freedom in choosing the centre of mass which is tracked by the solution of these equations. To close the system, a so called spin supplementary condition (SSC) must be specified. In this work we use the Tulczyjew-Dixon (TD) [43, 44] SSC

$$S^{\mu\nu} P_\mu = 0\,. \tag{4}$$

Under this SSC the mass of the body

$$\mu = \sqrt{-P^\mu P_\mu} \tag{5}$$

and the magnitude of its spin

$$S = \sqrt{S^{\mu\nu} S_{\mu\nu}/2} \tag{6}$$

are conserved. The relation between the four-velocity and four-momentum reads [45]

$$v^\mu = \frac{\mathsf{m}}{\mu} \left(u^\mu + \frac{\frac{1}{2} s^{\mu\nu} R_{\nu\rho\kappa\lambda} u^\rho s^{\kappa\lambda}}{1 + \frac{1}{4} R_{\alpha\beta\gamma\delta} s^{\alpha\beta} s^{\gamma\delta}} \right) \tag{7}$$

where

$$u^\mu = \frac{P^\mu}{\mu}\,, \qquad s^{\mu\nu} = \frac{S^{\mu\nu}}{\mu} \tag{8}$$

are specific momenta and $\mathsf{m} = -p^\mu v_\mu$ is a mass definition with respect to v_μ which is not conserved under TD SSC. Note that having fixed the centre of mass as a reference point for the body allows us to view it as a particle. Hence, quite often the term "spinning particle" is used instead of "spinning body".

From the spin tensor $s^{\mu\nu}$ and the specific four-momentum u^μ we can define the specific spin four-vector

$$s_\mu = -\frac{1}{2} \epsilon_{\mu\nu\rho\sigma}\, u^\nu\, s^{\rho\sigma} \tag{9}$$

for which the evolution equation

$$\frac{\mathrm{D}s^\mu}{\mathrm{d}\tau} = -u^\mu R^*_{\alpha\beta\gamma\delta} s^\alpha v^\beta u^\gamma s^\delta \tag{10}$$

holds [46], where the right dual of Riemann tensor has the form

$$R^*_{\alpha\beta\gamma\delta} = \frac{1}{2} R_{\alpha\beta}{}^{\mu\nu} \epsilon_{\mu\nu\gamma\delta}\,. \tag{11}$$

Note from Eq. (9) and the properties of $\epsilon_{\mu\nu\rho\sigma}$, it is clear that $s_\mu u^\mu = 0$.

In the context of an EMRI, it is convenient to define the dimensionless spin parameter

$$\sigma = \frac{S}{\mu M}\,, \tag{12}$$

since one can show that σ is of the order of the mass ratio $q = \dfrac{\mu}{M}$ [14]. For instance, if the small body is set to be an extremal Kerr black hole, then $S = \mu^2$ and hence $\sigma = q$. Having established that $\sigma \lesssim q$, one sees that this parameter is very small in the context of EMRI. Since the adiabatic order is calculated from the geodesic fluxes [27], every correction to the trajectory and the fluxes of the order of q influences the first postadiabatic order and higher order corrections are pushed to second postadiabatic order and further. By taking into account that the current consensus is that for the signals observed by LISA we need an accuracy in the waveforms up to the first postadiabatic order, it is reasonable to linearize the MPD equations in the secondary spin and discard all the terms of the order $\mathcal{O}(\sigma^2)$ and higher. Note that in Refs. [37, 38] a different dimensionless spin parameter is used, which is defined as

$$s = \frac{S}{\mu^2}\,. \tag{13}$$

It is related to σ as $s = \sigma/q$ and its magnitude is bounded by one.

After the linearization in σ the relation (7) reads

$$v^\mu = u^\mu + \mathcal{O}(s^2) \tag{14}$$

and the MPD equations themselves simplify to

$$\frac{\mathrm{D}u^\mu}{\mathrm{d}\tau} = -\frac{1}{2}\, R^\mu{}_{\nu\rho\sigma}\, u^\nu\, s^{\rho\sigma}\,, \tag{15a}$$

$$\frac{\mathrm{D}s^{\mu\nu}}{\mathrm{d}\tau} = 0 \tag{15b}$$

and

$$\frac{\mathrm{D}s^\mu}{\mathrm{d}\tau} = 0\,. \tag{16}$$

Eq. (16) is the equation of parallel transport along the trajectory. After rewriting this equation using the total derivative

$$\frac{\mathrm{d}s^\mu}{\mathrm{d}\tau} + \Gamma^\mu{}_{\alpha\beta} u^\alpha s^\beta = 0\,, \tag{17}$$

it can be seen that to keep the equation truncated to $\mathcal{O}(\sigma)$, the Christoffel symbol $\Gamma^{\mu}{}_{\alpha\beta}$ and the four-momentum has to be effectively taken at the geodesic limit [37]. Thus, the parallel transport of the spin has to take place along a geodesic.

A. Spinning particles in Kerr spacetime

In this work we treat the binary system as a spinning body moving on a Kerr background spacetime, which line element in "rational polynomial" coordinates [47] reads

$$\mathrm{d}s^2 = -\left(1-\frac{2Mr}{\Sigma}\right)\mathrm{d}t^2 - \frac{4aMr(1-z^2)}{\Sigma}\mathrm{d}t\mathrm{d}\phi + \frac{\left(\varpi^4 - a^2\Delta(1-z^2)\right)(1-z^2)}{\Sigma}\mathrm{d}\phi^2 + \frac{\Sigma}{\Delta}\mathrm{d}r^2 + \frac{\Sigma}{1-z^2}\mathrm{d}z^2 \tag{18}$$

where

$$\Sigma = r^2 + a^2z^2 \ ,$$
$$\Delta = r^2 - 2Mr + a^2 \ ,$$
$$\varpi^2 = r^2 + a^2 \ .$$

These coordinates are derived from the Boyer-Lindquist ones with $z = \cos\theta$ and are convenient for manipulations in an algebraic software such as *Mathematica*.

A Kerr black hole has its outer horizon located at $r_+ = M + \sqrt{M^2 - a^2}$. A Kerr spacetime is equipped with two Killing vectors $\xi^{\mu}_{(t)} = \delta^{\mu}_t$ and $\xi_{(\phi)} = \delta^{\mu}_{\phi}$, which are related respectively to the stationarity and the axisymmetry of the spacetime. Additionally for the Kerr spacetime, there is also a Killing-Yano tensor in the form

$$Y_{\mu\nu}\,\mathrm{d}x^{\mu}\wedge\mathrm{d}x^{\nu} = az\,\mathrm{d}r\wedge\left(\mathrm{d}t - a(1-z^2)\mathrm{d}\phi\right) + r\,\mathrm{d}z\wedge\left(a\mathrm{d}t - \varpi^2\mathrm{d}\phi\right), \tag{19}$$

from which a Killing tensor can be defined as

$$K_{\mu\nu} = Y_{\mu}{}^{\kappa}Y_{\nu\kappa} \ . \tag{20}$$

Thanks to these symmetries, there exist two constants of motion for the spinning particle in the Kerr background

$$E = -u_{\mu}\xi^{\mu}_{(t)} + \frac{1}{2}\xi^{(t)}_{\mu;\nu}s^{\mu\nu} \ , \tag{21a}$$

$$J_z = u_{\mu}\xi^{\mu}_{(\phi)} - \frac{1}{2}\xi^{(\phi)}_{\mu;\nu}s^{\mu\nu} \ , \tag{21b}$$

which can be interpreted respectively as the specific total energy measured at infinity and the component of the specific total angular momentum parallel to the axis of symmetry of the Kerr black hole measured at infinity.

Apart from the aforementioned constants, there are also a couple of quasiconserved quantities [19, 20]

$$C_Y = Y_{\mu\nu}u^{\mu}s^{\nu} \ , \tag{21c}$$

$$K_R = K_{\mu\nu}u^{\mu}u^{\nu} - 2u^{\mu}s^{\rho\sigma}(Y_{\mu\rho;\kappa}Y^{\kappa}{}_{\sigma} + Y_{\rho\sigma;\kappa}Y^{\kappa}{}_{\mu}), \tag{21d}$$

for which it holds

$$\frac{\mathrm{d}K_R}{\mathrm{d}\tau} = \mathcal{O}(\sigma^2) \ , \quad \frac{\mathrm{d}C_Y}{\mathrm{d}\tau} = \mathcal{O}(\sigma^2) \ . \tag{22}$$

The existence of these quasiconserved quantities causes the motion of a spinning particle in a Kerr background to be nearly-integrable in linear order in σ [21]. Actually, for Schwarzschild background ($a = 0$) it has been shown that the non-integrability effects appear at $\mathcal{O}(\sigma^2)$ [48]. K_R is analog to the geodesic Carter constant $K = K_{\mu\nu}u^{\mu}u^{\nu} = l_{\mu}l^{\mu}$ (see Appendix A),where $l^{\mu} = Y_{\nu}{}^{\mu}u^{\nu}$ can be interpreted as the total specific (geodesic) orbital angular momentum. Because of this, C_Y can be interpreted as a scalar product of the spin four-vector with the total orbital angular momentum. In other words, C_Y can be seen as a projection of the spin on the total orbital angular momentum.

The four-vector l^{μ} was used by Marck [49] and van de Meent [50] to find a solution to a parallel transport along a geodesic in the Kerr spacetime, i.e. a solution to Eq. (16). The resulting s^{μ} can be written as

$$s^{\mu} = M\left(\sigma_{\perp}(\cos\psi_p\tilde{e}^{\mu}_1 + \sin\psi_p\tilde{e}^{\mu}_2) + \sigma_{\parallel}e^{\mu}_3\right) \tag{23}$$

where we introduced $\sigma_{\perp}$ and $\sigma_{\parallel}$, which is a decomposition of the spin four-vector to a perpendicular component and to a parallel one, respectively, to the total orbital angular momentum; while $\tilde{e}^{\mu}_1$, $\tilde{e}^{\mu}_2$ and $e^{\mu}_3 = l^{\mu}/\sqrt{K}$ are the legs of the Marck tetrad [50]. (Note that the zeroth leg of the tetrad is taken to be along the four-velocity of the orbiting body: $e^{\mu}_0 = u^{\mu}$. Because $s_{\mu}u^{\mu} = 0$, this tetrad leg does not appear in s^{μ}.) Similarly to [37, 38] we define e^{μ}_3 with opposite sign from that [50]. The definition of C_Y implies that $\sigma_{\parallel} = C_Y/\sqrt{K}$.

Eq. (23) describes a vector precessing around e^{μ}_3 with precession phase ψ_p, which fulfils the evolution equation

$$\frac{\mathrm{d}\psi_p}{\mathrm{d}\lambda} = \sqrt{K}\left(\frac{(r^2+a^2)E - aL_z}{K + r^2} + a\frac{L_z - a(1-z^2)E}{K - a^2z^2}\right), \tag{24}$$

where λ is the Carter-Mino time, related to proper time along the orbit by $\mathrm{d}\lambda = \mathrm{d}\tau/\Sigma$. An analytic solution for $\psi_p(\lambda)$ can be found in [50]. The precession introduces a new frequency Υ_s to the system. Since the perpendicular component $\sigma_{\perp}$ is multiplied by sine and cosine of the precession phase, the contribution of this component in the linear order is purely oscillating. Therefore, the constants of motion and the frequencies depend only on the parallel component $\sigma_{\parallel}$ as well as the GW fluxes of energy and angular momentum in linear order in spin. Because of this, we neglect the perpendicular component and focus on a trajectory of a spinning body with spin aligned to the total orbital angular momentum.

B. Linearized trajectory in frequency domain

We follow the procedure of Refs. [37, 38], where the bounded orbits of a spinning particle were parametrized

in Mino-Carter time as

$$u_t = -\hat{E} + u_t^S(\lambda) \,, \tag{25a}$$
$$u_\phi = \hat{L}_z + u_\phi^S(\lambda) \,, \tag{25b}$$
$$r = \frac{pM}{1 + e\cos(\Upsilon_r\lambda + \delta\hat{\chi}_r(\lambda) + \delta\chi_r^S(\lambda))} + \text{𝓇}^S(\lambda) \,, \tag{25c}$$
$$z = \sin I \cos\big(\Upsilon_z\lambda + \delta\hat{\chi}_z(\lambda) + \delta\chi_z^S(\lambda)\big) + \text{𝓏}^S(\lambda) \tag{25d}$$

with

$$\Upsilon_r = \hat{\Upsilon}_r + \Upsilon_r^S \,, \tag{25e}$$
$$\Upsilon_z = \hat{\Upsilon}_z + \Upsilon_z^S \tag{25f}$$

where the hatted quantities denote geodesic quantities and quantities with index S are proportional to σ.[2]

This parametrization assumes that the particle oscillates between its radial and polar turning points, but, unlike in the geodesic case, which is described in Appendix A, the radial turning points depend on z and the polar turning points depend on r. This dependence is encoded in the corrections 𝓇^S and 𝓏^S, respectively. Υ_r and Υ_z are the radial and polar frequency, but because of the corrections 𝓇^S and 𝓏^S, the radial and polar motion has also a small contribution from a combination of all the frequencies $n\Upsilon_r + k\Upsilon_z + j\Upsilon_s$, where n, k, and j are integers. This parametrization assumes that a reference geodesic is given by the parameters: semi-latus rectum p, eccentricity e and inclination I (see Appendix A for their definition) and the trajectory of a spinning particle has the same turning points after averaging.

With these frequencies at hand, quantities in Eq. (25) parametrized with respect to λ can be expanded in the frequency domain as

$$f(\lambda) = \sum_{n,k,j} f_{nkj} e^{-in\Upsilon_r\lambda - ik\Upsilon_z\lambda - ij\Upsilon_s\lambda} \,. \tag{26}$$

In particular, $\delta\chi_r^S$ is summed only over positive and negative n; $\delta\chi_z^S$ is summed only over positive and negative k; k and j cannot be simultaneously zero for 𝓇^S and n and j cannot be simultaneously zero for 𝓏^S. In our numerical calculations we truncate the n and k sums at $\pm n_{\max}$ and $\pm k_{\max}$. These maxima are determined empirically from the convergence of contributions to the total flux from each mode, as well as from the mode's numerical properties; more details are shown in Sec. IV. The index j is summed from -1 to 1.

After introducing the phases

$$w_r = \Upsilon_r\lambda \,, \tag{27a}$$
$$w_z = \Upsilon_z\lambda \,, \tag{27b}$$
$$w_s = \Upsilon_s\lambda \,, \tag{27c}$$

we can write the inverse expression for Eq. (26) as

$$f_{knj} = \int \frac{\mathrm{d}w_r \mathrm{d}w_z \mathrm{d}w_s}{(2\pi)^3} f(w_r, w_z, w_s) e^{inw_r + ikw_z + ijw_s} \,. \tag{28}$$

Equations (15a) together with the normalization of the four-velocity $u^\mu u_\mu = -1$ are then used to find the quantities (25) in the frequency domain.

The coordinates can then be linearized with fixed phases as $r(w_r, w_z, w_s) = \hat{r}(w_r) + r^S(w_r, w_z, w_s)$, $z(w_r, w_z, w_s) = \hat{z}(w_z) + z^S(w_r, w_z, w_s)$, where the linear-in-spin parts can be expressed as [37, 38]

$$r^S = \frac{epM\delta\chi_r^S \sin(w_r + \delta\hat{\chi}_r)}{(1 + e\cos(w_r + \delta\hat{\chi}_r))^2} + \text{𝓇}^S \,. \tag{29}$$
$$z^S = -\sin I \delta\chi_z^S \sin(w_z + \delta\hat{\chi}_z) + \text{𝓏}^S \,. \tag{30}$$

For the calculation of gravitational-wave fluxes we need also the coordinate time and azimuthal coordinate. Both can be expressed as secularly growing part plus purely oscillating part, i.e.

$$t = \Gamma\lambda + \Delta t(\Upsilon_r\lambda, \Upsilon_z\lambda, \Upsilon_s\lambda) \,, \tag{31}$$
$$\phi = \Upsilon_\phi\lambda + \Delta\phi(\Upsilon_r\lambda, \Upsilon_z\lambda, \Upsilon_s\lambda) \,, \tag{32}$$

where the oscillating parts Δt and $\Delta\phi$ cannot be separated, unlike in the geodesic case in Eq. (A6) where they are broke up in a r and z part [51]. These oscillating parts can be calculated from the four-velocity with respect to Carter-Mino time, $U^\mu \equiv \mathrm{d}x^\mu/\mathrm{d}\lambda = \Sigma u^\mu \equiv \Sigma \mathrm{d}x^\mu/\mathrm{d}\tau$. After integrating

$$\frac{\mathrm{d}t}{\mathrm{d}\lambda} = U^t = \sum_{n,k,j} U^t_{nkj} e^{-in\Upsilon_r\lambda - ik\Upsilon_z\lambda - ij\Upsilon_s\lambda} \,, \tag{33}$$

the n,k,j-mode of $\Delta t(\lambda)$ in the frequency domain Eq. (26) reads

$$\Delta t_{nkj} = \frac{U^t_{nkj}}{-in\Upsilon_r - ik\Upsilon_z - j\Upsilon_s} \,, \tag{34}$$

where U^t_{nkj} is the harmonic mode of the four-velocity. By linearizing in spin the above equation we obtain

$$\Delta t^S_{nkj} = \frac{iU^t_{S,nkj}}{n\hat{\Upsilon}_r + k\hat{\Upsilon}_z + j\Upsilon_s} - \frac{i\hat{U}^t_{nkj}(n\Upsilon_r^S + k\Upsilon_z^S)}{(n\hat{\Upsilon}_r + k\hat{\Upsilon}_z)^2} \,. \tag{35}$$

The second term is zero for $j = \pm 1$ and Υ_s^S is not needed, since the geodesic motion is independent of Υ_s. The linear-in-spin part of the t component of the four-velocity can be expressed as

$$U^t_S = \frac{\partial V^t}{\partial r} r^S + \frac{\partial V^t}{\partial z} z^S - \frac{\partial V^t}{\partial E} u_t^S + \frac{\partial V^t}{\partial L_z} u_\phi^S \tag{36}$$

where V^t is given in Eq. (A5a). Similarly for $\Delta\phi^S$, we use U^ϕ to get $\Delta\phi_{nkj}$ and consequently $\Delta\phi^S_{nkj}$, in which U^ϕ_S is as Eq. (36), but instead of V^t we use V^ϕ.

[2] Υ_s does not need to be expanded to first order in σ because it appears in terms proportional to σ.

The linear-in-spin parts of Γ and ϕ are respectively $U^t_{S,000}$ and $U^\phi_{S,000}$ [38]. The coordinate-time frequencies read

$$\Omega_r = \frac{\hat{\Upsilon}_r + \Upsilon^S_r}{\hat{\Gamma} + \Gamma^S} \,, \tag{37a}$$

$$\Omega_z = \frac{\hat{\Upsilon}_z + \Upsilon^S_z}{\hat{\Gamma} + \Gamma^S} \,, \tag{37b}$$

$$\Omega_\phi = \frac{\hat{\Upsilon}_\phi + \Upsilon^S_\phi}{\hat{\Gamma} + \Gamma^S} \,, \tag{37c}$$

$$\Omega_s = \frac{\hat{\Upsilon}_s}{\hat{\Gamma} + \Gamma^S} \,. \tag{37d}$$

III. GRAVITATIONAL-WAVE FLUXES

In this work we calculate the gravitational waves generated by a spinning particle moving on a generic orbit around a Kerr black hole using the Newman-Penrose (NP) formalism. We calculate a perturbation of the NP scalar

$$\Psi_4 = -C_{\alpha\beta\gamma\delta} n^\alpha \overline{m}^\beta n^\gamma \overline{m}^\delta \tag{38}$$

where $C_{\alpha\beta\gamma\delta}$ is the Weyl tensor and n^μ and $\bar{m}^\mu$ are part of the Kinnersley tetrad $(\lambda^\mu_1, \lambda^\mu_2, \lambda^\mu_3, \lambda^\mu_4) = (l^\mu, n^\mu, m^\mu, \overline{m}^\mu)$ defined as

$$l^\mu = \left(\frac{r^2+a^2}{\Delta}, 1, 0, \frac{a}{\Delta}\right) , \tag{39a}$$

$$n^\mu = \frac{1}{2\Sigma}\left(\varpi^2, -\Delta, 0, a\right) \,, \tag{39b}$$

$$m^\mu = \frac{\sqrt{1-z^2}}{\sqrt{2}\bar{\zeta}}\left(ia, 0, -1, \frac{i}{1-z^2}\right) \,, \tag{39c}$$

$$\overline{m}^\mu = \frac{\sqrt{1-z^2}}{\sqrt{2}\zeta}\left(-ia, 0, -1, -\frac{i}{1-z^2}\right) \tag{39d}$$

with

$$\zeta = r - iaz.$$

From the NP scalar (38) we can calculate the strain at infinity using the equation

$$\Psi_4(r\to\infty) = \frac{1}{2}\frac{\mathrm{d}^2 h}{\mathrm{d}t^2} \,, \tag{40}$$

where $h = h_+ - ih_\times$ is expressed using the two polarizations of the GW. The NP scalar Ψ_4 can be found using Teukolsky equation [52]

$${}_{-2}\mathcal{O}\,{}_{-2}\psi(t,r,\theta,\phi) = 4\pi\Sigma T \,, \tag{41}$$

where ${}_{-2}\psi = \zeta^4\Psi_4$, ${}_{-2}\mathcal{O}$ is a second order differential operator and T is the source term defined from $T^{\mu\nu}$.

We solve the Eq. (41) in frequency domain, where it can be decomposed as

$${}_{-2}\psi = \sum_{l,m}^{\infty} \frac{1}{2\pi}\int_{-\infty}^{\infty} \mathrm{d}\omega\, \psi_{lm\omega}(r)\, {}_{-2}S^{a\omega}_{lm}(z) e^{-i\omega t + im\phi} \,. \tag{42}$$

Then, Eq. (41) can be separated into two ordinary differential equations, one for the radial part $\psi_{lm\omega}(r)$ and one for the angular part ${}_{-2}S^{a\omega}_{lm}(z)$, which is called the spin-weighted spheroidal harmonics and is normalized as

$$\int_{-1}^{1} |{}_{-2}S^{a\omega}_{lm}(z)|^2 \mathrm{d}z = \frac{1}{2\pi} \,. \tag{43}$$

The radial equation reads

$$\mathcal{D}_{lm\omega}\psi_{lm\omega}(r) = \mathcal{T}_{lm\omega} \,, \tag{44}$$

where $\mathcal{D}_{lm\omega}$ is a second order differential operator, which depends on r, and $\mathcal{T}_{lm\omega}$ is the source term which we describe later. Because the source term is zero around the horizon and infinity, the function $\psi_{lm\omega}(r)$ must satisfy boundary conditions at these points for the vacuum case that read [11]

$$\psi_{lm\omega}(r) \approx C^+_{lm\omega} r^3 e^{i\omega r^*} \qquad r\to\infty \,, \tag{45a}$$

$$\psi_{lm\omega}(r) \approx C^-_{lm\omega}\Delta e^{-ik_{\mathcal{H}} r^*} \qquad r\to r_+ \,, \tag{45b}$$

where $k_{\mathcal{H}} = \omega - ma/(2Mr_+)$ is the frequency at the horizon and $r^* = \int \varpi^2/\Delta \mathrm{d}r$ is the tortoise coordinate. The amplitudes at infinity and at the horizon $C^\pm_{lm\omega}$ can be determined using the Green function formalism as

$$C^\pm_{lm\omega} = \frac{1}{W}\int_{r_+}^{\infty} \frac{R^\mp_{lm\omega}\mathcal{T}_{lm\omega}}{\Delta^2}\mathrm{d}r \,, \tag{46}$$

where $R^\mp_{lm\omega}(r)$ are the solutions of the homogeneous radial Teukolsky equation satisfying boundary conditions at the horizon and at infinity, respectively, and $W = \left((\partial_r R^+_{lm\omega})R^-_{lm\omega} - R^+_{lm\omega}\partial_r R^-_{lm\omega}\right)/\Delta$ is the invariant Wronskian.

According to [32], the source term can be written as

$$\mathcal{T}_{lm\omega} = \int \mathrm{d}t\mathrm{d}\theta\mathrm{d}\phi\Delta^2 \sum_{ab} \mathcal{T}_{ab} e^{i\omega t - im\phi} \tag{47}$$

where $ab = nn, n\bar{m}, \bar{m}\bar{m}$ and

$$\mathcal{T}_{ab} = \sum_{i=0}^{I_{ab}} \frac{\partial^i}{\partial r^i}\left(f^{(i)}_{ab}\sqrt{-g}T_{ab}\right) \tag{48}$$

with $I_{nn} = 0$, $I_{n\bar{m}} = 1$, $I_{\bar{m}\bar{m}} = 2$. Note that the functions $f^{(i)}_{ab}$, which are defined in Appendix B, are slightly different than the definition in [32]. The projection of the stress-energy tensor into the tetrad can be written as [53]

$$\sqrt{-g}T_{ab} = \int \mathrm{d}\tau\big((A^{\mathrm{m}}_{ab} + A^{\mathrm{d}}_{ab})\delta^4 - \partial_\rho\big(B^\rho_{ab}\delta^4\big)\big) \tag{49a}$$

where

$$A^{\rm m}_{ab} = P_{(a}v_{b)} \,, \tag{49b}$$
$$A^{\rm d}_{ab} = S^{cd}v_{(b}\gamma_{a)dc} + S^{c}{}_{(a}\gamma_{b)dc}v^{d} \,, \tag{49c}$$
$$B^{\rho}_{ab} = S^{\rho}{}_{(a}v_{b)} \tag{49d}$$

and the spin coefficients are defined as

$$\gamma_{adc} = \lambda_{a\mu;\rho}\lambda^{\mu}_{d}\lambda^{\rho}_{c} \,. \tag{50}$$

After substituting Eqs. (47), (48), (49a) into Eq. (46) and integrating over the delta functions, the amplitudes $C^{\pm}_{lm\omega}$ can be computed as

$$C^{\pm}_{lm\omega} = \int_{-\infty}^{\infty} \frac{{\rm d}\tau}{\Sigma} e^{i\omega t(\tau) - im\phi(\tau)} I^{\pm}_{lm\omega}(r(\tau), z(\tau), u_a(\tau), S_{ab}(\tau)) \,, \tag{51}$$

where $I^{\pm}_{lm\omega}$ is defined as

$$I^{+}_{lm\omega} = \frac{\Sigma}{W}\sum_{ab}\sum_{i=0}^{I_{ab}}(-1)^i \left(\left(\left(A^{\rm m}_{ab} + A^{\rm d}_{ab} + i\Big(\omega B^{t}_{ab} - mB^{\phi}_{ab}\Big)\right) f^{(i)}_{ab} + B^{r}_{ab}\frac{\partial f^{(i)}_{ab}}{\partial r} + B^{z}_{ab}\frac{\partial f^{(i)}_{ab}}{\partial z}\right)\frac{{\rm d}^i R^{\mp}_{lm\omega}}{{\rm d}r^i} + B^{r}_{ab}f^{(i)}_{ab}\frac{{\rm d}^{i+1}R^{\mp}_{lm\omega}}{{\rm d}r^{i+1}}\right) . \tag{52}$$

Explicit expressions for $A^{\rm m}_{ab}$, $A^{\rm d}_{ab}$ and B^{μ}_{ab} are given in Appendix B.

Following a similar procedure to [27], it can be proven that the amplitudes can be written as a sum over discrete frequencies

$$C^{\pm}_{lm\omega} = \sum_{m,n,k,j} C^{\pm}_{lmnkj}\delta(\omega - \omega_{mnkj}) \quad \text{with} \quad \omega_{mnkj} = m\Omega_\phi + n\Omega_r + k\Omega_z + j\Omega_s \,. \tag{53}$$

The partial amplitudes are given by

$$C^{\pm}_{lmnkj} = \frac{1}{(2\pi)^2\Gamma}\int_0^{2\pi}{\rm d}w_r\int_0^{2\pi}{\rm d}w_z\int_0^{2\pi}{\rm d}w_s\, I^{\pm}_{lmnkj}(w_r, w_z, w_s) \times \exp(i\omega_{mnkj}\Delta t(w_r, w_z, w_s) - im\Delta\phi(w_r, w_z, w_s) + inw_r + ikw_z + ijw_s) \,, \tag{54}$$

where $I^{\pm}_{lmnkj}(w_r, w_z, w_s) = I^{\pm}_{lm\omega_{mnkj}}(r(w_r, w_z, w_s), z(w_r, w_z, w_s), u_a(w_r, w_z, w_s), S_{ab}(w_r, w_z, w_s))$.

The strain at infinity can be expressed from Eq. (40) as

$$h = -\frac{2}{r}\sum_{l,m,n,k,j}\frac{C^{+}_{lmnkj}}{\omega^2_{mnkj}}S_{lmnkj}(\theta)e^{-i\omega_{mnkj}u + im\phi} \,, \tag{55}$$

where $u = t - r^*$ is the retarded coordinate and $S_{lmnkj}(\theta) = {}_{-2}S^{a\omega_{mnkj}}_{lm}(\theta)$.

From the strain h and the stress energy tensor of a GW, the averaged energy and angular momentum fluxes can be derived as

$$\left\langle \mathcal{F}^{E} \right\rangle = \sum_{l,m,n,k,j}\mathcal{F}^{E}_{lmnkj} \,, \tag{56a}$$
$$\left\langle \mathcal{F}^{J_z} \right\rangle = \sum_{l,m,n,k,j}\mathcal{F}^{J_z}_{lmnkj} \tag{56b}$$

with

$$\mathcal{F}^{E}_{lmnkj} = \frac{\left|C^{+}_{lmnkj}\right|^2 + \alpha_{lmnkj}\left|C^{-}_{lmnkj}\right|^2}{4\pi\omega^2_{mnkj}} \,, \tag{56c}$$

$$\mathcal{F}^{J_z}_{lmnkj} = \frac{m\left(\left|C^{+}_{lmnkj}\right|^2 + \alpha_{lmnkj}\left|C^{-}_{lmnkj}\right|^2\right)}{4\pi\omega^3_{mnkj}} \,, \tag{56d}$$

where

$$\alpha_{lmnkj} = \frac{256(2Mr_+)^5 k_{\mathcal{H}}(k^2_{\mathcal{H}} + 4\epsilon^2)(k^2_{\mathcal{H}} + 16\epsilon^2)\omega^3_{mnkj}}{\left|\mathscr{C}_{lm\omega_{mnkj}}\right|^2} \,, \tag{57}$$

$\epsilon = \sqrt{M^2 - a^2}/(4Mr_+)$, and the Teukolsky-Starobinsky constant is

$$\begin{aligned}|\mathscr{C}_{lm\omega}|^2 = &\Big((\lambda_{lm\omega}+2)^2 + 4a\omega(m - a\omega)\Big) \\ &\times \left(\lambda^2_{lm\omega} + 36a\omega(m - a\omega)\right) \\ &- (2\lambda_{lm\omega} + 3)\left(48a\omega(m - 2a\omega)\right) \\ &+ 144\omega^2\left(M^2 - a^2\right) \,.\end{aligned} \tag{58}$$

Since all the terms proportional to the perpendicular component $\sigma_\perp$ are purely oscillating with frequency Ω_s, the only contribution to the fluxes from $\sigma_\perp$ comes from the modes with $j = \pm 1$. The amplitudes $C^{\pm}_{lmnkj}$ for $j = \pm 1$ are proportional to $\sigma_\perp$ and, therefore, the fluxes

for $j = \pm 1$ are quadratic in $\sigma_\perp$. We can neglect them in the linear order in σ and sum over l, m, n and k with $j = 0$. In this work we focus on the contribution of the parallel component $\sigma_\parallel$ to the fluxes and, therefore, calculate only the $j = 0$ modes. For simplicity, we omit in the rest of the article the j index and write ω_{mnk}, $\mathcal{F}_{lmnk}$.

Note that since the trajectory is computed up to linear order in σ, the amplitudes or the fluxes are valid up to $\mathcal{O}(\sigma)$ as well.

IV. NUMERICAL IMPLEMENTATION AND RESULTS

In this section we describe the process of numerically calculating the orbit and the fluxes described in the previous sections. If not stated otherwise, all calculations were done in *Mathematica*. In some parts of these calculations we used the *Black Hole Perturbation Toolkit* (BHPT) [54].

A. Calculating the trajectory

Our approach to calculate the linear-in-spin parts of the trajectory is the same as the approach described in [37, 38]. We managed to simplify the equations given in the latter papers and the respective details are given in Appendix C. To calculate the geodesic motion we employed the *KerrGeodesics* package of the BHPT.

Using the aforementioned simplifications, we first calculated $u^S_{t,nk}$ and $u^S_{\phi,nk}$ as

$$u^S_{t,nk} = \frac{i\mathcal{R}_{t,nk}}{n\hat{\Upsilon}_r + k\hat{\Upsilon}_z}\,, \quad u^S_{\phi,nk} = \frac{i\mathcal{R}_{\phi,nk}}{n\hat{\Upsilon}_r + k\hat{\Upsilon}_z} \tag{59}$$

for $n \neq 0$ or $k \neq 0$, where $\mathcal{R}_{t,nk}$ and $\mathcal{R}_{\phi,nk}$ are Fourier coefficients of functions given in Eqs. (C5). Then, the Fourier coefficients $u^S_{t,00}$, $u^S_{\phi,00}$, $\delta\chi^S_{r,n}$, $\delta\chi^S_{z,k}$, $\not{z}^S_{nk}$, $\not{\chi}^S_{nk}$ and the frequencies' components Υ^S_r and Υ^S_z were calculated as the least squares solution to the system of linear equations [37]

$$\mathbf{M}\cdot\mathbf{v} + \mathbf{c} = 0\,. \tag{60}$$

In the system of equations (60), the column vector $\mathbf{v}$ contains the unknown coefficients, the column vector $\mathbf{c}$ is given from Fourier expansion components of the functions $\mathcal{J}$, $\mathcal{V}$ and $\mathcal{P}$ in Eqs. (C5) that are not coefficients of the unknown quantities, while the elements of the matrix $\mathbf{M}$ are calculated from the Fourier coefficients of functions $\mathcal{F}_{r,\not{z}}$, $\mathcal{G}_{r,\not{z},\theta,\not{\chi}}$, $\mathcal{H}_{r,\not{z},\theta,\not{\chi}}$, $\mathcal{I}_{1r,1\theta,2,3}$, $\mathcal{Q}_{\theta,\not{\chi}}$, $\mathcal{S}_{r,\not{z},\theta,\not{\chi}}$, $\mathcal{T}_{r,\not{z},\theta,\not{\chi}}$, $\mathcal{U}_{1r,1\theta,2,3}$, $\mathcal{K}_{r,\not{z},\theta,\not{\chi}}$, $\mathcal{M}_{r,\not{z},\theta,\not{\chi}}$, $\mathcal{N}_{1r,1\theta}$, which are functions of the geodesic quantities and they are given in the supplemental material of [37].

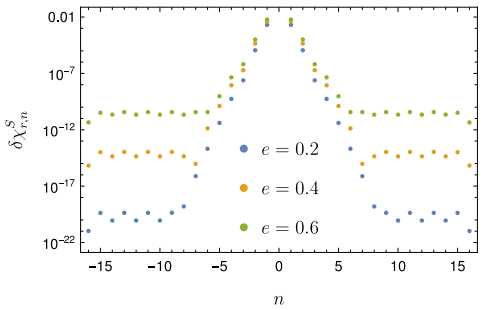

FIG. 1. Fourier coefficients $\delta\chi^S_{r,n}$ for generic orbits with $a = 0.9M$, $p = 15$, $I = 15°$ and different eccentricities. Because the Fourier series is truncated at $n_{\max} = 16$ and the coefficients have been calculated approximately using least squares, the convergence stops at certain $\pm n$.

In particular, the Fourier coefficients are calculated as, e.g.,

$$\mathcal{R}_{t,nk} = \sum_{a,b} \mathcal{R}_t(\hat{r}(w^a_r), \hat{z}(w^b_z)) F^a_n G^b_k \tag{61}$$

where F^a_n and G^b_k are matrices of a discrete Fourier transform

$$F^a_n = \exp\left(\frac{\pi i n}{N_r}(1+2a)\right)\frac{1}{N_r}\,, \tag{62a}$$

$$G^b_k = \exp\left(\frac{\pi i k}{N_z}(1+2b)\right)\frac{1}{N_z} \tag{62b}$$

and N_r (N_z) is the number of points along w_r (w_z). Each function $\mathcal{R}_t$ is evaluated at equidistant points along w_r and w_z as

$$w^a_r = \frac{2\pi}{N_r}\left(\frac{1}{2} + a\right)\,, \tag{63a}$$

$$w^b_z = \frac{2\pi}{N_z}\left(\frac{1}{2} + b\right) \tag{63b}$$

where $a = 0, 1, \ldots, N_r - 1$, $b = 0, 1, \ldots, N_z - 1$. The numbers of steps along w_r and w_z were chosen according to the orbital parameters, i.e., a higher number of steps is needed for higher eccentricity and higher inclination.

Actually, not all of the Fourier coefficients can be calculated accurately enough for highly eccentric and inclined orbits, as can be seen in Fig. 1, where the coefficients $\delta\chi^S_{r,n}$ are plotted for different eccentricities. Fig. 1 shows that after a certain value of n the coefficients stop decreasing. This is caused by the truncation of the series and by the fact that the system of equations is solved approximately using least squares. Similar behavior occurs for $\delta\chi^S_{z,k}$ and other Fourier series.

B. Gravitational-wave fluxes

After calculating the orbit, the partial amplitudes $C^{\pm}_{lmnk}$ are evaluated by numerically calculating the two-dimensional integral (54). The integral in Eq. (54) is computed over one period of w_r and of w_z; hence, we employ the midpoint rule, since the convergence is exponential [55]. The number of steps for the integration has been chosen as follows. We assume that the main oscillating part of the integrand comes from the exponential term. The number of oscillations in w_r and w_z is respectively n and k. However, because of Δt and $\Delta\phi$, the "frequency" of the oscillations can be higher at the turning points as can be seen in Fig. 3 in [36]. In order to have enough steps in each oscillation, the number of steps in w_r is calculated from the frequency of the oscillations at the pericentre ($w_r = 0$) and apocentre ($w_r = \pi$) as

$$\max\{|16\lceil\varphi_r'(0)+n\rceil|, |16\lceil\varphi_r'(\pi)+n\rceil|, 32\}\,. \tag{64}$$

Similarly, the number of steps in w_z comes from the frequency at the turning point ($w_z = 0, \pi$) and the equatorial plane ($w_z = \pi/2$) as

$$\max\{|8\lceil\varphi_z'(0)+k\rceil|, |8\lceil\varphi_z'(\pi/2)+k\rceil|, 32\}\,, \tag{65}$$

where $\varphi_y(w_y) = \omega_{mnk}\Delta\hat{t}_y(w_y) - m\Delta\hat{\phi}_y(w_y)$, $y = r, z$. The integration over w_s is trivial for $j = 0$, since the function is independent of w_s.

The homogeneous radial Teukolsky equation solutions $R^{\pm}_{lmn\omega}$ have been calculated using the *Teukolsky* package of the BHPT. There the radial Teukolsky equation is numerically integrated in hyperboloidal coordinates [56] and the initial conditions are calculated by using the Mano-Sasaki-Takasugi method [57]. On the other hand, the spin-weighted spheroidal harmonics ${}_{-2}S^{a\omega}_{lm}$ have been calculated using the *SpinWeightedSpheroidalHarmonics* package of the BHPT where the Leaver's method [58] is employed.

Similarly as in [27], we use the symmetries of the motion to reduce the integral (54) into a sum of four integrals over $0 < w_r < \pi$, $0 < w_z < \pi$. Apart from the geodesic symmetries $\hat{y}(w_y) = \hat{y}(2\pi - w_y)$, $\Delta\hat{x}_y(w_y) = -\Delta\hat{x}_y(2\pi - w_y)$, and $U^y(w_y) = -U^y(2\pi - w_y)$, where $x = t, \phi$, $y = r, z$, we used also symmetries of the linear-in-spin parts, which read $f(w_r, w_z) = f(2\pi - w_r, 2\pi - w_z)$ for r^S and z^S and $f(w_r, w_z) = -f(2\pi - w_r, 2\pi - w_z)$ for U^r_S, U^z_S, Δt^S, and $\Delta\phi^S$. Thanks to the reflection symmetry around the equatorial plane, there is also a symmetry $f(w_r, w_z) = f(w_r, w_z + \pi)$ for r^S, U^r_S, Δt^S, and $\Delta\phi^S$ and $f(w_r, w_z) = -f(w_r, w_z + \pi)$ for z^S and U^z_S. Combining these symmetries, it is sufficient to evaluate the linear-in-spin parts only for $0 < w_r < \pi$, $0 < w_z < \pi$, which reduces the computational costs, since the evaluation of the Fourier series (26) is slow. After these optimizations, calculating one mode takes seconds for low eccentricities, inclinations and mode numbers, while it takes tens of seconds for high eccentricities, inclinations and mode numbers.

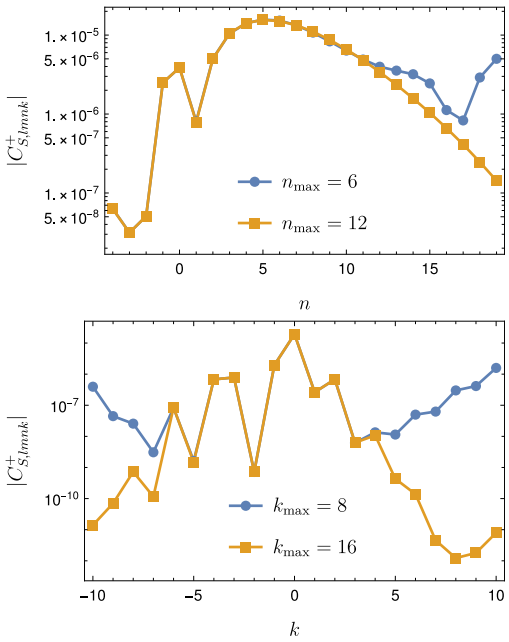

FIG. 2. Top: Dependence of the linear-in-spin parts of the partial amplitudes for $k = 0$ and different $n_{\max}$ for an orbit with $a = 0.9M$, $p = 15$, $e = 0.5$, $I = 15°$. Bottom: Dependence of the linear-in-spin parts of the partial amplitudes on k for $n = 0$ different $k_{\max}$ for an orbit with $a = 0.9M$, $p = 12$, $e = 0.2$, $I = 60°$. Note that the numbers n and k refer to the modes C^+_{lmnk} and $n_{\max}$ and $k_{\max}$ refer to the trajectory.

To extract the linear-in-spin part of the partial amplitudes or fluxes, i.e. their derivative with respect to σ, we use the fourth-order finite difference formula

$$f^S = \frac{\frac{1}{12}f(-2\sigma) - \frac{2}{3}f(-\sigma) + \frac{2}{3}f(\sigma) - \frac{1}{12}f(2\sigma)}{\sigma}\,, \tag{66}$$

where $f = C^{\pm}_{lmnk}$, $\mathcal{F}^E$ or $\mathcal{F}^{J_z}$ and $\sigma = 0.5$ in our calculations. This is necessary for comparisons with other results, since the $\mathcal{O}(\sigma^2)$ part of the fluxes is invalid due to the trajectory being linearized in spin.

Because the Fourier series (26) of the linear-in-spin part of the trajectory is truncated at $\pm n_{\max}$ and $\pm k_{\max}$, only a finite number of n and k modes of the amplitudes $C^{\pm}_{lmnk}$ and of the fluxes can be calculated accurately. In Fig. 2 we show the dependence of the absolute value of the linear-in-spin parts of the amplitudes $\left|C^+_{S,lmnk}\right|$ on n and k for different $n_{\max}$ and $k_{\max}$. The top panel shows amplitudes for an orbit with high eccentricity ($e = 0.5$). If the Fourier series in n is truncated at lower $n_{\max}$, the amplitudes stop being accurate after a certain value of n. Similarly, for an orbit with higher inclination ($I = 60°$) shown in the bottom panel of Fig. 2, when the series is truncated at lower $k_{\max}$, the amplitudes stop converg-

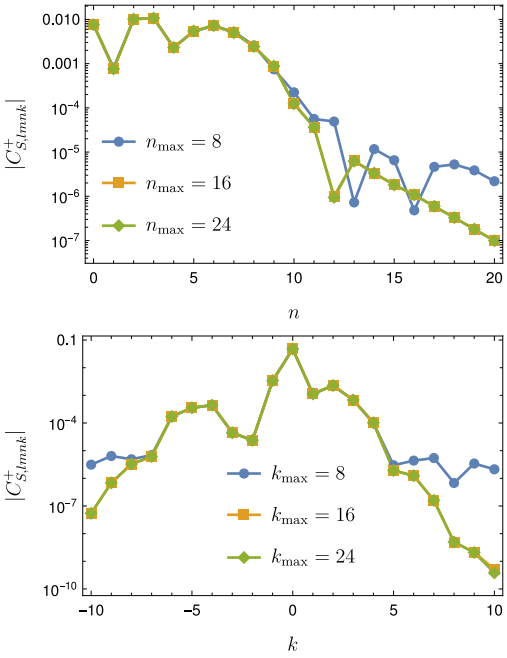

FIG. 3. Dependence of the linear parts of the amplitudes on n for different $n_{\max}$ (top) and on k for different $k_{\max}$ (bottom) for orbits near the separatrix. The orbital parameters are $a = 0.9M$, $p = 3.1$, $e = 0.5$, $I = 15°$ (top) and $a = 0.9M$, $p = 4.2$, $e = 0.2$, $I = 60°$ (bottom). Note that at the top panel the $n_{\max} = 16$ and $n_{\max} = 24$ almost coincide; the same holds for the $k_{\max} = 16$ and $k_{\max} = 24$ at the bottom panel.

ing with k. Such issues have been already reported for geodesic fluxes in [59].

Near the separatrix the calculations are difficult because of the divergence of some quantities as was already shown in the equatorial case [12]. In Fig. 3 we show the dependence of $\left|C^{+}_{S,lmnk}\right|$ on n and k for orbits near the separatrix $p_{\rm s}$, namely $p - p_{\rm s} = 0.19866$ for the top panel and $p - p_{\rm s} = 0.22076$ for the bottom panel. We can see that Figures 2 and 3 are qualitatively the same. This is because in both cases the dominant source of the error is the linear part of the trajectory caused by the behavior of the Fourier coefficients shown in Fig. 1. Since the coefficients $\delta\chi^{S}_{r,n}$ etc. are accurate only for $|n| \leq 3$ for $n_{\max} = 8$, $|n| \leq 6$ for $n_{\max} = 16$ and $|n| \leq 9$ for $n_{\rm namx} = 24$, the linear parts of the amplitudes are unreliable outside these bounds. Thus, although the linear parts of the amplitudes for $n_{\max} = 16$ and 24 seem to coincide and converge to zero, they are not trustworthy. The same argumrents hold for the bottom panel of Fig. 3. For better analysis the higher frequency modes of the trajectory must be calculated with higher accuracy.

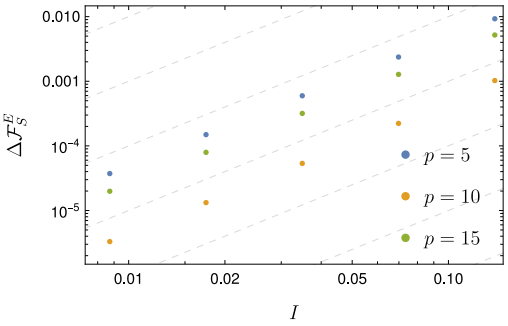

FIG. 4. Relative differences of the linear-in-spin part of the total energy flux $\mathcal{F}^{E}_{S}$ between equatorial and nearly equatorial cases of nearly spherical orbits for $a = 0.9M$ and different semi-latus rectum p. The dashed gray lines indicate the $\mathcal{O}(I^2)$ behavior.

Because this task is computationally expensive, we leave it for future work.

C. Comparison with the equatorial limit

To verify our results with the equatorial limit ($I \to 0$), we have compared the frequency domain results for several inclinations with a frequency domain code for equatorial orbits [36]. First, we have calculated the sum of the total energy flux over l and m for nearly spherical orbits with inclinations $I = 0.5°, 1°, 2°, 4°, 8°$. We plot the relative difference $\Delta\mathcal{F}^{E}_{S} = \left|1 - \mathcal{F}^{E}_{S}/\mathcal{F}^{E}_{S,I=0}\right|$ against I in logarithmic scale in both axes in Fig. 4. This way, we have verified that the linear-in-spin part $\mathcal{F}^{E}_{S}$ asymptotically approaches the equatorial limit as $I \to 0$ with an $\mathcal{O}(I^2)$ difference convergence.

Similar procedure has been repeated for the eccentric orbits. We have computed the l, m, n with $k = 0$ modes of the energy flux $\mathcal{F}^{E}_{S,lmnk}$ for different inclinations I and plot the relative differences $\Delta\mathcal{F}^{E}_{S,lmnk} = \left|1 - \mathcal{F}^{E}_{S,lmnk}/\mathcal{F}^{E}_{S,lmnk,I=0}\right|$ in Fig. 5. We again see that for all the modes the relative difference in fluxes $\mathcal{F}^{E}_{S,lmnk}$ follows an $\mathcal{O}(I^2)$ convergence as $I \to 0$. This behavior agrees with the behavior of a Post-Newtonian expansion of nearly-equatorial geodesic fluxes in Refs. [15, 60], because the parameters y and Y in these references are $\mathcal{O}(I^2)$.

D. Comparison of frequency and time domain results

To further verify the frequency domain calculation of the fluxes $\mathcal{F}^{E}$ and $\mathcal{F}^{J_z}$, we compared them with fluxes calculated using time domain Teukolsky equation solver *Teukode* [61]. This code solves the (2+1)-dimensional

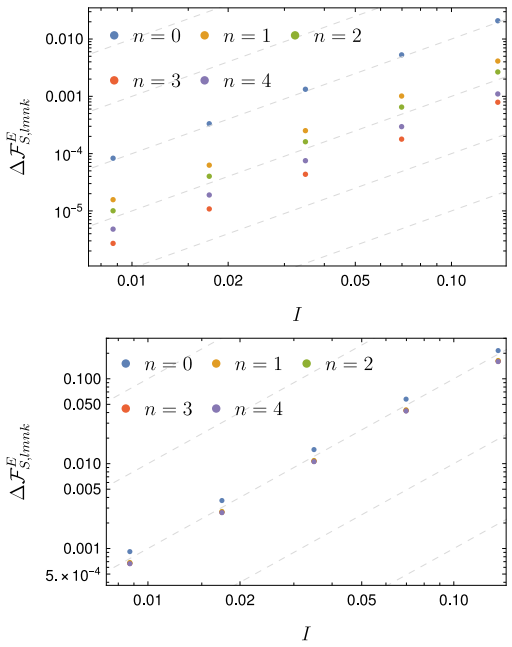

FIG. 5. Relative differences of the linear-in-spin part of the total energy flux $\mathcal{F}^E_{S,lmn0}$ between equatorial and nearly equatorial eccentric orbits with $a = 0.9M$, $p = 12$, $e = 0.3$. The top panel shows modes with $l = 2$, $m = 2$ and the bottom panel shows $l = 5$, $m = 4$. The dashed gray lines show the $\mathcal{O}(I^2)$ behavior.

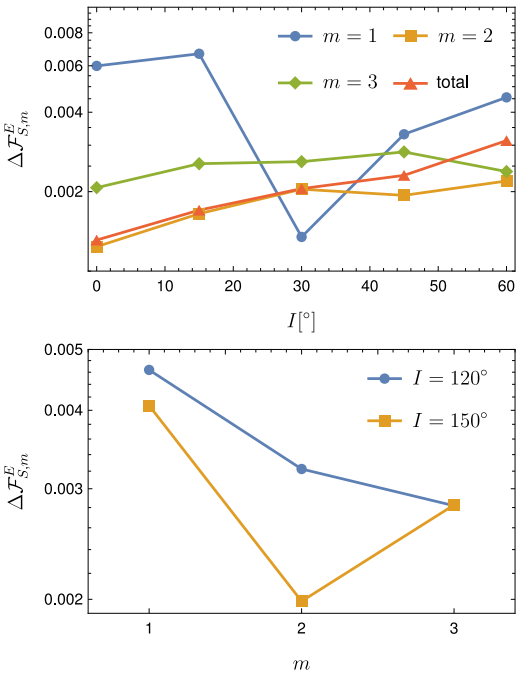

FIG. 6. Relative differences of the linear-in-spin part of the fluxes $\mathcal{F}^E_{S,m}$ between time domain and frequency domain calculations for different inclinations and m for nearly spherical orbits with $a = 0.9M$ and $p = 10$. The top panel shows prograde orbits and the bottom panel shows retrograde orbits.

p	e	$I/^\circ$	m	$\mathcal{F}^E_{S,m}$	$\Delta\mathcal{F}^E_{S,m}$
10	0.1	15	2	-2.8259×10^{-6}	1×10^{-3}
12	0.2	30	1	-1.1954×10^{-7}	2×10^{-5}
12	0.2	30	2	-1.0488×10^{-6}	1×10^{-3}
12	0.2	30	3	-1.4210×10^{-7}	3×10^{-3}
12	0.2	60	2	-8.0550×10^{-7}	5×10^{-4}
15	0.5	15	2	-4.2936×10^{-7}	2×10^{-3}

TABLE I. Relative differences $\Delta\mathcal{F}^E_{S,m}$ of the linear-in-spin part of the energy flux $\mathcal{F}^E_{S,m}$ between frequency domain and time domain computations for given orbital parameters and azimuthal number m. All orbits have $a = 0.9M$.

Teukolsky equation with spinning-particle source term in hyperboloidal horizon-penetrating coordinates. The fluxes of energy and angular momentum are extracted at the future null infinity. The numerical scheme consists of a method of lines with sixth order finite difference formulas in space and fourth order Runge-Kutta scheme in time.

First, we compare the computation of energy fluxes to infinity from nearly spherical orbits, i.e. orbits with $e = 0$. For details about the time domain calculation of the trajectory and the fluxes see Appendix D. Since the time domain outputs m-modes of the flux, we summed the frequency domain flux over l and k (for spherical orbits, only the $n = 0$ modes are nonzero). In Fig. 6, we show the relative difference between the time-domain and frequency-domain-computed linear-in-spin part of the energy flux $\Delta\mathcal{F}^E_{S,m} = \left|1 - \mathcal{F}^{E,\mathrm{fd}}_{S,m}/\mathcal{F}^{E,\mathrm{td}}_{S,m}\right|$ for several inclinations I and azimuthal numbers m. The top panel shows the dependence of the relative difference on I for prograde orbits and the lower panel shows the dependence on m for retrograde orbits. We can see that the error is at most 6×10^{-3} which is around the reported accuracy of Teukode in our previous paper [36]. The error of the frequency domain comes from the truncation of the Fourier expansion to $n_{\max}$ and $k_{\max}$ and from the summation of the fluxes over l and k. On top of that, one has to take into account that based on the order of the method and the length of the step we estimate that the relative error of linearization of both the time domain and frequency domain flux using the fourth-order finite difference formula should be around 10^{-5}. This estimation holds not only for the nearly spherical orbits, but for the generic orbits as well.

Next we moved to generic orbits. We have summed the energy flux over l, n and k for given m and orbital parameters, in order to calculate the relative difference

between the linear part of frequency domain fluxes and time domain fluxes $\Delta\mathcal{F}^{E}_{S,m}$. The results are presented in Table I. In this case, the relative difference is at most 3×10^{-3}.

Appendix E shows plots of linear-in-spin calculations of the amplitudes and of the fluxes and some reference data tables.

V. SUMMARY

In this work we provided asymptotic GW fluxes from off-equatorial orbits of spinning bodies in the Kerr spacetime. In our framework the spin of the small body is parallel to the orbital angular momentum and the calculations are valid up to linear order in the spin.

We employed the frequency-domain calculation of the orbits of spinning particles which was introduced in [37, 38]. In this setup, the linear-in-spin part of the trajectory is solved in the frequency domain using MPD equations under TD SSC. We extended this setup to calculate the corrections to the coordinate time Δt^S and the azimuthal coordinate $\Delta\phi^S$.

We calculated GW fluxes from the aforementioned orbits using the Teukolsky equation. To do that, we constructed the source of the Teukolsky equation for off-equatorial orbits of spinning particles for spin parallel to the orbital angular momentum. Then, by using this source, we developed a new frequency-domain inhomogeneous Teukolsky equation solver in *Mathematica*, which delivers the GW amplitudes $C^{\pm}_{lmnk}$ at infinity and at the horizon. Having these amplitudes allowed us to calculate the total energy and angular momentum fluxes, whose validity is up to linear order in the spin. Since at the linear order in spin the fluxes are independent of the precessing perpendicular component of the spin, our approach to compute the fluxes is sufficient for any linear-in-spin configuration.

We numerically linearized the fluxes and compared the results for nearly equatorial orbits with previously known frequency domain results [36] for equatorial orbits to verify their validity in the equatorial limit. We found that the difference of the off-equatorial and equatorial flux behaves as $\mathcal{O}\big(I^2\big)$. Furthermore, we compared the off-equatorial results with time domain results obtained by time domain Teukolsky equation solver *Teukode*. For different orbital parameters and azimuthal numbers m the relative difference is around 10^{-3}, which is the current accuracy of computations produced by *Teukode*.

This work is a part of an ongoing effort to find the postadiabatic terms [11, 12, 17, 62–64] needed to model EMRI waveforms accurately enough for future space-based gravitational wave observatories like LISA. Our work can be extended to model adiabatic inspirals of a spinning body on generic orbits in a Kerr background as we have done for the equatorial plane case in Ref. [12]; however, to achieve this the flux of the Carter-like constants K_R and the parallel component of the spin C_Y must be derived first. In the near future, the new frequency-domain Teukolsky equation solver *Mathematica* code is planned to be published in the *Black Hole Perturbation Toolkit* repository.

ACKNOWLEDGMENTS

VS and GLG have been supported by the fellowship Lumina Quaeruntur No. LQ100032102 of the Czech Academy of Sciences. V.S. acknowledges support by the project "Grant schemes at CU" (reg.no. CZ.02.2.69/0.0/0.0/19_073/0016935). We would like to thank Vojtěch Witzany and Josh Mathews for useful discussions and comments. This work makes use of the Black Hole Perturbation Toolkit. Computational resources were provided by the e-INFRA CZ project (ID:90140), supported by the Ministry of Education, Youth and Sports of the Czech Republic. LVD and SAH were supported by NASA ATP Grant 80NSSC18K1091, and NSF Grant PHY-2110384.

Appendix A: Geodesic motion in Kerr

In this Appendix we briefly discuss aspects of geodesic motion in the Kerr spacetime.

The specific energy

$$E=-u_t \tag{A1}$$

and the specific angular momentum along the symmetry axis

$$L_z=u_\phi \tag{A2}$$

are conserved thanks to two respective Killing vectors. Carter in Ref. [22] found a third constant

$$K=K_{\mu\nu}u^\mu u^\nu\,, \tag{A3}$$

and formulated the equations of motion as

$$\frac{\mathrm{d}t}{\mathrm{d}\lambda}=V_t(r,z,E,L_z)\,, \tag{A4a}$$

$$\frac{\mathrm{d}r}{\mathrm{d}\lambda}=\pm\sqrt{R(r,E,L_z,K)}\,, \tag{A4b}$$

$$\frac{\mathrm{d}z}{\mathrm{d}\lambda}=\pm\sqrt{Z(z,E,L_z,K)}\,, \tag{A4c}$$

$$\frac{\mathrm{d}\phi}{\mathrm{d}\lambda}=V_\phi(r,z,E,L_z)\,, \tag{A4d}$$

where

$$V^t=\frac{r^2+a^2}{\Delta}\big((r^2+a^2)E-aL_z\big)-a^2E(1-z^2)+aL_z, \tag{A5a}$$

$$R=\big((r^2+a^2)E-aL_z\big)^2-\Delta\big(K+r^2\big)\,, \tag{A5b}$$

$$Z=-\big((1-z^2)aE-L_z\big)^2+(1-z^2)\big(K-a^2z^2\big)\,, \tag{A5c}$$

$$V^\phi = \frac{a}{\Delta}\big((r^2+a^2)E - aL_z\big) + \frac{L_z}{1-z^2} - aE\,, \quad \text{(A5d)}$$

These equations are parametrized with Carter-Mino time $\mathrm{d}\tau/\mathrm{d}\lambda = \Sigma$. The motion in r oscillates between its radial turning points r_1 and r_2 with frequency Υ_r and, similarly, the z-motion oscillates between its polar turning points $\pm z_1$ with frequency Υ_z. Moreover, the evolution of t and ϕ can be written as

$$t(\lambda) = \Gamma\lambda + \Delta t_r(\lambda) + \Delta t_z(\lambda)\,, \quad \text{(A6a)}$$
$$\phi(\lambda) = \Upsilon_\phi\lambda + \Delta\phi_r(\lambda) + \Delta\phi_z(\lambda)\,, \quad \text{(A6b)}$$

where Γ and Υ_ϕ are average rates of change of t and ϕ; while Δt_r with $\Delta\phi_r$ are periodic functions with frequency Υ_r, and Δt_z with $\Delta\phi_z$ are periodic functions with frequency Υ_z.

It is convenient to define frequencies with respect to coordinate (Killing) time as

$$\Omega_r = \frac{\Upsilon_r}{\Gamma}\,, \quad \text{(A7a)}$$
$$\Omega_z = \frac{\Upsilon_z}{\Gamma}\,, \quad \text{(A7b)}$$
$$\Omega_\phi = \frac{\Upsilon_\phi}{\Gamma}\,, \quad \text{(A7c)}$$

but the system is not periodic in coordinate time and these frequencies should be understood as average frequencies.

The motion is often parametrized by its orbital parameters: the semi-latus rectum p, the eccentricity e and the inclination angle I which are defined from the turning points as

$$r_1 = \frac{Mp}{1-e}\,, \qquad r_2 = \frac{Mp}{1+e}\,, \qquad z_1 = \sin I \quad \text{(A8)}$$

where $0 < I < \pi/2$ for prograde orbits and $\pi/2 < I < \pi$ for retrograde orbits. Analytic expressions for the constants of motion in terms of the orbital parameters can be found in [27]. Fujita and Hikida gave analytical expressions for the frequencies and coordinates in [51].

Appendix B: Source term

In this Appendix we present explicit expressions for the functions appearing in the source term for the calculation of the partial amplitudes in Eq. (52).

Whereas A^{m}_{ab} is entirely given by Eq. (49b) with $P_a = \mu u_a$ and $v_a = u_a$ in the linear order, the terms in A^{d}_{ab} can be expressed with NP spin coefficients as

$$S^{cd}\gamma_{ndc} = S_{ln}(\gamma+\bar\gamma) + S_{n\bar m}(-\bar\pi+\bar\alpha+\beta) + S_{nm}(-\pi+\alpha+\bar\beta) + S_{m\bar m}(-\mu+\bar\mu)\,, \quad \text{(B1a)}$$
$$S^{cd}\gamma_{\bar m dc} = S_{ln}(\pi+\bar\tau) + S_{n\bar m}\bar\rho + S_{nm}(\alpha+\bar\beta) + S_{l\bar m}(-\bar\gamma+\gamma) + S_{m\bar m}(-\alpha+\bar\beta)\,, \quad \text{(B1b)}$$
$$S^{c}{}_{n}\gamma_{ndc}u^d = S_{ln}(\gamma+\bar\gamma)u_n + S_{n\bar m}((\bar\alpha+\beta)u_n - \mu u_m) + S_{nm}((\alpha+\bar\beta)u_n + \bar\mu u_{\bar m})\,, \quad \text{(B1c)}$$
$$S^{c}{}_{\bar m}\gamma_{\bar m dc}u^d = S_{n\bar m}(-\pi u_l) + S_{l\bar m}(\bar\tau u_n - (\bar\gamma-\gamma)u_{\bar m}) - S_{m\bar m}(-(-\alpha+\bar\beta)u_{\bar m})\,, \quad \text{(B1d)}$$
$$S^{c}{}_{(n}\gamma_{\bar m)dc}u^d = (S_{ln}(\bar\tau u_n - (\bar\gamma-\gamma)u_{\bar m}) + S_{n\bar m}(\bar\rho u_n - \mu u_l - (\bar\alpha-\beta+\bar\pi)u_{\bar m} - \pi u_m)$$
$$S_{nm}(-(-\alpha+\bar\beta)u_{\bar m}) + S_{l\bar m}(\gamma+\bar\gamma)u_n - S_{m\bar m}((\alpha+\bar\beta)u_n - \bar\mu u_{\bar m}))/2 \quad \text{(B1e)}$$

The tetrad components of the spin tensor for $\sigma_\perp = 0$ can be expressed as

$$S_{ln} = -\sigma_\parallel\frac{r(\hat K - a^2z^2)}{\sqrt{\hat K}\Sigma}\,, \quad S_{nm} = \sigma_\parallel\frac{\zeta}{\sqrt{\hat K}}u_m u_n\,, \quad \text{(B2a)}$$

$$S_{l\bar m} = -\sigma_\parallel\frac{\zeta}{\sqrt{\hat K}}u_l u_{\bar m}\,, \qquad S_{m\bar m} = \sigma_\parallel\frac{iaz(\hat K + r^2)}{\sqrt{\hat K}\Sigma}\,, \quad \text{(B2b)}$$

while the terms from the partial derivative for the dipole term have the form

$$i(\omega S^t{}_n - mS^\phi{}_n) = \frac{a\omega(1-z^2)-m}{\sqrt{2(1-z^2)}\Sigma}(\zeta S_{n\bar m} - \bar\zeta S_{nm}) - \frac{iK}{2\Sigma}S_{ln}\,, \quad \text{(B3a)}$$

$$i(\omega S^t{}_{\bar m} - mS^\phi{}_{\bar m}) = -iK\left(\frac{S_{n\bar m}}{\Delta} + \frac{S_{l\bar m}}{2\Sigma}\right) + \frac{a\omega(1-z^2)-m}{\sqrt{2(1-z^2)}\zeta}S_{m\bar m}\,, \quad \text{(B3b)}$$
$$S^r{}_n = \frac{\Delta}{2\Sigma}S_{ln}\,, \quad \text{(B3c)}$$
$$S^r{}_{\bar m} = -S_{n\bar m} + \frac{\Delta}{2\Sigma}S_{l\bar m}\,, \quad \text{(B3d)}$$
$$S^z{}_n = \frac{\sqrt{1-z^2}(S_{n\bar m}\zeta + S_{nm}\bar\zeta)}{\sqrt{2}\Sigma}\,, \quad \text{(B3e)}$$
$$S^z{}_{\bar m} = -\frac{\sqrt{1-z^2}S_{m\bar m}}{\sqrt{2}\zeta}\,, \quad \text{(B3f)}$$

where $K = (r^2+a^2)\omega - am$. The functions $f^{(i)}_{ab}$ are given

by

$$f^{(0)}_{nn} = -\frac{2\zeta^2}{\Delta^2}\left(\mathcal{L}_1^\dagger\mathcal{L}_2^\dagger - 2ia\zeta^{-1}\sqrt{1-z^2}\mathcal{L}_2^\dagger\right)S\,, \tag{B4a}$$

$$f^{(0)}_{n\bar{m}} = \frac{2\sqrt{2}\zeta^2}{\bar{\zeta}\Delta}\Bigg(\left(\frac{iK}{\Delta}+\zeta^{-1}+\bar{\zeta}^{-1}\right)\mathcal{L}_2^\dagger - a\sqrt{1-z^2}\frac{K}{\Delta}\left(\bar{\zeta}^{-1}-\zeta^{-1}\right)\Bigg)S\,, \tag{B4b}$$

$$f^{(1)}_{n\bar{m}} = \frac{2\sqrt{2}\zeta^2}{\bar{\zeta}\Delta}\left(\mathcal{L}_2^\dagger + ia\sqrt{1-z^2}\left(\bar{\zeta}^{-1}-\zeta^{-1}\right)\right)S\,, \tag{B4c}$$

$$f^{(0)}_{\bar{m}\bar{m}} = \frac{\zeta^2}{\bar{\zeta}^2}\left(i\partial_r\left(\frac{K}{\Delta}\right) - 2i\zeta^{-1}\frac{K}{\Delta} + \left(\frac{K}{\Delta}\right)^2\right)S\,, \tag{B4d}$$

$$f^{(1)}_{\bar{m}\bar{m}} = -\frac{2\zeta^2}{\bar{\zeta}^2}\left(\zeta^{-1}+i\frac{K}{\Delta}\right)S\,, \tag{B4e}$$

$$f^{(2)}_{\bar{m}\bar{m}} = -\frac{\zeta^2}{\bar{\zeta}^2}S\,, \tag{B4f}$$

where

$$\mathcal{L}_n^\dagger = -\sqrt{1-z^2}\left(\partial_z - \frac{m-nz}{1-z^2} + a\omega\right)\,. \tag{B5}$$

Appendix C: Trajectory

In this Appendix we present some formulas we derived to calculate the linear-in-spin contribution to the trajectory. We use the tetrad from Eqs. (47)–(51) in [50] where $\tilde{e}_2^\mu$ and e_3^μ have opposite sign to align e_3^μ with total angular momentum and to have right-handed system. Then the right hand side of MPD equations can be written as

$$f^\mu_{\rm MPD} = -\frac{1}{2}e^\mu_A\eta^{AB}R_{B0CD}S^{CD}\,, \tag{C1}$$

where R_{B0CD} are components of the Riemann tensor in the Marck tetrad. Because of the way this tetrad is constructed [21] and the fact that the Riemann tensor has a simple form in the Kinnersley tetrad, the components can be simplified to

$$R_{1012} = \frac{3\sqrt{(\hat{K}+r^2)(\hat{K}-a^2z^2)}\Big(\Big(a^2z^2(\hat{K}+r^2)-r^2(\hat{K}-a^2z^2)\Big)I_1 + arz(2\hat{K}+r^2-a^2z^2)I_2\Big)}{\hat{K}\Sigma^2}\,, \tag{C2a}$$

$$R_{3012} = \frac{6arz(\hat{K}+r^2)(\hat{K}-a^2z^2)I_1}{\hat{K}\Sigma^2} + \left(1+3\frac{-a^2z^2(\hat{K}+r^2)^2+r^2(\hat{K}-a^2z^2)^2}{\hat{K}\Sigma^2}\right)I_2\,, \tag{C2b}$$

$$R_{2013} = -I_2\,, \tag{C2c}$$

$$R_{1023} = -R_{3012} + R_{2013}\,, \tag{C2d}$$

$$R_{3023} = R_{1012}\,, \tag{C2e}$$

and $R_{2012} = R_{1013} = R_{3013} = R_{2023} = 0$, where

$$I_1 = \frac{Mr(r^2-3a^2z^2)}{\Sigma^3}\,, \tag{C3}$$

$$I_2 = \frac{Maz(3r^2-a^2z^2)}{\Sigma^3}\,. \tag{C4}$$

The functions $\mathcal{R}_{t,\phi}$, $\mathcal{J}$, $\mathcal{V}$, and $\mathcal{P}$ from Eqs. (3.24), (4.62), and (4.63) in [38] can be simplified to

$$\mathcal{R}_t = \Sigma f_t^{\rm MPD}\,, \tag{C5a}$$

$$\mathcal{R}_\phi = \Sigma f_\phi^{\rm MPD}\,, \tag{C5b}$$

$$\mathcal{J} = -\Sigma^2 f^r_{\rm MPD} + \mathcal{I}_2\delta u_t^S + \mathcal{I}_3\delta u_\phi^S\,, \tag{C5c}$$

$$\mathcal{V} = -\Sigma^2 f^\theta_{\rm MPD} + \mathcal{U}_2\delta u_t^S + \mathcal{U}_3\delta u_\phi^S\,, \tag{C5d}$$

$$\mathcal{P} = \mathcal{N}_2\delta u_t^S + \mathcal{N}_3\delta u_\phi^S\,, \tag{C5e}$$

where $\mathcal{I}_{2,3}$, $\mathcal{U}_{2,3}$ and $\mathcal{N}_{2,3}$ can be found in the supplemental material of [37]. These simplifications make the calculation of the trajectory significantly faster.

Appendix D: Trajectories and fluxes in time domain

In this Appendix we describe our procedure to calculate trajectories and GW fluxes in the time domain in order to compare them with the frequency domain results.

First, we calculate the orbits using the full (nonlinearized in spin) MPD equations (3) in the time domain. The initial conditions have been chosen such that the orbits are at most $\mathcal{O}(\sigma^2)$ from orbits with given orbital parameters in the frequency domain. As initial conditions we choose E, J_z, r, θ, u^r, s^r and s^θ according to the values computed in the frequency domain. Then, we find the other initial conditions from Eqs. (4), (5), (6) and (21). For the evolution we used an implicit Gauss-

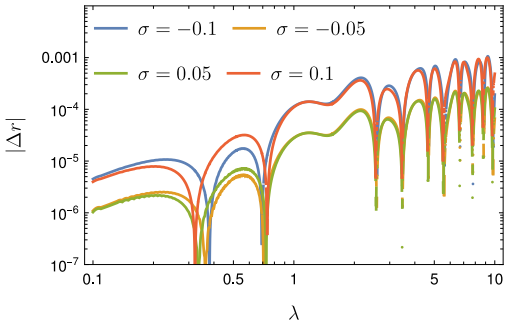

FIG. 7. Difference between the time domain calculation of r with the full MPD equations and linearized in spin frequency domain calculation of r for $a = 0.9M$, $p = 12.0$, $e = 0.2$, $I = 60°$ and different spins. The difference behaves as $\mathcal{O}(\sigma^2)$ and grows linearly in λ on average, because of the $\mathcal{O}(\sigma^2)$ difference in the frequencies.

Runge-Kutta integrator which is described in [65]. In Fig. 7 we plot for several spins the difference

$$\Delta r = r_{\rm td}(\lambda) - \hat{r}(\Upsilon_r \lambda) - r^S(\Upsilon_r \lambda, \Upsilon_z \lambda)\,,$$

where $r_{\rm td}(\lambda)$ is the evolution computed in time domain. It can be seen that the difference for $\sigma = \pm 0.1$ is four times larger than the difference for $\sigma = \pm 0.05$, thus it is indeed $\mathcal{O}(\sigma^2)$.

This trajectory was then used as an input to *Teukode* which numerically solves the Teukolsky equation. The output is the energy flux at infinity which must be averaged to compare it with the frequency domain result. For nearly spherical orbits it is straightforward since at linear order in spin the flux has period $2\pi/\Omega_z$. Thus, we can average the flux over several periods which have been calculated using the frequency domain approach.

For generic orbits the averaging procedure is more challenging, since the flux is not strictly periodic and it contains contributions from all the combinations of the frequencies Ω_r and Ω_z. This issue was resolved by consecutive moving averages with different periods. The main contribution to the oscillations of the flux comes from the radial motion between the pericentre and apocentre. Thus, we first compute the moving average of the time series with period $2\pi/\Omega_r$ to smooth-out the data. Then, we perform several other moving averages with periods $2\pi/\Omega_z$ and combinations $2\pi/(n\Omega_r + k\Omega_z)$. After several such averages, the time series is too short for another moving average, so we average all the remaining datapoints. This procedure appears to be reliable, since the results match the frequency domain calculations.

Appendix E: Plots and data tables

In this Appendix we show several plots of our frequency domain results and list the values for reference.

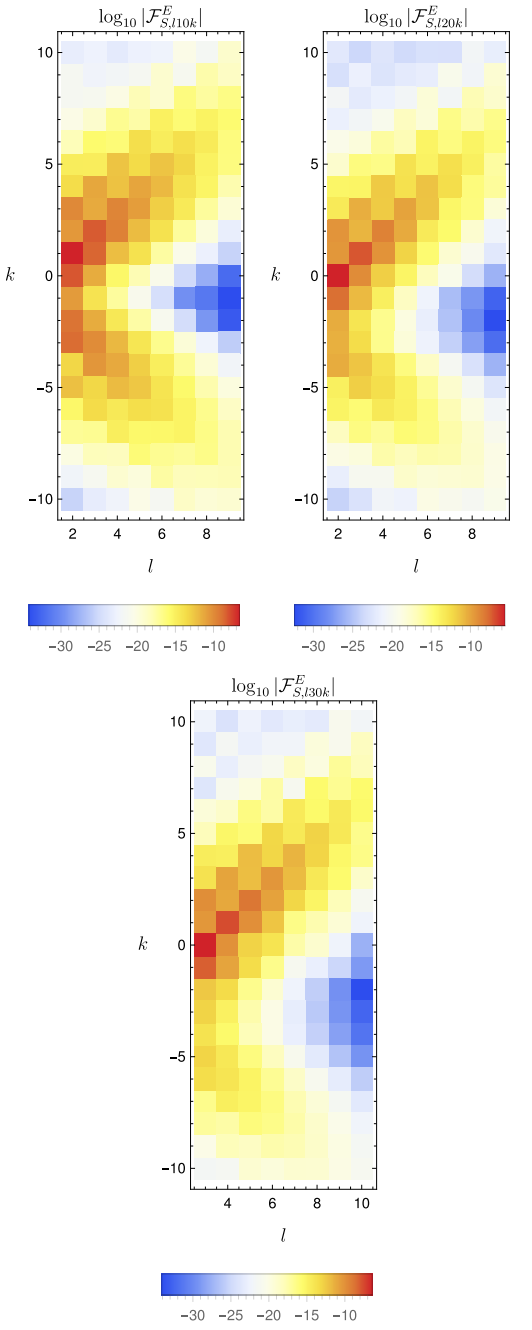

FIG. 8. linear-in-spin parts of the energy fluxes from nearly spherical orbits with $a = 0.9M$, $p = 10.0$, $I = 30°$ for different l, k modes and $m = 1, 2, 3$.

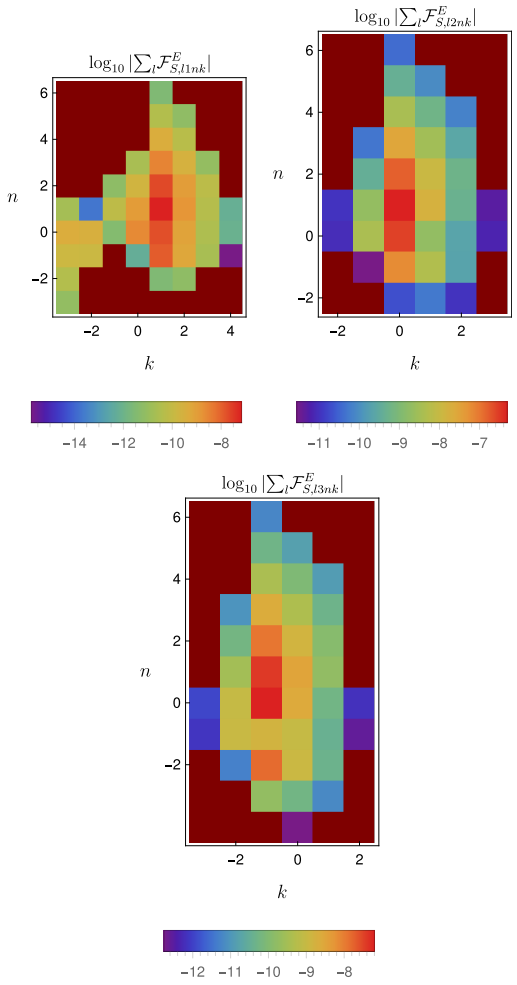

FIG. 9. The linear-in-spin parts of the energy fluxes from generic orbits $\log_{10}\left|\sum_l \mathcal{F}^E_{S,lmnk}\right|$ with $a = 0.9M$, $p = 12.0$, $e = 0.2$, $I = 30°$ for different n, k modes summed over l for $m = 1$ (top left), $m = 2$ (top right), $m = 3$ (bottom).

In Fig. 8 we plot the linear-in-spin part of the total energy flux from a nearly spherical orbit for different l, m and k. From these plots we can see that the linear-in-spin part of the flux has a global maximum at $k = l - m$ and a local maximum around $k = -l - m$. This behavior is similar to the behavior of geodesic flux that has been reported in [59].

In Fig. 9 we plot the m, n and k modes of the linearized in spin flux summed over l for a generic orbit. Because of the computational costs, we calculated only some of the l, m, n, k modes. We can see that the maximal mode is at $n = 1$ and $k = 2 - m$.

For reference, we list the m modes of the linear-in-spin part of the energy flux for spherical orbits in Table II and some of the l, m, n, k modes from generic orbits in Table III.

$I[°]$	m	$\mathcal{F}^E_{S,m}$	$\mathcal{F}^{J_z}_{S,m}$
30	1	-2.642×10^{-7}	-2.446×10^{-6}
30	2	-2.702×10^{-6}	-6.431×10^{-5}
30	3	-3.921×10^{-7}	-1.016×10^{-5}
60	1	-1.533×10^{-6}	-1.891×10^{-5}
60	2	-2.177×10^{-6}	-5.110×10^{-5}
60	3	-2.223×10^{-7}	-5.463×10^{-6}
120	1	-4.175×10^{-6}	3.021×10^{-5}
120	2	-1.796×10^{-6}	3.597×10^{-5}
120	3	-1.730×10^{-7}	4.020×10^{-6}
150	1	-2.859×10^{-6}	3.280×10^{-5}
150	2	-6.930×10^{-6}	1.658×10^{-5}
150	3	-1.069×10^{-6}	2.723×10^{-5}

TABLE II. linear-in-spin parts of the total energy fluxes and the angular momentum fluxes from nearly spherical orbits for given inclination I and azimuthal number m. The fluxes are summed over l and k.

[1] P. Amaro-Seoane, H. Audley, S. Babak, J. Baker, E. Barausse, P. Bender, E. Berti, P. Binetruy, M. Born, D. Bortoluzzi, J. Camp, C. Caprini, *et al.*, Laser Interferometer Space Antenna, arXiv e-prints , arXiv:1702.00786 (2017), arXiv:1702.00786 [astro-ph.IM].

[2] J. Luo, L.-S. Chen, H.-Z. Duan, Y.-G. Gong, S. Hu, J. Ji, Q. Liu, J. Mei, V. Milyukov, M. Sazhin, C.-G. Shao, V. T. Toth, H.-B. Tu, Y. Wang, Y. Wang, H.-C. Yeh, M.-S. Zhan, Y. Zhang, V. Zharov, and Z.-B. Zhou, TianQin: a space-borne gravitational wave detector, Classical and Quantum Gravity **33**, 035010 (2016), arXiv:1512.02076 [astro-ph.IM].

[3] W.-H. Ruan, Z.-K. Guo, R.-G. Cai, and Y.-Z. Zhang, Taiji program: Gravitational-wave sources, International Journal of Modern Physics A **35**, 2050075 (2020).

[4] S. Babak, J. Gair, A. Sesana, E. Barausse, C. F. Sopuerta, C. P. L. Berry, E. Berti, P. Amaro-Seoane, A. Petiteau, and A. Klein, Science with the space-based interferometer LISA. V. Extreme mass-ratio inspirals, Phys. Rev. D **95**, 103012 (2017), arXiv:1703.09722 [gr-qc].

[5] E. Poisson, A. Pound, and I. Vega, The Motion of Point Particles in Curved Spacetime, Living Reviews in Rela-

m	l	n	k	$\mathrm{Re}\left\{C^{+}_{S,lmnk}\right\}$	$\mathrm{Im}\left\{C^{+}_{S,lmnk}\right\}$	$\mathrm{Re}\left\{C^{-}_{S,lmnk}\right\}$	$\mathrm{Im}\left\{C^{-}_{S,lmnk}\right\}$
1	2	0	1	4.8962×10^{-6}	-1.6020×10^{-6}	-5.2716×10^{-6}	-2.7823×10^{-7}
1	2	1	1	9.9514×10^{-6}	-2.7846×10^{-6}	3.8592×10^{-6}	8.7391×10^{-7}
1	2	2	1	7.3027×10^{-6}	-2.1468×10^{-6}	3.7407×10^{-6}	7.8065×10^{-7}
1	2	3	1	3.6008×10^{-6}	-1.1232×10^{-6}	1.7742×10^{-6}	3.8842×10^{-7}
1	3	0	2	-9.4587×10^{-8}	1.3025×10^{-7}	-5.8770×10^{-7}	-4.1971×10^{-7}
1	3	1	2	-8.8801×10^{-7}	-1.7932×10^{-6}	-3.2098×10^{-7}	-2.1754×10^{-7}
1	3	2	2	-9.8569×10^{-7}	-1.9468×10^{-6}	-1.1060×10^{-7}	-6.4897×10^{-8}
1	3	3	2	-6.6574×10^{-7}	-1.2388×10^{-6}	-3.7354×10^{-8}	-1.4854×10^{-8}
2	2	0	0	-1.9890×10^{-5}	5.8986×10^{-6}	-7.5636×10^{-6}	-3.6977×10^{-6}
2	2	1	0	-3.6535×10^{-5}	1.0473×10^{-5}	-2.8727×10^{-5}	-9.5114×10^{-6}
2	2	2	0	-2.8239×10^{-5}	8.6430×10^{-6}	-2.1354×10^{-5}	-7.5839×10^{-6}
2	2	3	0	-1.5302×10^{-5}	4.9730×10^{-6}	-1.0601×10^{-5}	-4.1408×10^{-6}
2	3	0	1	8.2420×10^{-7}	9.2288×10^{-7}	6.8449×10^{-7}	1.3381×10^{-6}
2	3	1	1	3.8727×10^{-6}	7.7467×10^{-6}	-1.2893×10^{-7}	-2.4943×10^{-7}
2	3	2	1	4.3094×10^{-6}	8.2104×10^{-6}	-4.2520×10^{-7}	-8.2810×10^{-7}
2	3	3	1	3.0636×10^{-6}	5.4471×10^{-6}	-3.3219×10^{-7}	-6.4545×10^{-7}
3	3	0	0	-2.2312×10^{-6}	-3.3582×10^{-6}	-3.0967×10^{-7}	-1.2954×10^{-6}
3	3	1	0	-8.9746×10^{-6}	-1.7781×10^{-5}	5.0351×10^{-7}	3.8648×10^{-6}
3	3	2	0	-1.0099×10^{-5}	-1.8845×10^{-5}	6.2534×10^{-7}	4.8041×10^{-6}
3	3	3	0	-7.3942×10^{-6}	-1.2830×10^{-5}	4.0686×10^{-7}	3.3295×10^{-6}
3	4	0	1	1.1671×10^{-6}	-4.1185×10^{-7}	1.9807×10^{-7}	-2.0808×10^{-7}
3	4	1	1	-3.6720×10^{-6}	2.6844×10^{-6}	4.2934×10^{-8}	-4.2764×10^{-8}
3	4	2	1	-5.6428×10^{-6}	4.2331×10^{-6}	-8.4756×10^{-8}	9.4155×10^{-8}
3	4	3	1	-4.6912×10^{-6}	3.7655×10^{-6}	-1.0502×10^{-7}	1.1655×10^{-7}

TABLE III. Real and imaginary parts of the linear-in-spin parts of amplitudes computed at infinity and at the horizon for given l, m, n and k of a generic orbit with $a = 0.9M$, $p = 12$, $e = 0.2$, $I = 30^\circ$.

tivity **14**, 7 (2011), arXiv:1102.0529 [gr-qc].

[6] A. Pound and B. Wardell, Black hole perturbation theory and gravitational self-force, in *Handbook of Gravitational Wave Astronomy*, edited by C. Bambi, S. Katsanevas, and K. D. Kokkotas (Springer Singapore, Singapore, 2020) pp. 1–119.

[7] L. Barack and A. Pound, Self-force and radiation reaction in general relativity, Reports on Progress in Physics **82**, 016904 (2019), arXiv:1805.10385 [gr-qc].

[8] T. Hinderer and É. É. Flanagan, Two-timescale analysis of extreme mass ratio inspirals in Kerr spacetime: Orbital motion, Phys. Rev. D **78**, 064028 (2008), arXiv:0805.3337 [gr-qc].

[9] J. Miller and A. Pound, Two-timescale evolution of extreme-mass-ratio inspirals: Waveform generation scheme for quasicircular orbits in Schwarzschild spacetime, Phys. Rev. D **103**, 064048 (2021), arXiv:2006.11263 [gr-qc].

[10] R. Fujita and M. Shibata, Extreme mass ratio inspirals on the equatorial plane in the adiabatic order, Phys. Rev. D **102**, 064005 (2020), arXiv:2008.13554 [gr-qc].

[11] S. A. Hughes, N. Warburton, G. Khanna, A. J. K. Chua, and M. L. Katz, Adiabatic waveforms for extreme mass-ratio inspirals via multivoice decomposition in time and frequency, Phys. Rev. D **103**, 104014 (2021), arXiv:2102.02713 [gr-qc].

[12] V. Skoupý and G. Lukes-Gerakopoulos, Adiabatic equatorial inspirals of a spinning body into a Kerr black hole, Phys. Rev. D **105**, 084033 (2022), arXiv:2201.07044 [gr-qc].

[13] S. Isoyama, R. Fujita, A. J. K. Chua, H. Nakano, A. Pound, and N. Sago, Adiabatic Waveforms from Extreme-Mass-Ratio Inspirals: An Analytical Approach, Phys. Rev. Lett. **128**, 231101 (2022), arXiv:2111.05288 [gr-qc].

[14] M. D. Hartl, Dynamics of spinning test particles in Kerr spacetime, Phys. Rev. D **67**, 024005 (2003), arXiv:gr-qc/0210042 [gr-qc].

[15] N. Sago, T. Tanaka, W. Hikida, K. Ganz, and H. Nakano, Adiabatic Evolution of Orbital Parameters in Kerr Spacetime, Progress of Theoretical Physics **115**, 873 (2006), arXiv:gr-qc/0511151 [gr-qc].

[16] S. Akcay, S. R. Dolan, C. Kavanagh, J. Moxon, N. Warburton, and B. Wardell, Dissipation in extreme mass-ratio binaries with a spinning secondary, Phys. Rev. D **102**, 064013 (2020), arXiv:1912.09461 [gr-qc].

[17] J. Mathews, A. Pound, and B. Wardell, Self-force calculations with a spinning secondary, Phys. Rev. D **105**, 084031 (2022), arXiv:2112.13069 [gr-qc].

[18] V. Witzany, J. Steinhoff, and G. Lukes-Gerakopoulos, Hamiltonians and canonical coordinates for spinning particles in curved space-time, Classical and Quantum Gravity **36**, 075003 (2019), arXiv:1808.06582 [gr-qc].

[19] R. Rüdiger, Conserved quantities of spinning test particles in general relativity. I, Proc. R. Soc. Lond. A **375**, 185–193 (1981).

[20] R. Rüdiger, Conserved quantities of spinning test particles in general relativity. II, Proc. R. Soc. Lond. A **385**, 229–239 (1981).

[21] V. Witzany, Hamilton-Jacobi equation for spinning particles near black holes, Phys. Rev. D **100**, 104030 (2019), arXiv:1903.03651 [gr-qc].

[22] B. Carter, Global Structure of the Kerr Family of Gravitational Fields, Physical Review **174**, 1559 (1968).

[23] C. Cutler, D. Kennefick, and E. Poisson, Gravitational radiation reaction for bound motion around a schwarzschild black hole, Phys. Rev. D **50**, 3816 (1994).

[24] L. S. Finn and K. S. Thorne, Gravitational waves from a compact star in a circular, inspiral orbit, in the equatorial plane of a massive, spinning black hole, as observed by lisa, Phys. Rev. D **62**, 124021 (2000).

[25] K. Glampedakis and D. Kennefick, Zoom and whirl: Eccentric equatorial orbits around spinning black holes and their evolution under gravitational radiation reaction, Phys.Rev. **D66**, 044002 (2002), arXiv:gr-qc/0203086 [gr-qc].

[26] M. Shibata, Gravitational waves by compact star orbiting around rotating supermassive black holes, Phys. Rev. D **50**, 6297 (1994).

[27] S. Drasco and S. A. Hughes, Gravitational wave snapshots of generic extreme mass ratio inspirals, Phys.Rev. **D73**, 024027 (2006), arXiv:gr-qc/0509101 [gr-qc].

[28] W.-B. Han, Gravitational radiation from a spinning compact object around a supermassive Kerr black hole in circular orbit, Phys. Rev. D **82**, 084013 (2010), arXiv:1008.3324 [gr-qc].

[29] E. Harms, G. Lukes-Gerakopoulos, S. Bernuzzi, and A. Nagar, Asymptotic gravitational wave fluxes from a spinning particle in circular equatorial orbits around a rotating black hole, Phys. Rev. D **93**, 044015 (2016), arXiv:1510.05548 [gr-qc].

[30] E. Harms, G. Lukes-Gerakopoulos, S. Bernuzzi, and A. Nagar, Spinning test body orbiting around a Schwarzschild black hole: Circular dynamics and gravitational-wave fluxes, Phys. Rev. D **94**, 104010 (2016), arXiv:1609.00356 [gr-qc].

[31] G. Lukes-Gerakopoulos, E. Harms, S. Bernuzzi, and A. Nagar, Spinning test body orbiting around a Kerr black hole: Circular dynamics and gravitational-wave fluxes, Phys. Rev. D **96**, 064051 (2017), arXiv:1707.07537 [gr-qc].

[32] G. A. Piovano, A. Maselli, and P. Pani, Extreme mass ratio inspirals with spinning secondary: A detailed study of equatorial circular motion, Phys. Rev. D **102**, 024041 (2020), arXiv:2004.02654 [gr-qc].

[33] G. A. Piovano, R. Brito, A. Maselli, and P. Pani, Assessing the detectability of the secondary spin in extreme mass-ratio inspirals with fully relativistic numerical waveforms, Phys. Rev. D **104**, 124019 (2021), arXiv:2105.07083 [gr-qc].

[34] V. Skoupý and G. Lukes-Gerakopoulos, Gravitational wave templates from Extreme Mass Ratio Inspirals, arXiv e-prints , arXiv:2101.04533 (2021), arXiv:2101.04533 [gr-qc].

[35] M. Rahman and A. Bhattacharyya, Prospects for determining the nature of the secondaries of extreme mass-ratio inspirals using the spin-induced quadrupole deformation, Phys. Rev. D **107**, 024006 (2023), arXiv:2112.13869 [gr-qc].

[36] V. Skoupý and G. Lukes-Gerakopoulos, Spinning test body orbiting around a Kerr black hole: Eccentric equatorial orbits and their asymptotic gravitational-wave fluxes, Phys. Rev. D **103**, 104045 (2021), arXiv:2102.04819 [gr-qc].

[37] L. V. Drummond and S. A. Hughes, Precisely computing bound orbits of spinning bodies around black holes. I. General framework and results for nearly equatorial orbits, Phys. Rev. D **105**, 124040 (2022), arXiv:2201.13334 [gr-qc].

[38] L. V. Drummond and S. A. Hughes, Precisely computing bound orbits of spinning bodies around black holes. II. Generic orbits, Phys. Rev. D **105**, 124041 (2022), arXiv:2201.13335 [gr-qc].

[39] M. Mathisson, Neue mechanik materieller systemes, Acta Phys. Polon. **6**, 163 (1937).

[40] M. Mathisson, Republication of: New mechanics of material systems, Gen. Relativ. Gravit. **42**, 1011 (2010).

[41] W. Dixon, Isolated gravitating systems in general relativity, Proceedings of the International School of Physics "Enrico Fermi," Course LXVII, edited by J. Ehlers, North Holland, Amsterdam , 156 (1979).

[42] A. Papapetrou, Spinning test particles in general relativity. 1., Proc.Roy.Soc.Lond. **A209**, 248 (1951).

[43] W. Dixon, Dynamics of extended bodies in general relativity. I. Momentum and angular momentum, Proc. R. Soc. A **314**, 499 (1970).

[44] W. Tulczyjew, Motion of multipole particles in general relativity theory, Acta Phys. Pol. **18**, 393 (1959).

[45] J. Ehlers and E. Rudolph, Dynamics of extended bodies in general relativity center-of-mass description and quasirigidity, Gen. Relativ. Gravit. **8**, 197 (1977).

[46] S. Suzuki and K.-I. Maeda, Chaos in Schwarzschild spacetime: The motion of a spinning particle, Phys. Rev. D **55**, 4848 (1997), arXiv:gr-qc/9604020 [gr-qc].

[47] M. Visser, The Kerr spacetime: A brief introduction, arXiv e-prints , arXiv:0706.0622 (2007), arXiv:0706.0622 [gr-qc].

[48] O. Zelenka, G. Lukes-Gerakopoulos, V. Witzany, and O. Kopáček, Growth of resonances and chaos for a spinning test particle in the Schwarzschild background, Phys. Rev. D **101**, 024037 (2020), arXiv:1911.00414 [gr-qc].

[49] J.-A. Marck, Solution to the equations of parallel transport in kerr geometry; tidal tensor, Proceedings of the Royal Society of London. Series A, Mathematical and Physical Sciences **385**, 431 (1983).

[50] M. van de Meent, Analytic solutions for parallel transport along generic bound geodesics in Kerr spacetime, Classical and Quantum Gravity **37**, 145007 (2020), arXiv:1906.05090 [gr-qc].

[51] R. Fujita and W. Hikida, Analytical solutions of bound timelike geodesic orbits in kerr spacetime, Classical and Quantum Gravity **26**, 135002 (2009).

[52] S. A. Teukolsky, Perturbations of a rotating black hole. 1. Fundamental equations for gravitational electromagnetic and neutrino field perturbations, Astrophys. J. **185**, 635 (1973).

[53] T. Tanaka, Y. Mino, M. Sasaki, and M. Shibata, Gravitational waves from a spinning particle in circular orbits around a rotating black hole, Phys. Rev. D **54**, 3762 (1996), arXiv:gr-qc/9602038 [gr-qc].

[54] Black Hole Perturbation Toolkit, (bhptoolkit.org) (2023).

[55] S. Hopper, E. Forseth, T. Osburn, and C. R. Evans, Fast spectral source integration in black hole perturbation calculations, Phys. Rev. D **92**, 044048 (2015), arXiv:1506.04742 [gr-qc].

[56] R. P. Macedo, B. Leather, N. Warburton, B. Wardell, and A. Zenginoğlu, Hyperboloidal method for frequency-domain self-force calculations, Phys. Rev. D **105**, 104033 (2022), arXiv:2202.01794 [gr-qc].

[57] S. Mano, H. Suzuki, and E. Takasugi, Analytic solutions of the Teukolsky equation and their low frequency expansions, Prog.Theor.Phys. **95**, 1079 (1996), arXiv:gr-

qc/9603020 [gr-qc].
[58] E. W. Leaver, Spectral decomposition of the perturbation response of the Schwarzschild geometry, Phys.Rev. **D34**, 384 (1986).
[59] M. Kerachian, L. Polcar, V. Skoupý, C. Efthymiopoulos, and G. Lukes-Gerakopoulos, Action-Angle formalism for extreme mass ratio inspirals in Kerr spacetime, arXiv e-prints , arXiv:2301.08150 (2023), arXiv:2301.08150 [gr-qc].
[60] N. Sago and R. Fujita, Calculation of radiation reaction effect on orbital parameters in Kerr spacetime, Progress of Theoretical and Experimental Physics **2015**, 073E03 (2015), arXiv:1505.01600 [gr-qc].
[61] E. Harms, S. Bernuzzi, A. Nagar, and A. Zenginoglu, A new gravitational wave generation algorithm for particle perturbations of the Kerr spacetime, Class. Quant. Grav. **31**, 245004 (2014), arXiv:1406.5983 [gr-qc].
[62] M. van de Meent, Gravitational self-force on generic bound geodesics in Kerr spacetime, Phys. Rev. D **97**, 104033 (2018), arXiv:1711.09607 [gr-qc].
[63] B. Wardell, A. Pound, N. Warburton, J. Miller, L. Durkan, and A. Le Tiec, Gravitational waveforms for compact binaries from second-order self-force theory, arXiv e-prints , arXiv:2112.12265 (2021), arXiv:2112.12265 [gr-qc].
[64] P. Lynch, M. van de Meent, and N. Warburton, Eccentric self-forced inspirals into a rotating black hole, Classical and Quantum Gravity **39**, 145004 (2022), arXiv:2112.05651 [gr-qc].
[65] G. Lukes-Gerakopoulos, J. Seyrich, and D. Kunst, Investigating spinning test particles: spin supplementary conditions and the Hamiltonian formalism, Phys.Rev. **D90**, 104019 (2014), arXiv:1409.4314 [gr-qc].